An International Journal of Optimization and Control:

Theories & Applications

CONTENTS

RESEARCH ARTICLES

RESEARCH ARTICLE

Examination and experimental comparison of dc/dc buck converter topologies used in wireless electric vehicle charging applications

Hakan Akca [a *], Ahmet Aktas [b]

[a] Department of Electrical and Electronics Engineering, Faculty of Engineering, Ege University, 35040, Izmir, Türkiye
[b] Department of Energy Systems Engineering, Faculty of Technology, Gazi University, 06560, Ankara, Türkiye
hakan.akca@ege.edu.tr, a.aktas@gazi.edu.tr

ARTICLE INFO	ABSTRACT
	The studies on Wireless Power Transfer (WPT) technology and peripherals in Electric Vehicle (EV) applications are intensifying. While the energy received from the WPT system is transferred to the EV battery, the direct current (dc)/dc converter circuits are used. The dc/dc buck converter topologies are one of them. The converter circuits must be highly efficient, lightweight, and compact to have a high range in EV vehicles. There are asynchronous buck, synchronous buck, and interleaved synchronous buck converter circuit topologies from the literature. In this study, the efficiency results of these circuit topologies were analyzed using MATLAB/Simulink and experimental studies. This study contributes to the literature by conducting circuit-level efficiency analysis and component-level power loss analysis. It has been observed that the interleaved synchronous buck converter circuit operates at 99% efficiency at 1066 W. In addition, it has been shared with the oscilloscope results that the current ripples of this circuit topology are lower than other circuit converters. Specifically, there has been a significant reduction of 56% in power losses, particularly in the interleaved synchronous buck converter (ISBC). This study analyzes the dynamic behavior of the dc/dc buck converter topologies, and results about their performance are given.

1. Introduction

Electric vehicles play a crucial role in sustainable transportation solutions, standing out prominently as an eco-friendly alternative to fossil fuel-dependent conventional vehicles [1]. The growing demand requires developing and optimizing charging infrastructure for electric vehicles [2]. In this context, wireless charging systems for electric vehicles represent a significant technological advancement with the potential to make the charging process more user-friendly, accessible, and practical to reach a higher user rate. The wireless power transfer (WPT) system [3, 4] enables the transfer of energy by utilizing primary and secondary coils used for charging electric vehicles [5]. Figure 1 illustrates an example of a WPT system. This system includes two main parts: the ground station and the electric vehicle side.
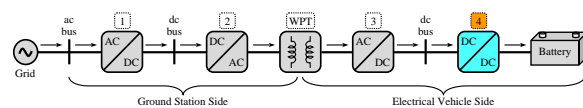
Figure 1. Unidirectional wireless power transfer system

On the ground station side, high-frequency alternating current (ac) is obtained to feed the coils on the primary coil of the WPT system. Firstly, ac obtained from the grid is rectified to direct current (dc) using an ac/dc converter. The obtained dc energy is then converted back to high-frequency ac energy using a dc/ac converter, making the primary coil ready for energy transfer. The electrical vehicle side includes the secondary side of the WPT system and has a battery connection. Different circuit structures and control algorithms play an important role during energy flow from the secondary coil to the battery. Some control techniques include primary control [6] and secondary side control [7]. This study implements secondary side control, where the ac energy at the output of the secondary coil is transferred to the battery using an ac/dc full bridge diode rectifier and a dc/dc converter in the block 4 (dc/dc) in Figure 1. The battery current and voltage are controlled by this converter, allowing for a more precise management of the charging process.

When examining battery charging systems [8], different dc/dc topologies [9] come into play. Buck converters are employed in applications with lower

---

battery voltage than the dc bus voltage. The dc bus is located between block 3 (ac/dc) and block 4 (dc/dc) in Figure 1.

Within the scope of buck converters, dc/dc buck converter topologies such as asynchronous buck, synchronous buck, and interleaved synchronous buck [10] will be comprehensively discussed. The asynchronous buck topology is a commonly used switching power converter type in dc/dc converters. The synchronous buck, unlike the asynchronous buck, incorporates a semiconductor switch. This reduces losses occurring on the diode, potentially increasing circuit efficiency and optimizing dynamic performance. The interleaved synchronous buck [11] topology is achieved by parallel operating multiple synchronous buck converters. This can provide higher efficiency and lower current ripples in high-power applications. This article will thoroughly discuss the performance of these topologies in battery charging applications.

This study includes the following sections: Section II asynchronous buck, synchronous buck, and interleaved synchronous buck converter circuit topologies and control algorithms are explained. Section III includes MATLAB/Simulink simulation studies of these dc/dc buck converters. Section IV describes the experimental study stages and gives the dc/dc buck converters' current, voltage, and efficiency comparisons. Section V covers the conclusion section.

2. dc/dc buck converter topologies

In power electronics converter applications, the dc/dc buck converter circuits reduce dc output voltage [12]. In this study, asynchronous buck converter (ABC), synchronous buck converter (SBC), and interleaved synchronous buck converter (ISBC) topologies were examined. The total circuit efficiency decreases when high powers are reached in the conventional asynchronous buck converter circuit [13]. In dc/dc buck converter circuit topologies, ISBC topology transfers power at high efficiency [14].The following headings explain the ABC, SBC, and ISBC topologies.

2.1. Asynchronous buck converter (ABC)

The ABC topology has the conventional dc/dc buck circuit structure. In this circuit topology, there is a switch and a diode. Depending on the control algorithm, the S1 is switched at a determined duty cycle rate. When S_1 is closed, current flows through the switch and inductance towards the output in Figure 2 (a). In this case, D_1 is closed, and no current flows through the diode. When the S_1 is open, D_1 turns into conduction due to inductance counter-electromotive force (CEMF) in Figure 2 (b).

The ABC circuit's continuous conduction mode (CCM) operating states are detailed in Figure 2.
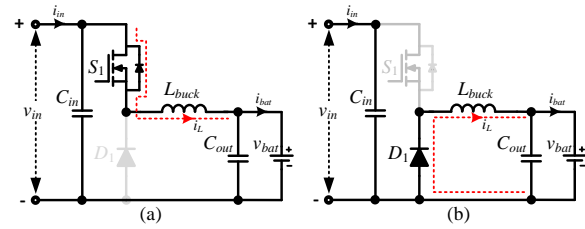
Figure 2. Operation modes of the asynchronous buck converter: (a) S_1 is on, (b) S_1 is off

Asynchronous buck converter output voltage depends on the v_{bat_ABC} duty cycle D ratio and can be written as in Eq. (1).

$$v_{bat\_ABC} = v_{in} D \tag{1}$$

where; v_{in} is the input voltage of the ABC. The inductance L_{buck} and capacitor C_{out} values in the ABC circuit can be determined by Eq. (2) and Eq. (3), respectively.

$$L_{buck} = \frac{v_{in} (v_{in} - v_{bat})}{f_s \, \Delta i_L \, v_{in}} \tag{2}$$

$$C_{out} = \frac{\Delta i_{L\_ABC}}{8 f_s \, \Delta v_{bat}} \tag{3}$$

where; f_s is the switching frequency, Δi_{L_ABC} is the inductor ripple current, Δv_{bat_ABC} is the output voltage ripple. In this study, i_{L_ABC} is designed to be a maximum of 20%, v_{bat_ABC} is designed to be a maximum of 0.15%, and these values are expressed as:

$$\Delta i_{L\_ABC} = \frac{D (v_{in} - v_{bat})}{f_s \, L_{buck}} \tag{4}$$

$$\Delta v_{bat\_ABC} = \frac{\Delta i_{L\_ABC}}{8 f_s \, C_{out}} \tag{5}$$

When the S_1 is closed, the inductance operates at $v_{in} - v_{bat}$ voltage. When S_1 is open, it induces a CEMF equal to the inductance voltage v_{bat}. The following equation can express inductance voltage according to the S_1 position.

$$\begin{cases} v_{in} - v_{bat} = L_{buck} \dfrac{di_{L\_ABC}}{dt} & | \quad S_1 \text{ - } on \\ -v_{bat} = L_{buck} \dfrac{di_{L\_ABC}}{dt} & | \quad S_1 \text{ - } off \end{cases} \tag{6}$$

2.2. Synchronous buck converter (SBC)

The difference between the synchronous buck converter circuit and the asynchronous topology [15] is that there is an S_2 instead of a D_1. The voltage drop on D_1 in the ABC circuit is higher than on a semiconductor switch. This situation causes high losses in high-power applications. The SBC topology is preferred in high-power applications due to low voltage drop and less power loss. The SBC circuit structure and current flow diagram according to operating states are given in detail in Figure 3. In the SBC circuit, S_1 and S_2 are operated with a phase shift of 180°.
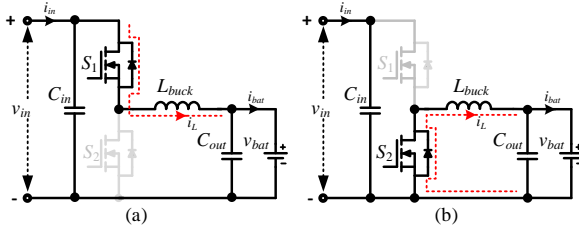
Figure 3. Operation modes of the synchronous buck converter: (a) S_1 is on, S_2 is off, (b) S_1 is off, and S_2 is on

The voltage gain of the SBC circuit can be described by Eq. (1) in the CCM as in the ABC structure. Because the only difference between the ABC and SBC is the use of SIC MOSFET instead of a diode, the output current and output voltage ripple of the SBC circuit can be calculated by Eq. (4) and Eq. (5), respectively, as in the ABC topology.

2.3. Interleaved synchronous buck converter (ISBC)

In conventional dc/dc buck converter circuits, inductance losses increase when high currents are reached. The interleaved topology structure shares the total current transferred to the output $i_L=i_{L1}+i_{L2}$. In this topology structure, more than one phase arm is created, and an inductance is connected to each. Thus, the losses of switching elements and the volumes of passive circuit elements can be reduced. The ISBC [16] circuit topology and operating ranges used in this study are detailed in Figure 4. The S_1-S_4 and S_2-S_3 switches in the ISBC circuit are switched with a phase shift of 180°.
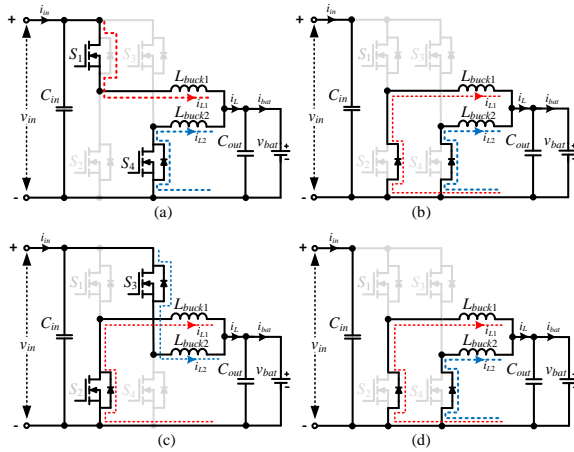
Figure 4. Operation modes of the interleaved synchronous buck converter: (a) S_1 and S_4 are on, S_2 and S_3 are off, (b) S_1 and S_4 are off, and S_2 and S_3 are on

In the ISBC circuit, the output current equals the sum of the coil currents. In this converter structure, when D 0.5, the output current ripple is theoretically equal to 0. The voltage gain of the ISBC circuit can be described by Eq. (1) in the case of the CCM as in the ABC structure. The output current ripple of the ISBC circuit can be explained as follows.

$$\Delta i_{L\_ISBC}=\frac{v_{bat}\,D\,(1-2D)}{L_{buck1}\,f_s} \qquad (7)$$
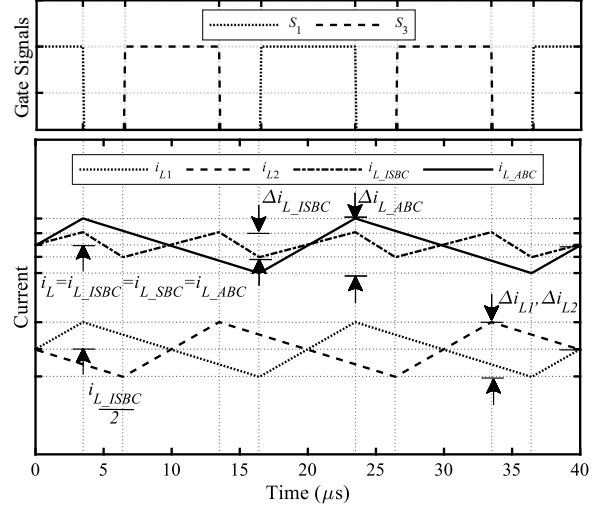
Figure 5. Gate signals and idealized current waveforms of the SBC and ISBC circuits

Since the two inductances in the ISBC structure reduce the current ripple, the voltage fluctuations at the circuit output are half as much as in the ABC circuit topology and are expressed as in Eq. (8).

$$\Delta v_{bat\_ISBC}=\frac{\Delta i_{L\_ISBC}}{16 f_s\,C_{out}} \qquad (8)$$

Figure 5 shows the inductance and the output current waveforms depending on the gate signals of the SBC and the ISBC circuits. In the idealized current waveforms, the output current ripple of the ISBC circuit is lower than the SBC circuit.

Advantages of the ISBC circuit topology: reduced input and output capacitors, high efficiency at high load currents, improved thermal performance, and low voltage ripple during load transitions [16]. Table 1 gives the design parameters of the dc/dc buck converter circuits used in this study.

Table 1. System the design parameters of the dc/dc buck converter topologies

Descriptions	Parameters	Value
Input dc bus voltage	v_{in}	200 V
Maximum input dc current	i_{in_max}	17 A
Maximum battery voltage	v_{bat_max}	200 V
Maximum battery current	i_{bat_max}	25 A
Nominal power	P_{nom}	3.5 kW
Inductance	L_{buck}	500 µH
Inductance resistance	R_{Lbuck}	40 mΩ
Input capacitance	C_{in}	560 µF × 2 ‖ 4 470 nF ‖ 4
Input capacitance resistance	R_{Cin}	54 mΩ (560 µF) 4.49 mΩ (470 nF)
Output capacitance	C_{out}	560 µF 470 nF
Output capacitance resistance	R_{Cout}	54 mΩ (560 µF) 4.49 mΩ (470 nF)
Inductance current ripple	Δi_L	20 %
Capacitance voltage ripple	Δv_C	0.15 %
Voltage PI$_1$ block	$Kp_1 - Ki_1$	0.2 – 0.05
Current PI$_2$ block	$Kp_2 - Ki_2$	0.01 – 1e-6

2.4. Control algorithms of the dc/dc buck converter topologies

This study used a battery group representing the electric vehicle (EV) battery. The EV battery group was charged with a closed-loop control method using the constant voltage method. Reference voltage values were entered into the control algorithm for three different situations: 160 V, 185 V, and 195 V, depending on the battery's state of charge (SOC).

Current reference is produced by the PI_1 block according to the measured voltage and defined reference voltage value of the EV battery group. Then, the PI_2 block has a switching signal according to the battery current and reference current value. The EV battery group's maximum charging current is i_{bat_ref} 25 A. Figure 6 shows the block diagram of the closed-loop control algorithm of the dc/dc buck converters. In the study, the ABC, SBC, and ISBC circuit switches at 50 kHz with a triangular carrier and comparator. The dead time between switches in the same branch is 200 nS. Table 1 gives the PI block coefficients in the control algorithm. The saturation limits for the PI_2 outputs are set with a minimum of D_{min} 0 and a maximum of D_{max} 1.
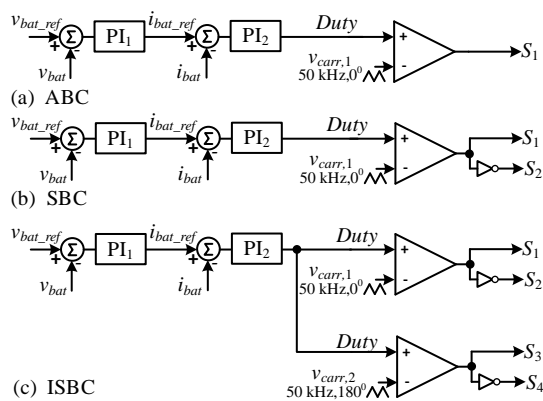
Figure 6. Block diagram of the control algorithm of the dc/dc buck converter topologies: (a) for the ABC, (b) for the SBC, and (c) for the ISBC

2.5. Operation area analysis

This study used a lithium iron phosphate (LifePO$_4$) battery with a capacity of 9.6 kWh was used as the EV battery group. The operating voltage of the battery group varies between 160 V – 200 V, and the charge graph at 1C is given in Figure 7.

This study determined the dc bus voltage at the dc/dc buck converter input as 200 V. Different voltages are needed to charge the EV battery group. For this reason, a dc/dc buck converter was used in the wireless EV charging system. When the charging graph of the EV battery group is examined, there is a voltage demand of 160 V and 200 V.

In this study, the EV battery group was charged with constant voltages of 160 V, 185 V, and 195 V, respectively.
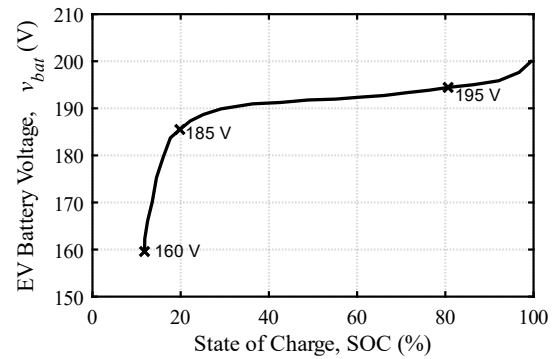
Figure 7. Charging graph of the LiFePO$_4$ type EV battery rated 9.6 kWh capacity

The battery charging and discharging operations are performed to keep the SOC within the range 20% to 80% for health of the battery. Therefore, 185V and 195V voltage values are selected. Additionally, the circuit's performance at the minimum voltage is examined, while the maximum voltage of 200V is excluded. Because D 1 is required to achieve 200V output voltage. For this D value, the SIC MOSFET always on, and the diode remains in an always off. In this configuration, SIC MOSFET has only conduction losses without any switching losses, as diode has no losses. Thus, the system's performance is analyzed where the D is less than 1. Initially, it was charged with 160 V until the SOC reached 20% to avoid charging at a high current for battery health. Then, the EV battery group was charged with a high current at 185 V until the SOC reached 80%. Finally, the battery charging process was completed with 195 V and a low current. This means there are different operating areas for different current and voltage levels. In this study, the performances of the dc/dc buck converter topologies in different operating areas were examined in detail.

3. Experimental and simulation results

A modular power circuit was prepared for the ABC, SBC, and ISBC circuits in the study. The experimental setup includes all power stages, measurements, and control units that enable the EV wireless charging. The experimental setup photo is given in Figure 8. The dc/dc buck converter part in the whole circuit given in the Figure 9 was examined for this study. The dc/dc buck converter part in the total circuit was examined for this study. The control unit contains an STM32H750 microcontroller of the STMicroelectronics. Wolfspeed brand's C3M0045065K model SIC MOSFET with 650 V, 49 A, and 4.5 mΩ internal resistance was used as the semiconductor switch in the power circuit. SIC MOSFETs are switched with Infineon Technologies' 1ED020I12B2XUMA1 model gate driver integrated circuits. Differential PWM's are applied to input of gate driver. Differential PWM signals may exhibit greater resilience against potential electromagnetic interference. In this study, the PWM signals is converted into a differential form by using a ST26C31BDR model differential line driver. Wolfspeed brand's E3D20065D SIC diode with 650 V

and 56 A rated was preferred for the reverse diode in the ABC circuit. The filter capacitors contain 560 µF aluminum electrolytic and 470 nF film capacitors of the Wurth brand. The inductances were produced as 52 turns using Magnetics brand 0078617A7 number ferrite core toroid material and 4mm^2 wire. AMC 1301 integrated circuit is used as a voltage sensor and LEM CAS 25-np is used as a current sensor. These sensors provide data to the microcontroller. A signal conditioning circuit is necessary to connect these sensors to the microcontroller. This circuit both converts the sensor output data to a suitable voltage level for the microcontroller and additionally protects the microcontroller ADC inputs. Chroma 62000S-H 600 V 17 A programmable power supply was used at the dc input of the dc/dc buck converter circuits. Auxiliary power supply (UTP3315TFL-II) was used to provide 12V for circuits such as control card, gate driver, fans, etc. Voltage probe (Pintek DP25) and current probe (TCPA3000) were used to measure input and output voltage and current data. These probes are compatible with both oscilloscope and data acq card (NI USB 6356). While the oscilloscope shows the signals waveform on its screen, daq card can transfer the measured data to computer.
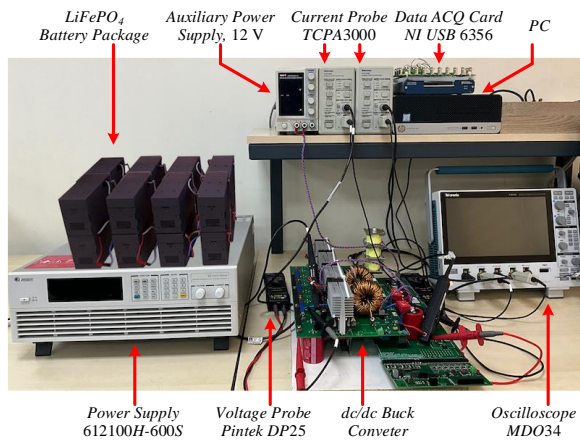
Figure 8. Photograph of the experimental setup
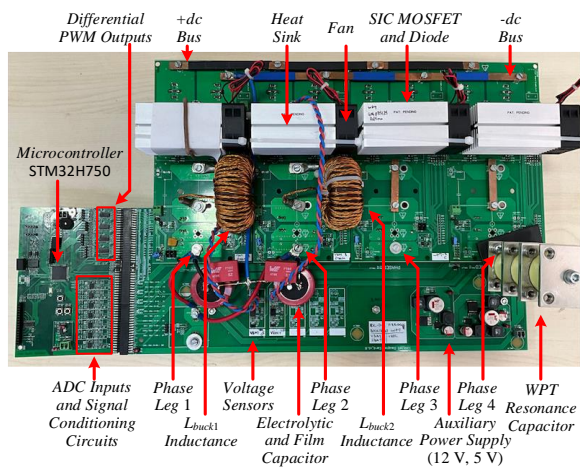
Figure 9. Photograph of the dc/dc buck converter and the control board

The 200 V 24 Ah rated LifePO$_4$ EV battery was connected to the output of the dc/dc buck converter circuits. Since the input/output current and voltage graphs of the ABC and SBC circuits are the same, the oscilloscope results for the SBC topology are given in Figure 10. In this operating state, the input voltage and current of the SBC circuit are 198.7 V and 7.856 A, and the output voltage and current are 149.2 V and 10.58 A. In this case, the EV battery group is charged with 1578 W. The oscilloscope results also give the gate signals of the SIC MOSFETs in the circuit.

The ISBC circuit was operated at the same input/output voltage and current values as the SBC circuit. In this case, the input/output current and voltage graphs of the ISBC circuit are given in Figure 11. In this case, the total circuit output current is the same as the SBC and 10.79 A. However, it is understood from the oscilloscope that the total current is shared with the two inductances in the circuit $i_L = i_{L1} + i_{L2}$. The current ripples in SBC and ISBC circuits are Δi_{L_SBC} 1600 mA and Δi_{L_ISBC} 840 mA, respectively. Experimental results have shown that the current ripple at the ISBC circuit output decreases.

In the experimental study, a comprehensive investigation of circuit-level efficiency and component-level power loss was conducted. The efficiency measurement at the circuit level, which constitutes the first phase, was examined for ABC, SBC, and ISBC.
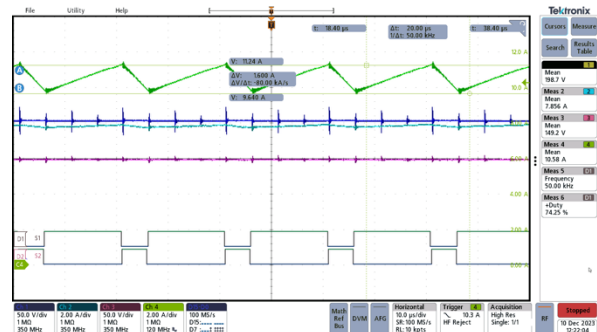
Figure 10. The input/output voltage and current waveforms of the SBC circuit (Ch$_1$:v_{in}, Ch$_2$: i_{in}, Ch$_3$: v_{bat}, Ch$_4$: i_L)
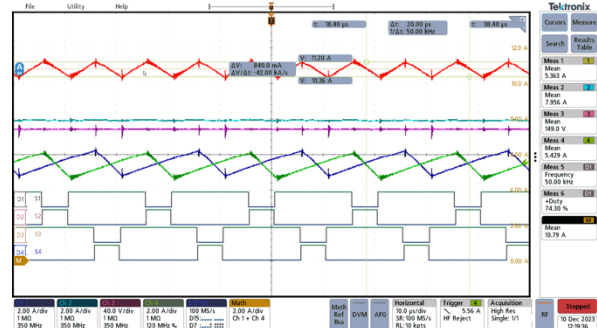
Figure 11. The input/output voltage and current waveforms of the ISBC circuit (Ch$_1$: i_{L_buck2}, Ch$_2$: i_{in}, Ch$_3$: v_{bat}, Ch$_4$: i_{L_buck1}, Ch$_{math}$: i_{L_buck1}+ i_{L_buck2})

In the second stage, a component-level loss analysis was performed to explore the factors affecting efficiency during transitions between circuit

topologies, specifically focusing on the losses associated with the diode, SIC MOSFET, and output capacitor. The first component-level analysis aims to explain the shift from ABC to SBC by conducting a loss analysis for the diode and SIC MOSFET on the low side. Another loss analysis was carried out for the transition from SBC to ISBC to help explain the reasons behind the high-side SIC MOSFET losses. The final component-level study involves power loss analysis on the output capacitor.

Firstly, for circuit-level efficiency analysis of the dc/dc buck converter, the topologies mentioned in the study were modeled with MATLAB/Simulink. The simulation processes considered the circuit elements' internal resistances and conduction losses. The dc/dc buck converter circuits were run in a simulation environment at three different charging voltages. The dc-to-dc efficiencies were analyzed in simulation studies depending on the dc/dc buck circuit output powers. The comparison graph of the obtained simulation and experimental results is given in Figure 12. According to this power-efficiency graph, it can be seen that the modeling and experimental results coincide. When simulation results are compared to experimental results, the letter shows higher values. This difference between them is derived from factors including parasitic elements, simulation model accuracy, measurement errors, nonlinear behavior of components, etc.
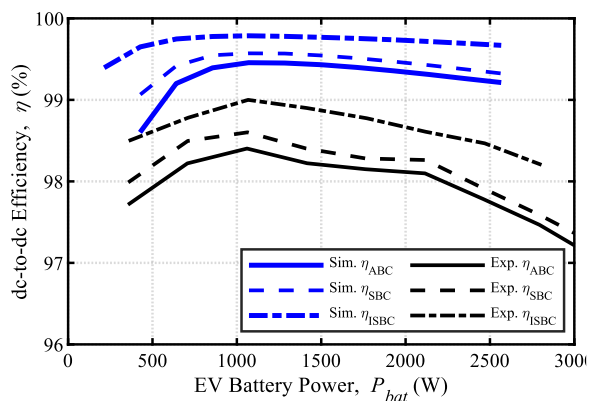
Figure 12. Simulation and experimental efficiency graph for v_{bat} 185 V according to the output power change of the dc/dc buck converters

According to experimental results, Figure 13 shows the efficiency contour graphs on the voltage/current axes of dc/dc buck converter topologies. In these efficiency graphs, the maximum efficiencies of the ABC, SBC, and ISBC circuits are 98.3%, 98.5%, and 99%, respectively. In the literature, some studies provide 97% [17], 95% [18], 93% [19], and 92% [20] efficiency for ISBC. Compared with the studies in the literature, satisfactory results were achieved thanks to the SIC MOSFET and two-phase structure of dc/dc converter.

At high current values, higher values of the ISBC circuit efficiency have a wider operating area. The simulation and experimental studies conducted in this study show that the ISBC circuit, one of the dc/dc buck

converter topologies, should be preferred in the charging circuits of EVs due to its high efficiency.

The diode, SIC MOSFET, and output capacitor were selected due to their lifecycle considerations in the component-level loss analysis. The voltage stress and current stress on the component result in power losses. The power loss brings about a thermal swing on the component. This thermal swing contributes to a reduction in the component's lifespan. Therefore, in the component-level analysis, graphs depicting instantaneous power variations on the component are provided to better understand and address these issues.

The first component-level analysis aims to explain the shift from ABC to SBC by conducting a loss analysis for the diode and SIC MOSFET in the low side. The SBC circuit uses a SIC MOSFET (S_2) instead of the diode (D_1) used in the ABC circuit. The total loss occurring on the diode and SIC MOSFET is composed of conduction and switching losses. Figure 14 illustrates these power losses. The instantaneous power on the graph represents the loss occurring on the diode for the ABC, while it indicates the loss on the SIC MOSFET for the SBC. The diode losses in the ABC are mitigated in SBC by employing MOSFETs instead of diodes. The power loss graph was obtained using the currents and voltages across D_1 and S_2. The figure shows that the instantaneous power loss on the ABC diode is greater than the instantaneous power loss on the SIC MOSFET.

When the average values are calculated, $P_{D1\text{-}ABC}$ 39.72 W and $P_{S2\text{-}SBC}$ 34.17 W Calculating the loss ratio with reference to diode losses, the loss of the S_2 switch is 14% lower, resulting in an 86% loss

A second component-level loss analysis was carried out for the change from SBC to ISBC to help explain the reasons behind the high-side SIC MOSFET losses. Figure 15 illustrates S_1 SIC MOSFETs of the SBC and ISBC switching losses. The power loss graph was obtained using the currents and voltages across the elements S_1 SIC MOSFET of the SBC and ISBC. As illustrated in Figure 15, the instantaneous variations in the total loss predominantly arise from the conduction losses during the conduction phase of the SIC MOSFET. The figure shows that the instantaneous power loss on the S_1 SIC MOSFET of the SBC is greater than the instantaneous power loss on the S_1 SIC MOSFET of the ISBC. When the average values are calculated, $P_{S1\text{-}SBC}$ 10.31 W and $P_{S1\text{-}ISBC}$ 4.56 W Calculating the loss ratio with reference to the SBC, the loss of the ISBC is 56 % lower, resulting in an 44% loss.

The final component-level study involves power loss analysis on the output capacitor. Figure 16 illustrates the instantaneous power on the output capacitor of the SBC and ISBC. This graph is plotted using the voltage across the capacitor and the current flowing through it. The maximum current value on the capacitor is 0.5 A for the SBC, whereas it is 1.0 A for the ISBC.
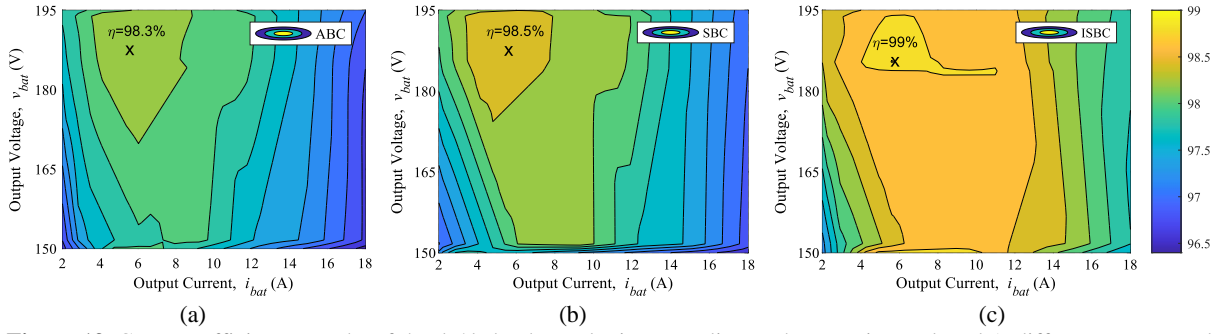
Figure 13. Contour efficiency graphs of the dc/dc buck topologies according to the experimental study's different current and voltage values: (a) for the ABC, (b) for the SBC, and (c) for the ISBC
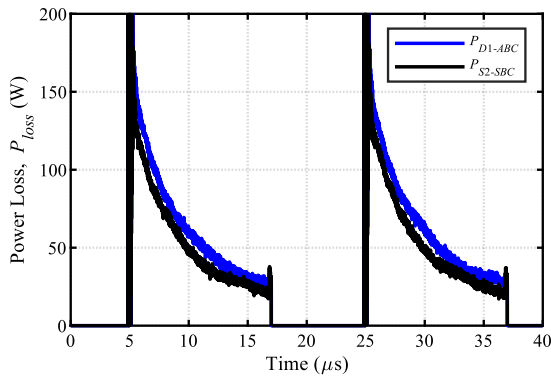
Figure 14. D_1 diode of the ABC and S_2 SIC MOSFET of the SBC instantaneous power for D=0.4 and P_{bat}=1050W according to the experimental of the dc/dc buck converters
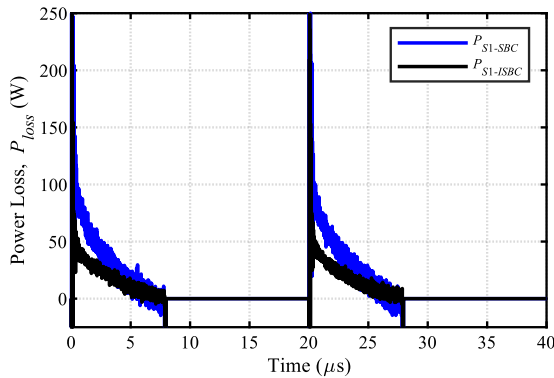
Figure 15. S_1 SIC MOSFET of the SBC and ISBC instantaneous power for D=0.4 and P_{bat}=1050W according to the experimental of the dc/dc buck converters
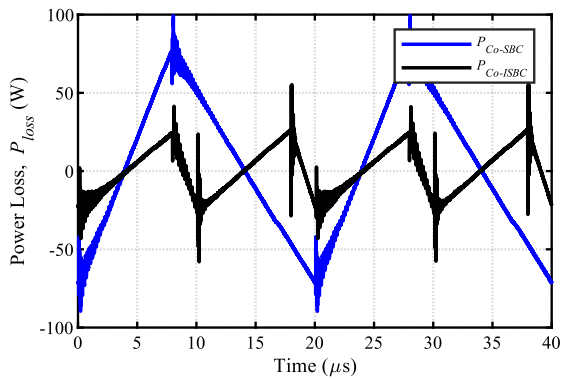
Figure 16. Output capacitor of the SBC and ISBC instantaneous power for D=0.4 and P_{bat}=1050W according to the experimental of the dc/dc buck converters

Consequently, the power loss due to the internal resistance of the output capacitor is reduced in the ISBC. The given equivalent series resistance value R_{Cout} in the table is 54 mΩ. A small loss is expected considering the capacitor current and this R_{Cout} value. When the average values are calculated, $P_{Co\text{-}SBC}$ 17.8 mW and $P_{Co\text{-}ISBC}$ 10.8 mW Calculating the loss ratio concerning SBC, the loss of the ISBC is 40% lower, resulting in a 60% loss.

4. Conclusion

This study analyzed the simulation and experimental results of the dc/dc buck converter topologies used in electric vehicle wireless charging systems. The fact that this converter circuit inside the vehicle in EVs is light, low-volume, and high-efficiency will increase the vehicle's range. This study shares the results of asynchronous buck, synchronous buck, and interleaved synchronous buck converter circuit topologies in the literature. In experimental test results, the ABC circuit was operated with 98.3% efficiency at 1060 W power, the SBC circuit with 98.5% efficiency at 1063 W power, and the ISBC circuit with 99% efficiency at 1066 W power. The loss analysis has revealed that the most significant losses occur across the diode between SIC MOSFET and the output capacitor. This emphasizes the advantage of change from ABC to SBC. Moreover, the loss analysis indicates that transitioning to the ISBC from SBC results in a more advantageous circuit, as the current phases are shared, enhancing the overall efficiency of the circuit. These circuit-level and component-level results show that the ISBC circuit topology should be preferred as it operates with low current ripple and high efficiency at high powers. Compared with the studies in the literature, satisfactory results were achieved thanks to the SIC MOSFET and the ISBC structure of the dc/dc converter.

References

[1] Ucer, E., Buckreus, R., Haque, M. E., Kisaciklioglu, M., Sozer, Y., Harasis, S., Guven, M., & Giubbolini, L. (2021). Analysis, Design, and Comparison of V2V Chargers for Flexible Grid Integration. *IEEE Transaction on Industry Application*, 57(4), 4143-4154.

[2] Nguyen, H. V., Jeung, Y. C., & Lee, D. C. (2016). Battery charger with small DC-link capacitors for G2V applications. *IEEE International Conference on Sustainable Energy Technologies (ICSET)*, Hanoi, Vietnam, 315-319.

[3] Calgan, H. (2023). Optimal C-type filter design for wireless power transfer system by using support vector machines. *An International Journal of Optimization and Control: Theories & Applications (IJOCTA)*, 13(2), 151-160.

[4] Aktas, A., Onar, O. C., Asa, E., Mohammad, M., Ozpineci, B., & Tolbert, L. M. (2023). Sensitivity Analysis of a Polyphase Wireless Power Transfer System under Off-Nominal Conditions. *IEEE Transactions on Transportation Electrification*, (Early Access).

[5] Sis, S. A., & Akca, H. (2020). Maximizing the efficiency of wireless power transfer systems with an optimal duty cycle operation. *AEU - International Journal of Electronics and Communications*, 116, 1-10.

[6] Shi, W., Deng, J., Wang, Z., & Cheng, X. (2018). The strategy of combining one cycle control and PD control for primary-side controlled wireless power transfer system. *IEEE Access*, 6, 14439-14450.

[7] Hata, K., Imura, T., & Hori, Y. (2016). Simultaneous estimation of primary voltage and mutual inductance based on secondary-side information in wireless power transfer systems. *IEEE Wireless Power Transfer Conference (WPTC)*, Aveiro, Portugal, 1-3.

[8] Xue, L., Su, G. J., Galigekere, V., Onar, O., & Mohammad, M. (2023). Design Considerations of DC/DC Regulator for High-Power Dynamic Wireless Charging Systems. *IEEE Transportation Electrification Conference & Expo (ITEC)*, Detroit, USA, 1-5.

[9] Drobnič, K., Grandi, G., Hammami, M., Mandrioli, R., Viatkin, A., & Vujacic, M. (2018). A Ripple-Free DC Output Current Fast Charger for Electric Vehicles Based on Grid-Tied Modular Three-Phase Interleaved Converters. *International Symposium on Industrial Electronics (INDEL)*, Banja Luka, Bosnia and Herzegovina, 1-7.

[10] Sagar, A., Sugali, H., & Bhisade, S. (2020). Design and Analysis of Robust Interleaved Buck Converter with Minimal Ripple Current. *International Conference for Emerging Technology (INCET)*, Balgaum, India, 1-5.

[11] Eirea, G., & Sanders, S. R. (2008). Phase Current Unbalance Estimation in Multiphase Buck Converters. *IEEE Transaction on Power Electronics*, 23(1), 137-143.

[12] Singh, R., Gawre, S. K., & Dyanamina, G. (2021). Review and Analysis of DC-DC Power Converter Performance for Fast Charging of EVs. *IEEE 2nd International Conference On Electrical Power and Energy Systems (ICEPES)*, Bhopal, India, 1-5.

[13] Haque, Md. R., Das, S., Uddin, M. R., Islam M. S., & Razzak, Md. A. (2020). Performance Evaluation of 1kW Asynchronous and Synchronous Buck Converter-based Solar-powered Battery Charging System for Electric Vehicles. *IEEE Region 10 Symposium (TENSYMP)*, Dhaka, Bangladesh, 770-773.

[14] Garg, A., & Das, M. (2021). High Efficiency Three Phase Interleaved Buck Converter for Fast Charging of EV. *International Conference on Power Electronics and Energy (ICPEE)*, Bhubaneswar, India, 1-5.

[15] Nowakowski, R., & Tang, N. (2009). *Efficiency of synchronous versus nonsynchronous buck converters* [online]. Texas Instrument. Available from: https://www.ti.com/lit/pdf/slyt358 [Date Accessed 10 December 2023].

[16] Parisi, C. (2021). *Multiphase Buck Design From Start to Finish (Part 1)* [online]. Texas Instrument. Available from: www.ti.com [Date Accessed 10 December 2023].

[17] Hinov, N., & Tsvetana, G. (2023). Design Considerations of Multi-Phase Buck DC-DC Converter. *Applied Sciences*, 13(19), 11064.

[18] Cabrera, M. & Hudson, T. (2022). *Designing a Multi-Phase Buck Converter with Digital Controllers* [online]. Available from:https://www.powerelectronicsnews.com/designing-a-multi-phase-buck-converter-with-digital-controllers [Date Accessed 26 December 2023].

[19] Eraydın, H. (2021). *Senkron düşürücü dönüştürücü tasarımı ve uygulması*. MSc Thesis. Yildiz Technical University.

[20] Yener, B. (2023). *Dört fazlı senkron düşürücü dönüştürücünün tasarımı, analizi ve gerçekleştirilmesi*. MSc Thesis. Yildiz Technical University.

Hakan Akca received the Bachelor's degree in Department of Electrical and Electronics Engineering at Selcuk University, Konya, Turkey, in 2009. Subsequently, he received his Masters and Ph.D. degrees in Department of Electrical Engineering, at Yildiz Technical University, Istanbul, Turkey, in 2011 and 2017, respectively. Currently serving as an Assistant Professor in the Department of Electrical and Electronics Engineering at Ege University in Izmir, Turkey. His research interests include power converters, renewable energy sources, and electric vehicles. Ongoing projects include the wireless charging of electric vehicle batteries in a photovoltaic

solar panel and grid-powered system. He is currently continuing project studies on wireless charging system for electric vehicles based on photovoltaic integrated and grid connected, supported by The Scientific and Technological Research Council of Turkey.

iD *https://orcid.org/0000-0001-9138-0755*

Ahmet Aktas *received his B.Sc. in Electrical Education from Kocaeli University in 2010. He received the M.Sc. degree from the Department of Energy Systems Engineering, Kocaeli University 2013. Finally, he got his PhD in Energy Systems Engineering at Kocaeli University in 2016. He is an Associate Professor Doctor with the Department of Energy Systems Engineering, Technology Faculty, Gazi University, Turkey. He has published many papers on different subjects, including multilevel*

inverters, photovoltaic power generation systems, renewable energy sources, energy management, energy storage technologies, battery and ultracapacitor modeling, smart energy management, microcontroller programming, smart grid integration, microprocessor-based application systems, offshore wind turbine, and marine current energy. He carried out project management on offshore wind, marine current flow, and hybrid energy storage systems supported by The Scientific and Technological Research Council of Turkey. He worked as a postdoctoral researcher at Oak Ridge National Laboratory and the University of Tennessee to study wireless power transfer for electric vehicles.

iD *https://orcid.org/0000-0003-1027-1579*

An International Journal of Optimization and Control: Theories & Applications (http://ijocta.balikesir.edu.tr)

RESEARCH ARTICLE

New generalized integral transform via Dzherbashian–Nersesian fractional operator

Rachid Belgacem^a, Ahmed Bokhari^{a*}, Dumitru Baleanu^{b,c}, Salih Djilali^a

^{a}Department of Mathematics, Hassiba Benbouali University, Chlef, Algeria
^{b}Department of Computer Science and Mathematics, Lebanese American University, Beirut, Lebanon
^{c}Institute of Space Sciences, Magurele-Bucharest, Romania
 belgacemrachid02@yahoo.fr, a.bokhari@univ-chlef.dz, dumitru.baleanu@lau.edu.lb, s.djilali@univ-chlef.dz

ARTICLE INFO	ABSTRACT
	In this paper, we derive a new generalized integral transform on Dzherbashian–Nersesian fractional operator and give some special cases. We make a generalization of the application of integral transformations to different fractional operators, where several previous results can be invoked from a single relation. We also use the new results obtained to solve some fractional differential equations involving the recent revival of Dzherbashian-Nersesian fractional operators.

1. Introduction

Fractional calculus is used to investigate fractional integral operators and derivatives of any order. This is a well-known idea that has shown to be quite helpful in explaining many memory and internal process phenomena. These phenomena are extremely valuable for tackling a variety of problems related to science and technology, including physics, chemistry, biology, cybernetics, economics, electronics, and many more domains that have emerged in recent decades. We refer the readers to the following references for more details [1–7], and [8].

Despite its long history, fractional calculus still has a large number of unsolved remaining problems, from both theoretical and applied perspectives (see references [4, 9] and [10]). Over the

last few years, various forms of fractional operators have been introduced in the scientific literature [11].

Obtaining generalized fractional operators is a major challenge in the present time. It was recently demonstrated that the use of a large class of fractional operators yields interesting mathematical results. However, in practice, real data is important in determining which fractional operator produces the best results for a certain kind of models.

In this context, the interesting Dzherbashian–Nersesian fractional operator was first proposed in 1968 [12], but was rarely studied. This is a generalized fractional operator for which the fractional operators; Riemann–Liouville (R–L) fractional integral, Caputo derivative and Hilfer (HF)

---

*Corresponding Author

are special cases, that can be obtained by a special setting of parameter values in the fractional operator of Dzherbashian - Nersesian [13, 14].

Integral transformations are mathematical operations that transform a function from one domain to another. They are tools used in various fields to simplify difficulties and discover answers. These transformations map a function from the time or space domain to the frequency or complex plane domain, making it easier to study and solve problems.

These integral transformations, on the other hand, are important for the simplification they provide, most commonly in the processing of differential equations under precise boundary conditions. A well-chosen set of integral transformations aid in the conversion of differential equation and integro-differential equation into easily solvable algebraic equations. To complete the procedure, the solution that is found is the transform of the solution of the original differential equation, which must be inverted. Many integral Laplace transformations have been introduced over the last two decades, including the Sumudu [15], Elzaki [16], Natural [17], Aboodh [18], Pourreza [19, 20], Mohand [21], Sawi [22], Shehu [23] and Kamal transformations [24].

In ref. [25], H. Jafari proposed a new integral transform in 2021. This new generalized integral transform, which will be abbreviated as NG-Transform in the remainder of this article, includes a variety of the family of Laplace transforms, and is particularly useful for solving differential equations and integro-differential equations. Recently, some authors applied this transform to some fractional operators, such as: AB fractional derivative [38], CF fractional derivative [26], R–L fractional integral and Caputo derivative of fractional order [41], Hilfer–Prabhakar fractional derivatives in [27], and Costa et al. in [28] for the k–Hilfer fractional derivative. On the other hand, others have applied this transform in several works, e.g., [29–33], and [34].

Based on the above, the motivation of this research is to investigate and demonstrate certain important properties of NG-Transform that have not before been employed as solutions to some types of Cauchy problems involving the Dzherbashian–Nersesian fractional operators.

This paper is organised into five sections: Section 2 covers important key definitions, properties, theorems and lemmas, and some useful results about the new generalised integral transform, which are used throughout the remainder of the paper. In section 3, we provide some key findings derived via the NG-Transform of the Dzherbashian–Nersesian fractional operator, and give some special cases in section 4. Various applications of the Dzherbashian–Nersesian fractional operator implementing the NG-Transform to solve some Cauchy-type problems are given in Section 5. The conclusion follows next in Section 6.

2. Preliminary

For the sake of clarity, we give in following paragraphs some fundamental definitions and concepts. There are also interesting results regarding the new transform.

Definition 1. *(see [35]). The left sided R–L fractional integral $I_{0^+,t}^\alpha$ of $v \in L^1([a,b])$ is given by the following formula*

$$I_{0^+,t}^\alpha v(t) = \int_0^t \frac{(t-\tau)^{\alpha-1} v(\tau)}{\Gamma(\alpha)} d\tau, \quad t > 0, \alpha > 0. \tag{1}$$

Definition 2. *(see [36]). The Caputo derivative of fractional order α for the function $v(t)$ is described as*

$$^C D_{a^+}^\alpha v(t) = \begin{cases} \int_a^t \frac{(t-\tau)^{m-\alpha-1} v^{(m)}(\tau)}{\Gamma(m-\alpha)} d\tau, \\ \quad if \; 0 < m-1 < \alpha < m, \\ \frac{d^m}{dt^m} v(t) \;\; if \; \alpha = m. \end{cases} \tag{2}$$

Definition 3. *(see [37]). Let $\alpha \in (0,1)$, $\sigma \in [0,1]$, $v \in L^1[a,b]$, $v * \frac{t^{(1-\sigma)(1-\alpha)}}{\Gamma((1-\sigma)(1-\alpha))} \in AC^1[a,b]$. The Hilfer fractional derivative (H–FD) is expressed as*

$$D_{a^+}^{\alpha,\sigma} v(t) = \left(I_{a^+}^{\sigma(1-\alpha)} \frac{d}{dt} \left(I_{a^+}^{(1-\sigma)(1-\alpha)} v \right) \right)(t). \tag{3}$$

Remark 1.
for $\sigma = 0$ in (3), the H–FD coincides with the fractional operator $D_{0^+,t}^\alpha$ (2).

Definition 4. *(see [12]). The fractional operator Dzherbashian–Nersesian $D_{0^+,t}^{\alpha_m}$ of order m is expressed as*

$$D_{0^+,t}^{\alpha_m} v(t) = I_{0^+,t}^{1-\sigma_m} D_{0^+,t}^{\sigma_{m-1}} D_{0^+,t}^{\sigma_{m-2}} ... D_{0^+,t}^{\sigma_1} D_{0^+,t}^{\sigma_0} v(t),$$
$$t > 0, m \in \mathbb{N}, 0 < \alpha_m \le m, \tag{4}$$

where

$$\alpha_m = \sum_{r=0}^m \sigma_r - 1, \; \sigma_r \in (0,1]. \tag{5}$$

Special cases

(1) for $m = 1$ in (4), we have (see [12])
$$D_{0^+,t}^{\alpha_1} v(t) = I_{0^+,t}^{1-\sigma_1} D_{0^+,t}^{\sigma_0}. \tag{6}$$

(2) For $\sigma_1 = \sigma_2 = ... = \sigma_m = 1$ and $\sigma_0 = 1 + \alpha - m$, where $\sigma_0 \in (0,1)$, in (4) we have (see [14])

$$D_{0^+,t}^{\alpha_m} v(t) = \frac{d^m}{dt^m} I_{0^+,t}^{m-\alpha} v(t) = D_{0^+,t}^{\alpha} v(t). \quad (7)$$

In this case, Dzherbashian–Nersesian fractional operator reduces to the fractional operator $D_{0^+,t}^{\alpha}$ of order $m-1 < \alpha \leq m$ which given by the equation 2.

(3) For $\sigma_0 = \sigma_2 = ... = \sigma_{m-1} = 1$ and $\sigma_m = 1 + \alpha - m$, where $\sigma_m \in (0,1)$, in (4) we have (see [14])

$$D_{0^+,t}^{\alpha_m} v(t) = I_{0^+,t}^{m-\alpha} \frac{d^m}{dt^m} v(t) = {}^c D_{0^+,t}^{\alpha} v(t). \quad (8)$$

This case, Dzherbashian–Nersesian fractional operator interpolates to the CFD operator ${}^C D_{0^+,t}^{\alpha}$ of order α.

(4) For $\sigma_m = 1 - \sigma m - +\sigma \alpha$, $\sigma_0 = 1 + \alpha - m - \sigma_m$, where $\sigma_0, \sigma_m \in (0,1)$ and $\sigma_1 = \sigma_2 = ... = \sigma_{m-1} = 1$ in (4) we have (see [14])

$$D_{0^+,t}^{\alpha_m} v(t) = \frac{d^m}{dt^m} v(t) = D_{0^+,t}^{\alpha} v(t). \quad (9)$$

In this instance, the Dzherbashian–Nersesian fractional operator is reduced to HFD of order $m-1 < \alpha < m$, and type $0 < \sigma < 1$.

Definition 5. *(see [25]) Let $v(t)$ be a integrable function defined for $t \geq 0$, $\zeta(p) \neq 0$ and $\psi(p)$ are positive real functions. The NG-Transform of $v(t)$ is expressed as*

$$\mathcal{T}_{\mathcal{NG}} \{v(t), p\} = \mathfrak{F}(p)$$
$$= \xi(p) \int_0^\infty v(t) \exp(-\psi(p)t) \, dt, \quad (10)$$

provided the integral exists for some $\psi(p)$.

The new transform $\mathfrak{F}(p)$ exists for all $\psi(p) > \phi$ and has numerous properties such as linear operator for example, a more detailed discussion about this can be found in [25]. Inversion formula of (10), is given by [38]

$$\mathfrak{F}^{-1}(p) = \mathcal{T}_{\mathcal{NG}}^{-1} \left\{ \xi(p) \int_0^\infty v(t) \exp(-\psi(p)t) \, dt \right\}$$
$$= v(t). \quad (11)$$

This new integral transform can be easily implemented directly to an appropriate problem by specifically selecting $\xi(p)$ and $\psi(p)$. In the table 1, we mention some of them.

Theorem 1. *(See [25]). Let $\xi(p), \psi(p) > 0$, the NG-Transform of derivatives of $v(t)$ is defined as*

$$\mathcal{T}_{\mathcal{NG}} \{v^{(m)}(t), p\} = (\psi(p))^m [\mathfrak{F}(p) - \xi(p) \sum_{r=0}^{m-1} (\psi(p))^{-1-r} v^{(r)}(0)], \forall m \in \mathbb{N}. \quad (12)$$

Theorem 2. *(See [25, 38]). Let $\mathfrak{F}_1(p) = \mathcal{T}_{\mathcal{NG}} \{v_1, p\}$ and $\mathfrak{F}_2(p) = \mathcal{T}_{\mathcal{NG}} \{v_2, p\}$, then*

$$\mathcal{T}_{\mathcal{NG}} \{v_1 \star v_2, p\} = \int_0^\infty v_1(t) v_2(t-z) \, dz$$
$$= \frac{1}{\phi(s)} \mathfrak{F}_1(p).\mathfrak{F}_2(p). \quad (13)$$

Definition 6. *(See [10, 39, 40]). For any $w \in \mathbb{C}$, The usual Mittag-Leffler (ML) function is defined as*

$$E_\eta(w) = \sum_{i=0}^\infty \frac{w^i}{\Gamma(\eta i + 1)}, \quad w \in \mathbb{C}, \ \text{Re}(\eta) > 0. \quad (14)$$

where Re denotes the real part. The 2-parameters ML function is given by [10]

$$E_{\eta,\beta}(w) = \sum_{i=0}^\infty \frac{w^i}{\Gamma(\eta i + \beta)}, w \in \mathbb{C}, \quad (15)$$
$$Re(\eta) > 0, Re(\sigma) > 0,$$

such that $E_{\eta,1}(z) = E_\eta(w)$, and the 3-parameters ML function is stated as [39, 40]

$$E_{\eta,\beta}^\gamma(w) = \frac{1}{\Gamma(\gamma)} \sum_{i=0}^\infty \frac{\Gamma(\gamma+i)}{\Gamma(\eta i + \beta)} \frac{w^i}{i!}, \quad w \in \mathbb{C},$$
$$Re(\eta) > 0, Re(\beta) > 0, Re(\gamma) > 0. \quad (16)$$

Lemma 1. *(See [38]). Let $\eta \in (0,1)$ and $z \in \mathbb{R}$ such that $0 < \psi(p) < |z|^{\frac{1}{\eta}}$, then*

$$\mathcal{T}_{\mathcal{NG}} \left\{ t^{\sigma-1} E_{\eta,\sigma}^\gamma(zt^\eta), p \right\} = \frac{\xi(p)}{\psi(p)^\sigma} \left(1 - \frac{z}{\psi(p)^\eta} \right)^{-\gamma}. \quad (17)$$

Proposition 1. *(See [38, 41]). The NG-Transform of t^α is expressed as*

$$\mathcal{T}_{\mathcal{NG}} \{t^\alpha, p\} = \Gamma(\alpha+1) \frac{\xi(p)}{\psi(p)^{\alpha+1}}, \ \alpha > 0. \quad (18)$$

Theorem 3. *(See [41]). The NG-Transform of RLF integral of v is presented as*

$$\mathcal{T}_{\mathcal{NG}} \left\{ I_{0^+,t}^\alpha v(t), p \right\} = \frac{\mathfrak{F}(p)}{\psi(p)^\alpha}, \quad (19)$$

where $\alpha > 0$ and $\mathfrak{F}(p)$ is denoted by the NG-Transform of the function $v(t)$.

3. Main results

In the following part, we will derive the NG-Transform on the Dzherbashian–Nersesian fractional operator and discuss some particular cases. Let $v(t) \in \mathcal{A}$ with $\mathcal{T}_{\mathcal{NG}} \{v(t), p\} = \mathfrak{F}(p)$.

Lemma 2. *The NG-Transform of RLF derivative of v is given as follows*

$$\mathcal{T}_{\mathcal{NG}} \left\{ D_{0^+,t}^\alpha v(t), p \right\} = [\psi(p)]^\alpha \mathfrak{F}(p)$$
$$- \xi(p) \sum_{k=0}^{m-1} [\psi(p)]^k \left[D_{0^+,t}^{\alpha-k-1} v(t) \right]_{t=0^+},$$
$$m - 1 < \alpha \leq m. \quad (20)$$

Table 1. Relation between the NG-Transform and other integral transforms.

Transform	Definition	Jafari transform
Laplace [7]	$\mathcal{L}\{v(t),p\} = \int_0^\infty v(t)e^{-pt}dt$	$\xi(p) = 1$ and $\psi(p) = p$
Sumudu [15]	$\mathcal{S}\{v(t),p\} = \frac{1}{p}\int_0^\infty v(t)e^{-pt}dt$	$\xi(p) = \psi(p) = \frac{1}{p}$
Elzaki [16]	$E\{v(t),p\} = p\int_0^\infty v(t)e^{\frac{t}{p}}$	$\xi(p) = 1$ and $\psi(p) = \frac{1}{p}$
Natural [17]	$N\{v(t),p,u\} = p\int_0^\infty v(ut)e^{-pt}dt$	$\xi(p) = u$ and $\psi(p) = \frac{p}{u}$
Aboodh [18]	$A\{v(t),p\} = \frac{1}{p}\int_0^\infty v(t)e^{-pt}dt$	$\xi(p) = \frac{1}{p}$ and $\psi(p) = 1$
Mohand [21]	$\mathcal{M}\{v(t),p\} = p^2\int_0^\infty v(t)e^{-pt}dt$	$\xi(p) = p^2$ and $\psi(p) = p$
Sawi [22]	$\mathcal{R}\{v(t),p\} = \frac{1}{p^2}\int_0^\infty v(t)e^{-\frac{t}{p}}dt$	$\psi(p) = \frac{1}{p}$ and $\xi(p) = \psi(p)^2$
Kamel [24]	$\mathcal{K}\{v(t),p\} = p\int_0^\infty v(t)e^{-\frac{t}{p}}dt$	$\xi(p) = 1$ and $\psi(p) = \frac{1}{p}$
Shehu [23]	$\mathcal{SH}\{v(t),p,u\} = \int_0^\infty v(t)e^{-\frac{pt}{u}}dt$	$\xi(p) = 1$ and $\psi(p) = \frac{p}{u}$

Proof. Using the NG-Transform on both sides of (2) and subsequently the relation (12), we get

$$\mathcal{T}_{\mathcal{NG}}\left\{D_{0^+,t}^{\alpha}v(t),p\right\}$$
$$= \mathcal{T}_{\mathcal{NG}}\left\{\frac{d^m}{dt^m}I_{0^+,t}^{m-\alpha}v(t),p\right\}$$
$$= [\psi(p)]^m \mathcal{T}_{\mathcal{NG}}\left\{I_{0^+,t}^{m-\alpha}v(t),p\right\}$$
$$-\xi(p)\sum_{k=0}^{m-1}[\psi(p)]^k$$
$$\times\left[\left(\frac{d}{dt}\right)^{(m-1-k)}I_{0^+,t}^{m-\alpha}v(t)\right]_{t=0^+}$$
$$= [\psi(p)]^{\alpha}\mathfrak{F}(p)$$
$$-\xi(p)\sum_{k=0}^{m-1}[\psi(p)]^k\left[D_{0^+,t}^{\alpha-k-1}v(t)\right]_{t=0^+}.$$

This is the desired result (20). □

Remark 2. *Lemma (2) generalizes some results that already exist, so for example:*

(1) *The Laplace integral transform of R–L fractional operator, which is given by equation (2), is obtained when $\xi(p) = 1$ and $\psi(p) = p$ (see [35]), i.e.*

$$\mathcal{L}\left\{D_{0^+,t}^{\alpha}v(t),p\right\}$$
$$= p^{\alpha}\mathcal{L}\{v(t),p\} - \sum_{k=0}^{m-1}p^k\left[D_{0^+,t}^{\alpha-k-1}v(t)\right]_{t=0^+}.$$

(2) *If we take $\xi(p) = \psi(p) = \frac{1}{p}$, yields Sumudu's integral transform witch is mentioned in the work [42], i.e.,*

$$\mathcal{S}\left\{D_{0^+,t}^{\alpha}v(t),p\right\} = p^{-\alpha}\mathcal{S}\{v(t),p\}$$
$$-\sum_{k=0}^{m-1}p^{-(k+1)}\left[D_{0^+,t}^{\alpha-k-1}v(t)\right]_{t=0^+}. \quad (21)$$

The NG-Transform of the Dzherbashian–Nersesian fractional operator is obtained by the following theorem.

Theorem 4. *The NG-Transform of Dzherbashian–Nersesian fractional operator of order α_m $(0 < \alpha_m < m)$ is expressed as follows*

$$\mathcal{T}_{\mathcal{NG}}\left\{D_{0^+,t}^{\alpha_m}v(t),p\right\}$$
$$= [\psi(p)]^{\alpha_m}\mathcal{T}_{\mathcal{NG}}\{v(t),p\}$$
$$-\xi(p)\sum_{r=1}^{m}[\psi(p)]^{\alpha_m-\alpha_{m-r}-1}\left[D_{0^+,t}^{\alpha_{m-r}}v(t)\right]_{t=0^+}. \quad (22)$$

Proof. Using the Dzherbashian–Nersesian fractional operator formulation, the NG-Transform of the Equation (4), and the lemma (2), we get

$$\mathcal{T}_{\mathcal{NG}}\left\{D_{0^+,t}^{\alpha_m}v(t),p\right\}$$
$$= \mathcal{T}_{\mathcal{NG}}\left\{I_{0^+,t}^{1-\sigma_m}D_{0^+,t}^{1-\sigma_{m-1}}D_{0^+,t}^{1-\sigma_{m-2}}...D_{0^+,t}^{1-\sigma_1}D_{0^+,t}^{1-\sigma_0}v(t),p\right\}$$
$$= [\psi(p)]^{\sigma_m-1}\mathcal{T}_{\mathcal{NG}}\left\{D_{0^+,t}^{\sigma_{m-1}}D_{0^+,t}^{\sigma_{m-2}}...D_{0^+,t}^{1-\sigma_1}D_{0^+,t}^{1-\sigma_0}v(t),p\right\}$$
$$= [\psi(p)]^{\sigma_m-1+\sigma_{m-1}}\mathcal{T}_{\mathcal{NG}}\left\{D_{0^+,t}^{\sigma_{m-2}}...D_{0^+,t}^{\sigma_1}D_{0^+,t}^{\sigma_0}v(t),p\right\}$$
$$-\xi(p)[\psi(p)]^{\sigma_m-1}\left[D_{0^+,t}^{\sigma_{m-1}-1}D_{0^+,t}^{\sigma_{m-2}}...D_{0^+,t}^{\sigma_1}D_{0^+,t}^{\sigma_0}v(t)\right]_{t=0^+}.$$

Continuing in the similar manner, we have

$$\mathcal{T}_{\mathcal{NG}}\left\{D_{0^+,t}^{\alpha_m}v(t),p\right\}$$
$$= [\psi(p)]^{\sum_{r=0}^{m}\sigma_r-1}\mathcal{T}_{\mathcal{NG}}\{v(t),p\}$$
$$-\xi(p)\sum_{r=0}^{m-1}[\psi(p)]^{\sigma_{m-r}}\left[D_{0^+,t}^{\sigma_{m-r}-1}v(t)\right]_{t=0^+}.$$

Using Formula $\alpha_m = \sum_{r=0}^{m}\sigma_r - 1$ and after some calculations, we finally get the desired result (22). □

4. Special cases

The following corollary presents a few important results in different cases of the Jafari integral transform of the Dzherbashian–Nersesian fractional operator.

Corollary 1. *The NG-Transform of the Dzherbashian–Nersesian fractional operator of order α_m ($0 < \alpha_m < m$) is expressed as*

$$\mathcal{T}_{\mathcal{NG}}\left\{D_{0^+,t}^{\alpha_m}v(t),p\right\}$$
$$= [\psi(p)]^{\alpha_m}\left(\mathcal{T}_{\mathcal{NG}}\{v(t),p\}\right.$$
$$\left.- \xi(p)\sum_{r=1}^{m}[\psi(p)]^{-\alpha_{m-r}-1}\left[D_{0^+,t}^{\alpha_{m-r}}v(t)\right]_{t=0^+}\right).$$

- *When $\xi(p) = 1$ and $\psi(p) = p$, we obtain the Laplace transform of the fractional operator of Dzherbashian–Nersesian, which is studied in [14], i.e.,*

$$\mathcal{L}\left\{D_{0^+,t}^{\alpha_m}v(t),p\right\} = p^{\alpha_m}\left(\mathcal{L}\{v(t),p\}\right.$$
$$\left.- \sum_{r=1}^{m}p^{-\alpha_{m-r}-1}\left[D_{0^+,t}^{\alpha_{m-r}}v(t)\right]\right)_{t=0^+},$$

where $\mathcal{L}\{v(t),p\}$ denotes the Laplace transform of a function $v(t)$.

- *The Sumudu integral transform of the Dzherbashian–Nersesian fractional operator is obtained, when $\xi(p) = \dfrac{1}{p}$ and $\psi(p) = \dfrac{1}{p}$. If we represent the Sumudu transform of a function $v(t)$ as $\mathcal{S}\{v(t),p\}$, we get*

$$\mathcal{S}\left\{D_{0^+,t}^{\alpha_m}v(t),p\right\} = p^{-\alpha_m}\mathcal{S}\{v(t),p\}$$
$$- \sum_{r=1}^{m}p^{\alpha_{m-r}-\alpha_m}\left[D_{0^+,t}^{\alpha_{m-r}}v(t)\right]_{t=0^+}. \tag{23}$$

- *When $\xi(p) = 1$ and $\psi(p) = \dfrac{p}{u}$, we get the formula for the Shehu transformation of the Dzherbashian–Nersesian fractional operator. If $V(p,u)$ denotes the Shehu transform of a function $v(t)$, then*

$$\mathcal{SH}\left\{D_{0^+,t}^{\alpha_m}v(t),p,u\right\} = \left(\frac{p}{u}\right)^{\alpha_m}\left(V(p,u)\right.$$
$$\left.- \sum_{r=1}^{m}\left(\frac{u}{p}\right)^{\alpha_{m-r}+1}\left[D_{0^+,t}^{\alpha_{m-r}}v(t)\right]_{t=0^+}\right). \tag{24}$$

- *The Elzaki transform of the Dzherbashian–Nersesian fractional operator is obtained, when $\xi(p) = 1$ and $\psi(p) = \dfrac{1}{p}$, we have*

$$E\left\{D_{0^+,t}^{\alpha_m}v(t),p\right\} = p^{-\alpha_m}E\{v(t),p\}$$
$$- \sum_{r=1}^{m}p^{\alpha_{m-r}-\alpha_m+1}\left[D_{0^+,t}^{\alpha_{m-r}}v(t)\right]_{t=0^+}, \tag{25}$$

where the Elzaki transform of $v(t)$ is denotes by $E\{v(t),p\}$.

- *When $\xi(p) = \dfrac{1}{p^2}$ and $\psi(p) = \dfrac{1}{p}$, the NG-Transform yields in the Sawi transform of the Dzherbashian–Nersesian fractional operator. If we designate the Sawi transform of $v(t)$ as $\mathcal{R}\{v(t),p\}$, then*

$$\mathcal{R}\left\{D_{0^+,t}^{\alpha_m}v(t),p\right\} = p^{-\alpha_m}\mathcal{R}\{v(t),p\}$$
$$- \sum_{r=1}^{m}p^{\alpha_{m-r}-\alpha_m-1}\left[D_{0^+,t}^{\alpha_{m-r}}v(t)\right]_{t=0^+}. \tag{26}$$

- *When $\xi(p) = \dfrac{1}{p}$ and $\psi(p) = 1$, the NG-Transform produces the Aboodh integral transform of the Dzherbashian–Nersesian fractional operator. If the Aboodh transform of $v(t)$ is denoted by $A\{v(t),p\}$, we get*

$$A\left\{D_{0^+,t}^{\alpha_m}v(t),p\right\} = A\{v(t),p\}$$
$$- \frac{1}{p}\sum_{r=1}^{m}\left[D_{0^+,t}^{\alpha_{m-r}}v(t)\right]_{t=0^+}. \tag{27}$$

- *The Natural integral transform of the Dzherbashian–Nersesian fractional operator is obtained when $\xi(p) = u$ and $\psi(p) = \dfrac{p}{u}$. If the Natural integral transform of $v(t)$ is represented by $W(p,u)$, then*

$$N\left\{D_{0^+,t}^{\alpha_m}v(t),p,u\right\} = \left(\frac{p}{u}\right)^{\alpha_m}W(p,u)$$
$$- u\sum_{r=1}^{m}\left(\frac{p}{u}\right)^{\alpha_m-\alpha_{m-r}-1}\left[D_{0^+,t}^{\alpha_{m-r}}v(t)\right]_{t=0^+}. \tag{28}$$

- *When $\xi(p) = p^2$ and $\psi(p) = p$, the NG-Transform yields the Mohand transform to the Dzherbashian–Nersesian fractional operator. If we represent the Mohand transform of $v(t)$ by $\mathcal{M}\{v(t),p\}$, we obtain*

$$\mathcal{M}\left\{D_{0^+,t}^{\alpha_m}v(t),p\right\} = p^{\alpha_m}\left(\mathcal{M}\{v(t),p\}\right.$$
$$\left.- \sum_{r=1}^{m}p^{1-\alpha_{m-r}}\left[D_{0^+,t}^{\alpha_{m-r}}v(t)\right]_{t=0^+}\right). \tag{29}$$

- *When $\xi(p) = 1$ and $\psi(p) = \dfrac{1}{p}$, the NG-Transform yields the Kamal integral transform of the fractional operator of Dzherbashian–Nersesian. If we denote the Kamal integral transform of a function $v(t)$ by $\mathcal{K}\{v(t),p\}$, then*

$$\mathcal{K}\left\{D_{0^+,t}^{\alpha_m}v(t),p\right\} = p^{-\alpha_m}\mathcal{K}\{v(t),p\}$$
$$- \sum_{r=1}^{m}p^{\alpha_{m-r}-\alpha_m+1}\left[D_{0^+,t}^{\alpha_{m-r}}v(t)\right]_{t=0^+}. \tag{30}$$

Proof. The preceding conclusions are clearly demonstrated by the Equation (22) and the table 1.

$\qquad\qquad\qquad\qquad\qquad\qquad\square$

Remark 3. *If $\sigma_1 = \sigma_2 = ... = \sigma_m = 1$ and $\sigma_0 = 1 + \alpha - m$, where $\sigma_0 \in (0,1)$, then, the NG-Transform of RLF derivative of order $\alpha \in (m-1,m)$ is obtained , i.e.,*

$$\mathcal{T}_{\mathcal{NG}}\left\{D_{0^+,t}^{\alpha}v(t),p\right\} = [\psi(p)]^{\alpha}\mathcal{T}_{\mathcal{NG}}\left\{v(t),p\right\}$$
$$-\xi(p)\sum_{r=0}^{m-1}[\psi(p)]^{m-r-1}\left[D_{0^+,t}^{r}I_{0^+,t}^{m-\alpha}v(t)\right]_{t=0^+}. \tag{31}$$

Remark 4. *When $\sigma_0 = \sigma_2 = ... = \sigma_{m-1} = 1$ and $\sigma_m = 1 + \alpha - m$, where $\sigma_m \in (0,1)$, Equation (22) interpolates The NG-Transform of CFD operator of order $\alpha \in (m-1,m)$, i.e.,*

$$\mathcal{T}_{\mathcal{NG}}\left\{{}^cD_{0^+,t}^{\alpha}v(t),p\right\} = [\psi(p)]^{\alpha}\mathcal{T}_{\mathcal{NG}}\left\{v(t),p\right\}$$
$$-\xi(p)\sum_{r=0}^{m-1}[\psi(p)]^{\alpha-r-1}\left[D_{0^+,t}^{r}v(t)\right]_{t=0^+}. \tag{32}$$

In this particular case, it was studied in [41] .

Remark 5. *For $\sigma_m = 1 + \sigma(\alpha-m)$, $\sigma_0 = 1 + (\alpha-m)(1-\sigma)$, where $\sigma_0, \sigma_m \in (0,1)$ and $\sigma_1 = \sigma_2 = ... = \sigma_{m-1} = 1$ in (4, we gain The NG-Transform of Hilfer–fractional derivative of order $\alpha \in (m-1,m)$ and $0 < \sigma < 1$, i.e.,*

$$\mathcal{T}_{\mathcal{NG}}\left\{D_{0^+,t}^{\alpha}v(t),p\right\} = [\psi(p)]^{\alpha}\mathcal{T}_{\mathcal{NG}}\left\{v(t),p\right\}$$
$$-\xi(p)\sum_{r=0}^{m-1}[\psi(p)]^{r-\sigma(m-\alpha)}$$
$$\times\left[D_{0^+,t}^{m-r-1}I_{0^+,t}^{(m-\alpha)(1-\sigma)}v(t)\right]_{t=0^+}. \tag{33}$$

5. Applications

In this part, we will illustrate how to resolve certain Cauchy-type problems employing the Dzherbashian–Nersesian fractional operator and the NG-Transform.

Example 1. *Consider the following problem (See [12]):*

$$\begin{cases} D^{\alpha_m}v(t) = u(t), & t \in (0,b), \quad b > 0, \\ D^{\alpha_r}v(t)|_{t=0} = v_r^0, & r = 0,1,...,m-1. \end{cases} \tag{34}$$

$u(t)$ denotes an arbitrary function such that $I_{0^+,t}^{\alpha_m}u(t)$ exists and $\{v_r^0\}_{r=0}^{m-1}$ is a specified set of real numbers. In the work [12], the existence of the solution and its uniqueness are proved, and they found the solution explicitly in a direct way. Here we will try to find the solution by employing The NG-Transform of the fractional operator of Dzherbashian–Nersesian.

To start, we apply the NG-Transform to both sides of (34) to get

$$\mathcal{T}_{\mathcal{NG}}\left\{D^{\alpha_m}v(t),p\right\} = \mathcal{T}_{\mathcal{NG}}\left\{u(t),p\right\},$$

which yields

$$[\psi(p)]^{\alpha_m}\mathcal{T}_{\mathcal{NG}}\left\{v(t),p\right\}$$
$$-\xi(p)\sum_{r=1}^{m}[\psi(p)]^{\alpha_m-\alpha_{m-r}-1}\left[D^{\alpha_m}v(t)\right]_{t=0}$$
$$= \mathcal{T}_{\mathcal{NG}}\left\{u(t),p\right\}$$

or

$$\mathcal{T}_{\mathcal{NG}}\left\{v(t),p\right\} = \xi(p)\sum_{r=1}^{m}[\psi(p)]^{-\alpha_{m-r}-1}v_m^0$$
$$+ [\psi(p)]^{-\alpha_m}\mathcal{T}_{\mathcal{NG}}\left\{u(t),p\right\}. \tag{35}$$

When implementing the general inverse transformation of (35) with (18) and (19), we obtain

$$v(t) = \mathcal{T}_{\mathcal{NG}}^{-1}\left(\sum_{r=1}^{m}\frac{\xi(p)}{[\psi(s)]^{\alpha_{m-r}+1}}v_m^0\right)$$
$$+ \mathcal{T}_{\mathcal{NG}}^{-1}\left(\frac{\mathcal{T}_{\mathcal{NG}}\left\{u(t),p\right\}}{[\psi(s)]^{\alpha_m}}\right)$$
$$= \sum_{r=1}^{m}v_m^0\frac{t^{\alpha_{m-r}}}{\Gamma(\alpha_{m-r}+1)} + I_{0^+,t}^{\alpha_m}u(t).$$

which is the exact solution of (34).

Example 2. *Consider the following problem (See [12]):*

$$D^{\alpha_m}v(t) = \lambda v(t), \tag{36}$$

subject to,

$$D^{\alpha_k}v(t)|_{t=0} = \begin{cases} 1, & k = j, \\ 0, & k = 0,1,...,j-1,j+1 \end{cases}, \tag{37}$$

where λ is an arbitrary parameter.

Applying the NG-Transform to both sides of Eq.(36), yields

$$[\psi(p)]^{\alpha_m}\mathcal{T}_{\mathcal{NG}}\left\{v(t),p\right\}$$
$$-\xi(p)\sum_{r=1}^{m}[\psi(p)]^{\alpha_m-\alpha_{m-r}-1}\left[D^{\alpha_m}v(t)\right]_{t=0}$$
$$= \lambda\mathcal{T}_{\mathcal{NG}}\left\{v(t),p\right\}.$$

Therefore

$$\mathcal{T}_{\mathcal{NG}}\left\{v(t),p\right\}$$
$$= \frac{\xi(p)}{[\psi(p)]^{\alpha_m}-\lambda}\sum_{r=1}^{m}[\psi(p)]^{\alpha_m-\alpha_{m-r}-1}\left[D^{\alpha_m}v(t)\right]_{t=0},$$
$$= \sum_{r=1}^{m}\frac{\xi(p)}{[\psi(p)]^{\alpha_{m-r}+1}}\frac{1}{1-\frac{\lambda}{[\psi(p)]^{\alpha_m}}}\left[D^{\alpha_m}v(t)\right]_{t=0},$$
$$= \sum_{k=0}^{m-1}\frac{\xi(p)}{[\psi(p)]^{\alpha_k+1}}\frac{1}{1-\frac{\lambda}{[\psi(p)]^{\alpha_m}}}\left[D^{\alpha_k}v(t)\right]_{t=0}.$$

Using the initial conditions (37), *we get*

$$\mathcal{T}_{\mathcal{NG}}\{v(t), p\} = \frac{\xi(p)}{[\psi(p)]^{\alpha_j+1}}\left(1 - \frac{\lambda}{[\psi(p)]^{\alpha_m}}\right)^{-1}.$$
(38)

By taking the inverse transform $\mathfrak{F}^{-1}$ *of both sides of the eq.(38) and using relation* (17) *we get*

$$v(t) = t^{\alpha_m-r}E_{\alpha_m, \alpha_{m-r}+1}\left(\lambda t^{\alpha_m}\right).$$

6. Conclusion

New results of the NG-Transform on the Dzherbashian–Nersesian fractional operator are presented in this paper. First, the expression for the NG transform of fractional Dzherbashia–Nersesian operator is constructed. Then the expression for Laplace transform of fractional Dzherbashian-Nersesian operator of [14] is shown to be a special case of this new results. It has also been shown that the Riemann-Liouville, Caputo, and Hilfer derivatives are special cases of the fractional Dzherbashian–Nersesian operator [13] .

It is possible to deduce many expressions which relate integral transforms to the various operators from the relation that give the NG-transform of the Dzherbashian-Nersesian fractional operator.

The initial-boundary value problems for a fourth-order differential equation within the powerful fractional Dzherbashian–Nersesian operator (FDNO) are investigated in the research [13] . The current study, illustrates how it can be used to solve some Cauchy-type fractional differential equations with the Dzherbashian-Nersesian fractional operator.

In the near future, we will try to use this operator to model phenomena related to the real world, especially modeling diseases and social pests.

Acknowledgments

References

[1] Agarwal, P., Baleanu, D., Chen, Y., Momani, S., & Machado, J.A.T. (1998). Fractional Calculus, *ICFDA 2018, Springer Proceedings in Mathematics and Statistics*, 303.

[2] Baleanu, D. & Agarwal, P. (2014). A composition formula of the Ppathway integral transform operator, *Note di Matematica*, 34(2), 145-155.

[3] Baleanu, D. & Agarwal, P. (2014). On generalized fractional integral operators and the generalized gauss hypergeometric functions, *Abstract and Applied Analysis*, 2014.

[4] Baleanu, D., Diethelm, K., Scalas, E., & Trujillo, JJ. (2017). *Fractional Calculus: Models and Numerical Method.* 2nd ed. World Scientific, New York.

[5] Mainard, F. (2010). *Fractional Calculus and Waves in Linear Viscoelasticity: An Introduction to Mathematical Models.* World Scientific.

[6] Miller, KS., & Ross, B. (1993). *An Introduction to the Fractional Integrals and Derivatives Theory and Applications.* John Willey and Sons, New York.

[7] Oldham, K., & Spanier, J. (1974). *The Fractional Calculus Theory and Applications of Differentiation and Integration to Arbitrary Order*, Elsevier.

[8] Aychluh, M., Purohit, S. D., Agrawal, P., & Suthar, D. L. (2022). Atangana–Baleanu derivative-based fractional model of COVID-19 dynamics in Ethiopia. *Applied Mathematics in Science and Engineering* , 30(1), 635-660.

[9] Magin, RL. (2006). *Fractional Calculus in Bioengineering.* Begell House Publishers.

[10] Podlubny, I. (1998). *Fractional Differential Equations: An Introduction to Fractional Derivatives, Fractional Differential Equations, to Methods of Their Solution and Some of Their Applications,* Academic Press, San Diego.

[11] Baleanu, D., & Fernandez, A. (2019). On fractional operators and their classifications. *Mathematics,* 7(9), 830.

[12] Dzhrbashyan, M.M., & Nersesyan, A.B. (2020). Fractional derivatives and the cauchy problem for fractional differential equations. *Fractional Calculus and Applied Analysis*, 23(6), 1810-1836.

[13] Ahmad, A., & Baleanu, D. (2023). On two backward problems with Dzherbashian-Nersesian operator. *AIMS Mathematics,* 8(1), 887-904.

[14] Ahmad, A., Ali, M., & Malik, SA. (2021). Inverse problems for diffusion equation with fractional Dzherbashian–Nersesian operator. *Fractional Calculus and Applied Analysis,* 24, 1899-1918.

[15] Watugala, G.K. (1993). Sumudu transform: a new integral Transform to solve differential equations and control engineering problems. *International Journal of Mathematical Education in Science and Technology,* 24, 35-43.

[16] Elzaki, T.M. (2011). The new integral transform Elzaki transform. *Global Journal of Pure and Applied Mathematics*, 7, 57-64.

[17] Khan, M., Salahuddin, T., Malik, M.Y., Alqarni, M.S., & Alkahtani, A.M. (2020). Numerical mobeling end analysis of bioconvection on MHD flow due to an upper paraboloid surface of revolution. *Physica A: Statistical Mechanics and its Applications* 553, Article 124231.

[18] Aboodh, K.S. (2023). The new integral transform. *Global Journal of Pure and Applied Mathematics,* 9(1), 35-43.

[19] Ahmadi, S.A.P., Hosseinzadeh, H., & Cherat, A.Y. (2019). A new integral transform for solving higher order linear ordinary differential equations. *Nonlinear Dynamics and Systems Theory*, 19(2), 243-252.

[20] Ahmadi, S.A.P., Hosseinzadeh, H., & Cherat A.Y. (2019). A new integral transform for solving higher order linear ordinary Laguerre and Hermite differential equations. *International Journal of Applied and Computational Mathematics*. 5, 142.

[21] Mohand, M., & Mahgoub, A. (2017). The new integral transform Mohand transform. *Advances in Theoretical and Applied Mathematics,* 12(2), 113-20.

[22] Mahgoub, MA., & Mohand, M. (2019). The new integral transform " Sawi Transform ". *Advances in Theoretical and Applied Mathematics*, 14(1), 81-87.

[23] Maitama, S., & Zhao, W. (2019). New integral transform: Shehu transform a generalization of Sumudu and Laplace transform for solving differential equations. *International Journal of Analysis and Applications*, 17(2), 167-190.

[24] Kamal, H., & Sedeeg, A. (2016). The new integral transform Kamal transform. *Advances in Theoretical and Applied Mathematics*, 11(4), 451-8.

[25] Jafari, H. (2021). A new general integral transform for solving integral equations. *Journal of Advanced Research*, 32, 133-138.

[26] Hussein, M.A., & Hussein A. (2022). A review on integral transforms of the fractional derivatives of Caputo Fabrizio and Atangana-Baleanu. *Eurasian Journal of Media and Communications,* 7,17-23.

[27] Khalid, M., & Alha, S. (2023). New generalized integral transform on Hilfer-Prabhakar fractional derivatives and its applications. *Authorea.*

[28] Costa, F.S., Soares, J.C.A., Jarosz, S., & Sousa, J. (2022). Integral transforms of the hilfer-type fractional derivatives. *Asian Research Journal of Mathematics,* 18 (12), 57-74.

[29] El-Mesady, A.I., Hamed, Y.S., & Alsharif, A.M. (2021). Jafari transformation for solving a system of ordinary differential equations with medical application. *Fractal and Fractional*, 5(3), 130.

[30] Meddahi, M., Jafari, H., & Yang X.J. (2021). Towards new general double integral transform and its applications to differential equations. *Mathematical Methods in the Applied Sciences*, 1-18.

[31] Mansour, E.A., & Meftin, N.K. (2021). Mathematical modeling for cryptography using Jafari transformation method. *Periodicals of Engineering and Natural Sciences*, 9(4), 892-897.

[32] Rashid, S., Sultana, S., Ashraf, R., & Kaabar, M.K.A. (2021). On comparative analysis for the black-scholes model in the generalized fractional derivatives sense via Jafari transform. *Journal of Function Spaces,* 2021, 1-22.

[33] Rashid, S., Ashraf, R., & Jarad, F. (2022). Strong interaction of Jafari decomposition method with nonlinear fractional-order partial differential equations arising in plasma via the singular and nonsingular kernels. *AIMS Mathematics,* 7(5), 7936-7963.

[34] Rashid, S., Ashraf, R., & Bonyah, E. (2022). On analytical solution of time-fractional biological population model by means of generalized integral transform with their uniqueness and convergence analysis. *Journal of Function Spaces*, Article ID 7021288, 29 pages.

[35] Kilbas, A.A., Srivastava, H.M., & Trujillo, J.J. (2006). *Theory and Applications of Fractional Differential Equations.* vol.204, North-Holland Mathematics Studies, Elsevier Science B.V., Amsterdam.

[36] Caputo, M., & Fabrizio, M. (2015). A new definition of fractional derivative without singular kernel. *Progress in Fractional Differentiation and Applications,* 73,1-13.

[37] Hilfer, R. (2008). *Threefold Introduction to Fractional Derivative, Anomalous Transport:Foundations and Application.* Wiley-VCH, Weinheim, Germany.

[38] Meddahi, M., Jafari, H., & Ncube, M.M. (2021). New general integral transform via Atangana-Baleanu derivatives. *Advances in Continuous and Discrete Models,* 385, 2021.

[39] Prabhakar, T.R. (1971). A singular integral equation with a generalized Mittag-Leffler

function in the kernel. *Yokohama Mathematical Journal*, 19 , 7-15.

[40] Garra, R., & Garrappa, R. (2018). The Prabhakar or three parameter Mittag–Leffler function: Theory and application. *Communications in Nonlinear Science and Numerical Simulation*, 56, 314-329.

[41] Khalouta, A. (2023). A new general integral transform for solving Caputo fractional-order differential equations. *International Journal of Nonlinear Analysis and Applications*, 14(1), 67-78.

[42] Bodkhe, D.S., & Panchal, S.K. (2016). On sumudu transform of fractional derivatives and its applications to fractional differential equations. *Asian Journal of Mathematics and Computer Research*, 11(1), 69-77.

Rachid Belgacem's *academic career began with a Diploma of Higher Studies in Mathematics, specializing in Operational Research, from the Houari Boumediene University of Sciences and Technologies (USTHB) in Algiers, Algeria, in 1999. He then obtained his Magister degree in Mathematics in 2012, from the University of Mostaganem. Subsequently, he obtained his doctorate in mathematics, specializing in optimization and optimal control, at the same university. Belgacem obtained his Habilitation (HDR) on July 6, 2021, where his research interests were focused on fractional calculus, optimal control, numerical optimization and applied mathematics. Currently, Belgacem is an associate professor in the Department of Mathematics of the Faculty of Exact Sciences and Computer Science of Hassiba Benbouali University of Chlef, Algeria.*

https://orcid.org/0000-0002-1697-4075

Ahmed Bokhari *is an Associate Professor at the Department of Mathematics, Exact Sciences, and Informatics Faculty, Hassiba Benbouali University of Chelef, Algeria. He received his magister (2012) and Ph.D. (2017) degrees from the Department of Mathematics, Mostaganem University, Algeria. His research areas include optimization, optimal control, and fractional differential equations.*

https://orcid.org/0000-0002-0402-5542

Dumitru Baleanu *is a Professor of mathematics in the Computer Science and Mathematics Department, Lebanese American University, Beirut. He received his B.Sc. from the University of Craiova, M.Sc. from the University of Bucharest, and obtained his Ph.D. from the Institute of Atomic Physics, Romania. Dr. Baleanu is a pioneer of the fractional variational principles and their applications in control theory. His research areas include fractional differential equations.*

https://orcid.org/0000-0002-0286-7244

Salih Djilali *is an Associate Professor in the Department of Mathematics at the University of Chlef. He obtained his Ph.D. from the University of Tlemcen in 2018. Dr. Djilali's current research focuses on applied mathematics, employing various methodologies such as partial differential equations, delay differential equations, and fractional calculus.*

https://orcid.org/0000-0002-4030-6499

RESEARCH ARTICLE

Some results regarding observability and initial state reconstruction for time-fractional systems

Hamza Ben Brahim^a, Fatima-Zahrae El Alaoui^a, Khalid Zguaid^{b*}

^{a} *TSI Team, Faculty of Sciences, Moulay Ismail University, Meknes, Morocco*
^{b} *LRST Laboratory, The Higher School of Education and Training of Agadir (ESEFA), Ibn Zohr University, Agadir, Morocco*
 brahim.hamzaben@edu.umi.ac.ma, f.elalaoui@umi.ac.ma, zguaid.khalid@gmail.com

ARTICLE INFO	ABSTRACT
	The aim of this study is to present the notion of observability for a specific class of linear time-fractional systems of Riemann-Liouville type with a differentiation order between 1 and 2. To accomplish this goal, we first define the concept of observability and its features, then we extend the Hilbert Uniqueness Method (HUM) to determine the system's initial state. This method converts the reconstruction problem into a solvability one, leading to an algorithm that calculates the initial state. The effectiveness of the proposed algorithm is demonstrated through numerical simulations, which are presented in the final section.

1. Introduction

Over the past two decades, fractional differential systems have been widely used in the mathematical modeling of real phenomena such as diffusion, fluid mechanics, and viscoelasticity [1, 2]. These applications have motivated many researchers in the field of differential systems to study fractional differential systems with different fractional derivatives. In many processes or phenomena with long-range temporal cumulative memory effects and/or long-range spatial interactions, numerical and theoretical results have also shown that fractional differential systems offer more advantages than integer-order systems. Recently, the theory of fractional differential systems has become an important research topic in the field of evolutionary systems [3–5].

In this paper, we consider Ω as a bounded region in $\mathbb{R}^n$ whose boundary is sufficiently smooth

$\partial\Omega$, and $\varepsilon \in]1,2[$. From now on, we denote $Q = \Omega \times]0,T]$ and $\Sigma = \partial\Omega \times]0,T]$ and we consider the following fractional system on the finite interval $]0,T]$:

$$
\begin{cases}
^{RL}\mathcal{D}_{0^+}^{\varepsilon}\Theta(x,t) = A\Theta(x,t) & in\ Q, \\
\lim_{t \to 0^+} \mathcal{I}_{0^+}^{2-\varepsilon}\Theta(x,t) = \Theta_0(x) & in\ \Omega, \\
\lim_{t \to 0^+} \frac{\partial}{\partial t}\mathcal{I}_{0^+}^{2-\varepsilon}\Theta(x,t) = \Theta_1(x) & in\ \Omega, \\
\Theta(\xi,t) = 0 & on\ \Sigma,
\end{cases}
\tag{1}
$$

where $^{RL}\mathcal{D}_{0^+}^{\varepsilon}$ is the Riemann-Liouville fractional order derivative, A is a second order, linear, differential operator, and $\mathcal{I}_{0^+}^{\varepsilon}$ is the Riemann–Liouville fractional integral of order ε. The Riemann-Liouville fractional derivative is one of the most important extensions of ordinary integer order derivatives. Differential equations with this type of fractional derivative require special forms of

---

*Corresponding Author

initial conditions. The study of distributed systems involves analyzing and designing these systems based on their mathematical models, including tasks such as determining system stability and observability, as well as designing control and observer algorithms to ensure the system behaves as desired. Fractional calculus provides a powerful tool for analyzing and designing fractional distributed systems, as it allows for a more complete and accurate description of the system's behavior.

In recent years, the observability of fractional equations has received considerable attention. Observability refers to the ability to determine an initial state on the basis of its inputs and outputs, and is a crucial concept in the analysis of control systems. In general, the observability of fractional equations in abstract spaces comprises two cases: exact observability and approximate observability. When studying the exact observability of fractional systems in abstract spaces, we assume that the observability operator has a bounded inverse operator. Approximate observability, as opposed to exact observability, is better suited to describing natural phenomena. Previous research has extensively studied observability in classical systems, including integer-order distributed parameter systems. For instance, Wang [6] discussed observability in such systems, while Goodson and Klein [7] established observability criteria for simple systems, such as the wave equation and heat equation. More recent studies have examined observability through regional analysis. For example, Bourray, Boutoulout, and El Alaoui [8, 9] studied the regional boundary observability and the regional gradient observability for distributed parameter systems of integer order, while [10] developed regional enlarged observability for integer-order linear parabolic systems. For time-fractional distributed parameter systems with Riemann-Liouville fractional derivative, [11] developed the regional gradient observability. Zguaid, El Alaoui, and Boutoulout [12] studied the observability of a class of linear time-fractional diffusion systems with Caputo derivative of order $0 < \varepsilon < 1$. Additionally, other definitions of observability have been proposed in the literature, such as the fractional observability Gramian and matrix, studied by the authors in [13]. They also derived controllability and observability conditions for fractional continuous-time linear systems based on Gramian matrices. Furthermore, [14] explored regional observability for Hadamard-Caputo time fractional distributed parameter systems, and in [15], the pseudo-state representation was used to construct Luenberger-like observers for estimating various

variables. For a deeper understanding of observability for classical and fractional systems we refer the reader to the literature [16–28]. According to the academic literature, the observability of linear systems has been widely studied, with multiple methods proposed for calculation. One such method is the Hilbert Uniqueness Method (HUM). The HUM approach is based on the principles of Hilbert space theory and can be extended to time-fractional distributed systems. Using HUM, observability can be determined by converting the reconstruction problem into a solvency one [29]. There are many articles that discuss the applications of the HUM approach, and we refer the reader to [30–34].

Inspired by the above-mentioned articles, the aim of this work is to study the observability of Riemann-Liouville time-fractional system (1). Our contribution consists of giving several characterizations for the exact and approximate observability of the linear system under consideration. We present a method for reconstructing the initial state in the desired region. In addition, we provide some simple numerical simulations that support our theoretical results.

This work is structured as follows: The first section provides an overview of the mathematical and conceptual foundations that will be used throughout the work. The second section focuses on the definitions and observability characteristics of fractional linear-time distributed systems with a Riemann-Liouville type derivative of order $1 < \varepsilon < 2$, including exact and approximate observability. In the third section, we introduce the concept of fractional Green's formula with order $1 < \varepsilon < 2$, and apply the HUM approach to determine the initial state of the system. To validate the effectiveness of the HUM approach, we present some examples and conclude with a numerical simulation.

2. Considered system and preliminaries

In this section, we give some definitions of fractional derivatives and integrals of Riemann-Liouville and Caputo types with an order of differentiation between 1 and 2. In addition, we introduce the essential concepts related to the theory of the cosine family, which will be used in this work. Moreover, we define the two-parameter Mittag-Leffler function, which has many important applications in fractional calculus. Let $\mathfrak{X}$ be a Hilbert space with the norm $\|.\|_{\mathfrak{X}}$.

We begin by outlining the definitions and key properties of fractional integrals and derivatives

of Riemann-Liouville and Caputo types with order ε in the interval $]1, 2[$.

Definition 1. *[35] Let us consider* $\mathcal{Q} \in L^1(]a, b[; \mathfrak{X})$. *We define the left-sided fractional integral of ζ with order $\varepsilon \in]1, 2[$ by the following from:*

$$\mathcal{I}_{a+}^{\varepsilon} \mathcal{Q}(t) = \frac{1}{\Gamma(\varepsilon)} \int_a^t (t-s)^{\varepsilon-1} \mathcal{Q}(s) ds, \quad a < t \leq b.$$

Where $\Gamma(\varepsilon) = \int_0^{+\infty} \theta^{\varepsilon-1} e^{-\theta} d\theta$, *is the Gamma function.*

We define $AC([a, b]; \mathfrak{X}) := \{\varphi : [a, b] \to \mathfrak{X}, \varphi$ *is absolutely continuous*$\}$.

Definition 2. *[35] Let us consider* $\zeta \in AC([a, b]; \mathfrak{X})$ *then:*

(1) *The left-sided Riemann–Liouville fractional derivative of order $\varepsilon \in]1, 2[$ of a function ζ is defined by:*

$$^{RL}\mathcal{D}_{a+}^{\varepsilon} \mathcal{Q}(t) = \frac{1}{\Gamma(2-\varepsilon)} \frac{d^2}{dt^2} \int_a^t (t-s)^{1-\varepsilon} \mathcal{Q}(s) ds,$$

for $a < t \leq b$.

(2) *The right-sided Caputo fractional derivative of order $\varepsilon \in]1, 2[$ of a function ζ is defined by:*

$$^{C}\mathcal{D}_{b-}^{\varepsilon} \mathcal{Q}(t) = \frac{1}{\Gamma(2-\varepsilon)} \int_t^b (s-t)^{1-\varepsilon} \frac{d^2}{ds^2} \mathcal{Q}(s) ds,$$

for $a \leq t < b$.

Next, we will explore the key concepts of cosine family theory that are relevant to this work. For the rest of this paper, the adjoint of any operator P, is denoted by P^*.

Definition 3. *[36] A one parameter family* $(\mathfrak{W}(t))_{t \in \mathbb{R}}$ *of bounded linear operators mapping the Banach space $\mathfrak{X}$ into itself is called a strongly continuous cosine family if and only if:*

(1) $\mathfrak{W}(0) = \mathfrak{I}$, *where $\mathfrak{I}$ is the identity function of $\mathfrak{X}$.*

(2) $\mathfrak{W}(t+s) + \mathfrak{W}(t-s) = 2\mathfrak{W}(t)\mathfrak{W}(s), \forall(t, s) \in \mathbb{R}^2$.

(3) *The map $\eta \mapsto \mathfrak{W}(t)\eta$, is continuous in t for each fixed point $\eta \in \mathfrak{X}$.*

The sine family $(\mathfrak{U}(t))_{t \in \mathbb{R}}$ associated with the strongly continuous cosine family $(\mathfrak{W}(t))_{t \in \mathbb{R}}$ is defined by:

$$\mathfrak{U}(t)\eta = \int_0^t \mathfrak{W}(s)\eta ds, \quad \eta \in \mathfrak{X}, \quad t \in \mathbb{R}.$$

The infinitesimal generator of the cosine family $(\mathfrak{W}(t))_{t \in \mathbb{R}}$, which we denote A, is defined by:

$$A\eta = \frac{d^2}{dt^2} \mathfrak{W}(0)\eta, \quad \forall \eta \in \mathcal{D}(A).$$

Where $\mathcal{D}(A) = \{\eta \in \mathfrak{X} : \mathfrak{W}(t)\eta \in C^2(R, \mathfrak{X})\}$. This infinitesimal generator A is a closed, densely-defined operator in $\mathfrak{X}$.

We have the following proposition

Proposition 1. *[37] Let A be the infinitesimal generator of a strongly continuous cosine family of bounded linear operators $(\mathfrak{W}(t))_{t \in \mathbb{R}}$ on $\mathfrak{X}$, we have:*

$$\mathfrak{W}(t) = \sum_{n=0}^{+\infty} \frac{A^n t^{2n}}{2n!}, \quad \forall t \in \mathbb{R}.$$

For more details about strongly continuous cosine and sine families, we refer the reader to [38, 39].

The two-parameter Mittag-Leffler function, which plays an important role in this work, is given in the coming definition.

Definition 4. *[40] The two parameter Mittag-Leffler function is defined as:*

$$E_{p,\zeta}(u) = \sum_{j=0}^{+\infty} \frac{u^j}{\Gamma(jp+\zeta)}; \quad p, \zeta > 0; \quad u \in \mathbb{C}.$$

For more details, we refer to [41].

Throughout this paper, we maintain the assumption that $\mathfrak{X} := L^2(\Omega)$, and that the family of linear operators $(\mathfrak{W}(t))_{t \in \mathbb{R}}$ is uniformly bounded. This means that there exists a constant $\mathbf{G} \geq 1$, such that for any t in the real numbers ($t \in \mathbb{R}$), the norm of the operator $\mathfrak{W}(t)$ in the space of all linear and bounded operators from $\mathfrak{X}$ to itself is bounded by $\mathbf{G}$.

In addition, we define the operator $A : \mathcal{D}(A) \subset \mathfrak{X} \longrightarrow \mathfrak{X}$ as the infinitesimal generator of the cosine family of uniformly bounded linear operators $(\mathfrak{W}(t))_{t \in \mathbb{R}}$ on the space $\mathfrak{X}$ is defined as follows:

$$A\Theta(x, t) = \sum_{h,k=1}^n \frac{\partial}{\partial x_d} \left[\sigma_{hk}(x) \frac{\partial \Theta(x, t)}{\partial x_k} \right] + \sigma_0 \Theta(x, t), \tag{2}$$

$\forall x \in \Omega, \forall t \in]0, T]$, where the coefficients σ_{hk} are in $C^1(\overline{\Omega})$, with $1 \leq h \leq n$ and $1 \leq k \leq n$, and σ_0 is in $C^1(\overline{\Omega})$, such that:

$$\begin{cases} \sigma_{hk} = \sigma_{kh}, \quad 1 \leq h \leq n, \ 1 \leq k \leq n, \\ \exists B > 0, \ \forall \varsigma \in \mathbb{R}^n, \ \sum_{h,k=1}^n \sigma_{dk}(x)\varsigma_h\varsigma_k \geq B\|\varsigma\|^2, \end{cases} \tag{3}$$

for $\varsigma = (\varsigma_1, \varsigma_2, \ldots, \varsigma_n) \in \mathbb{R}^n$ and $\|\varsigma\|^2 = \sum_{i=1}^n \varsigma_i^2$.

We consider the system (1) augmented by the following output functional:

$$\varpi(t) = \mathfrak{C}\Theta(.,t), \quad \forall t \in]0,T]. \tag{4}$$

Where $\mathfrak{C}$ is a linear, possibly unbounded, operator called the observation operator with dense domain in $\mathfrak{X}$ and range in $\mathfrak{O}$, where $\mathfrak{O}$ is a Hilbert space (observation space).

Next, we give the definition of the mild solution for the system (1).

Definition 5. *[42] For any $t \in]0,T]$ and $1 < \varepsilon < 2$, a function $\Theta(.,.) \in C(]0,T];\mathfrak{X})$, is said to be a mild solution of the system (1) if it satisfies:*

$$\Theta(x,t) = M_q(t)\Theta_0(x) + R_q(t)\Theta_1(x), q = \frac{\varepsilon}{2}. \tag{5}$$

for all $t \in]0,T], x \in \Omega$.

Where

$$M_q(t) = \frac{d}{dt}t^{q-1}P_q(t), \quad t \in]0,T],$$

$$R_q(t) = t^{q-1}P_q(t) = \int_0^t M_q(s)ds, \quad t \in]0,T],$$

$$P_q(t) = \int_0^\infty q\theta S_q(\theta)\mathfrak{W}(t^q\theta)d\theta, \quad t \in]0,T],$$

and

$$S_q(\rho) = \frac{1}{q}\rho^{-1-\frac{1}{q}}\xi_q(\rho^{\frac{-1}{q}}), \quad \rho \in]0,+\infty[,$$

$$\xi_q(\rho) = \frac{1}{\pi}\sum_{k=1}^\infty (-1)^{n-1}(\rho)^{-nq-1}\frac{\Gamma(nq+1)}{n!}sin(n\pi q),$$

for all $\rho \in]0,+\infty[$.

Note that $S_q(.)$ is the Mainardi's Wright-type function, which is defined on $]0,+\infty[$ and satisfies:

- $S_q(\rho) \geq 0, \rho \in]0,+\infty[$.
- $\int_0^{+\infty} \rho^n S_q(\rho)d\rho = \frac{\Gamma(n+1)}{\Gamma(1+nq)}$.

The measurement functional (4) can also be written as:

$$\varpi(t) = \mathfrak{J}_\varepsilon(t)\begin{pmatrix}\Theta_0\\\Theta_1\end{pmatrix}, \quad \forall t \in]0,T], \tag{6}$$

where $\mathfrak{J}_\varepsilon : \mathfrak{X}^2 \longrightarrow L^2(]0,T];\mathfrak{O})$ is called the observability operator, and it's defined by:

$$\mathfrak{J}_\varepsilon(t)\begin{pmatrix}\Theta_0\\\Theta_1\end{pmatrix} = \mathfrak{C}M_q(t)\Theta_0 + \mathfrak{C}R_q(t)\Theta_1.$$

Note that the operator $\mathfrak{J}_\varepsilon$ is bounded if $\mathfrak{C}$ is bounded, and it plays an important role in the characterization of observability.

The objective is to determine the initial state of a system from the output function (4). To achieve this, the adjoint of $\mathfrak{J}_\varepsilon$ must be calculated

which is not always defined when $\mathfrak{C}$ is unbounded. This calculation will later aid in defining and understanding the characteristics of observability. Then, we consider the following definition.

Definition 6. *[43] We say that the operator $\mathfrak{C}$ is an admissible observation operator, respectively, for M_q and R_q, if:*

- *$\exists N_1$, such that:*

$$\forall z \in \mathcal{D}(A), \quad \int_0^T \|\mathfrak{C}M_q(t)z\|_\mathfrak{O}^2 dt \leq N_1\|z\|_\mathfrak{X}^2,$$

and

- *$\exists N_2$, such that:*

$$\forall z \in \mathcal{D}(A), \quad \int_0^T \|\mathfrak{C}R_q(t)z\|_\mathfrak{O}^2 dt \leq N_2\|z\|_\mathfrak{X}^2.$$

Remark 1. *The admissibility condition for M_q and R_q is always satisfied in the case where $\mathfrak{C}$ is bounded. Therefore, a bounded observation operator $\mathfrak{C}$ is an admissible one.*

Throughout this paper, we suppose that $\mathfrak{C}$ is an admissible observation operator. Then, the adjoint operator of $\mathfrak{J}_\varepsilon$ is given as follows:

$$\mathfrak{J}_\varepsilon^* : \quad L^2(]0,T];\mathfrak{O}) \longrightarrow \mathfrak{X}^2$$

$$\mathcal{Y} \longmapsto \begin{pmatrix}\int_0^T M_q^*(t)\mathfrak{C}^*\mathcal{Y}(t)dt\\\int_0^T R_q^*(t)\mathfrak{C}^*\mathcal{Y}(t)dt\end{pmatrix}. \tag{7}$$

Indeed:
Let us consider $(y_0, y_1) \in \mathfrak{X}^2$, and $\mathcal{Y} \in L^2(]0,T];\mathfrak{O})$, then:

$$\left\langle \mathfrak{J}_\varepsilon(.)\begin{pmatrix}y_0\\y_1\end{pmatrix}, \mathcal{Y}\right\rangle_{L^2(]0,T];\mathfrak{O})}$$

$$= \int_0^T \left\langle \mathfrak{J}_\varepsilon(t)\begin{pmatrix}y_0\\y_1\end{pmatrix}, \mathcal{Y}(t)\right\rangle_\mathfrak{O} dt$$

$$= \int_0^T \langle \mathfrak{C}M_q(t)y_0 + \mathfrak{C}R_p(t)y_1, \mathcal{Y}(t)\rangle_\mathfrak{O} dt$$

$$= \int_0^T \left\langle y_0, M_q^*(t)\mathfrak{C}^*\mathcal{Y}(t)\right\rangle_\mathfrak{X} dt$$

$$+ \int_0^T \left\langle y_1, R_q^*(t)\mathfrak{C}^*\mathcal{Y}(t)\right\rangle_\mathfrak{X} dt$$

$$= \left\langle \begin{pmatrix}y_0\\y_1\end{pmatrix}, \begin{pmatrix}\int_0^T M_q^*(t)\mathfrak{C}^*\mathcal{Y}(t)dt\\\int_0^T R_q^*(t)\mathfrak{C}^*\mathcal{Y}(t)dt\end{pmatrix}\right\rangle_{\mathfrak{X}^2}.$$

We extend the definitions of observability for hyperbolic systems to the fractional case $\varepsilon \in]1,2[$. Consequently, we have the following definition:

Definition 7. • *The system* (1) *with* (4) *is said to be exactly observable if:*

$$\text{Im}\,(\mathfrak{J}_\varepsilon{}^*) = \mathfrak{X}^2.$$

• *The system* (1) *with* (4) *is said to be approximately observable if:*

$$\overline{\text{Im}\,(\mathfrak{J}_\varepsilon{}^*)} = \mathfrak{X}^2.$$

We now present some useful properties regarding the exact and approximate observablity. This first proposition gives us many characterizations regarding the approximate observability of the system (1).

Proposition 2. *The following properties are equivalent:*

(1) *The system* (1) *with* (4) *is approximately observable .*
(2) $\text{Ker}\,(\mathfrak{J}_\varepsilon) = \{0\}$.
(3) $\underline{\text{Ker}\,(\mathfrak{J}_\varepsilon{}^*\mathfrak{J}_\varepsilon)} = \{0\}$.
(4) $\overline{Im(\mathfrak{J}_\varepsilon{}^*\mathfrak{J}_\varepsilon)} = \mathfrak{X}^2$.
(5) $(\mathfrak{J}_\varepsilon\mathfrak{J}_\varepsilon{}^*)$ *is positive definite.*

Proof. We show that $1 \Leftrightarrow 2$, $2 \Leftrightarrow 3$, $3 \Leftrightarrow 4$, and $2 \Leftrightarrow 5$.

• (1)⇔(2) We know that the space $\mathfrak{X}^2$ is a reflexive Banach space, then:

$$Im\,(\mathfrak{J}_\varepsilon{}^*) = \mathfrak{X}^2 \Leftrightarrow \left[\overline{Im\,(\mathfrak{J}_\varepsilon{}^*)}\right]^\perp = \left[\mathfrak{X}^2\right]^\perp$$
$$\Leftrightarrow \text{Ker}\,(\mathfrak{J}_\varepsilon) = \{0\}.$$

• (2)⇔(3)
   i) First, let us show that: $Ker(\mathfrak{J}_\varepsilon{}^*\mathfrak{J}_\varepsilon) = \{0\} \Rightarrow Ker(\mathfrak{J}_\varepsilon) = \{0\}$.
   Let us consider $y \in Ker(\mathfrak{J}_\varepsilon)$, then:

$$\mathfrak{J}_\varepsilon(t)y = 0 \Rightarrow \mathfrak{J}_\varepsilon{}^*\mathfrak{J}_\varepsilon(t)y = 0$$
$$\Rightarrow y \in Ker(\mathfrak{J}_\varepsilon{}^*\mathfrak{J}_\varepsilon)$$
$$\Rightarrow y = 0.$$

   Then, we get: $Ker(\mathfrak{J}_\varepsilon) = \{0\}$.
   ii) Second, let us show that: $Ker(\mathfrak{J}_\varepsilon) = \{0\} \Rightarrow Ker(\mathfrak{J}_\varepsilon{}^*\mathfrak{J}_\varepsilon) = \{0\}$.
   Let us consider $y \in Ker(\mathfrak{J}_\varepsilon{}^*\mathfrak{J}_\varepsilon)$, we have:

$$\langle \mathfrak{J}_\varepsilon{}^*\mathfrak{J}_\varepsilon(.)y, y \rangle_{\mathfrak{X}^2} = \langle \mathfrak{J}_\varepsilon(.)y, \mathfrak{J}_\varepsilon(.)y \rangle_{L^2(]0,T];\mathfrak{O})}$$
$$= \|\mathfrak{J}_\varepsilon(.)y\|^2_{L^2(]0.T];\mathfrak{O})}.$$

   We have $\mathfrak{J}_\varepsilon{}^*\mathfrak{J}_\varepsilon(.)y = 0$, then, $\mathfrak{J}_\varepsilon(.)y = 0$, which implies that $y \in Ker(\mathfrak{J}_\varepsilon)$. Thus, $y = 0$.
   Consequently $Ker(\mathfrak{J}_\varepsilon{}^*\mathfrak{J}_\varepsilon) = \{0\}$.
• (3) ⇔ (4) This is a direct consequence from the fact that:

$$\text{Ker}\,(\mathfrak{J}_\varepsilon{}^*\mathfrak{J}_\varepsilon) = \left[\overline{Im\,(\mathfrak{J}_\varepsilon{}^*\mathfrak{J}_\varepsilon)}\right]^\perp$$

• (5)⇔ (2)   If $\mathfrak{J}_\varepsilon{}^*\mathfrak{J}_\varepsilon$ is positive definite. Then:

$$\langle \mathfrak{J}_\varepsilon{}^*\mathfrak{J}_\varepsilon u, u \rangle \geq 0, \quad \forall u \in \mathfrak{X}^2,$$

and

$$\langle \mathfrak{J}_\varepsilon{}^*\mathfrak{J}_\varepsilon u, u \rangle = 0 \Rightarrow u = 0, \quad \forall u \in \mathfrak{X}^2.$$

We have

$$\langle \mathfrak{J}_\varepsilon{}^*\mathfrak{J}_\varepsilon u, u \rangle_{\mathfrak{X}} = \langle \mathfrak{J}_\varepsilon{}^*u, \mathfrak{J}_\varepsilon{}^*u \rangle_{L^2(]0,T];\mathfrak{O})}$$
$$= \|\mathfrak{J}_\varepsilon(.)u\|^2_{L^2(0,T;\mathfrak{O})} \geq 0, \forall u \in \mathfrak{X}^2.$$

On the other hand
$$[\langle \mathfrak{J}_\varepsilon{}^*\mathfrak{J}_\varepsilon u, u \rangle_{\mathfrak{X}} = 0 \Longrightarrow u = 0]$$
$$\Leftrightarrow \left[\|\mathfrak{J}_\varepsilon(.)u\|^2_{L^2(]0,T];\mathfrak{O})} = 0 \Longrightarrow u = 0\right]$$
$$\Leftrightarrow [\mathfrak{J}_\varepsilon u = 0 \Longrightarrow u = 0]$$
$$\Leftrightarrow \quad Ker(\mathfrak{J}_\varepsilon) = \{0\}.$$

This completes the proof. □

In this next proposition, we shed light on some characterizations regarding the exact observability of the systeme (1).

Proposition 3. *The mentioned statements are equivalent:*

(1) *The system* (1) *with* (4) *is exactly observable.*
(2) $\exists M > 0$, *such that:*

$$\|z\|_{\mathfrak{X}^2} \leq M\|\mathfrak{J}_\varepsilon(.)z\|_{L^2(]0,T],\mathfrak{O})}, \quad \forall z \in \mathfrak{X}^2.$$

(3) *The operator* $\mathfrak{J}_\varepsilon\mathfrak{J}_\varepsilon{}^*$ *is coercive .*
(4) $Im(\mathfrak{J}_\varepsilon{}^*)$ *is closed and* $Ker(\mathfrak{J}_\varepsilon) = \{0\}$.

Before proving the main proposition, we recall the following lemma:

Lemma 1. *[44] Let* $\mathcal{F}$, $\mathcal{G}$ *and* $\mathcal{H}$ *be three reflexive Banach spaces. Let us consider* $\mathcal{N} \in \mathcal{L}(\mathcal{F};\mathcal{H})$ *and* $\mathcal{T} \in \mathcal{L}(\mathcal{G};\mathcal{H})$. *The mentioned statements are equivalent:*

(1) $Im(\mathcal{N}) \subset Im(\mathcal{T})$,
(2) $\exists M > 0$, *such that:*

$$\|\mathcal{N}^*z^*\|_{\mathcal{F}^*} \leq M\|\mathcal{T}^*z^*\|_{\mathcal{G}^*}, \quad \forall z^* \in \mathcal{H}^*.$$

Now, we give the proof of the proposition (3).

Proof. We show that $1 \Leftrightarrow 2$, $2 \Leftrightarrow 3$ and $1 \Leftrightarrow 4$.

• 1 ⇔ 2 This is a direct application of Lemma (1) with:
   • $\mathcal{F} = \mathcal{H} = \mathfrak{X}^2$.
   • $\mathcal{G} = L^2(]0,T];\mathfrak{O})$.
   • $\mathcal{N} = Id_{\mathfrak{X}^2}$.
   • $\mathcal{T} = \mathfrak{J}_\varepsilon{}^*$.
   Where $Id_{\mathfrak{X}^2}$ is the identity function of $\mathfrak{X}^2$.
• 3 ⇔ 2 If $\mathfrak{J}_\varepsilon{}^*\mathfrak{J}_\varepsilon$ is coercive, then there exists $M > 0$ such that $\forall(z_0, z_1) \in \mathfrak{X}^2$

$$\left\langle \mathfrak{J}_\varepsilon{}^*\mathfrak{J}_\varepsilon \begin{pmatrix} z_0 \\ z_1 \end{pmatrix}, \begin{pmatrix} z_0 \\ z_1 \end{pmatrix} \right\rangle_{\mathfrak{X}^2} \geq M \left\| \begin{pmatrix} z_0 \\ z_1 \end{pmatrix} \right\|^2_{\mathfrak{X}^2}$$

$$\Leftrightarrow \left\| \mathfrak{J}_\varepsilon(.) \begin{pmatrix} z_0 \\ z_1 \end{pmatrix} \right\|^2_{L^2(]0,T];\mathfrak{O})} \geq M \left\| \begin{pmatrix} z_0 \\ z_1 \end{pmatrix} \right\|^2_{\mathfrak{X}^2}$$

$$\Leftrightarrow \left\| \mathfrak{J}_\varepsilon(.) \begin{pmatrix} z_0 \\ z_1 \end{pmatrix} \right\|_{L^2(]0,T];\mathfrak{O})} \geq \sqrt{M} \left\| \begin{pmatrix} z_0 \\ z_1 \end{pmatrix} \right\|_{\mathfrak{X}^2}.$$

- $1 \Leftrightarrow 4$
  - (1) $1 \Rightarrow 4$

    Since system (1) with (4) is exactly observable it also approximately observable . Then,

    $$\text{Im}\,(\mathfrak{J}_\varepsilon{}^*) = \mathfrak{X}^2 \ and \ \overline{\text{Im}\,(\mathfrak{J}_\varepsilon{}^*)} = \mathfrak{X}^2.$$

    Then $Im(\mathfrak{J}_\varepsilon{}^*)$ is closed. By using the proposition (2) we get $\text{Ker}\,(\mathfrak{J}_\varepsilon) = \{0\}$.
    Thus, $Im(\mathfrak{J}_\varepsilon{}^*)$ is closed and $\text{Ker}\,(\mathfrak{J}_\varepsilon) = \{0\}$.
  - (2) $4 \Rightarrow 1$

    We have $\text{Ker}\,(\mathfrak{J}_\varepsilon) = \{0\}$, Hence, by using the proposition (2), we get $\overline{\text{Im}\,(\mathfrak{J}_\varepsilon{}^*)} = \mathfrak{X}^2$, this, together with the fact that $Im(\mathfrak{J}_\varepsilon{}^*)$ is closed, we obtain $\text{Im}\,(\mathfrak{J}_\varepsilon{}^*) = \mathfrak{X}^2$.

This completes the proof. $\qquad\square$

We give the following proposition.

Proposition 4. *If the system* (1) *with* (4) *exactly observable then the application* $(\mathfrak{J}_\varepsilon{}^*\mathfrak{J}_\varepsilon)^{-1}$ *is continuous* .

Proof. We know that a linear operator $\mathfrak{B}$ is invertible and of continuous inverse if and only if:

$$\exists m > 0, \ such \ that \ \ m\|z\| \leq \|\mathfrak{B}z\|, \quad (8)$$

see [44].
If the system (1) with (4) exactly observable, then:

$\exists m > 0, \ such \ that, \forall (z_0, z_1) \in \mathfrak{X}^2,$

$$\left\langle \mathfrak{J}_\varepsilon{}^*\mathfrak{J}_\varepsilon \begin{pmatrix} z_0 \\ z_1 \end{pmatrix}, \begin{pmatrix} z_0 \\ z_1 \end{pmatrix} \right\rangle_{\mathfrak{X}^2} \geq m \left\| \begin{pmatrix} z_0 \\ z_1 \end{pmatrix} \right\|^2_{\mathfrak{X}^2}$$

$\implies \exists m > 0, \ such \ that, \ \forall (z_0, z_1) \in \mathfrak{X}^2,$

$$m \left\| \begin{pmatrix} z_0 \\ z_1 \end{pmatrix} \right\|^2_{\mathfrak{X}^2} \leq \left\| \mathfrak{J}_\varepsilon{}^*\mathfrak{J}_\varepsilon(.) \begin{pmatrix} z_0 \\ z_1 \end{pmatrix} \right\|_{L^2(0,T;\mathfrak{O})} \left\| \begin{pmatrix} z_0 \\ z_1 \end{pmatrix} \right\|_{\mathfrak{X}^2}$$

$\implies \exists m > 0, \ such \ that, \ \forall (z_0, z_1) \in \mathfrak{X}^2,$

$$m \left\| \begin{pmatrix} z_0 \\ z_1 \end{pmatrix} \right\|_{\mathfrak{X}^2} \leq \left\| \mathfrak{J}_\varepsilon{}^*\mathfrak{J}_\varepsilon(.) \begin{pmatrix} z_0 \\ z_1 \end{pmatrix} \right\|_{L^2(0,T;\mathfrak{O})}$$

$\implies (\mathfrak{J}_\varepsilon{}^*\mathfrak{J}_\varepsilon)^{-1}$ *is continus.*

This completes the proof. $\qquad\square$

By the conditions 3, it is well known that A is symmetric and $-A$ is uniformly elliptic. In this case, it is well known that $-A$ has a set of eigenvalues $(\lambda_j)_{j\geq 1}$, such that:

$$0 < \lambda_1 < \lambda_2 < \lambda_3 < \lambda_4 < \cdots \lambda_{j+1} < \cdots \to +\infty.$$

Each eigenvalue λ_j corresponds with r_j eigenfunctions $\{\varphi_{jk}\}_{1\leq k \leq r_j}$, where $r_j \in \mathbb{N}^*$ is the multiplicity of λ_j, such that $A\varphi_{jk} = \lambda_j \varphi_{jk}$ and $\varphi_{jk} \in \mathcal{D}(A), \forall j \in \mathbb{N}^*$ and $1 \leq k \leq r_j$. In addition, the set $\{\varphi_{jk}\}_{\substack{j \geq 1 \\ 1 \leq r_j \leq j}}$ form an orthogonal basis of $\mathfrak{X}$, [45].
We give the following proposition.

Proposition 5. *Let us consider* $\Theta_0, \Theta_1 \in \mathfrak{X}$ *and* $t \in]0, T]$, *we have:*

1. $$R_q(t)\Theta_1(x) = \sum_{j=1}^{+\infty}\sum_{k=1}^{r_j} t^{2q-1}E_{2q,2q}\left(\lambda_j t^{2q}\right)$$
$$\times \langle \Theta_1, \varphi_{jk}\rangle_{\mathfrak{X}}\,\varphi_{jk}(x).$$

2. $$M_q(t)\Theta_0(x) = \sum_{j=1}^{+\infty}\sum_{k=1}^{r_j} t^{2q-2}E_{2q,2q-1}(\lambda_j t^{2q})$$
$$\times \langle \Theta_0, \varphi_{jk}\rangle_{\mathfrak{X}}\,\varphi_{jk}(x).$$

Proof. Let us consider $\Theta_0, \Theta_1 \in \mathfrak{X}$ and $t \in]0, T]$. From (1), we can write the cosine family $(\mathfrak{W}(t))_{t\geq 0}$ in the following form:

$$\mathfrak{W}(t)\Theta_0(x) = \sum_{n=0}^{+\infty}\sum_{j=1}^{+\infty}\sum_{k=1}^{r_j} \frac{t^{2n}\lambda_j^n}{2n!}\,\langle \Theta_0, \varphi_{jk}\rangle_{\mathfrak{X}}\,\varphi_{jk}(x).$$

Thus,

1. $R_q(t)\Theta_1(x)$

$$= t^{q-1}\int_0^\infty q\theta S_q(\theta)\mathfrak{U}(t^q\theta)\Theta_1(x)d\theta$$

$$= t^{q-1}\int_0^\infty q\theta S_q(\theta)\int_0^{t^q\theta} \mathfrak{W}(s)\Theta_1(x)ds\,d\theta$$

$$= t^{q-1}\int_0^\infty \sum_{j=1}^{+\infty}\sum_{k=1}^{r_j}\sum_{n=0}^{+\infty} \frac{(t^q\theta)^{2n+1}\lambda_j^n}{2n!(2n+1)}$$
$$\times q\theta S_q(\theta)\,\langle \Theta_1, \varphi_{jk}\rangle_{\mathfrak{X}}\,\varphi_{jk}(x)d\theta$$

$$= t^{q-1}\sum_{j=1}^{+\infty}\sum_{k=1}^{r_j}\sum_{n=0}^{+\infty}\langle \Theta_1, \varphi_{jk}\rangle_{\mathfrak{X}}\,\varphi_{jk}(x)$$
$$\times \int_0^\infty q\theta S_q(\theta)\frac{\lambda_j^n(t^q\theta)^{2n+1}}{2n!(2n+1)}d\theta$$

$$= t^{q-1}\sum_{j=1}^{+\infty}\sum_{k=1}^{r_j}\sum_{n=0}^{+\infty}\langle \Theta_1, \varphi_{jk}\rangle_{\mathfrak{X}}\,\varphi_{jk}(x)$$
$$\times \frac{q\lambda_j^n(t^q)^{2n+1}}{(2n+1)!}\int_0^\infty S_q(\theta)\theta^{2n+2}d\theta$$

$$= t^{q-1} \sum_{j=1}^{+\infty} \sum_{k=1}^{r_j} \sum_{n=0}^{+\infty} \langle \Theta_1, \varphi_{jk} \rangle_{\mathfrak{X}} \varphi_{jk}(x)$$

$$\times \frac{q\lambda_j^n (t^q)^{2n+1}}{(2n+1)!} \times \frac{\Gamma(1+2n+2)}{\Gamma(1+q(2n+2))}$$

$$= t^{2q-1} \sum_{j=1}^{+\infty} \sum_{k=1}^{r_j} \langle \Theta_1, \varphi_{jk} \rangle_{\mathfrak{X}} \varphi_{jk}(x)$$

$$\times \sum_{n=0}^{+\infty} \frac{(\lambda_j t^{2q})^n}{\Gamma(2q+2qn)}$$

$$= \sum_{j=1}^{+\infty} \sum_{k=1}^{r_j} t^{2q-1} E_{2q,2q} \left(\lambda_j t^{2q} \right)$$

$$\times \langle \Theta_1, \varphi_{jk} \rangle_{\mathfrak{X}} \varphi_{jk}(x).$$

And,

2. $$M_q(t)\Theta_0(x) = \sum_{j=1}^{+\infty} \sum_{k=1}^{r_j} \langle \Theta_0, \varphi_{jk} \rangle_{\mathfrak{X}} \varphi_{jk}(x)$$

$$\times \frac{d}{dt} t^{2q-1} E_{2q,2q} \left(\lambda_j t^{2q} \right)$$

$$= \sum_{j=1}^{+\infty} \sum_{k=1}^{r_j} \langle \Theta_0, \varphi_{jk} \rangle_{\mathfrak{X}} \varphi_{jk}(x)$$

$$\times \sum_{n=0}^{+\infty} \frac{(2qn+2q-1)\lambda_j^n t^{2qn+2q-2}}{\Gamma(2q+2qn)}$$

$$= \sum_{j=1}^{+\infty} \sum_{k=1}^{r_j} \langle \Theta_0, \varphi_{jk} \rangle_{\mathfrak{X}} \varphi_{jk}(x)$$

$$\times \sum_{n=0}^{+\infty} \frac{\lambda_j^n t^{2qn+2q-2}}{\Gamma(2qn+2q-1)}$$

$$= \sum_{j=1}^{+\infty} \sum_{k=1}^{r_j} t^{2q-2} E_{2q,2q-1}(\lambda_j t^{2q})$$

$$\times \langle \Theta_0, \varphi_{jk} \rangle_{\mathfrak{X}} \varphi_{jk}(x).$$

This completes the proof. $\square$

3. The steps of HUM approach

In this section, we give an approach that allows the reconstruction of the initial state. First, we will give a new version of Green's fractional formula, which is of major importance in the field of control theory [29].

Proposition 6. (*Fractional Green's formula of order* $1 < \alpha < 2$.)

For any $\psi \in C^{\infty} \overline{(\Omega \times [0,T])}$, we have:

$$\int_0^T \int_\Omega \left({}^{RL}D_{0^+}^\alpha \Theta(x,t) + A\Theta(x,t) \right) \psi(x,t) dx dt$$

$$= \int_0^T \int_\Omega \left({}^C D_{T^-}^\alpha \psi(x,t) + A^*\psi(x,t) \right) \Theta(x,t) dx dt$$

$$- \int_\Omega I_{0^+}^{2-\alpha} \Theta(x,T) \frac{\partial}{\partial t} \psi(x,T) dx$$

$$+ \int_\Omega \frac{\partial}{\partial t} I_{0^+}^{2-\alpha} \Theta(x,T) \psi(x,T) dx$$

$$+ \int_\Omega \lim_{t \to 0^+} I_{0^+}^{2-\alpha} \Theta(x,t) \frac{\partial}{\partial t} \psi(x,0) dx$$

$$- \int_\Omega \lim_{t \to 0^+} \frac{\partial}{\partial t} I_{0^+}^{2-\alpha} \Theta(x,t) \psi(x,0) dx$$

$$+ \int_0^T \int_{\partial\Omega} \left(\Theta(\xi,t) \frac{\partial \psi(\xi,t)}{\partial \nu_{A^*}} - \psi(\xi,t) \frac{\partial \Theta(\xi,t)}{\partial \nu_A} \right) d\xi dt.$$

Proof. For any $\psi \in C^{\infty} \overline{(\Omega \times [0,T])}$, we have:

$$\int_0^T \int_\Omega \left({}^{RL}\mathcal{D}_{0^+}^\alpha \Theta(x,t) + A\Theta(x,t) \right) \psi(x,t) dx dt$$

$$= \int_0^T \int_\Omega \left({}^{RL}\mathcal{D}_{0^+}^\alpha \Theta(x,t) \right) \psi(x,t) dx dt$$

$$+ \int_0^T \int_\Omega \left(A\Theta(x,t) \right) \psi(x,t) dx dt, \tag{9}$$

Now, we recall the two useful properties. The first one is the fractional integration by parts formula, see [46],

$$\int_0^T {}^{RL}\mathcal{D}_{0^+}^\alpha \Theta(t) \psi(t) dt = \int_0^T {}^C\mathcal{D}_{T^-}^\alpha \psi(t) \Theta(t) dt$$

$$- \left[\mathcal{I}_{0^+}^{2-\alpha} \Theta(t) \frac{d}{dt} \psi(t) - \frac{d}{dt} \mathcal{I}_{0^+}^{2-\alpha} \Theta(t) \psi(t) \right]_0^T$$

$$= \int_0^T {}^C\mathcal{D}_{T^-}^\alpha \psi(t)) \Theta(t) dt - \mathcal{I}_{0^+}^{2-\alpha} \Theta(T) \frac{d}{dt} \psi(T)$$

$$+ \frac{d}{dt} \mathcal{I}_{0^+}^{2-\alpha} \Theta(T) \psi(T) + \lim_{t \to 0} \mathcal{I}_{0^+}^{2-\alpha} \Theta(t) \frac{d}{dt} \psi(0)$$

$$- \lim_{t \to 0} \frac{d}{dt} \mathcal{I}_{0^+}^{2-\alpha} \Theta(t) \psi(0). \tag{10}$$

The second property is,

$$\int_\Omega A\Theta(x,t) \psi(x,t) dx = \int_\Omega \Theta(x,t) A^*\psi(x,t) dx$$

$$+ \int_{\partial\Omega} \Theta(\xi,t) \frac{\partial \psi(\xi,t)}{\partial \nu_{A^*}} d\xi - \int_{\partial\Omega} \psi(\xi,t) \frac{\partial \Theta(\xi,t)}{\partial \nu_A} d\xi, \tag{11}$$

and it can be found in [47].

Using (10) and (11), we obtain:

$$\int_0^T \int_\Omega \left(^{RL}\mathcal{D}_{0^+}^\alpha \Theta(x,t) + A\Theta(x,t)\right) \psi(x,t)dxdt$$

$$= \int_0^T \int_\Omega \left(^{C}\mathcal{D}_{T^-}^\alpha \psi(x,t) + A^*\psi(x,t)\right)\Theta(x,t)dxdt$$

$$+ \int_0^T \int_{\partial\Omega} \left(\Theta(\xi,t)\frac{\partial\psi(\xi,t)}{\partial\nu_{A^*}} - \psi(\xi,t)\frac{\partial\Theta(\xi,t)}{\partial\nu_A}\right)d\xi dt$$

$$- \int_\Omega \lim_{t\to T} \mathcal{I}_{0^+}^{2-\alpha}\Theta(x,t)\frac{\partial}{\partial t}\psi(x,t)dx$$

$$+ \int_\Omega \lim_{t\to T} \frac{\partial}{\partial t}\mathcal{I}_{0^+}^{2-\alpha}\Theta(x,t)\psi(x,t)dx$$

$$+ \int_\Omega \lim_{t\to 0^+} \mathcal{I}_{0^+}^{2-\alpha}\Theta(x,t)\frac{\partial}{\partial t}\psi(x,t)dx$$

$$- \int_\Omega \lim_{t\to 0^+} \frac{\partial}{\partial t}\mathcal{I}_{0^+}^{2-\alpha}\Theta(x,t)\psi(x,t)dx.$$

Thus, we finally get that:

$$\int_0^T \int_\Omega \left(^{RL}D_{0^+}^\alpha \Theta(x,t) + A\Theta(x,t)\right) \psi(x,t)dxdt$$

$$= \int_0^T \int_\Omega \left(^{C}D_{T^-}^\alpha \psi(x,t) + A^*\psi(x,t)\right)\Theta(x,t)dxdt$$

$$- \int_\Omega I_{0^+}^{2-\alpha}\Theta(x,T)\frac{\partial}{\partial t}\psi(x,T)dx$$

$$+ \int_\Omega \frac{\partial}{\partial t}I_{0^+}^{2-\alpha}\Theta(x,T)\psi(x,T)dx$$

$$+ \int_\Omega \lim_{t\to 0^+} I_{0^+}^{2-\alpha}\Theta(x,t)\frac{\partial}{\partial t}\psi(x,0)dx$$

$$- \int_\Omega \lim_{t\to 0^+} \frac{\partial}{\partial t}I_{0^+}^{2-\alpha}\Theta(x,t)\psi(x,0)dx$$

$$+ \int_0^T \int_{\partial\Omega} \left(\Theta(\xi,t)\frac{\partial\psi(\xi,t)}{\partial\nu_{A^*}} - \psi(\xi,t)\frac{\partial\Theta(\xi,t)}{\partial\nu_A}\right)d\xi dt.$$

This completes the proof. □

Let us now present the steps of the method that we use in order to reconstruct the initial state. This method is an extension of the Hilbert uniqueness method (HUM) presented by Lions in [29].

For any $(\beta_0, \beta_1) \in \mathfrak{X} \times \mathfrak{X}$. Consider the system:

$$\begin{cases} ^{RL}\mathcal{D}_{0^+}^\varepsilon \beta(x,t) = A\beta(x,t) & in\ Q, \\ \lim_{t\to 0^+} \mathcal{I}_{0^+}^{2-\varepsilon}\beta(x,t) = \beta_0(x) & in\ \Omega, \\ \lim_{t\to 0^+} \frac{d}{dt}\mathcal{I}_{0^+}^{2-\varepsilon}\beta(x,t) = \beta_1(x) & in\ \Omega, \\ \beta(\xi,t) = 0 & on\ \Sigma, \end{cases} \tag{12}$$

which has a unique mild solution:

$$\varphi(x,t) = M_q(t)\beta_0(x) + R_q(t)\beta_1(x). \tag{13}$$

We introduce the semi-norm on $\mathfrak{X}^2$:

$$\|\cdot\|_{\mathcal{S}_{\mathrm{II}}}: \quad \mathfrak{X}^2 \longrightarrow \mathbb{R}^+$$

$$(\beta_0, \beta_1) \quad \longmapsto \|(\beta_0,\beta_1)\|_{\mathcal{S}_{\mathrm{II}}} = \sqrt{\int_0^T \|\mathfrak{C}\beta(x,t)\|_{\mathbb{O}}^2 dt}. \tag{14}$$

We then have the following results:

Lemma 2. *If the system* (12) *together with the output equation* (4) *is approximately observable then the semi-norm* $\|\cdot\|_{\mathcal{S}_{\mathrm{II}}}$ *becomes a norm .*

Proof. We need to show that: $\forall (\beta_0, \beta_1) \in \mathfrak{X}^2$, we have:

$$\|(\beta_0, \beta_1)\|_{\mathcal{S}_{\mathrm{II}}} = 0 \Rightarrow \beta_0 = \beta_1 = 0.$$

Let us consider $(\beta_0, \beta_1) \in \mathfrak{X}^2$, then:

$$\|(\beta_0,\beta_1)\|_{\mathcal{S}_{\mathrm{II}}}^2 = 0 \Leftrightarrow \int_0^T \|\mathfrak{C}\beta(x,t)\|_{\mathfrak{O}}^2 dt = 0$$

$$\Leftrightarrow \|\mathfrak{C}\beta(x,t)\|_{\mathfrak{O}} = 0, \quad \forall t \in]0,T]$$

$$\Leftrightarrow \mathfrak{C}\beta(x,t) = 0, \quad \forall t \in]0,T]$$

$$\Leftrightarrow \mathfrak{J}_\varepsilon(t)\begin{pmatrix} \beta_0 \\ \beta_1 \end{pmatrix} = 0, \quad \forall t \in]0,T]$$

$$\Leftrightarrow \begin{pmatrix} \beta_0 \\ \beta_1 \end{pmatrix} \in Ker(\mathfrak{J}_\varepsilon),$$

using the fact that (1) with (4) is approximately observable, we get that:

$$\beta_0 = \beta_1 = 0.$$

This completes the proof.

□

We define the retrograded system of (12) as follows:

$$\begin{cases} ^{C}\mathcal{D}_{T^-}^\varepsilon \psi(x,t) = A^*\psi(x,t) - \mathfrak{C}^*\mathfrak{C}\beta(x,t) & inQ, \\ \psi(x,T) = 0, \quad \frac{\partial}{\partial t}\psi(x,T) = 0 & in\ \Omega, \\ \psi(\xi,t) = 0 & on\ \Sigma, \end{cases} \tag{15}$$

which has a unique mild solution in $C\left(]0,T]; \mathfrak{X}\right)$, see: [48].

$$\psi(x,t) = -\int_t^T (\tau-t)^{q-1}P_q^*(\tau-t)\mathfrak{C}^*\mathfrak{C}\beta(x,\tau)d\tau, \tag{16}$$

where

$$P_q^*(t) = \int_0^\infty qyS_q(y)\mathfrak{U}^*(t^q y)dy.$$

We now present a new alternative result that plays an important role in solving the reconstruction problem.

Proposition 7. *The mild solution ψ of system (15) satisfies:*

1. $\psi(x,0) = -\displaystyle\int_0^T R_q^*(\tau)\mathfrak{C}^*\mathfrak{C}\beta(x,\tau)d\tau.$

2. $\dfrac{\partial}{\partial t}\psi(x,0) = \displaystyle\int_0^T M_q^*(\tau)\mathfrak{C}^*\mathfrak{C}\beta(x,\tau)d\tau.$

(17)

Proof. 1) Let ψ a mild solution of system (15), then:

$$\psi(x,t) = -\int_t^T (\tau-t)^{q-1}P_q^*(\tau-t)\mathfrak{C}^*\mathfrak{C}\beta(x,\tau)d\tau.$$

Thus, if $t = 0$, we obtain:

$$\psi(x,0) = -\int_0^T (\tau)^{q-1}P_q^*(\tau)\mathfrak{C}^*\mathfrak{C}\beta(x,\tau)d\tau,$$

$$= -\int_0^T R_q^*(\tau)\mathfrak{C}^*\mathfrak{C}\beta(x,\tau)d\tau.$$

2) Using equation (16), we obtain:

$$\frac{\partial}{\partial t}\psi(x,t)$$

$$= \frac{\partial}{\partial t}\left[-\int_t^T (\tau-t)^{q-1}P_q^*(\tau-t)\mathfrak{C}^*\mathfrak{C}\beta(x,\tau)d\tau\right]$$

$$= \left[-\int_t^T \frac{\partial}{\partial t}((\tau-t)^{q-1}P_q^*(\tau-t))\mathfrak{C}^*\mathfrak{C}\beta(x,\tau)d\tau\right]$$

$$\quad - \lim_{\tau\longrightarrow T} R_q(\tau-t)\mathfrak{C}^*\mathfrak{C}\beta(x,\tau)\frac{\partial}{\partial t}(T)$$

$$\quad + \lim_{\tau\longrightarrow t} R_q(\tau-t)\mathfrak{C}^*\mathfrak{C}\beta(x,\tau)\frac{\partial}{\partial t}(t)$$

$$= \int_t^T M_q^*(\tau-t))\mathfrak{C}^*\mathfrak{C}\beta(x,\tau)d\tau,$$

thus, if $t = 0$, we obtain:

$$\frac{\partial}{\partial t}\psi(x,0) = \int_0^T M_q^*(\tau)\mathfrak{C}^*\mathfrak{C}\beta(x,\tau)d\tau.$$

This completes the proof. $\qquad\square$

If (β_0,β_1) is chosen such that $C\beta(.,t) = \varpi(t)$ in Ω, then, by using the fractional Green's formula, the following system can be seen as the adjoint system of(1) with (4).

$$\begin{cases} {}^C\mathcal{D}_{T^-}^\varepsilon\Upsilon(x,t) = A^*\Upsilon(x,t) - \mathfrak{C}^*\varpi(.,t) & in\ Q, \\ \Upsilon(x,T) = 0, \quad \dfrac{\partial}{\partial t}\Upsilon(x,T) = 0 & in\ \Omega, \\ \Upsilon(\xi,t) = 0 & on\ \Sigma. \end{cases}$$

(18)

We define the mapping:

$$\Lambda: \quad \mathfrak{X}^2 \longrightarrow \mathfrak{X}^2$$

$$(\beta_0,\beta_1) \longrightarrow \Lambda(\beta_0,\beta_1) = \left(\frac{\partial}{\partial t}\psi(x,0), -\psi(x,0)\right).$$

(19)

Then, the problem of reconstruction is reduced to solve the following equation:

$$\Lambda(\beta_0,\beta_1) = \left(\frac{\partial}{\partial t}\Upsilon(x,0), -\Upsilon(x,0)\right). \quad (20)$$

We then have the following theorem.

Theorem 1. *If the system (12) is approximately observable, then the equation (20) has a unique solution which corresponds with the initial state in Ω.*

Proof. We need to prove that Λ is coercive: (i.e) $\exists\ C > 0,$ such that

$$\langle\Lambda(\beta_0,\beta_1),(\beta_0,\beta_1)\rangle_{\mathfrak{X}^2} \geq C\ \|(\beta_0,\beta_1)\|_{\mathfrak{X}^2}^2. \quad (21)$$

Then:

$$\langle\Lambda(\beta_0,\beta_1),(\beta_0,\beta_1)\rangle_{\mathfrak{X}^2}$$

$$= \left\langle \left(\frac{\partial}{\partial t}\Upsilon(x,0), -\Upsilon(x,0)\right),(\beta_0,\beta_1)\right\rangle_{\mathfrak{X}^2}$$

$$= \left\langle \int_0^T M_q^*(\tau)\mathfrak{C}^*\mathfrak{C}\beta(\tau)d\tau, \beta_0\right\rangle_{\mathfrak{X}}$$

$$\quad + \left\langle \int_0^T R_q^*(\tau)\mathfrak{C}^*\mathfrak{C}\beta(\tau)d\tau, \beta_1\right\rangle_{\mathfrak{X}}$$

$$= \int_0^T \langle\mathfrak{C}\beta(\tau),\mathfrak{C}\beta(\tau)\rangle_{\mathfrak{O}}\,d\tau$$

$$= \|(\beta_0,\beta_1)\|_{\mathfrak{X}^2}^2.$$

This completes the proof. $\qquad\square$

4. Numerical approach

In this section, we present an approach that gives the initial state in cases where pointwise and zonal sensors are used. Let Ω be an open bounded subset on $\mathbb{R}^n$, we consider the abstract time-fractional system:

$$\begin{cases} {}^{RL}\mathcal{D}_{0^+}^\varepsilon\beta(x,t) = A\beta(x,t) & in\ Q, \\ \lim_{t\to0^+}\mathcal{I}_{0^+}^{2-\varepsilon}\beta(x,t) = \beta_0(x) & in\ \Omega, \\ \lim_{t\to0^+}\dfrac{\partial}{\partial t}\mathcal{I}_{0^+}^{2-\varepsilon}\beta(x,t) = \beta_1(x) & in\ \Omega, \\ \beta(\xi,t) = 0 & on\ \Sigma, \end{cases}$$

(22)

for simplicity, we can safely assume that the eigenvalues of $-A$ are of multiplicity equal to 1, eventhough this is not always the case. The reason behind this consideration is to work with a single iterator in the index of the eigenfunctions in order to simplify the mathematical expressions, which is always possible since we can always find a possible rearrangement of the eigenvalues and eigenfunctions which makes this possible. Note that in the new arrangement, many eigenvalues

will have the same value. We denote the eigenvalues of $-A$ by λ_j, for every $j \in \mathbb{N}^*$, and the corresponding normalized eigenfunctions by $\varphi_j(x)$, for every $j \in \mathbb{N}^*$.

Hence, the system (22) has a unique mild solution given by the following formula:

$$\beta(x,t) = \sum_{j=1}^{+\infty} t^{2q-2} \langle \beta_0(.), \varphi_j \rangle_{\mathfrak{X}} E_{2q,2q-1}\left(\lambda_j t^{2q}\right)$$
$$+ t^{2q-1} \langle \beta_1(.), \varphi_j \rangle_{\mathfrak{X}} E_{2q,2q}\left(\lambda_j t^{2q}\right) \varphi_j(x).$$

The adjoint system of (22) is written as:

$$\begin{cases} {}^C\mathcal{D}_{T^-}^{\varepsilon} \Upsilon(x,t) = A\Upsilon(x,t) - \mathfrak{C}^*\varpi(t) & in\ Q, \\ \Upsilon(x,T) = 0, \qquad \dfrac{\partial}{\partial t}\Upsilon(x,T) = 0 & in\ \Omega, \\ \Upsilon(\xi,t) = 0 & on\ \Sigma. \end{cases} \tag{23}$$

Hence, by using (17) and proposition (5) , we get:

1. $\displaystyle -\Upsilon(x,0) = \int_0^T R_q(t)\mathfrak{C}^*\varpi(t)dt$
$$= \int_0^T \sum_{j=1}^{+\infty} t^{2q-1} E_{2q,2q}\left(\lambda_j t^{2q}\right)$$
$$\times \langle \mathfrak{C}^*\varpi(t), \varphi_j \rangle_{\mathfrak{X}} \varphi_j(x)dt,$$

2. $\displaystyle \frac{\partial}{\partial t}\Upsilon(x,0) = \int_0^T M_q(t)\mathfrak{C}^*\varpi(t)dt$
$$= \int_0^T \sum_{j=1}^{+\infty} t^{2q-2} E_{2q,2q-1}(\lambda_j t^{2q})$$
$$\times \langle \mathfrak{C}^*\varpi(t), \varphi_j \rangle_{\mathfrak{X}} \varphi_j(x)dt.$$

For any $(\beta_0, \beta_1) \in \mathfrak{X}^2$, we also have:

$$\langle \Lambda(\beta_0,\beta_1),(\beta_0,\beta_1) \rangle_{\mathfrak{X}^2} = \int_0^T \|\mathfrak{C}\beta(x,t)\|_{\mathfrak{D}}^2 dt, \tag{24}$$

by using the expression of $\beta(.,.)$, we obtain:

$$\int_0^T \|\mathfrak{C}\beta(x,t)\|_{\mathfrak{D}}^2 dt =$$
$$\sum_{j,i=1}^{+\infty} \int_0^T t^{4q-4} E_{2q,2q-1}\left(\lambda_j t^{2q}\right) E_{2q,2q-1}\left(\lambda_i t^{2q}\right) dt$$
$$\times \mathfrak{C}\varphi_j(x)\mathfrak{C}\varphi_i(x) \langle \beta_0, \varphi_j \rangle_{\mathfrak{X}} \langle \beta_0, \varphi_i \rangle_{\mathfrak{X}}$$
$$+ \int_0^T t^{4q-3} E_{2q,2q-1}\left(\lambda_j t^{2q}\right) E_{2q,2q}\left(\lambda_i t^{2q}\right) dt\mathfrak{C}\varphi_j(x)$$
$$\times \mathfrak{C}\varphi_i(x) \langle \beta_1, \varphi_j \rangle_{\mathfrak{X}} \langle \beta_0, \varphi_i \rangle_{\mathfrak{X}}$$
$$+ \int_0^T t^{4q-3} E_{2q,2q}\left(\lambda_j t^{2q}\right) E_{2q,2q-1}\left(\lambda_i t^{2q}\right) dt\mathfrak{C}\varphi_j(x)$$
$$\times \mathfrak{C}\varphi_i(x) \langle \beta_0, \varphi_j \rangle_{\mathfrak{X}} \langle \beta_1, \varphi_i \rangle_{\mathfrak{X}}$$
$$+ \int_0^T t^{4q-2} E_{2q,2q}\left(\lambda_j t^{2q}\right) E_{2q,2q}\left(\lambda_i t^{2q}\right) dt\mathfrak{C}\varphi_j(x)$$
$$\times \mathfrak{C}\varphi_i(x) \langle \beta_1, \varphi_j \rangle_{\mathfrak{X}} \langle \beta_1, \varphi_i \rangle_{\mathfrak{X}}. \tag{25}$$

Then, the problem (24) can be approached by the linear systems:

$$\sum_{j=1}^N \begin{pmatrix} A_{i,j} & B_{i,j} \\ C_{i,j} & D_{i,j} \end{pmatrix} \begin{pmatrix} \beta_0^j \\ \beta_1^j \end{pmatrix} = \begin{pmatrix} \Upsilon_1^i(x,0) \\ \Upsilon_0^i(x,0) \end{pmatrix}, \tag{26}$$

for　i=1,2,3,…,N . Where:

- $A_{i,j} = \displaystyle\int_0^T t^{4q-4} E_{2q,2q-1}\left(\lambda_j t^{2q}\right) E_{2q,2q-1}\left(\lambda_i t^{2q}\right) dt$
  $\times \mathfrak{C}\varphi_j(x)\mathfrak{C}\varphi_i(x).$

- $B_{i,j} = \displaystyle\int_0^T t^{4q-3} E_{2q,2q-1}\left(\lambda_j t^{2q}\right) E_{2q,2q}\left(\lambda_i t^{2q}\right) dt$
  $\times \mathfrak{C}\varphi_j(x)\mathfrak{C}\varphi_i(x).$

- $C_{i,j} = \displaystyle\int_0^T t^{4q-3} E_{2q,2q}\left(\lambda_j t^{2q}\right) E_{2q,2q-1}\left(\lambda_i t^{2q}\right) dt$
  $\times \mathfrak{C}\varphi_j(x)\mathfrak{C}\varphi_i(x).$

- $D_{i,j} = \displaystyle\int_0^T t^{4q-2} E_{2q,2q}\left(\lambda_j t^{2q}\right) E_{2q,2q}\left(\lambda_i t^{2q}\right) dt$
  $\times \mathfrak{C}\varphi_j(x)\mathfrak{C}\varphi_i(x).$

- $\beta_0^j = \langle \beta_0, \varphi_j \rangle_{\mathfrak{X}}.$
- $\beta_1^j = \langle \beta_1, \varphi_j \rangle_{\mathfrak{X}}.$
- $\Upsilon_0^i(x,0) = \langle -\Upsilon(.,0), \varphi_i \rangle_{\mathfrak{X}}.$
- $\Upsilon_1^i(x,0) = \left\langle \dfrac{\partial}{\partial t}\Upsilon(.,0), \varphi_i \right\rangle_{\mathfrak{X}}.$

In the case where the output function is given by a pointwise sensor $\varpi(t) = \beta(b,t)$, where $b \in \Omega$. Then, we get:

- $\Upsilon(x,0) = -\displaystyle\sum_{j=1}^{+\infty} \int_0^T t^{2q-1} E_{2q,2q}\left(\lambda_j t^{2q}\right) \beta(b,t)dt$
  $\times \varphi_j(b)\varphi_j(x).$

- $\dfrac{\partial}{\partial t}\Upsilon(x,0) = \displaystyle\sum_{j=1}^{+\infty} \int_0^T t^{2q-2} E_{2q,2q-1}\left(\lambda_j t^{2q}\right) \beta(b,t)dt$
  $\times \varphi_j(b)\varphi_j(x).$

And

- $A_{i,j} = \displaystyle\int_0^T t^{4q-4} E_{2q,2q-1}\left(\lambda_j t^{2q}\right) E_{2q,2q-1}\left(\lambda_i t^{2q}\right) dt$
  $\times \varphi_j(b)\varphi_i(b).$

- $B_{i,j} = \displaystyle\int_0^T t^{4q-3} E_{2q,2q-1}\left(\lambda_j t^{2q}\right) E_{2q,2q}\left(\lambda_i t^{2q}\right) dt$
  $\times \varphi_j(b)\varphi_i(b).$

- $C_{i,j} = \displaystyle\int_0^T t^{4q-3} E_{2q,2q}\left(\lambda_j t^{2q}\right) E_{2q,2q-1}\left(\lambda_i t^{2q}\right) dt$
  $\times \varphi_j(b)\varphi_i(b).$

- $D_{i,j} = \displaystyle\int_0^T t^{4q-2} E_{2q,2q}\left(\lambda_j t^{2q}\right) E_{2q,2q}\left(\lambda_i t^{2q}\right) dt$
  $\times \varphi_j(b)\varphi_i(b).$

In the case where the output function is given by a zonal sensor (g, D), where $g(x) = \chi_D(x)$ is the spatial distribution of the sensor and D is the spatial domain of g. Then, we get:

- $\Upsilon(x,0) = -\sum_{j=1}^{+\infty} \int_0^T t^{2q-1} E_{2q,2q} \left(\lambda_j t^{2q}\right) \varpi(t) dt$
  $\times \langle g(.), \varphi_j(.)\rangle_{L^2(D)} \varphi_j(x).$

- $\frac{\partial}{\partial t} \Upsilon(x,0) = \sum_{j=1}^{+\infty} \int_0^T t^{2q-2} E_{2q,2q-1}(\lambda_j t^{2q}) \varpi(t) dt$
  $\times \langle g(.), \varphi_j\rangle_{L^2(D)} \varphi_j(x).$

Where:

- $A_{i,j} = \int_0^T t^{4q-4} E_{2q,2q-1}\left(\lambda_j t^{2q}\right) E_{2q,2q-1}\left(\lambda_i t^{2q}\right) dt$
  $\times \langle g, \varphi_j(.)\rangle_{L^2(D)} \langle g, \varphi_i(.)\rangle_{L^2(D)}.$

- $B_{i,j} = \int_0^T t^{4q-3} E_{2q,2q-1}\left(\lambda_j t^{2q}\right) E_{2q,2q}\left(\lambda_i t^{2q}\right) dt$
  $\times \langle g, \varphi_j(.)\rangle_{L^2(D)} \langle g, \varphi_i(.)\rangle_{L^2(D)}.$

- $C_{i,j} = \int_0^T t^{4q-3} E_{2q,2q}\left(\lambda_j t^{2q}\right) E_{2q,2q-1}\left(\lambda_i t^{2q}\right) dt$
  $\times \langle g, \varphi_j(.)\rangle_{L^2(D)} \langle g, \varphi_i(.)\rangle_{L^2(D)}.$

- $D_{i,j} = \int_0^T t^{4q-2} E_{2q,2q}\left(\lambda_j t^{2q}\right) E_{2q,2q}\left(\lambda_i t^{2q}\right) dt$
  $\langle g, \varphi_j(.)\rangle_{L^2(D)} \langle g, \varphi_i(.)\rangle_{L^2(D)}.$

5. Simulations

In this section, we present two numerical simulations illustrating the previous results, to make it easier to understand, let's focus on the one-dimensional case. Throughout this section, we work with we consider $A = \Delta = \frac{\partial^2}{\partial x^2}$ to be the Laplace operator with a domain:

$$\mathcal{D}(\Delta) = \{\sigma \in H_1^0(\Omega) \ , \ \Delta\sigma \in L^2(\Omega)\}$$
$$= H^2(\Omega) \cap H_0^1(\Omega).$$

The operator Δ in this case generates a uniformly bounded strongly continuous cosine family $\{\mathfrak{W}(t)\}_{t \geq 0}$. It is well known that $-\Delta$ has a discrete spectrum and its eigenvalues are λ_j for every $j \in \mathbb{N}^*$, with the corresponding normalized eigenvectors $\varphi_j(x)$ for every $j \in \mathbb{N}^*$.

Example 1. *Consider the abstract time-fractional system:*

$$\begin{cases} {}^{RL}\mathcal{D}_{0^+}^{\frac{3}{2}}\Theta(x,t) = \Delta\Theta(x,t) & in\ Q, \\ \lim_{t \to 0^+} \mathcal{D}_{0^+}^{\frac{1}{2}}\Theta(x,t) = \Theta_0(x) = \frac{1}{2} \times x(1-x) & in\ \Omega, \\ \lim_{t \to 0^+} \frac{\partial}{\partial t}\mathcal{D}_{0^+}^{\frac{1}{2}}\Theta(x,t) = \Theta_1(x) & in\ \Omega, \\ \Theta(\xi,t) = 0 & on\ \Sigma. \end{cases}$$
(27)

where $Q =]0,1[\times]0,3], \Sigma = \{0,1\} \times]0,3]$.
The output function is given by a pointwise sensor $\varpi(t) = \Theta(0.09, t), \forall t \in]0,3]$. According to the numerical algorithm, we obtain the figure (1).
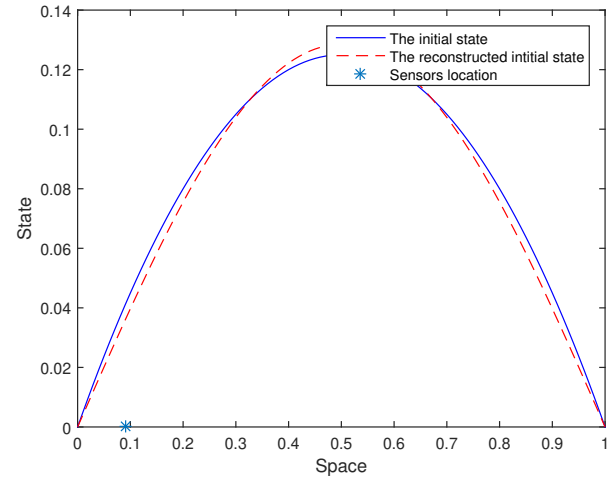
Figure 1. The initial state is represented by a continuous line, while the reconstructed initial state is shown as a dashed line within the interval $]0, 1[$.

In figure (1), the starting state of the system is established with a reconstruction error of $\|\Theta_0 - \beta_0\|_{L^2(]0,1[)} = 3.5 \times 10^{-3}$, and it can be observed that the starting state is close to the estimated starting state in the interval $]0.1[$.

Example 2. *Consider the abstract time-fractional system:*

$$\begin{cases} {}^{RL}\mathcal{D}_{0^+}^{\frac{3}{2}}\Theta(x,t) = \Delta\Theta(x,t) & in\ Q, \\ \lim_{t \to 0^+} \mathcal{I}_{0^+}^{\frac{1}{2}}\Theta(x,t) = \Theta_0(x) = \eta \times x(1-x) & in\ \Omega, \\ \lim_{t \to 0^+} \frac{\partial}{\partial t}\mathcal{I}_{0^+}^{\frac{1}{2}}\Theta(x,t) = \Theta_1(x) & in\ \Omega, \\ \Theta(\xi,t) = 0 & on\ \Sigma. \end{cases}$$
(28)

where $Q =]0,1[\times]0,6], \Sigma = \{0,1\} \times]0,3]$. In this example, we utilize a zonal sensor (g, D) where $D =]\frac{1}{4}, \frac{1}{2}[$ is the spatial domain and $g(x) = \chi_D(x)$ is the spatial distribution of the sensor. The performance of the sensor is measured by the function $\varpi(t) = \langle g, \beta\rangle_{L^2(D)}$. The numerical

process requires the selection of η to ensure that $\Theta_0(x)$ has a suitable magnitude. As a result, we can see the outcome displayed in figure (2).
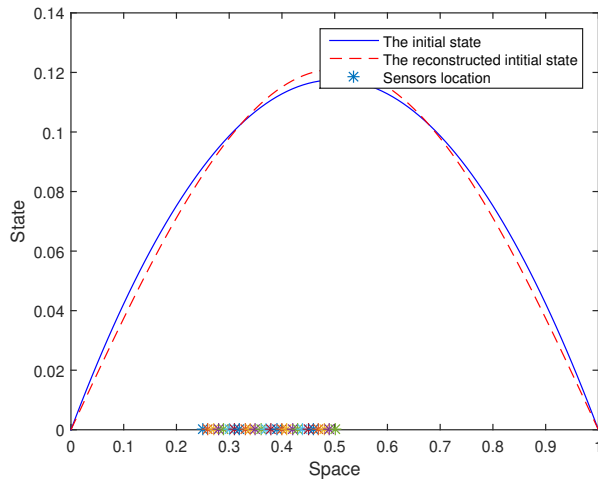
Figure 2. The starting state (continous line) and the reconstructed starting state (dashed line) in]0,1[.

As depicted in Figure (2), the actual initial state is nearly equivalent to the estimated initial state in]0.1[. The error in the reconstruction is $\|\Theta_0 - \beta_0\|_{L^2(]0,1[)} = 3.2 \times 10^{-3}$.

The figures (1) and (2) clearly demonstrate the effectiveness of the approach being considered (i.e. the HUM method and numerical algorithm are suited to solving reconstruction problems).

6. Conclusion

In this article, we have discussed some characterizations concerning the exact and approximate observability of the time-fractional system under consideration. We focused on the steps of the Hilbert uniqueness method to globally reconstruct the initial state for a specific class of linear time-fractional systems, where the Riemann-Liouville derivative has an order of ε in the interval]1, 2[. The difficulty of this process lies in transforming the reconstruction problem into a solvability issue of equation (20), which requires precision in finding its solution. Numerical methods must therefore be employed. To demonstrate the effectiveness of this method, two successful numerical examples were presented at the end of the study.

References

[1] Renardy, M., Hrusa, W.J., & Nohel, J.A. (1987). *Mathematical Problems in Viscoelasticity.* Longman Science & Technology, Longman Scientific and Technical, Essex.

[2] Metzler, R., & Klafter, J. (2000). The Random Walk's Guide to Anomalous Diffusion: A Fractional Dynamics Approach. *Physics Reports*, 339(1), 1–77.

[3] Atangana, A. (2014). Convergence and stability analysis of a novel iteration method for fractional biological population equation. *Neural Computing and Applications*, 25(5), 1021-1030, doi: `https://doi.org/10.1007/s00521-014-1586-0`.

[4] Hilfer, R. (2000). *Applications Of Fractional Calculus In Physics.* World Scientific, Singapore.

[5] Sabatier, J., Agrawal, O.P. & Machado, J.A.T. (2007). *Advances in Fractional Calculus: Theoretical Developments and Applications in Physics and Engineering.* Springer, Dordrecht.

[6] Wang, P.K.C. (1964). Control of Distributed Parameter Systems. *Advances in Control Systems*, 1, 75–172, doi:`https://doi.org/10.1016/B978-1-4831-6717-6.50008-5`.

[7] Goodson, R., & Klein, R.A. (1970). Definition and Some Results for Distributed System Observability. *IEEE Transactions on Automatic Control*, 15(2), 165–174, doi: `https://doi.org/10.1109/TAC.1970.1099407`.

[8] Boutoulout, A., Bourray, H., & El Alaoui, F.Z. (2010). Regional Boundary Observability for Semi-Linear Systems Approach and Simulation. *International Journal of Mathematical Analysis*, 4(24), 1153–1173.

[9] Boutoulout, A., Bourray, H., & El Alaoui, F.Z. (2013). Boundary gradient observability for semi-linear parabolic systems: Sectorial approach. *Mathematical Sciences Letters*, 2(1), 45–54.

[10] Zouiten, H., Boutoulout, A., & El Alaoui, F.Z. (2017). On the Regional Enlarged Observability for Linear Parabolic Systems. *Journal of Mathematics and System Science*, 7, 79-87, doi: `https://doi.org/10.17265/2159-5291/2017.03.001`.

[11] Ge, F., Chen, Y., & Kou, C. (2016). On the Regional Gradient Observability of Time Fractional Diffusion Processes. *Automatica*, 74, 1–9, doi: `https://doi.org/10.1016/j.automatica.2016.07.023`.

[12] Zguaid, K., El Alaoui, F.Z., & Boutoulout, A. (2021). Regional Observability for Linear Time Fractional Systems. *Mathematics and Computers in Simulation*, 185, 77-87, doi: `https://doi.org/10.1016/j.matcom.2020.12.013`.

[13] Awais, Y., Javaid, I., & Zehra, A. (2017). On Controllability and Observability of Fractional Continuous-Time Linear Systems with Regular Pencils. *Bulletin of the Polish Academy of Sciences Technical Sciences*, 65(3), 297-304, doi: `https://doi.org/10.1515/bpasts-2017-0033`.

[14] Cai, R., Ge, F., Chen, Y., & Kou, C. (2019). Regional Observability for Hadamard-Caputo Time Fractional Distributed Parameter Systems. *Applied Mathematics and Computation*, 360, 190–202, doi: `https://doi.org/10.1016/j.amc.2019.04.081`.

[15] Sabatier, J., Farges, C., Merveillaut, M., & Feneteau, L. (2012). On Observability and Pseudo State Estimation of Fractional Order Systems. *European Journal of Control*, 18(3), 260–271, doi: `https://doi.org/10.3166/ejc.18.260-271`.

[16] Zguaid, K., & El Alaoui, F.Z. (2023). The Regional Observability Problem for a Class of Semilinear Time-Fractional Systems With Riemann-Liouville Derivative. *In: Advanced Mathematical Analysis and its Applications, P. Debnath, D. F. M. Torres, and Y. Je Cho, eds., CRC Press, Boca Raton*, 251–264.

[17] Boutoulout, A., Bourray, H., & El Alaoui, F.Z. (2012). Regional Gradient Observability for Distributed Semilinear Parabolic Systems. *Journal of Dynamical and Control Systems*, 18(2), 159–179, doi: `https://doi.org/10.1007/s10883-012-9138-3`.

[18] Boutoulout, A., Bourray, H., El Alaoui, F.Z., & Benhadid, S. (2014). Regional Observability for Distributed Semi-Linear Hyperbolic Systems. *International Journal of Control*, 87(5), 898–910, doi: `https://doi.org/10.1080/00207179.2013.861929`.

[19] Zguaid, K., & El Alaoui, F.Z. (2022). Regional boundary observability for linear time-fractional systems. Partial Differential Equations in Applied Mathematics, 6, 100432.

[20] Zguaid, K., & El Alaoui, F.Z. (2023). Regional Boundary Observability for Semilinear Fractional Systems with Riemann-Liouville Derivative. Numerical Functional Analysis and Optimization, 44(5), 420–437.

[21] El Alaoui, F.Z., Boutoulout, A., & Zguaid, K. (2021). Regional Reconstruction of Semilinear Caputo Type Time-Fractional Systems Using the Analytical Approach. *Advances in the Theory of Nonlinear Analysis and its Application,* 5(4), 580-599.

[22] Zerrik, E., Bourray, H., & El Jai, A. (2004). Regional Observability for Semilinear Distributed Parabolic Systems. *Journal of Dynamical and Control Systems*, 10(3), 413–430, doi: `https://doi.org/10.1023/B:JODS.0000034438.72863.ca`.

[23] Zguaid, K., El Alaoui, F.Z., & Torres, D. F. M. (2023). Regional Gradient Observability for Fractional Differential Equations with Caputo Time-Fractional Derivatives. *International Journal of Dynamics and Control*, 11(5), 2423-2437, doi: `https://doi.org/10.48550/arXiv.2301.00238`.

[24] Zguaid, K., El Alaoui, F.Z., & Boutoulout, A. (2021). Regional Observability of Linear Fractional Systems Involving Riemann-Liouville Fractional Derivative. *In*: Z. Hammouch, H. Dutta, S. Melliani, and M. Ruzhansky, eds. *Nonlinear Analysis: Problems, Applications and Computational Methods.* Springer, Cham, 164-179.

[25] Enrique, C., Jimenez, P., Menendez, J.M., & Conejo, A.J. (2008) *The Observability Problem in Traffic Models: Algebraic and Topological Methods.* IEEE Transactions on Intelligent Transportation Systems, 9(2), 275-87, doi:`https://doi.org/10.1109/TITS..922929`.

[26] Jose, A.L.G., María, N., Enrique, C., & Jose, T. (2013) *Application of Observability Techniques to Structural System Identification.* Computer-Aided Civil and Infrastructure Engineering, 28(6), 434-450, doi: `https://doi.org/10.1111/mice.12004`.

[27] Elbukhari, A.B., Fan, Z., & Li, G. (2023) *The Regional Enlarged Observability for Hilfer Fractional Differential Equations.* Axioms 12(7), 648, doi: `https://doi.org/10.3390/axioms12070648`.

[28] Viti, F., Rinaldi, M., Corman, F., & Tampère, C.M.J. (2014) *Assessing partial observability in network sensor location problems.* Transportation Research Part B: Methodological, 70, 65-89, doi: `https://doi.org/10.1016/j.trb.2014.08.002`.

[29] Lions, J.L. (1998). *Contrôlabilité Exacte Perturbations et Stabilisation de Systèmes Distribués, Tome 1: Contrôlabilité exacte.* Dunod, Paris.

[30] Zguaid, K., El Alaoui, F.Z., & Boutoulout, A. (2023). Regional observability of Caputo semilinear fractional systems, *Asian Journal of Control*, doi: `https://doi.org/10.1002/asjc.3218`.

[31] Lagnese, J. (2006). The Hilbert Uniqueness Method: A Retrospective. *In*: K.H. Hoffmann, W. Krabs, eds. *Optimal Control of Partial Differential Equations.* Springer, Berlin, 158–181.

[32] Zguaid, K., & El Alaoui, F.Z. (2023). On the regional boundary observability of semilinear time-fractional systems with Caputo derivative. *An International Journal of Optimization and Control: Theories & Applications (IJOCTA)*, 13(2), 161-170.

[33] Pedersen, M. (2020). *Functional Analysis in Applied Mathematics and Engineering.* CRC Press, Boca Raton.

[34] Zguaid, K., & El Alaoui, F.Z. (2022). Regional boundary observability for Riemann–Liouville linear fractional evolution systems. *Mathematics and Computers in Simulation*, 199, 272-286.

[35] Kilbas, A.A., Srivastava, H.M. & Trujillo, J.J. (2006). *Theory And Applications of Fractional Differential Equations.* Elsevier, Boston.

[36] Travis, C.C., & Webb, G.F. (1978). Cosine Families and Abstract Nonlinear Second Order Differential Equations. *Acta Mathematica Academiae Scientiarum Hungarica*, 32(1), 75–96.

[37] Vasil'ev, V.V., Krein, S., & Sergey, P. (1991). Semigroups of Operators, Cosine Operator Functions, and Linear Differential Equations. *Journal of Mathematical Sciences*, 54, 1042–1129.

[38] Boua, H. (2021). Spectral Theory For Strongly Continuous Cosine. *Concrete Operators*, 8, 40–47.

[39] Hassani, R.A., Blali, A., Amrani, A.E., & Moussaouja, K. (2018). Cosine Families of Operators in a Class of Fréchet Spaces. *Proyecciones (Antofagasta)*, 37(1), 103–118.

[40] Ge, F., Chen, Y., & Kou, C. (2018). *Regional Analysis of Time-Fractional Diffusion Processes.* Springer, Cham.

[41] Gorenflo, R., Kilbas, A.A., Mainardi, F., & Rogosin, S. (2020). Mittag-Leffler Functions, Related Topics and Applications. Springer, Berlin.

[42] Brahim, H.B., Zguaid, K., & El Alaoui, F.Z. (2024). A New and specific definition for the mild solution of Riemann-Liouville time-fractional systems with $1 < \alpha < 2$,, *To appear.*

[43] Tucsnak, M., & Weiss, G. (2009). *Observation and Control for Operator Semigroups.* Birkhäuser, Basel.

[44] El Jai, A., & Pritchard, A.J. (1986). *Capteurs et actionneurs dans l'analyse des systèmes distribués.* Elsevier Masson, Paris.

[45] Floridia, G., & Yamamoto, M. (2020). Backward Problems in Time for Fractional Diffusion-Wave Equation. *Inverse Problems*, 36(12), 125016, doi: `https://dx.doi.org/10.1088/1361-6420/abbc5e`.

[46] Almeida, R. (2016). *A Caputo Fractional Derivative of a Function with Respect to Another Function.* Communications in Nonlinear Science and Numerical Simulation, 44, doi: `https://doi.org/10.1016/j.cnsns.2016.09.006`.

[47] Lions, J.L., & Magenes, E. (1972). *Non-Homogeneous Boundary Value Problems and Applications.* Springer, Berlin.

[48] Zhou, Y., & Wei, H.J. (2020). New Results on Controllability of Fractional Evolution Systems with Order $\alpha \in (1,2)$. *Computers & Evolution Equations and Control Theory*, 10(3), 491–509, doi: `https://doi.org/10.3934/eect.2020077`.

Hamza Ben Brahim *is a researcher at TSI Team, Faculty of Sciences, Moulay Ismail University, Meknes, Morocco. His fields of research are: regional observability, existence of solutions for fractional systems, fractional calculus.*
🆔 `https://orcid.org/0009-0000-0602-6242`

Fatima-Zahrae El Alaoui *obtained her Ph.D. degree in Analysis and Control of Systems, in 2011, from the Faculty of Sciences, University Moulay Ismail, Meknes, Morocco. She is currently working as a professor at the Department of Mathematics, Faculty of Sciences, University Moulay Ismail, Meknes, Morocco. She is an active member of TSI team. Her fields of research are optimal control, regional observability, regional controllability, fractional calculus, and applied mathematics. She has published many papers in these areas.*
🆔 `https://orcid.org/0000-0001-8912-4031`

Khalid Zguaid *obtained his Ph.D. degree in Analysis and Control of Systems, in 2022, from the Faculty of Sciences, University Moulay Ismail, Meknes, Morocco. He is currently a professor at the Higher School of Education and Training of Agadir (ESEFA), Ibn Zohr University, Agadir, Morocco. He is also an active member of TSI team (Systems Theory & Informatics). His fields of research are optimal control, regional observability, fractional calculus, and applied mathematics, and he has published many papers in these areas.*
🆔 `https://orcid.org/0000-0003-3027-8049`

RESEARCH ARTICLE

Proposing a novel mathematical model for hospital pneumatic system

Büşra Takgil[*], Resul Kara

Department of Computer Engineering, Düzce University, Türkiye
busratakgil@duzce.edu.tr, resulkara@duzce.edu.tr

ARTICLE INFO	ABSTRACT
	Hospital Pneumatic Systems, specializing in pneumatic systems, are among the most essential components for hospitals. It offers efficient and cost-effective solutions to problems related to the transportation of various materials in hospitals. However, in existing systems, the need for compressed air is met without worrying about cost control and without depending on the sample transported, and this not only makes the system inefficient but also may cause sample degradation. The main purpose of this study is to provide speed/pressure control according to the type of material transported to eliminate the disadvantages of existing systems such as energy use and sample degradation. In this study, a new mathematical model is presented that can be used to make more energy-efficient hospital pneumatic systems. Although there are many studies on various pneumatic systems in the literature, there is not enough for the control of hospital pneumatic systems. According to the results obtained in this study, the system parameters were determined and the mathematical model of the system was obtained by using the Multivariate nonlinear regression method. A genetic algorithm was used to test the validity of the obtained mathematical model and to optimize the coefficient of the input parameters of the model. It is expected that this proposed model will contribute to the use of hospital pneumatic systems and provide a scientific and practical solution to the proposed mathematical model. The proposed mathematical model provides up to 43% more efficient transportation over the currently used system that has been tested.

1. Introduction

Pneumatic systems are used in many fields, especially in various industrial applications. Today, it is frequently preferred in industrial units due to its easy maintenance, low cost, safety, and applicability features in different processes [1]. These systems make power transmission with compressed air attractive because they are economical, clean, safe, and simple in structure [2]. There are also interesting studies on the future of systems using air as a source. The Hyperloop project [3] aims to transport people in tubes. The main idea is to reduce the frictional forces between the capsule and the capsule, which creates pressure in the tube to reduce air resistance and reuse air.

Hospital pneumatic systems, which is a specialized field of pneumatic systems, are one of the most important elements for hospitals. Pneumatic transport systems in hospitals ideally connect all units. These systems can reduce the need for medical personnel, allow staff to focus on core patient care tasks, and reduce the risk of disease transmission [4]. Pneumatic systems provide efficient and cost-effective solutions for healthcare. Hospital pneumatic systems provide high health

---

*Corresponding Author

safety, low operating costs, and high system efficiency. However, despite important advantages such as low cost, high force/weight ratio, and cleanliness, pneumatic systems have a non-linear structure that prevents precise control. The compressibility of the air and the nonlinearity of the pressure and friction relationship between the system elements make it difficult to control the system. These limitations imply the need for a solution with more robust controllers [5].

Pneumatic systems use air blown from a pipeline. The biggest factor controlling the efficiency of these systems is the efficient use of blown air. However, in existing systems, the demand for compressed air is met without worrying about controlling the cost and without being dependent on the sample being transported. For example, for a sample that can be transported with 3 *bar*, the system produces a constant pressure of 5 *bar*. This event causes inefficiency and wastage of energy. In addition, the overpowered air system is not only inefficient but also leads to the deterioration of the samples being transported. For example, hemolysis may occur while transporting blood samples from the pneumatic tube system [6]. In addition, in hospitals, pneumatic tube systems allow rapid transport of patient blood samples but can damage blood cells and change test results [7]. In this article, a mathematical model is proposed to make the energy source used in hospital pneumatic systems more efficient. A mathematical model was proposed using the multivariable non-linear regression method since the pneumatic systems have a non-linear structure that prevents precise control. The proposed model reduces material handling cost and is aims to prevent deterioration by generating a special pressure (transport velocity) value per sample. Although pneumatic systems are a common subject of study, studies on the control of hospital pneumatic systems are very few. The use of appropriate pressure according to the sample to optimize the system makes our study unique.

The following parts of the study are organized as follows: Section 2 gives details related works. Section 3 describes the system model is introduced by giving information about the pneumatic system design and system parameters of the proposed model. Section 4 details about the results and discussion part of the proposed model are included. Section 5 describes the conclusions.

2. Literature review

Studies on the control of hospital pneumatic systems are scarce in the literature. The most relevant studies on pneumatic systems are as follows. Control studies in the literature have focused on the rapid and precise control of pneumatic actuators. There are various studies on this subject [8–12].

For the studies on improving the performance of pneumatic conveying systems: Wamba et al. [13] investigated the place of RFID technology in the health sector. The distribution of samples in hospitals is a complex process that requires coordination between all units. One of the important parameters for the system is the transport speed. Transportation speed affects both the energy consumed by the system and the transport of the samples at the appropriate speed is an important factor that prevents sample deterioration. Lee et al. [14] propose a mixed integer programming model and a broad neighborhood search algorithm to optimize the delivery of the radioisotope F-18 used for cancer diagnosis and monitoring to minimize the delivery time. Ruan et al. [15] examined the problem of intermodal transport of drugs with fuzzy methods to improve the level of health care. In his study, Abhinandu [16] aimed to use fewer compressors by reusing and storing compressed air in pipes. A specially designed smart road is used to reduce traffic.

Studies on mathematical modeling of pneumatic systems are as follows. Zhu and Ursavas [17] proposed a mathematical model for drug delivery modeling. Campbell and Jones [18] calculated the cost to balance the safety and speed of drug delivery with a mathematical model in the event of a natural disaster. Similarly; Erbeyoglu and Bilge [19] develop a mixed-integer linear model that aims to achieve a better response by considering the effectiveness of fair delivery and drug distribution to the affected areas during a disaster. Turkowski and Szudarek [20] modeled the behavior of a pipeline transport system used to push light capsules and presented theoretically optimum solutions. Pandian et al. [21] in their study, compared the performance of the pneumatic motor with the electric motor and produced the mathematical model of the pneumatic motor. In another study, a detailed mathematical model was developed for a pneumatic actuator to provide high-performance force control for robotics and automation applications [22].

Most of the studies directly related to hospital pneumatic systems have focused on whether pneumatic conveying has a detrimental effect on

blood components. In one of these studies, HPS was shown to give reliable results for transporting blood samples [23]. Another study on hospital pneumatic systems describes a general approach to obtain traffic analysis of pneumatic tube systems [24]. Mavaji et al. [25] proved that hospital pneumatic conveying systems save manpower and time, and these systems are more suitable for vertical structures. As seen in the literature, studies on HPS are very limited, and a comprehensive and effective mathematical model has not been encountered yet. In this context, this study proposes a mathematical model with a new approach that enables more efficient system utilization. This proposed model is compared with existing models in terms of energy consumption, energy efficiency, and impact on sample degradation. The innovations offered by the current study are the transport speed and pressure adjustment specific to the sample type. Transport according to sample type involves determining the transport speed and pressure of the system, taking into account the characteristics of the sample.

3. Material and method

3.1. System design

In the installation of hospital systems, HPS terminals are located at all major receiving and sending locations. These are called stations. According to this system, where the blower is the energy source of the system, various samples such as blood and urine can be transported along the transport line using routers between different stations. The system consists of tubes circulating in the hospital, sending and receiving stations, and a control center. In this system, the samples inside the carrier move horizontally and vertically between rooms, floors, and even buildings at a speed of approximately $6-7\,m/sec$ per second. HPS can be configured as a single-zone system or a multi-zone system. The components of such a system include the blower, transportation lines, stations, diverters, conveyors, and the central system. Figure 1 shows a basic single-zone HPS diagram.

The Pneumatic Transport System (PTS) of the Düzce University Hospital, where the experimental studies were carried out, is a computer-controlled PTS with transport tubes of different diameters, operating at a certain and constant pressure value. The system has more than 20 receiving and sending stations divided into two different regions. This PTS operates at a certain speed ($6\,m/s$) and constant pressure ($320\,mBar$).

Figure 1. Basic hospital pneumatic system diagram.

3.2. Components of the proposed model

All of the parameters used in designing the system are the most critical parameters for reducing energy costs. These parameters were determined according to the data obtained as a result of the experiments conducted in Düzce University Hospital and based on the studies in the literature and presented to the literature as a new model proposal. The entire data set was obtained as a result of experimental studies that were carried out on the of the Düzce University Research Hospital HPS and consists of 150 lines of data. Input and output parameters have been determined to adjust the transport speed according to the material to be transported in the transmission line and to make the power consumption efficient. The proposed system contains 5 parameters, where 4 of them are used for input, and 1 of them is used for output. The effect of temperature, which is one of the parameters affecting the performance of HPS, was not taken into account as it would not vary significantly between hospital rooms. Table 1 shows the range of values for the input and output parameters.

Table 1. Value ranges of system parameters.

		Min Value	Max Value
Input	Pipe Diameter (mm)	20	100
	Distance (m)	1	100
	Transport Direction Coef.	1	23
	Material Weight (g)	1	2000
Output	Pressure ($mBar$)	1	800

If an HPS is to be designed for maximum efficiency, the handling characteristics of the material to be transported must be well known. It is necessary to know the conveying characteristics, what

the minimum conveying rate of the designed system is, whether there is an optimum rate at which the material can be conveyed, and what pipe diameter and air carrier ratio will be required for a given material flow rate and conveying. Also, for an existing HPS, proper handling characteristics need to be determined at what flow rate a different material needs to be conveyed. Figure 2 shows the input and output parameters of the proposed model.
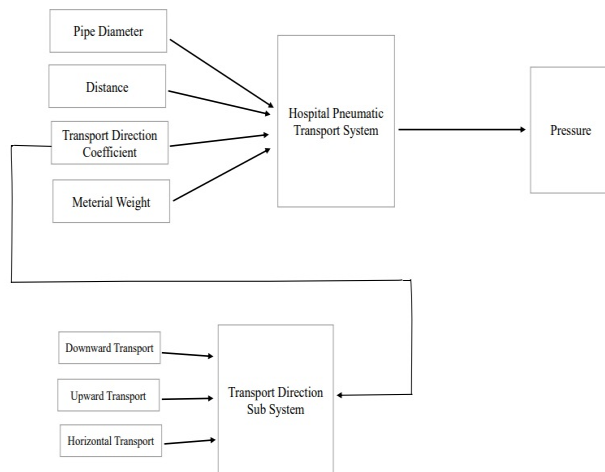
Figure 2. Model structure of the proposed system.

3.2.1. Pressure source/blower

The heavy-duty 3-phase blower was used, with a fully adjustable positioning valve, providing one system line with a variable air volume (suction and pressure).

3.2.2. Pipe/Capsule diameter

Depending on the type of material to be transported, hospitals use different pneumatic tube conveyors/capsules. For a pneumatic system to work properly, the selection of the pipe diameter of the tube to which the material will be transported is very important. As the pipe diameter increases, the power required for transmission increases. A small selection of pipe diameter causes an increase in flow rate and a pressure drop, while a large selection of pipe diameter can cause air loss. When choosing the dimensions of the capsule, the angle of the capsule should be designed in such a way that the tube does not get stuck in the turns. It should be designed so that the friction between the tube and the capsule is less [16]. Carrier and tube diameters are available in many sizes, most hospitals use 110 mm and 160 mm. Medical carriers are durable, sterilizable (autoclave 10 min at 120°C),

and provided with a swivel lid which guarantees the best closure available

3.2.3. Distance

One of the important factors affecting pressure value and power consumption is the transport distance. When designing pressure conveying lines, the correct line design should be made with minimum pressure loss. Pipeline length depends on hospital size. Figure 3 shows the pressure drop due to the increase in the distance during the transportation of materials in a fixed-diameter pipeline [26].
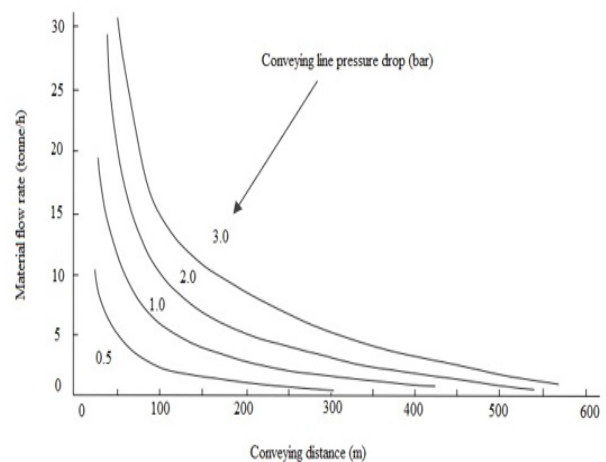
Figure 3. Effect of transport distance on pressure drop [24].

3.2.4. Material weight

Material properties (weights) and their effects on both transport conditions and material flow rate are very important. [26]. Different weights of materials such as blood samples, drugs, documents, X-Ray films, and pathology samples can be transported through pneumatic tubes. Increasing the weight of the transported material increases the required power consumption. Typical carrier loads in hospitals range from 0.1-2 kg and carrier speeds range from 3-6 m/s.

3.3. Regression analysis and proposed mathematical model

Regression analysis is a statistical method used to predict and model the relationship between different variables [27]. If the regression analysis is between more than one independent variable and the dependent variable, it is expressed as multiple regression analysis

3.3.1. Mathematical model optimization with genetic algorithm

A genetic algorithm was used to test the validity of the mathematical model obtained by using the regression method and to optimize the coefficient of the input parameters of the model. Experimental data from the hospital pneumatic systems were used with genetic algorithms and system input parameters (pipe diameter, distance, transport direction coefficient, material weight) were optimized. Constraint function has been determined in line with the needs of pneumatic systems. Values aimed for optimization were defined as genes and these genes came together to form the chromosome structure. Data on genetic algorithm structure are shown in Table 2.

Table 2. Genetic algorithm data.

Property	Values
Chromosome Count	50
Starting Population	Random
Operators Used	Crossover and Mutation Operators
Crossover Operator	Discrete Crossover
Mutation Operator	Non-Uniform
Number of Algorithm Repetitions	50
Selection Mechanism	Fitness Proportionate Selection
Algorithm Stopping Criteria	Number of Iterations (1000)

There is no huge search space to use a mathematical model in this study. However, since genetic algorithms are effective in optimizing model parameters, parameter adaptation was made using genetic algorithms and thus the performance of the model was increased. According to the results obtained by using a genetic algorithm, it has been observed that it is appropriate to use a genetic algorithm in determining the outlet pressure values of pneumatic systems. It is seen that the values obtained using this method are compatible with the coefficients of the mathematical model. This demonstrates the accuracy of the mathematical model created.

4. Results and discussions

The correlation matrix was used to determine the degree and direction of the relationship between the system parameters. Pearson's coefficient (r), which takes values between -1 and $+1$, was used to evaluate this relationship. According to the classification in the literature studies, the value of the correlation coefficient is interpreted as follows [28]:

$\quad | \ r \ | \geq 0.8$ very strong relationship;

$0.6 \leq | \ r \ | < 0.8$ strong relationship;

$0.4 \leq | \ r \ | < 0.6$ moderate relationship;

$0.2 \leq | \ r \ | < 0.4$ weak relationship;

$\quad | \ r \ | < 0.2$ very weak relationship.

If the r-value is greater than 0.8, it can be concluded that the two properties are highly correlated. The correlation coefficients between system parameters are shown in Table 3. According to the results, there was a strong positive relationship between the pressure (P) and pipe diameter (Pd) parameters, with a value of $+0.914985$. It was observed that the correlation coefficients of the other parameters were low. This experimental result indicated that there was no strong linear relationship between the variables. In addition, there was a negative relationship between the pressure and the direction-of-transport parameter. The parameters in the table are as follows: P: Pressure, Pd: Pipe Diameter, D: Distance, Tdc: Transport Direction Coefficient, and Mw: Material Weight.

Table 3. Correlation matrix for system parameters.

	Pd	D	Tdc	Mw	P
Pd	1				
D	-0.01911	1			
Tdc	-0.09559	0.052842	1		
Mw	0.118139	0.037434	0.092037	1	
P	0.914985	0.285	-0.03275	0.099406	1

The air compressor/blower is the basic and essential part of the system as it supplies compressed air. For this reason, the determination of compressed air consumption and compressor capacity is an important planning issue. By making proper planning, uneconomical compressed air costs can be reduced. Compressed air production, which is used more than necessary, causes both energy loss and an increase in losses at leakage points [29]. The efficiency of the system is directly linked to the selection and installation of various system components. Therefore, it is crucial to install compressed air systems under ideal conditions. This involves factors like determining compressor capacity and quantity during project design, sizing and setting up the compressed air system, designing appropriate circuits and selecting elements for pneumatic control circuits, and conducting necessary maintenance to ensure the

longevity of these components. Another vital consideration is to avoid excessive compressor pressure, which can lead to wasted energy and the deterioration of transported materials. Thus, it's essential to generate pressure in accordance with actual requirements. The design of a pneumatic system conveying lines is one of the most important parameters affecting system efficiency [4]. The transport direction coefficient is used to distinguish the situations that require maximum power during transportation from those that require less power. The length of the pipeline, the number of horizontal, and vertical orientations, and the number of bends in the pipeline form the pipeline from geometry. Using the pipelines as straight as possible reduces the high losses in the elbows [29]. The friction distribution changes depending on the piston movement directions [30]. Since the friction force acting on each conveying direction is different during pneumatic conveying, the pressure value to be applied is different. For example, the pressure required to activate a horizontal carrier is different and less than the pressure required to move a vertical carrier. Properties such as air compressibility and friction force make pneumatic systems non-linear [22]. For this reason, there are non-linear relationships between pneumatic system variables. The multivariable nonlinear regression method can be used to express this relationship.

The simple form representation of nonlinear regression models is as follows:

$$Y_i = f(X_i + \gamma) + \epsilon. \qquad (1)$$

It is the uncorrelated error term such that $E(e) = 0$ and $Var(e) = \sigma 2.f(x_i, \gamma)$ is called the expectation function for the nonlinear regression model [31]. The most used methods for parameter estimation of nonlinear regression models are least squares, maximum likelihood, and Gaussian Newton methods [32].

Mathematical modeling is defined as the process of expressing real-life components with mathematical representations [33]. The general model for a volume of gas consists of the equation of state, conservation of mass, and energy equation. The equation should be written for each room, using the assumptions that the gas is ideal, the pressure and temperature in the room are homogeneous, and the kinetic and potential energy terms are negligible. Considering the control volume V, density ρ, mass m, pressure P, and temperature T, the ideal gas equation is:

$$P = p \cdot R \cdot T. \qquad (2)$$

In the literature [34], the two basic equations that consider flow variation in pneumatic systems are:

$$\frac{\partial p}{\partial s} = -R_i \cdot u - \rho \cdot \frac{\partial \omega}{\partial t}, \qquad (3)$$

$$\frac{\partial u}{\partial s} = -\frac{1}{\rho \cdot c^2} \frac{\partial \rho}{\partial t}. \qquad (4)$$

P is the pressure through the tube, u is the velocity, ρ is the air density, c is the sound velocity, s is the tube axis coordinate R_i is the tube resistance, and ∂t is the cross-sectional area.

The following assumptions were made in our study as well as in creating the models in the literature:

- Air is an ideal gas.
- The temperatures in the cylinder chambers are constant and equal to the feed tank temperature.
- Valve piston and hose dynamics are neglected.

The mathematical model of the pneumatic actuator, which can be a reference while creating the mathematical model, was proposed by Richer et al. [22]. According to this model:

$$(M_L + M_P) \cdot \frac{d}{dt} \cdot \dot{x} + \beta \cdot \dot{x} + F_f + F_L \\ = P_1 \cdot A_1 - P_2 \cdot A_2 - P_a \cdot A_r \qquad (5)$$

M_L is the external mass, M_p is the piston and rod mass, x represents the piston position, β is the viscous friction coefficient, F_f is the Coulomb friction force, F_L is the external force, P_1 and P_2 are the absolute pressures inside the chambers of the actuator. P_a is the absolute ambient pressure, A_1 and A_2 are the effective areas of the piston, and A_r is the cross-sectional area of the rod. These equations show the effect and importance of mass and friction force.

In this study, a mathematical model has been proposed to be used in the control of hospital pneumatic systems with the multi-variable nonlinear regression method using Matlab, which is a programming and numeric computing platform. The output parameter of the obtained mathematical model is the pressure value expected to be produced by the system. The purpose of the system is to control the pressure value that the blower should produce, which is the output parameter. According to the proposed mathematical model, the pressure value that the system should produce is determined according to the material to be transported. Pressure measurement is easier than velocity measurement and allows the use of cheaper materials. For this reason, the pressure value was selected as the output parameter instead of the speed, and the control of this

value was provided with the help of a mathematical model. Pressure/velocity-controlled transport provides the opportunity to transmit laboratory materials, blood, etc. samples without any damage. This is only possible with speed/pressure control. Input parameters are Conveying Tube Diameter/ Capsule Diameter, Distance, Material Weight, and Transport Direction parameters. The obtained non-linear regression model and the parameters of the model are as follows: P: Pressure, Pd: Pipe Diameter, D: Distance, Tdc: Transport Direction Coefficient, and Mw: Material Weight.

$$
\begin{aligned}
P =\ & 0.20607 + (0.68846 \times Pd)^2 \\
& + (0.28 \times D)^2 + (0.28 \times Tdc)^2 \quad (6) \\
& - 0.017623 \times Mw^2
\end{aligned}
$$

The R-squared and p-value of the proposed mathematical model were obtained as 0.851 and $3.71e-60$, respectively. These values show that the proposed model is statistically significant and successful.

Research on modern control applications of pneumatic systems has become very popular in recent years. Hospital pneumatic systems provide high health safety, low operating costs, and high system efficiency. However, the measures to be taken for energy and cost savings in pneumatic systems should also be evaluated with system-specific data. A poorly designed system can lead to inefficiency. Multiple steps in the hospital pneumatic conveying process affect efficiency and increase the risk of contamination. Therefore, performance is very important for these systems. A properly designed hospital pneumatic system should be optimized to use the least air at the lowest possible pressure, and it is aimed to provide the lowest air demand. Keeping energy efficiency at the highest level in hospital pneumatic systems is also the main purpose of this study. However, in existing systems, the demand for the compressed air system is met at a constant value without worrying about controlling the cost and without being dependent on the sample being transported. This causes inefficiency and waste of energy. In addition to this, the overpowered air system is not only inefficient but also leads to the deterioration of the samples being transported. Pneumatic systems are not suitable for handling sensitive or non-carrying materials. One of the aims of our study is to provide speed control and to allow sensitive samples to be transported in hospital pneumatic systems. However, since pneumatic systems have a non-linear structure, difficulties in modeling these systems and applying control algorithms are encountered.

This study includes a mathematical model proposal to be used in the control of hospital pneumatic systems. In the existing systems used in hospitals, each sample is transported at the same pressure and velocity regardless of its characteristics, while the proposed model aims to carry the material at the most appropriate value. In the proposed mathematical model, the system input parameters are (i) pipe radius, (ii) transport distance, (iii) transport direction coefficient, and (iv) transported material weight. Using this model, it was tried to obtain the most appropriate pressure output according to the material carried in the system. The mathematical model was obtained by the multi-variable nonlinear regression method. When the statistical performance of the model was revealed. According to the experimental result, the R-squared and p were obtained as 0.851 and $3.71e - 60$, respectively. Considering that the model detects nonlinear relationships, this value makes it even more meaningful. Increasing the dataset can improve the performance of this model. The results show that the nonlinear regression method is a successful method that can be used in pressure modeling and the proposed model offers an effective and efficient solution to the use of hospital pneumatic systems. The proposed model could result in a significant cost reduction. In addition, minimizing the energy loss of the system and transporting at a suitable speed for the material type will prevent unnecessary wear of the system elements and hemolysis of the samples.

To evaluate the effectiveness of the proposed mathematical model, experimental studies were carried out by transporting materials of different types, weights, and different transport properties in the system. Considering the transport conditions, the samples and conditions of the max and min power values that the system should produce are given in Table 4. These materials are of 5 different types: blood, urine, drugs, x-rays pictures, and documents. The distance and transport direction between the sending and receiving units are different for each sample type. The results produced by the current system and the proposed model were compared and the following results were obtained.

Table 4. Comparison of existing and proposed systems

Sample type	Current System Pressure (mBar)	Proposed Model Pressure (mBar)
Blood	320	198
Urine	320	240
Drug	320	300
X-Ray pictures	320	320
Document	320	180

According to this table, the proposed model produces a pressure value for different types of samples, according to the sample's carrying properties. While the current system carries the same speed/pressure value for each sample, the value is produced according to the sample property carried according to this proposed model. The data obtained show that the proposed model provides efficiency in different value ranges according to the properties of the material to be transported. According to the table, the most energy gain was obtained while the material in the document type was being transported, while there was no change in the value produced in the system during the X-Ray transport. The reason for this is the occurrence of situations that require maximum power during the transportation of this material (such as vertical and longest-distance transportation). When the data obtained is evaluated, it is seen that the proposed model can provide up to 43% efficiency to the existing pneumatic conveying system.

This study provides a perspective on the determination of the most valuable system parameters for hospital pneumatic systems and the factors that should be considered in the installation of these systems in the hospital. Pressure/velocity control according to the type of sample to be transported in the system will contribute to the prevention of unnecessary energy consumption and sample deterioration. Also, the proposed system will make a significant contribution to reducing the material handling cost. It will also be possible to transfer the types of samples that are not suitable for transport (e.g. sensitive samples) in systems with speed/pressure-controlled transport. Thus, the variety of materials that can be transported in these systems will increase. The proposed model will reduce unnecessary energy waste and material wear and will ensure that the system elements can be used for a longer period.

One of the assumptions of the model is to ignore the temperature differences in the hospital building where the system is used. Since the temperature difference between different units in these buildings varies so little it is not important. This difference has been ignored. Moreover, this developed model can also be applied to pneumatic systems in different hospitals. Overall, the development of a mathematical model for a hospital pneumatic system can help to optimize system performance, reduce energy consumption, and improve cost-effectiveness.

5. Conclusion

In this study, a mathematical model was developed to be used in the control of hospital pneumatic systems and the following results were obtained.

1. Modifying the current system of the proposed mathematical model provides up to 43% more efficient transportation.
2. The results obtained from the genetic algorithm demonstrate its compatibility with the mathematical model in determining pneumatic system outlet pressure values, thus affirming its suitability for pneumatic systems and enhancing the validity of the mathematical model.
3. Special solutions can be provided according to needs, allowing control of the system's energy requirements and optimizing workload.
4. It has been observed that faster/slower transport can prevent cases such as sample deterioration and hemolysis, depending on the sample feature.
5. Speed adjustment according to the sample feature will allow more sensitive samples to be transported in the system.
6. The safe transport of various sample types in the system ensures the elimination of material-based contagion risks and guarantees their secure conveyance.
7. Reducing material wear is possible by preventing unnecessary power consumption in the system, thereby extending the system's operational lifespan.
8. The ease of implementation of the proposed model makes it suitable for systems of varying scales.
9. The developed model provides a control for the blowers of existing hospital pneumatic systems. It can be used via a controller on any type of pneumatic system that is applied in various industries.

10. The most valuable contribution of the proposed model is that it can be integrated into different pneumatic systems, optimizing the energy consumption of these systems and allowing the transportation of different types of samples without damage or the need for re-sampling.

References

[1] Beater, P. (2007). *Pneumatic Drives: System Design and Modelling.* Springer-Verlag, Berlin.

[2] Wang, J., Pu, J. & Moore, P. (1999). A practical control strategy for servo-pneumatic actuator systems. *Control Engineering Practice*, 7(12), 1483-1488.

[3] Chin, J. C. & Gray, J. S. (2015). Open-source conceptual sizing models for the hyperloop passenger pod. In 56th AIAA/ASCE/AHS/ASC Structures, Structural Dynamics, and Materials Conference, p. 15870.

[4] Chen, W. A., De Koster, R. B. & Gong, Y. (2021). Performance evaluation of automated medicine delivery systems. *Transportation Research Part E: Logistics and Transportation Review*, 147, 102242.

[5] Schlüter, M. S. & Perondi, E. A. (2018). Mathematical modeling of pneumatic semi-rotary actuator with friction. *Journal of the Brazilian Society of Mechanical Sciences and Engineering*, 40(11), 1-17.

[6] Kara, H., Bayir, A., Ak, A., Degirmenci, S., Akinci, M., Agacayak, A., & Azap, M. (2014). Hemolysis associated with pneumatic tube system transport for blood samples. *Pakistan Journal of Medical Sciences*, 30(1), 50.

[7] Farnsworth C. W., Webber D. M., Krekeler J. A, Budelier M. M., Bartlett N. L. & Gronowski A. M. (2019). Parameters for Validating a Hospital Pneumatic Tube System. *Clinical Chemistry.* 65(5), 694–702.

[8] Abry, F., Brun, X., Sesmat, S.,& Bideaux, E. (2013). Non-linear position control of a pneumatic actuator with closed-loop stiffness and damping tuning. In 2013 European Control Conference (ECC), 1089-1094.

[9] Cukla, A. R. (2012). Arquitetura microcontrolada programável aplicada ao controle de um servoposicionador pneumático. Porto Alegre (in Portuguese).

[10] Mao, X. T., Yang, Q. J., Wu, J. J., & Bao, G. (2009). Control strategy for pneumatic rotary position servo systems based on feed forward compensation pole-placement self-tuning method. *Journal of Central South University of Technology*, 16(4), 608-613.

[11] Perondi E. A. (2002) Controle Não-Linear em Cascata de um Servoposicionador Pneumático

com Compensação do Atrito. Thesis (PhD in Mechanical Engineering), Technological Center, Federal University of Santa Catarina, Florianópoli (in Portuguese).

[12] Perondi, E. A. & Guenther, R. (2003). Modelagem de um servoposicionador pneumático com atrito. *Science & Engineering. Uberlândia*, 12(1), 43–52 (in Portuguese).

[13] Wamba, S. F., Anand, A., & Carter, L. (2013). A literature review of RFID-enabled healthcare applications and issues. *International Journal of Information Management*, 33(5), 875-891.

[14] Lee, J., Kim, B. I., Johnson, A. L., & Lee, K. (2014). The nuclear medicine production and delivery problem. *European Journal of Operational Research*, 236(2), 461-472.

[15] Ruan, J. H., Wang, X. P., Chan, F. T. S., & Shi, Y. (2016). Optimizing the intermodal transportation of emergency medical supplies using balanced fuzzy clustering. *International Journal of Production Research*, 54(14), 4368-4386.

[16] Abhinandu, K., Kumar, K. P., Srikanth, T., & Prashanth, B. N. (2019). Design and development of pneumatic drug delivery system. *In IOP Conference Series: Materials Science and Engineering*, 577(1), 012128.

[17] Zhu, S. X., & Ursavas, E. (2018). Design and analysis of a satellite network with direct delivery in the pharmaceutical industry. *Transportation Research Part E: Logistics and Transportation Review*, 116, 190-207.

[18] Campbell, A. M., & Jones, P. C. (2011). Prepositioning supplies in preparation for disasters. *European Journal of Operational Research*, 209(2), 156-165.

[19] Erbeyoğlu, G., & Bilge, Ü. (2020). A robust disaster preparedness model for effective and fair disaster response. *European Journal of Operational Research*, 280(2), 479-494.

[20] Turkowski, M., & Szudarek, M. (2019). Pipeline system for transporting consumer goods, parcels and mail in capsules. *Tunnelling and Underground Space Technology*, 93, 103057.

[21] Pandian, S. R., Takemura, F., Hayakawa, Y., & Kawamura, S. (1999). Control performance of an air motor-can air motors replace electric motors. In Proceedings 1999 IEEE International Conference on Robotics and Automation. 1, 518-524.

[22] Richer, E., & Hurmuzlu, Y. (2000). A high performance pneumatic force actuator system: Part I—Nonlinear mathematical model. *Journal of Dynamic Systems: Measurement and Control*, 122(3), 416-425.

[23] Koçak, F. E., Yöntem, M., Yücel, Ö., Çilo, M., Genç, Ö., & Meral, A. (2013). The effects of transport by pneumatic tube system on blood cell count, erythrocyte sedimentation and coagulation tests. *Biochemia Medica*, 23(2), 206-210.

[24] Isken, M. W., & Littig, S. J. (2002). Simulation analysis of pneumatic tube systems. *Journal of Medical Systems*, 26(1), 9-19.

[25] Mavaji, A. S., Kantipudi, S., & Somu, G. (2013). Innovative methods to improve hospital efficiency-study of pneumatic transport systems (Pts). *IOSR Journal of Business and Management*, 9(6), 10-15.

[26] Mills, D. (2003). *Pneumatic Conveying Design Guide.* Elsevier, London.

[27] Cakici, M., Oğuzhan, A. & Özdil, T. (2015). Istatistik, Ekin Basım Yayın Dağıtım, Bursa. (In Turkish).

[28] Swinscow, T. D. V., & Campbell, M. J. (2002). *Statistics at Square One.* Elsevier, London

[29] Fleischer, H. (1995). *Manual of Pneumatic Systems Optimization.* McGraw-Hill Companies, London.

[30] Wang, J., Wang, J. D., Daw, N., & Wu, Q. H. (2004). Identification of pneumatic cylinder friction parameters using genetic algorithms. *IEEE/ASME transactions on Mechatronics*, 9(1), 100-107.

[31] Ratkowsky D. A. (1983). *Nonlinear Regression Modeling.* Marcel Dekker, New York.

[32] Kutner, M. H., Nachtsheim, C. J., Neter, J., & Wasserman, W. (2004). Applied linear regression models. 4, 563-568.

[33] Blum, W., & Ferri, R. B. (2009). Mathematical modelling: Can it be taught and learnt?. *Journal of Mathematical Modelling and Application*, 1(1), 45-58.

[34] Andersen, B. W., & Binder, R. C. (1967). The analysis and design of pneumatic systems. *Journal of Applied Mechanics*, 34(4), 1055

Büşra Takgil *works as a lecturer in the Department of Computer Engineering at Džce University. The master's thesis is about mobile programming tests. In 2022, she received her doctorate degree with an interdisciplinary study on hospital pneumatic systems. Her research interests are modeling, artificial intelligence, fuzzy logic, and hospital pneumatic systems.*
https://orcid.org/0000-0002-7927-0083

Resul Kara *works as a lecturer in the Department of Computer Engineering at Džce University. His professional life has been continuing for 27 years. Since 2004, He has been teaching computer networks, mobile programming, and web programming. He managed a large number of undergraduate and graduate projects in IT sector.*
https://orcid.org/0000-0001-8902-6837

An International Journal of Optimization and Control: Theories & Applications (http://www.ijocta.org)

IJOCTA
An International Journal of
Optimization and Control:
Theories & Applications
2010

RESEARCH ARTICLE

Rotor design optimization of a 4000 rpm permanent magnet synchronous generator using moth flame optimization algorithm

Deniz Perin [a], Aslan Deniz Karaoglan [b*], Kemal Yilmaz [a]

[a] *Department of R&D, ISBIR Electric Company, Turkey*
[b] *Department of Industrial Engineering, Balikesir University, Turkey*
gls01@isbirelektrik.com.tr, deniz@balikesir.edu.tr, arg60@isbirelektrik.com.tr

ARTICLE INFO	ABSTRACT
	The goal of this paper is to optimize the rotor design parameters of 4000 rpm permanent magnet synchronous generator. The factors namely embrace, offset, outer diameter, and magnet thickness are selected as the design parameters those will be optimized in order to hold the magnetic flux density (MFD) distribution and the flux density on stator teeth and stator yoke within a desirable range while maximizing efficiency. The numerical simulations are carried out in the Maxwell environment for this purpose. The mathematical relationships between the responses and the factors are then derived using regression modeling over the simulation data. Following the modeling phase, the moth flame optimization is applied to these regression models to optimize the rotor design parameters. The motivation is determining mathematical relation between the important design parameters of the high speed generator and the measured responses, when standard M530-50A lamination material is used and then to demonstrate the utility of MFO to the readers on this design problem. The optimum factor levels for embrace, offset, outer diameter, and magnet thickness are calculated as 0.68, 30, 161.56, and 8.92 respectively. Additionally, confirmations are done by using Maxwell and the efficiency is calculated as 94.85%, and magnetic distributions are calculated as 1.64, 0.26, and 0.93 Tesla for stator teeth flux density, stator yoke flux density, and MFD; respectively. The results show that the efficiency is maximized and the magnetic distributions are kept within an appropriate range.

1. Introduction

Thin (0.20 and 0.35 mm) lamination is often used in high efficiency alternator designs. However, this alternator design significantly increases manufacturing costs. In addition, the availability of this special lamination in the market is limited. It is very difficult to obtain from the market in small quantities, and it is possible to obtain it in case of high purchases in the sector. However, the supply of raw materials for a small amount of production in the sector is a difficult task. The production of high speed alternators with standard materials (eg M530-50A etc. lamination) is the preferred production method, especially in mass production. However, this causes core loss. In this case, alternator design optimization becomes important [1, 2].

There are four different structures in high speed generators: (*i*) salient-pole generator, (*ii*)

asynchronous generator (SG), (*iii*) permanent magnet synchronous generator (PMSG), and (*iv*) switched reluctance generator. PMSG is the easiest and most common generator type to manufacture. There are many studies on PMSG design optimization in the literature. The related remarkable studies are as follows:

Fang et al. [3] investigated the optimization of SG design. They used double layer interior PMSG (IPMSG). The break angles and length of the PM segments were determined as the factors, while rotor saliency ratio, motor efficiency performance, and back electromotive force (back EMF) are measured as responses. They used finite element analyis (FEA) and the equivalent circuit approach. During the optimization phase, response surface methodology (RSM) is applied. Li and Liu [4] investigated the optimization of the PMSG shape and assessed magnetic field intensity and magnetic flux density

(MFD). Kurt et al. [5] studied on optimizing axial flux PMSG (AFPMSG) design using the Taguchi method. The factors were internal radius, pole number, magnet thickness, and pole utilization factor; and the response was air-gap MFD (AGMFD). They performed optimization using the simplex algorithm, and validated the results using FEA. Hasanien and Muyeen [6] employed genetic algorithm (GA) and RSM to offer an optimum design technique for the controller used in the frequency converter of a variable speed wind turbine (VSWT) driven PMSG. The purpose was to find the best parameters for the PI controllers. Settling time, maximum percentage overshoot (MPOS), maximum percentage undershoot (MPUS), and steady-state error of the voltage profile are the measured responses. The performance of the specified parameters acquired with GA-RSM are then compared to those obtained with a generalized reduced gradient (GRG) approach that takes into account both unsymmetrical and symmetrical errors. Oh et al. [7] conducted research on the design of an IPMSM with concentrated windings. Authors minimized the PM eddy-current loss by moving the magnets at the rotor and keep the MFD in the air gap at a desired range. They used rotor shape and rpm as factors. Several rotor design parameters (bridge size and magnet height) were taken into account in Neubauer et al.'s [8] study. They focused on the IPMSG's rotor design optimization in order to determine their impact on the MFD and machine's performance. A direct-driven surface-mounted PMSG (D-SPMSG)'s magnetic flux linkage optimization was researched by Xie et al. [9]. They used FEA to do simulations and determined winding arrangements, PM specifications and dimensions, as the factors those will be optimized. Demir and Akuner [10] investigated the critical rotor pole data of a line-start PMS motor (LSPMSM). They employed Taguchi for determining factor values of LSPMSM critical rotor pole data in order to optimize efficiency and power factor. They considered the magnet duct dimensions, width of the rib, magnet width, magnet thickness as the factors. Sabioni et al. [11] optimized the design of a 10 kW axial-flux PMSG for direct-coupled wind turbines using non-dominated sorting GA-III (NSGA-III). Material cost, efficiency, outer diameter, and weight are chosen as responses. The authors considered the electromagnetic factors and the dimensions during the design procedure. In order to enhance the design of SPMSG, Dai et al. [12] combined Taguchi and GA. They made an effort to increase efficiency while reducing expense and THD of surface-mounted permanent magnet synchronous machines (SPMSMs). FEA is used to verify the results. They selected the design parameters namely inner radius of rotor, height of air gap, height of magnet, height of stator yoke, width of stator tooth, height of slot, pole-arc to pole-pitch ratio, core length, pole shift angle, magnet eccentricity, magnet segmentation as the factors those have to be optimized. Gul et al. [13] investigated the DSSR PMSG (dual-stator single-rotor PMSG) optimization. They employed GA to efficiently reduce the cost of the DSSR PMSG and weight. The authors additionally investigated into the MFD distribution. They used power distribution factor, thickness of magnet, axial length, thickness of rotor yoke, thickness of stator yokes, ratio of magnet pole arc to pole pitch as the factors. Semon et al. [14] used RSM for rotor design optimization of a V-type IPMSM to reduce THD while maintaining the desired range of airgap MFD. They used geometrical dimensions of rotor pole shape as the factors. To optimize the THD and voltage regulation rate, Jun et al. [15] explored the design optimization of PMSG for wind power generators using the Taguchi. They tried to determine the optimum fator levels of polar arc coefficient, air gap length, PM thickness, number of turns per phase coil. Karimpour et al. [16] optimized the design of IPMSG using FEA and Taguchi in order to improve efficiency, THD, and the amplitude of induction EMF. They used stator tooth width, stator slot depth, magnet thickness, magnet width, magnet inset, magnet spread angle as the factors. In the following year, Karimpour et al.'s [17] research focused on improving the IPMSG design using FEA and the Taguchi Method. They took into consideration the effects of the magnet inset, magnet thickness, stator tooth width, slot depth, and magnet breadth. The efficiency of the generator, output power, and torque ripple were the measured responses to be optimized. Agrebi et al. [18] employed GA to optimize the design parameters (ratio of the bore radius to the active length of the machine, ratio of the slot depth to the bore radius of the machine, pole pairs number, current surface density, rated power, rated angular rotation speed, induction in the stator yoke, slot number per pole and per phase) of a direct drive PMSG (DDPMSG) for a smart wind turbine, and the results were validated by FEA. Alemi-Rostami et al. [19] investigated the construction of a step-by-step strategy for the design of a PMSG to achieve improved efficiency and power factor while requiring less voltage regulation and PM volume. They employed FEA validation and GA to optimize the design. They determined air gap length, conductor current density, stator slot width, stator slot height, magnet height, magnet width as the factors those have to be optimized. The literature summary is presented in Table 1.

Numerous studies have investigated at the design optimization of PSMG, according to studies that have been published in the literature. The objective of this study is to determine the 16-poled, 3 kVA, 4000 rpm optimum rotor design. In order to do this, we researched the best factors to use while adjusting the rotor's embrace, offset, outer diameter, and magnet thickness in order to maintain the desired range of MFD distribution while increasing efficiency. Maxwell simulations are used to measure the efficiency and distribution of MFD. The mathematical

modeling is done using regression modeling, and the multi-objective optimization is done using the Moth Flame Optimization (MFO) Algorithm.

Table 1. Literature summary.

Author(s)	Electric Machine Type	Optimization Method	Responses
Fang et al. [3]	IPMSG	RSM	Rotor saliency ratio, motor efficiency, back EMF
Li and Liu [4]	PMSG	ANSYS Simulations	PMSG shape, magnetic field intensity, MFD.
Kurt et al. [5]	AFPMSG	Taguchi	Air-gap MFD
Hasanien and Muyeen [6]	VSWT driven PMSG	GA, RSM	Settling time, MPOS, MPUS, steady-state error of the voltage profile
Oh et al. [7]	IPMSM	FEA	PM eddy-current loss, air-gap MFD
Neubauer et al. [8]	IPMSG	FEA	MFD inside the PM, voltage, power, maximum power, short circuit current
Xie et al. [9]	D-SPMSG	FEA	Magnetic flux linkage
Demir and Akuner [10]	LSPMSM	Taguchi	Efficiency, power factor
Sabioni et al. [11]	Axial-flux PMSG for direct-coupled wind turbines	NSGA-III	Material cost, efficiency, outer diameter, weight
Dai et al. [12]	SPMSM	Taguchi, GA	Efficiency, cost, THD, MFD
Gul et al. [13]	DSSR PMSG	GA	Cost, weight, MFD
Semon et al. [14]	V-type IPMSM	RSM	THD, air-gap MFD
Jun et al. [15]	PMSG for wind power generators	Taguchi	THD, voltage regulation rate
Karimpour et al. [16]	IPMSG	Taguchi	Efficiency, THD, amplitude of induction EMF
Karimpour et al. [17]	IPMSG	Taguchi	Efficiency, output power, torque ripple
Agrebi et al. [18]	DDPMSG for a smart wind turbine	GA	Mass of the generator's active parts (iron, copper, PMs).
Alemi-Rostami et al. [19]	PMSG	GA	Efficiency, power factor, PM volume

MFO algorithm is a recent and very effective swarm-based optimization technique [20, 21]. MFO is not used for design optimization of PMSGs previously. Using the design parameters namely embrace, offset, outer diameter, and magnet thickness together for optimizing efficiency and magnetic distributions of PMSG by using MFO, is the novelty of this research.

This research's first motivation is determining the relationship between the important design parameters (embrace, offset, outer diameter, and magnet thickness) of the highspeed alternator and the measured responses, when standard M530-50A lamination material is used.

The second motivation is to demonstrate to the readers the utility of MFO with regard to these design problems. As demonstrated by the "No Free Lunch", none of the offered methods in the literature can handle all difficulties with optimization alone [20, 22]. Therefore, there is always a need to investigate the performance of newly presented algorithms on the presented problems in the literature.

2. Mathematical modeling

In this paper, it is aimed to determine the optimum level of the factors (embrace, offset, outer diameter, and magnet thickness) to hold the MFD distribution within a desired range while maximizing the efficiency. To do this, the mathematical relation between these responses and factors have to be calculated in the first stage (then MFO will be run through these models in order to do the optimization). Regression modeling is used to do this. The terms in regression models might be linear, quadratic, or interaction. The models those have these three terms together are referred to as a full quadratic model. The general representation for this type of regression model is given in Eq. (1). This model is used to fit mathematical models to the Maxwell simulations presented in Section 4 [23-26].

$$Y_u = \beta_0 + \sum_{i=1}^n \beta_i X_{iu} + \sum_{i=1}^n \beta_{ii} X_{iu}^2 + \qquad (1)$$
$$\sum_{i<j}^n \beta_{ij} X_{iu} X_{ju} + e_u$$

$$\beta^T = [\beta_0, \beta_1, \beta_2, ..., \beta_n] \qquad (2)$$

Y_u is the response for uth run. Responses of this study are the MFD distributions (stator teeth flux density, stator yoke flux density, MFD) and efficiency, which means that in Section 4 four separate regression equations will be calculated. X terms are the factors (X_1: embrace, X_2: offset, X_3: outer diameter, and X_4: magnet thickness). $X_{iu} X_{ju}$ terms represents the interaction terms (in this study maximum 3 interaction terms can be used such as $X_1 X_2 \, X_1 X_3, X_2 X_3$). e_u is the prediction error (PE) for the uth experimental run [23-26]. The regressin models are calulated by the aid of Minitab Statistical Package in this study. The R^2 (coefficient of determination) calculations and "Analysis of Variance (ANOVA)" are also performed by the aid of Minitab.

R^2 is used to assess if the factors included in the mathematical model are adequate to account for the change in response and it is expected to R^2 be nearer to 1 (which means 100 percent). Finally, the significance for each model have to be determined before the performing optimization with MFO algorithm. To do this "Analysis of Variance (ANOVA)" is used. ANOVA is a statistical hypothesis test that use the F-test to measure the significance of a model. ANOVA includes two hypotheses (H0 and H1). H0 indicates that the regression model is insignificant, whereas H1 indicates that it is significant. So, H1 must be true in

order to employ these models during the optimization phase. If the "p-value" (in this study Minitab is used to calculate the P-Value) is lower than the type-I error (α) then this means the model is significant (H1 is true) [23-26]. In this study, the confidence level is choosen as 95% (which means α=5%). After completing the modeling, MFO algorithm was utilized for optimization by running through these models [23-26].

3. Moth flame optimization (MFO) algorithm

Population based optimization algorithms are widely classified into three main categories: physic-based (such as gravitational search algorithm (GSA), and etc.), evolutionary-based (such as biogeography-based optimization (BBO) algorithm, human evolutionary model, and etc.), and swarm-based (such as artificial bee colony (ABC) algorithm, grey wolf optimizer (GWO) algorithm, and etc.) algorithms.

MFO is a nature-inspired swarm-based meta-heuristic optimization algorithm which is inspired from the moths' navigation mechanism. This mechanism is called transverse orientation. Moths use a very effective method for covering great distances in a straight line at night by maintaining a stable angle with respect to the moon. Because the light source (such as the moon) is far away from the moth, and this ensures that it will fly in a straight line. Regardless of the effectiveness of transverse orientation, moths fly in a spiral around artificial light sources (such as the street lamps and etc.). This is the inefficiency of the transverse orientation and this result in a useless or lethal spiral fly path for moths [20, 21].

In MFO algorithm, the behaviors of the moth-flames are mathematically modeled. In this mathematical model, the candidate solutions are represented by the moths and the factors (input variables) are represented by the positions of the moths (moths can fly in hyper dimensional space). Because of being MFO a population-based algorithm, the set of moths must be represented in a matrix form [20, 21]:

$$M = \begin{bmatrix} m_{1,1} & m_{1,2} & \dots & m_{1,d} \\ m_{21} & m_{2,2} & \dots & m_{2,d} \\ \vdots & \vdots & & \vdots \\ m_{3,1} & m_{3,2} & \dots & m_{n,d} \end{bmatrix} \quad (3)$$

In Eq. (3), n represents the number of moths and d represents the number of factors (dimensions). It is also assumed that for each moth, there is an array OM with nx1 dimensions for storing the corresponding fitness values (those are the return value of the fitness (objective) function for each moth). Each moth's position vector (for example, the first row in the matrix M) is passed to the fitness function, and the output of the fitness function is assigned to the corresponding moth as its fitness value in the OM matrix (for example the components of OM matrix are: OM_1 for the first row in the matrix M, OM_2 for the second row in the matrix M, and etc.). Flames are another important component of the proposed algorithm. Flames are also represented by a matrix which has an equal dimension (nxd) with M matrix [20, 21]:

$$F = \begin{bmatrix} F_{1,1} & F_{1,2} & \dots & F_{1,d} \\ F_{21} & F_{2,2} & \dots & F_{2,d} \\ \vdots & \vdots & & \vdots \\ F_{3,1} & F_{3,2} & \dots & F_{n,d} \end{bmatrix} \quad (4)$$

As been at M matrix, it is also assumed that for each flames, there is an array OF with nx1 dimensions for storing the corresponding fitness values for the flames where n is the moths' number. Moths and flames are both solutions, it should be mentioned. The difference is in how we handle and update them at each iteration. Moths are genuine search agents that wander across the search space, whereas flames represent the best moth position obtained thus far. In other terms, flames can be compared to flags or pins dropped by moths when hunting for food. As a result, each moth looks for a flag (flame) and changes it when a better solution is found. With this technique, a moth's optimal answer is never lost [20, 21].

MFO algorithm approximates the global optimal of the optimization problems by using the *I*, *P*, and *T* functions. The *I* function generates a random population of moths (M matrix) and their fitness values (OM array). The main function, the P function, moves the moths around the search space. This function receives the matrix M and eventually returns its updated version. If the termination criterion is satisfied, the T function returns true; otherwise, it returns false (which is represented by M=*P*(M) while *T*(M) is equal to false). In the *I* function, any random distribution may be used [20, 21]:

$$M(i,j) = (ub(i) - lb(i)) * rand() + lb(i) \quad (5)$$

where i=1:n, j=1:d, ub and lb are the upper and lower bounds respectively. Following the *I* function's initialization, the *P* function (main function) is executed iteratively until the *T* function returns true. The *P* function moves the moths around the search space inspiring from the transverse orientation. Each moth's position in proximity to a flame is updated using the equation below [20, 21]:

$$M_i = S(M_i, F_j) \quad (6)$$

where M_i and F_j are the i-th moth and j-th flame. S is the spiral function which is the moth's primary updating mechanism. The initial point of the spiral must be start from the moth and final point must be the flame's position. The fluctuation should not exceed the search space [20, 21]:

$$S(M_i, F_j) = D_i . e^{bt} . \cos(2\pi t) + F_j \quad (7)$$

In this logarithmic spiral function the spiral flying path of moths is simulated where b is a constant term that defines the shape of S, D_i is the absolute distance of the i-th moth for the j-th flame ($|F_j - M_i|$), and t is a random number between [-1, 1]. The t in the equation defines how close the next position of the moth should be to the flame (where t=1 is the furthest and t=-1 is the closest). By changing t, a moth can converge on any point in the vicinity of the flame. The

moth's next position would be within a hyper ellipse, which may be assumed in all directions around the flame as a result. Because it governs how moths update their positions around flames, the spiral movement is the most important component of the proposed method. Because of the spiral equation, a moth can fly "around" a flame rather than in the space between them. As a result, the exploration and exploitation of the search space can be ensured. The spiral equation enables a moth to fly ''around" a flame rather than in the space between them. As a result, the exploration and exploitation of the search space can be ensured. The position updating guarantees the exploitation around the flames. To increase the likelihood of finding better solutions, the best solutions obtained thus far are referred to as flames. As a result, the matrix F always contains the n most recent best solutions obtained thus far. During optimization, the moths must update their positions in relation to this matrix. To emphasize exploitation, it is assumed that t is a random number in the range [r; 1], with r decreasing linearly from -1 to -2 over the course of the iteration. It is worth noting that r is referred to as the convergence constant. Moths using this method tend to exploit their corresponding flames more precisely proportional to the number of iterations. Another issue to consider is that the position updating of moths in relation to n different locations in the search space may impair the exploitation of the most promising solutions. An adaptive system for the number of flames is suggested to address this issue [20, 21]:

$$flame\ no = round\left(N - 1 * \frac{N-1}{T}\right) \quad (8)$$

where l is the current iteration count, N denotes the maximum number of flames, and T denotes the total number of iterations. The pseudocode for P function is as follows [20, 21]:

```
Update flame no = round(N - 1 * (N-1)/T)
OM= FitnessFunction(M)
If iteration == 1
        F=sort(M)
        OF=sort(OM)
Else
        F=sort(M_{t-1}, M_t)
        OF=sort(M_{t-1}, M_t)
End
For i=1:n
        For j=1:d
                Update r and T
                Calculate D_i = |F_j − M_i|
                Update M(i,j) using M_i = S(M_i, F_j) and
                        S(M_i, F_j) = D_i . e^{bt} . cos(2πt) + F_j
        End
End
```
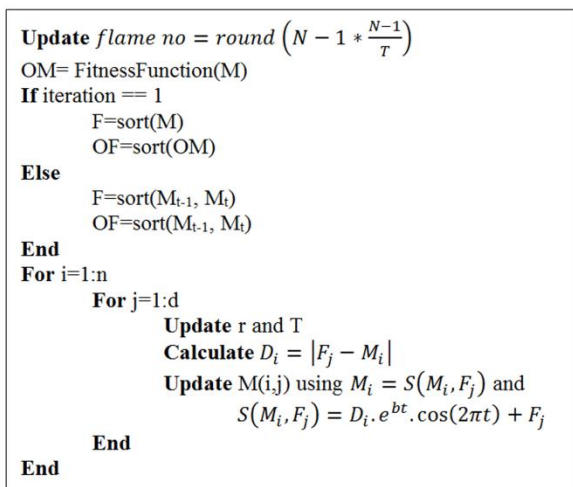
Figure 1. Pseudo code for MFO

Until the T function returns true, the P function is executed. The best moth is returned as the best attainable approximation of the optimum when the P function is terminated.

4. Results and discussions

In this paper, we studied on a 16-poled 4000 rpm 3 kVA PMSG. This PMSG is designed in the Maxwell environment. Some important design parameters of this PMSG are presented in Table 2. The PMSG has a rated power factor of 0.8. All winding material in the Maxwell design is ordinary copper. For lamination, M530-50A Si-Fe is employed. Finally, an H-Class insulating material is chosen. The goal of the first step is to use regression modeling to discover the mathematical relationship between the parameters (embrace (X_1), offset (X_2), outer diameter (X_3), magnet thickness (X_4)) and the responses (stator teeth flux density (Y_1), stator yoke flux density (Y_2), MFD (Y_3), and efficiency (Y_4)). An experiment is designed to carry out this phase.

Table 2. Basic design specifications for a 3 kVA PMSG.

Name	Value	Unit	Description	Part
Length	65	mm	Length of core	Stator
Inner Ø of Stator	90	mm	Core diameter (gap side)	Stator
Slot Type	3	N/A	Circular (slot type: 1 to 6)	Stator
Skew Width	1	units	Range number of slot	Stator
Slots	36	units	Number of slots	Stator
Hs0	0.5	mm	Slot opening height	Stator
Bs0	2.5	mm	Slot opening width	Stator
Hs2	14.95	mm	Slot height	Stator
Bs1	4	mm	Slot width	Stator
Bs2	6.27	mm	Slot width	Stator
Rs	1.5	mm	Slot bottom radius	Stator
Inner Ø of Rotor	89	mm	Core diameter (gap side)	Rotor
Length	65	mm	Core length	Rotor
Poles	16	-	Number of poles	Rotor

The flowchart for the mathematical modeling and optimization phase is presented in Figure 2.
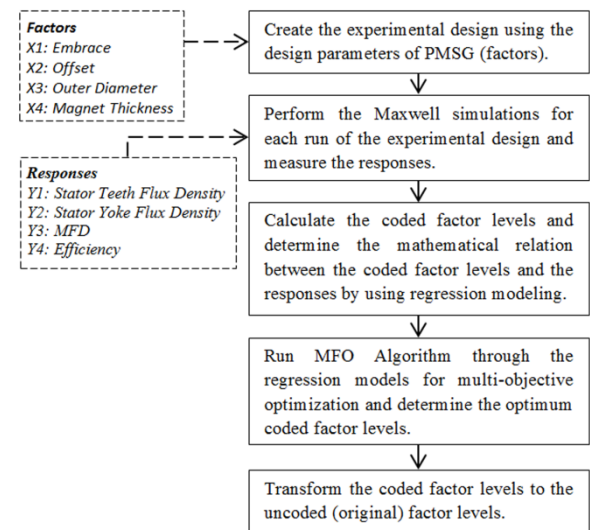

Figure 2. Flowchart for the mathematical modeling and optimization phase.

Table 3 shows the factor levels for this experimental design. Regression models will be generated for both

factor levels with coded and uncoded versions. During the optimization phase, we actually require the coded model. However, in order to demonstrate the true mathematical relationship to the readers, the original models with uncoded factor values are also generated. As a result, uncoded and coded factor levels are presented jointly in Table 4. The experiment has been planned. Eq. (9) is used to code the data.

Table 3. Factor levels.

Factors	Sym.	Unit	Levels		
			1	2	3
Embrace	X_1	-	0.196	0.588	0.98
Offset	X_2	-	10	20	30
Outer Diameter	X_3	mm	135	150	165
Magnet Thickness	X_4	mm	2	6	10

$$X_{coded} = \frac{X_{uncoded} - ((X_{max} + X_{min})/2)}{((X_{max} - X_{min})/2)} \quad (9)$$

Maxwell simulations are used to execute 25 experimental runs, and the results are shown in Table 4. The disadvantage of manufacturing real PMSG prototypes - which is not appropriate due to expenses - is avoided.

Table 4. Maxwell simulations.

Run	Factors (uncoded levels)				Factors (coded levels)			
I	X_{i1}	X_{i2}	X_{i3}	X_{i4}	X_{i1}	X_{i2}	X_{i3}	X_{i4}
1	0.196	10	135	2	-1	-1	-1	-1
2	0.196	10	165	2	-1	-1	1	-1
3	0.98	10	135	2	1	-1	-1	-1
4	0.98	10	165	2	1	-1	1	-1
5	0.196	30	135	2	-1	1	-1	-1
6	0.196	30	165	2	-1	1	1	-1
7	0.98	30	135	2	1	1	-1	-1
8	0.98	30	165	2	1	1	1	-1
9	0.196	10	135	10	-1	-1	-1	1
10	0.196	10	165	10	-1	-1	1	1
11	0.98	10	135	10	1	-1	-1	1
12	0.98	10	165	10	1	-1	1	1
13	0.196	30	135	10	-1	1	-1	1
14	0.196	30	165	10	-1	1	1	1
15	0.98	30	135	10	1	1	-1	1
16	0.98	30	165	10	1	1	1	1
17	0.588	20	135	6	0	0	-1	0
18	0.588	20	165	6	0	0	1	0
19	0.196	20	150	6	-1	0	0	0
20	0.98	20	150	6	1	0	0	0
21	0.588	10	150	6	0	-1	0	0
22	0.588	30	150	6	0	1	0	0
23	0.588	20	150	2	0	0	0	-1
24	0.588	20	150	10	0	0	0	1
25	0.588	20	150	6	0	0	0	0

After several preliminary trials, the full quadratic regression models are derived by linear terms & square termes & interaction terms for the responses. Minitab is used for fitting the regression models and performing the significance tests. Eq. (10) and Table 5 shows the general representation of the fitted regression model and the coefficients of the uncoded (original) models, respectively.

Table 4. (Continues).

Run	Responses			
i	Y_{i1}	Y_{i2}	Y_{i3}	Y_{i4}
1	1.390	0.243	0.754	75.950
2	1.396	0.065	0.754	76.150
3	1.434	1.078	0.754	94.597
4	1.435	0.291	0.754	95.405
5	1.402	0.242	0.764	73.093
6	1.403	0.065	0.764	73.295
7	1.435	0.812	0.754	94.796
8	1.435	0.219	0.754	95.248
9	1.544	0.275	0.955	82.404
10	1.544	0.074	0.773	82.525
11	1.636	1.219	0.947	94.227
12	1.636	0.329	0.947	95.236
13	1.520	0.276	0.957	82.178
14	1.520	0.074	0.957	82.303
15	1.636	1.007	0.947	94.152
16	1.636	0.272	0.947	94.838
17	1.637	0.805	0.902	94.375
18	1.637	0.217	0.902	94.811
19	1.522	0.118	0.918	81.813
20	1.637	0.485	0.902	95.190
21	1.637	0.346	0.902	94.825
22	1.637	0.333	0.902	94.695
23	1.435	0.292	0.754	94.486
24	1.636	0.344	0.947	94.764
25	1.637	0.287	0.902	94.759

$$Y_1 = \beta_0 + \beta_1 X_1 + \beta_2 X_2 + \beta_3 X_3 + \beta_4 X_4 + \beta_5 X_1^2 + \beta_6 X_2^2 + \beta_7 X_3^2 + \beta_8 X_4^2 + \beta_9 X_1 X_2 + \beta_{10} X_1 X_3 + \beta_{11} X_1 X_4 + \beta_{12} X_2 X_3 + \beta_{13} X_2 X_4 + \beta_{14} X_3 X_4 \quad (10)$$

Table 5. Regression coefficients for the uncoded factor levels.

Coef.	Term	Y_1	Y_2	Y_3	Y_4
β_0	Const.	1.8561875	16.266952	0.444961	-6.084172
β_1	X_1	0.4186154	4.674439	-0.271387	74.32474
β_2	X_2	-0.0022243	-0.015897	-0.007847	0.102591
β_3	X_3	-0.0091662	-0.217367	0.004506	0.880733
β_4	X_4	0.0893993	0.067595	0.083571	1.450213
β_5	X_1^2	-0.3286391	-0.317811	0.019376	-43.91885
β_6	X_2^2	0.0000700	-0.000108	-0.000050	-0.004902
β_7	X_3^2	0.0000311	0.000714	-0.000022	-0.002921
β_8	X_4^2	-0.0059063	-0.002021	-0.003533	-0.039078
β_9	$X_1 X_2$	0.0004783	-0.009678	-0.003284	0.091342
β_{10}	$X_1 X_3$	-0.0000638	-0.023884	0.001935	0.024522
β_{11}	$X_1 X_4$	0.0106824	0.013672	0.006617	-1.296038
β_{12}	$X_2 X_3$	-0.0000025	0.000145	0.000076	-0.000280
β_{13}	$X_2 X_4$	-0.0001063	0.000111	0.000259	0.007420
β_{14}	$X_3 X_4$	-0.0000083	-0.000305	-0.000190	0.000291

*Coef. : Coefficient, Const.: Constant

Programming MFO and optimization are done in Matlab. In order to use these equations in the Matlab environment for the MFO approach, the models must be constructed for coded factor values that range from -1 to 1. In this manner, the models are made independent of the units, making multi-objective optimization simple. Table 6 provide the regression models for the levels of coded factors.

The regression models for the responses ($Y_1, Y_2, Y_3,$ and Y_4) have R^2 statistics of 99.29%, 98.88%, 93.93%, and 99.28%, respectively. Table 7 displays the regression models' prediction capabilities. The $\hat{Y}_i$ values in this table represent the projected outcomes from using the coefficients presented in Table 5. For

each response, the prediction error percentage (PE(%)) is also provided.

Table 6. Regression coefficients for the coded factor levels.

Coef.	Term	$Y_{1,coded}$	$Y_{2,coded}$	$Y_{3,coded}$	$Y_{4,coded}$
β_0	Const.	1.631000	0.341288	0.906305	95.180068
β_1	X_1	0.037722	0.237778	0.006111	7.998778
β_2	X_2	-0.001556	-0.034444	0.011444	-0.373389
β_3	X_3	0.000444	-0.241722	-0.010111	0.224389
β_4	X_4	0.085722	0.031278	0.087278	1.644833
β_5	X_1^2	-0.050500	-0.048836	0.002977	-6.748746
β_6	X_2^2	0.007000	-0.010836	-0.005023	-0.490246
β_7	X_3^2	0.007000	0.160664	-0.005023	-0.657246
β_8	X_4^2	-0.094500	-0.032336	-0.056523	-0.625246
β_9	X_1X_2	0.001875	-0.037938	-0.012875	0.358063
β_{10}	X_1X_3	-0.000375	-0.140438	0.011375	0.144187
β_{11}	X_1X_4	0.016750	0.021438	0.010375	-2.032188
β_{12}	X_2X_3	-0.000375	0.021813	0.011375	-0.042063
β_{13}	X_2X_4	-0.004250	0.004438	0.010375	0.296812
β_{14}	X_3X_4	-0.000500	-0.018312	-0.011375	0.017438

Coef. : Coefficient, Const.: Constant

Table 7. The accuracy of the models' predictions.

Run	Stator Teeth Flux Density			Stator Yoke Flux Density		
i	Y_{i1}	$\hat{Y}_{i1}$	$PE_{i1}(\%)$	Y_{i2}	$\hat{Y}_{i2}$	$PE_{i2}(\%)$
1	1.390	1.391	0.06	0.243	0.268	9.35
2	1.396	1.394	0.13	0.065	0.058	11.14
3	1.434	1.430	0.30	1.078	1.057	1.94
4	1.435	1.432	0.24	0.291	0.286	1.69
5	1.402	1.393	0.63	0.242	0.223	8.74
6	1.403	1.395	0.57	0.065	0.100	35.14
7	1.435	1.440	0.32	0.812	0.860	5.61
8	1.435	1.440	0.35	0.219	0.176	24.32
9	1.544	1.538	0.37	0.275	0.315	12.83
10	1.544	1.540	0.28	0.074	0.033	126.54
11	1.636	1.644	0.50	1.219	1.191	2.38
12	1.636	1.644	0.49	0.329	0.346	4.94
13	1.520	1.524	0.24	0.276	0.288	4.07
14	1.520	1.524	0.23	0.074	0.092	19.70
15	1.636	1.637	0.07	1.007	1.011	0.41
16	1.636	1.635	0.03	0.272	0.254	7.16
17	1.637	1.638	0.03	0.805	0.744	8.25
18	1.637	1.638	0.09	0.217	0.260	16.61
19	1.522	1.543	1.35	0.118	0.055	115.82
20	1.637	1.618	1.16	0.485	0.530	8.53
21	1.637	1.640	0.16	0.346	0.365	5.18
22	1.637	1.636	0.03	0.333	0.296	12.50
23	1.435	1.451	1.09	0.292	0.278	5.16
24	1.636	1.622	0.85	0.344	0.340	1.11
25	1.637	1.631	0.37	0.287	0.341	15.91

ANOVA is used for determining the significance of the model and summarized in Table 8 (confidence level: 95%) and the confirmation test results are given in Table 7. When there are replicates (multiple observations with identical x-values) in the data, Minitab displays the lack-of-fit test. Replicates are considered "pure error" because only random variation can cause differences in observed response values. In this study, the experimental design is conducted without replicates, so lack-of-fit is not observed in the Minitab reports. Instead of lack of fit test, the p-value test results of ANOVA for the mathematical models are presented in Table 8.

Table 7. (Continues).

Run	MFD			Efficiency		
i	Y_{i3}	$\hat{Y}_{i3}$	$PE_{i3}(\%)$	Y_{i4}	$\hat{Y}_{i4}$	$PE_{i4}(\%)$
1	0.754	0.767	1.73	75.950	75.906	0.06
2	0.754	0.724	4.10	76.150	76.116	0.04
3	0.754	0.762	1.01	94.597	94.964	0.39
4	0.754	0.764	1.34	95.405	95.750	0.36
5	0.764	0.772	1.09	73.093	73.934	1.14
6	0.764	0.775	1.41	73.295	73.975	0.92
7	0.754	0.715	5.40	94.796	94.424	0.39
8	0.754	0.763	1.23	95.248	95.042	0.22
9	0.955	0.923	3.46	82.404	82.632	0.28
10	0.773	0.835	7.38	82.525	82.911	0.47
11	0.947	0.959	1.25	94.227	93.560	0.71
12	0.947	0.916	3.38	95.236	94.417	0.87
13	0.957	0.970	1.31	82.178	81.847	0.40
14	0.957	0.927	3.27	82.303	81.958	0.42
15	0.947	0.954	0.75	94.152	94.208	0.06
16	0.947	0.957	1.01	94.838	94.895	0.06
17	0.902	0.911	1.03	94.375	94.298	0.08
18	0.902	0.891	1.22	94.811	94.747	0.07
19	0.918	0.903	1.64	81.813	80.433	1.72
20	0.902	0.915	1.46	95.190	96.430	1.29
21	0.902	0.890	1.37	94.825	95.063	0.25
22	0.902	0.913	1.18	94.695	94.316	0.40
23	0.754	0.763	1.12	94.486	92.910	1.70
24	0.947	0.937	1.06	94.764	96.200	1.49
25	0.902	0.906	0.48	94.759	95.180	0.44

Table 8. Summary for ANOVA results.

Response	F-Value	P-Value	Result
Stator Teeth Flux Density	100.02	0.000	Significant
Stator Yoke Flux Density	63.17	0.000	Significant
MFD	11.05	0.000	Significant
Efficiency	98.31	0.000	Significant

The results of the ANOVA indicates that P-values for each mathematial model is less than 0.05 – which means that the models are significant. Also the confirmation tests are performed and presented in Table 9.

Table 9. Confirmation results.

Run	Factors (uncoded levels)				Factors (coded levels)			
i	X_{i1}	X_{i2}	X_{i3}	X_{i4}	X_{i1}	X_{i2}	X_{i3}	X_{i4}
26	0.392	14	140	4	-0.50	-0.60	-0.67	-0.50
27	0.392	24	140	4	-0.50	0.40	-0.67	-0.50
28	0.392	24	140	8	-0.50	0.40	-0.67	0.50
29	0.784	14	140	4	0.50	-0.60	-0.67	-0.50
30	0.784	14	155	4	0.50	-0.60	0.33	-0.50
31	0.784	14	155	8	0.50	-0.60	0.33	0.50
32	0.784	24	155	8	0.50	0.40	0.33	0.50

Table 9. (Continues).

Run	Stator Teeth Flux Density			Stator Yoke Flux Density		
i	Y_{i1}	$\hat{Y}_{i1}$	$PE_{i1}(\%)$	Y_{i2}	$\hat{Y}_{i2}$	$PE_{i2}(\%)$
26	1.580	1.542	2.44	0.367	0.387	5.14
27	1.587	1.541	3.00	0.366	0.357	2.57
28	1.624	1.617	0.45	0.379	0.391	3.16
29	1.592	1.571	1.35	0.702	0.730	3.88
30	1.592	1.569	1.45	0.363	0.361	0.58
31	1.646	1.666	1.18	0.377	0.394	4.35
32	1.646	1.661	0.93	0.363	0.352	3.01

Table 9. (Continues).

Run	MFD			Efficiency		
i	Y_{i3}	$\hat{Y}_{i3}$	$PE_{i3}(\%)$	Y_{i4}	$\hat{Y}_{i4}$	$PE_{i4}(\%)$
26	0.859	0.848	1.24	92.361	87.846	5.14
27	0.857	0.855	0.28	92.278	87.271	5.74
28	0.932	0.948	1.73	92.509	90.039	2.74
29	0.856	0.850	0.76	95.045	96.550	1.56
30	0.856	0.846	1.23	95.362	97.082	1.77
31	0.923	0.928	0.56	95.201	97.539	2.40
32	0.929	0.943	1.49	95.132	97.577	2.51

The PE(%) results presented in Table 7 indicates that the prediction performance of the mathematical models for the observations those are not used in the modeling phase is good. As conclusion, results indicate that, the regression models provided in Table 5 and Table 6 are significant, according to the findings.

MFO is coded using the Matlab application [20, 21]. After conducting numerous preliminary tests, it is determined to use 30 search agents in the algorithm. There may be up to 100 iterations. Through a series of early experiments, the number of iterations and the number of search agents were determined. In these preliminary studies, several combinations were tested by gradually increasing the maximum number of iterations from 50 to 5000 and the number of search agents from 10 to 100. A constrained continuous optimization problem is used to model the issue. For this reason the models with coded factor levels presented in Table 6 are used and the factors in this model are then optimized using the MFO technique while adhering to the specified restriction. The goal function and the constraint for the factors are given in Eqs. (11) and (12). According to these functions; While the target for stator teeth flux density ($Y_{1,coded}$) and efficiency ($Y_{4,coded}$) are maximization; the target for stator yoke flux density ($Y_{2,coded}$) is minimization. The target for MFD ($Y_{3,coded}$) is 1.5 tesla. Since the stator tooth is the region exposed to the most intense magnetic field, the stator teeth flux density in this region was tried to be minimized and the maximum saturation point of the material was 1.5 Tesla. It is aimed to maximize the magnetic field value (flux density value) in the stator yoke so that the magnetic flux entering the stator through the tooth can stay in the stator and complete the magnetic circuit. The target values for the MFD value are determined by the additive material of the lamination. For M530-50A used in this study, 1-1.5 Tesla value should be reached.

$$Z = \left|Y_{1,coded}/max(Y_{i1})\right| - \left|Y_{2,coded}/max(Y_{i2})\right| - \left|1.5/max(Y_{i3}) - Y_{3,coded}/max(Y_{i3})\right| + \left|Y_{4,coded}/max(Y_{i4})\right| \quad (11)$$

$$Min\ Z\ s.t.\ X_1 \in [-1,1]; X_2 \in [-1,1]; X_3 \in [-1,1] \quad (12)$$

Keep in mind that the signs provided in the Z equation must be reversed in the Matlab code (see [20, 21, 25,

26] for further information). The CPU time is 5 seconds (on a PC which has 4GB RAM and Intel i5 2.4 GHz processor). In the previous studies published in the literature, the statistical results of the algorithms on multimodal test function are presented by Mirjalili [20] to determine the performance of MFO. Since the multi-modal functions have an exponential number of local solutions, there results show that the MFO algorithm is able to explore the search space extensively and find promising regions of the search space. Results of [20] indicated that the MFO algorithm highly outperforms other well-known algorithms (GA, PSO, and etc.).

Performance index figure that shows the reduction values of the objective function (fitness) during each iteration is presented in Figure 3.
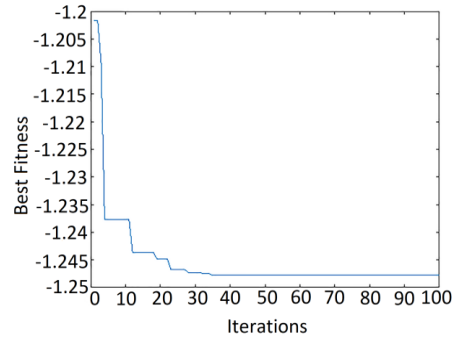
Figure 3. Best fitness values in each iteration.

MFO is calculated the optimized factor levels as $X_1 = 0.68$ (coded value: 0.23), $X_2 = 30$ (coded value: 1), $X_3 = 161.56$ (coded value: 0.77), and $X_4 = 8.92$ (coded value: 0.73). For this optimized factor level combination; the stator teeth flux density is calculated as 1.66 Tesla, stator yoke flux density is calculated as 0.24 Tesla, MFD distribution is calculated as 0.95 Tesla, and efficiency is calculates as 96.43% by MFO algorithm. Maxwell simulations are used for the confirmations and responses are calculated as: stator teeth flux density=1.64 Tesla, stator yoke flux density=0.26 Tesla, MFD=0.93 Tesla, and efficiency= 94.85%. Structure of the optimized PMSG, voltage graph of optimized PMSG, and MFD ditributon for the optimized PMSG are displayed in Figures 4-6 respectively. The THD is calculated as 0.21 for the PMSG. The outcomes show that the maximum efficiency has been attained and that the MFD distribution is within acceptable bounds (Figure 6's green zone).

As shown in Figure 6, the slot surface between the rotor and the stator (on the surface of the lamination) is still in the green region from top to bottom. In addition, in the range of 1.4 – 1.6 Tesla, which is between normal and forced zone. Orange zones can be calledfoced zones. Other colour from orange to red can be called over loaded but in this design we avoided from red zones and stay in max orange zone and do not affect the efficiency.

In general, no negative magnetic flux effect - that will

decrease the efficiency of the optimized PMSG – is observed. Because the red parts are rather minor and the green areas are predominate.
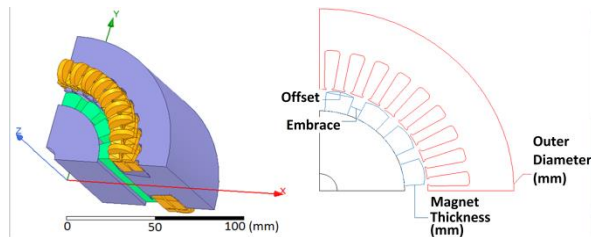

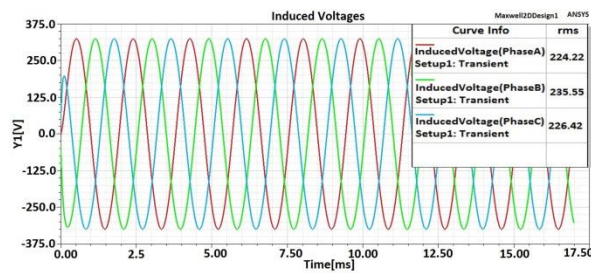**Figure 4.** Structure of the optimized PMSG.

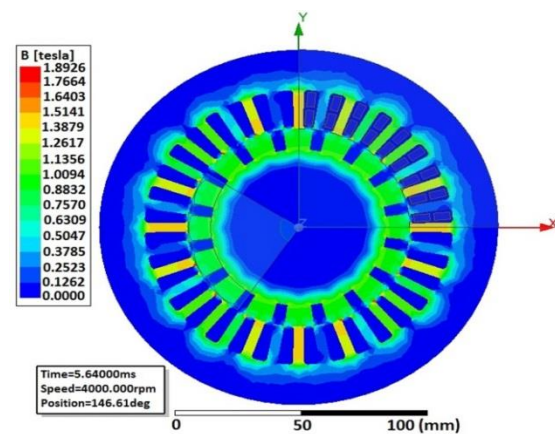**Figure 5.** Voltage graph of the optimized PMSG.

Figure 6. MFD distribution of the optimized PMSG.

The standard lamination (M530-50A) used in this study is normally used in alternators where the magnet structure is thin. In this study, it has been concluded that in the optimized high-speed alternator design, thick magnets should be used in order to achieve the lamination M530-50A saturation and the desired tesla value. In order to use thinner magnets, it is necessary to use more efficient lamination material. The results show that it would be appropriate to use thick magnets in order to obtain the desired Tesla values in high-speed alternators using M530-50A lamination material (the magnet thickness of the unoptimized generator is not specified for commercial confidentiality reasons).

5. Conclusion

In this work, 16-poled, 4000 rpm, 3 kVA PMSG rotor design optimization is carried out. Goal is to optimize the factor levels of embrace, offset, outer diameter (mm), and magnet thickness (mm) for maximizing

efficiency and keeping the magnetic distributions in a desired range. The calculated second order regression equations are fitted to the Maxwell simulation data, and MFO, a successful and recently developed optimization method inspired by nature, is utilized to run through these models. In this study the goal is to show the readers how the MFO algorithm can be used to obtain the desired response values by using the fewest possible experimental runs. Efficiency of the PMSG is maximized to 96.43% and the magnetic distributions are determined as 1.66, 0.24, and 0.95 Tesla for stator teeth flux density, stator yoke flux density, and MFD; respectively. The optimum factor levels for embrace, offset, outer diameter, and magnet thickness are calculated as 0.68, 30, 161.56, and 8.92 respectively. For the optimized factor levels, simulations for confirmation are performed using Maxwell. According to the Maxwell confirmation results: the efficiency is calculated as 94.85%, and magnetic distributions are calculated as 1.64, 0.26, and 0.93 Tesla for stator teeth flux density, stator yoke flux density, and MFD; respectively. Results proved that MFO and regression modeling is effectively used for these type of problems. MFO's striking advantage over previously employed nature-inspired algorithms (such as PSO, GA, and others) is its ability to execute optimization with a relatively low number of iterations (100 for this study). Therefore, we can draw the conclusion that MFO, like the previously discussed nature-inspired algorithms, can be employed successfully for optimization in this field. There is no limitation of MFO and it has only one controllable parameter (that is the number of search agents). So optimization results can not be further improved significantly. Additionally, in the lamination used in the non-optimized stator currently produced by the manufacturer, the thickness of the magnet has been reduced without reducing the useful flux value induced by the magnet in the rotor. This reduced value of 1.08 mm for each magnet corresponds to a total of approximately 17.28 mm for 16 poles considering the total pole in the rotor, which corresponds to two magnets. Compared to the non-optimized PMSG, there was a slight decrease in weight while the size remained the same. This work can be expanded for higher power groups in the future researches. Also the performance of MFO can be compared with the other well-known optimization algorithms in the future researchs.

References

[1] The company Vacuumschmelze (2021). *Soft Magnetic Cobalt-Iron Alloys Vacoflux and Vacodur* (1st ed.). VACUUMSCHMELZE GmbH & Co. KG, Hanau.

[2] Bartolo, J.B., Zhang, H., Gerada, D., De Lillo, L.,

& Gerada, C. (2013). High speed electrical generators, application, materials and design. *1st IEEE Workshop on Electrical Machines Design, Control and Diagnosis (WEMDCD)*, March 11-12, Paris, France.

[3] Fang, L., Jung, J.W., Hong, J.P. & Lee, J.H. (2008). Study on high-efficiency performance in interior permanent-magnet synchronous motor with double-layer PM design. *IEEE Transactions on Magnetics*, 44(11), 4393-4396.

[4] Li, H., & F. Liu (2011). The electromagnetic field analysis of permanent magnet synchronous generator based on ANSYS. *2nd International Conference on Advanced Measurement and Test (AMT 2011)*, Nanchang, PRC, June 24-26, 2011.

[5] Kurt, U., Onbilgin, G., & Ozgonenel, O. (2012). Defining design criteria of an axial flux permanent magnet synchronous generator. *International Review of Electrical Engineering (IREE)*, 7(1), 3290-3296.

[6] Hasanien, H.M., & Muyeen, S.M. (2013). A Taguchi approach for optimum design of proportional-integral controllers in cascaded control scheme. *IEEE Transaction on Power Systems*, 28 (2), 1636-1644.

[7] Oh, S.Y., Cho, S.Y., Han, J.H., Lee, H.J., Ryu, G.H., Kang, D., & Lee, J. Design of IPMSM rotor shape for magnet eddy-current loss reduction. *IEEE Transactions on Magnetics*, 50(2), Article Number: 7020804.

[8] Neubauer, M., Neudorfer, H., & Schrodl, M. (2016). Influence of the rotor optimization of an interior permanent magnet synchronous generator on the short circuit behavior. *22nd International Conference on Electrical Machines (ICEM)*, 1828-1834, Sep. 04-07, Lausanne, Switzerland.

[9] Xie, Q., Zhang, Y.B., Yu, Y.A., Si, G.Q., Yang, N.N., & Luo, L.F. (2016). A novel method to magnetic flux linkage optimization of direct-driven surface-mounted permanent magnet synchronous generator based on nonlinear dynamic analysis. *Energies*, 9(7), Article Number: 557.

[10] Demir, U., & Akuner, M.C. (2017). Using Taguchi method in defining critical rotor pole data of LSPMSM considering the power factor and efficiency. *Tehnicki Vjesnik-Technical Gazette*, 24(2), 347-353.

[11] Sabioni, C.L., Ribeiro, M.F.O, & Vasconcelos, J.A. (2018). Robust design of an axial-flux permanent magnet synchronous generator based on many-objective optimization approach. *IEEE Transactions on Magnetics*, 54(3), Article Number: 8101704.

[12] Dai, L., Gao, J., Zhang, W. & Huang, S. (2019). A genetic-Taguchi global design optimization strategy for surface-mounted PM machine. *22nd International Conference on Electrical Machines and Systems (ICEMS)*, pp. 1-6, Harbin, China.

[13] Gul, W., Gao, Q. & Lenwari, W. (2020). Optimal design of a 5-MW double-stator single-rotor PMSG for offshore direct drive wind turbines. *IEEE Transactions on Industry Applications*, 56(1), 216-225.

[14] Semon, A., Melcescu, L., Craiu, O. and Crăciunescu, A. (2019). Design optimization of the rotor of a V-type interior permanent magnet synchronous motor using response surface methodology. *11th International Symposium on Advanced Topics in Electrical Engineering (ATEE)*, pp. 1-4, Bucharest, Romania, Mar. 28-30.

[15] Jun, Z., Guanghua, L., Di, C., & Zhenyi, Z. (2019). Voltage regulation rate and THD optimization analysis of coreless axial flux PM synchronous generator for wind power generation. *IEEJ Transactions on Electrical and Electronic Engineering, 14*(10), 1485-1493.

[16] Karimpour, S.R., Besmi, M.R., & Mirimani, S.M. (2020). Optimal design and verification of interior permanent magnet synchronous generator based on FEA and Taguchi method. *International Transactions on Electrical Energy Systems*, 30(11), Article Number: E12597.

[17] Karimpour, S.R., Besmi, M.R., & Mirimani, S.M. (2021). Multi-objective optimization design and verification of interior PMSG based on finite element analysis and Taguchi method. *International Journal of Engineering*, 34(9), 2097-2106.

[18] Agrebi, H.Z., Benhadj, N., Chaieb, M., Sher, F., Amami, R., Neji, R., & Mansfield, N. (2021). Integrated optimal design of permanent magnet synchronous generator for smart wind turbine using genetic algorithm. *Energies*, 14(15), Article Number: 4642.

[19] Alemi-Rostami, M., Rezazadeh, G., Alipour-Sarabi, R., & Tahami, F. (2022). Design and optimization of a large-scale permanent magnet synchronous generator. *Scientia Iranica*, 29(1), 217-229.

[20] Mirjalili, S. (2015). Moth-flame optimization algorithm: A novel nature-inspired heuristic paradigm. *Knowledge-Based Systems*, 89, 228-249.

[21] Mirjalili, S. https://seyedalimirjalili.com/mfo. (Access: Apr 04, 2023)

[22] Wolpert, D.H., & Macready, W.G. (1997). No free lunch theorems for optimization. *IEEE Transactions on Evolutionary Computation*, 1, 67–82.

[23] Montgomery, D.C. (2013). *Design and analysis of experiments* (8th ed.). John Wiley & Sons, New Jersey, USA.

[24] Mason, R.L., Gunst, R.F., & Hess, J.L. (2003). *Statistical Design and Analysis of Experiments* (2nd ed.). John Wiley & Sons, New Jersey, USA.

[25] Ileri, E., Karaoglan, A.D., & Akpinar, S. (2020). Optimizing cetane improver concentration in biodiesel-diesel blend via grey wolf optimizer algorithm. *Fuel*, 273, Article Number:117784.

[26] Karaoglan, A.D., Perin D. (2022). Rotor Design Optimization of a synchronous generator by considering the damper winding effect to minimize THD using grasshopper optimization algorithm. *An International Journal of Optimization and Control: Theories & Applications (IJOCTA)*, 12(2), 90-98, https://doi.org/10.11121/ijocta.2022.1181.

Deniz Perin *received MSc. and Ph.D. Degrees in Physics from Balikesir University in the years 2008 and 2015 in Turkey, respectively. He has studied magnetic flux leakage (MFL) and magnetic non-destructive testing in Ph.D. and in research program of Cardiff University Wolfson Centre for magnetics. From 2017 till now, he is working on magnetic design & simulations of synchronous generators with ANSYS Maxwell in Isbir Electric Co Research & Development Department as a research and development expert.*

https://orcid.org/0000-0003-3697-3499

Aslan Deniz Karaoglan *received his Industrial Engineering diploma from Gazi University in Turkey in 2001, MSc. from Balikesir University in 2006, and Ph.D. from Dokuz Eylul University in 2010 in Turkey. His research interests are design of experiments, statistical process control, artificial intelligence, and optimization. He is a professor at Balikesir University (Turkey), Department of Industrial Engineering.*

https://orcid.org/0000-0002-3292-5919

Kemal Yilmaz *received the B.S. degree in in 2015 from the Department of Mechatronics Engineering - Karabuk University in 2015. Since 2017, he has been working as project and simulation Engineer in Isbir Electric Co Research & Development Department. His research interests are magnetic design and simulations of synchronous generators with Ansys Maxwell.*

https://orcid.org/0000-0001-5371-4267

IJOCTA
An International Journal of
Optimization and Control:
Theories & Applications
2010

RESEARCH ARTICLE

A Fractional-order mathematical model to analyze the stability and develop a sterilization strategy for the habitat of stray dogs

Zafer Öztürk [a], Ali Yousef [b,c], Halis Bilgil [d*], Sezer Sorgun [e]

[a] Institute of Science, Nevşehir Hacı Bektaş Veli University, 50300, Nevşehir, Türkiye
[b] Department of Natural Sciences and Mathematics, College of Engineering, International University of Science and Technology in Kuwait, 92400 Al-Ardiya, Kuwait
[c] Engineering Sciences Department, Abdullah Gul University, 38080 Kayseri, Türkiye
[d] Faculty of Engineering, Architecture and Design, Kayseri University, 38280, Kayseri, Türkiye
[e] Department of Mathematics, Nevşehir Hacı Bektaş Veli University, 50300, Nevşehir, Türkiye
zaferozturk@aksaray.edu.tr, ayousef.math@gmail.com, halisbilgil@kayseri.edu.tr, ssorgun@nevsehir.edu.tr

ARTICLE INFO	ABSTRACT
	Today, the socio-cultural lack of some countries with increased urbanization has led to the unconscious breeding of stray dogs. The failure to care for the offspring of possessive dogs or ignoring the responsibility to find a suitable family for the offspring increased the dog population on the streets and in the shelters. In this study, our main target is to analyze the habitat of stray dogs and the strategy of how to control the population without damaging the ecosystem of the species. For this aim, we establish a fractional-order differential equation system to investigate the fractal dimension with long-term memory that invovles two compartments; the non-sterilized dog population $(x(t))$ and the sterilized one $(y(t))$. Firstly, we analyze the stability of the equilibrium points using the Routh-Hurwitz criteria to discuss cases that should not affect the ecosystem of the dog population, but control the stray dog population in the habitat. Since the intervention to the stray dog population occurs at discrete time impulses, we use the Euler method's discretization process to analyse the local and global stability around the equilibrium points. Besides this, we show that the solutions of the system represent semi-cycle behaviors. At the end of the study, we use accurate data to demonstrate the sterilization rate of stray dogs in their habitat.

1. Introduction

The dog population is generally split into possessive and unattended dogs, which can be grouped under three main topics. This suggests that dogs have been lost while possessing an unclaimed population, dogs abandoned by the owner, and dogs already unclaimed. Dogs with masters are owned and maintained by one or more people [1]. Unattended dogs attempt to coalesce in a specific habitat and survive. This habitat consists of dog breeding, dog acceptance into the habitat from the outside, death, etc., and dog populations. Some factors affect the isolated dog population.

This means that the attitude and behavior of the surrounding people, the ability of dogs to breed, and the ability of dogs to access resources such as food and water within a group determine the size of the population. The lack of control of the unclaimed dog population brings several risks as the population grows. This suggests that the number of stray dogs in a habitat increases the number of zoonotic diseases. Zoonotic diseases are common in individuals, including both groups, transmitted from animals to humans. Zoonosis includes bacterial, viral, fungal (fungal-induced), rickettsial

*Corresponding Author

(a type of parasitic microorganism), and parasitic infections. Unattended dogs attack people and cause traffic accidents in their habitats, rabies, and zoonosis. As a result, the lack of control over the unattended dog population threatens human health [2]. Keeping the breeding of dogs under control and preventing unwanted breeding will help strike a balance between the animal owners' demands and the dog population's size. Sterilizations are being made to prevent the growing number of stray dogs. Sterilization of dogs is a surgical operation that removes the ovaries and uteruses of female dogs and the testicles of male dogs. This will prevent the uncontrolled increase in the number of stray dogs. Another method of controlling the populations of stray dogs is to provide training for animal owners. Those who possess unconscious animals may leave them on the street after a while. Adopted dogs have been introduced to chips, increasing the population if they do not have chips for their dogs and newborn cubs [1, 2].

The main goal of mathematical modeling is to describe the process through a mathematical description of real-life problems. A.A. Thirthar et al. analysed in [3] an aquatic ecological model with aggregation of fear and harvesting effects. Similar mathematical models that investigates species in ecosystems can be seen in [4–6]. Thus, mathematical models were developed to help explain a system, examine the effects of its various components, and make predictions about its behavior [7–9].

Models containing fractional derivatives yield better results than integer-based models in the theory of control of dynamical systems through various physical and biological processes [10–12]. In [11], C.M. Nunes et al. considered a case study in Brazil, where the management of visceral leishmaniasis has primarily involved the spraying of residual insecticides to eliminate vectors and the identification and removal of infected dogs.

It is particularly appropriate to use fractional operators to explain the memory and inherited characteristics of many materials and processes, as such properties are ignored in the derivative of the integer digit. The future status of a population in population models depends on its past status. It is called the memory effect. The memory effect of the population can be examined by adding a delay term or using a fractional derivative in the model [13–15]. In time-variable events, fractional models show more realistic and accurate results than models of integers because they have memory. Therefore, many biological events

are represented as fractional-order models. See, for example, [16–21].

This study develops a new mathematical model that deals with the parameters that affect the population of stray dogs. The most critical factor in the population, the neutering effect, was examined in different scenarios. Results have been released on the ideal sterilization strategy to prevent dog population extinction or uncontrolled escalation.

Let us say that the end limit value of the logistical growth $x(t)$ size over time is K (the maximum value that a population $x(t)$ can take, which is known as the maximum carrying capacity). The logistic model assumes that when $\frac{x(t)}{K} \sim 0$ exists, then the relative growth rate goes to zero, and when $\frac{x(t)}{K} \sim 1$ is reduced as a linear function, and the solution of the logistic equation tends to zero. A single species model (here, dog population) with carrying capacity K and growth rate r is given by [13], such as

$$D_t^\alpha x(t) = rx(t)(1 - \frac{x(t)}{K}). \qquad (1)$$

In including a ratio of natural deaths in the unsterilized dog compartment to equation (1.1), we obtain

$$D_t^\alpha x(t) = rx(t)(1 - \frac{x(t)}{K}) - \mu x(t). \qquad (2)$$

The overhead compartment decreases with a rate of β to build another compartment for sterilized dogs. Here, β denotes the rate of sterilization.

$$D_t^\alpha x(t) = rx(t)(1 - \frac{x(t)}{K}) - \mu x(t) - \beta x(t). \qquad (3)$$

Since the unsterilized dog compartment would have deaths due to illness, starvation, or other causes, we include a rate of θ to denote the death of this class caused by non-natural reasons. Finally, the non-sterilized compartment can be defined as follows;

$$D_t^\alpha x(t) = rx(t)(1 - \frac{x(t)}{K}) - \mu x(t) - \beta x(t) - \theta x(t). \qquad (4)$$

The sterilized compartment $y(t)$ exists from the rate β and compartment $x(t)$, which is given by

$$D_t^\alpha y(t) = \beta x(t). \qquad (5)$$

The $y(t)$ population also involves the same parameters μ and θ, that denote natural and non-natural causes of death. Thus, the equation can be improved such as

$$D_t^\alpha y(t) = \beta x(t) - \mu y(t) - \theta y(t). \qquad (6)$$

Now, the fractional dog population model can be expressed as a fractional differential equation system, where $(x(t))$ denotes the non-sterilized dogs and $(y(t))$ represents the sterilized dogs;

$$\begin{cases} D_t^\alpha x(t) = rx(t)\left(1 - \dfrac{x(t)}{K}\right) \\ \qquad\quad - \mu x(t) - \beta x(t) - \theta x(t) \\ D_t^\alpha y(t) = \beta x(t) - \mu y(t) - \theta y(t) \end{cases} \quad (7)$$

where D_t^α is the Caputo fractional derivative concerning time t and $0 < \alpha \le 1$. Initial values are given as, $x(0) = x_0 > 0$ and $y(0) = y_0 > 0$.
All compartments and parameters are given in Table 1 and Table 2.

Table 1. Variables used in the systems and their meanings.

Variables used in the systems	Meaning
$x(t)$	Not sterilized dog population
$y(t)$	Sterilized dog population
$N(t)$	Total population

Table 2. Parameters and their meanings.

Parameters	Meaning
β	Annual sterilization rate
μ	Annual natural mortality rate
θ	The annual death rate due to illness, hunger and other causes
K	Carrying capacity ratio
r	Annual growth rate

Definition 1. *[10] Let $f(t)$ be a function that can be continuously differentiable n times. The value of the function $f(t)$ for the value of α that satisfies the condition $n - 1 < \alpha < n$. The Caputo fractional derivative of $\alpha-th$ order $f(t)$ is defined by*

$$D_t^\alpha f(t) = \frac{1}{\Gamma(n-\alpha)} \int_a^n (t-x)^{(n-\alpha-1)} f^n(x) dx. \quad (8)$$

Definition 2. *[23] Given a function a function $\varphi(t)$, the fractional integral with order $\alpha > 0$ is given by Abdel's formula as*

$$I_t^\alpha \varphi(t) = \frac{1}{\Gamma(\alpha)} \int_0^x (x-t)^{(\alpha-1)} \varphi(t) dt, x > 0. \quad (9)$$

Definition 3. *[24] The Mittag-Leffler function of one variable is $(\lambda \ne 0, z \in \mathbb{C}\colon \mathrm{Re}(\alpha) > 0)$:*

$$E_\alpha(\lambda, z) = E_\alpha(\lambda z^\alpha) = \sum_{k=0}^\infty \frac{\lambda^k z^{\alpha k}}{\Gamma(1 + \alpha k)}. \quad (10)$$

2. Stability analysis

2.1. Perturbation and the Equilibrium Points

Let us consider the system.

$$\begin{cases} D_t^\alpha x(t) &= f(x(t), y(t)) \\ &= rx(t)\left(1 - \frac{x(t)}{K}\right) - \\ & \quad (\mu + \beta + \theta) x(t), \\ D_t^\alpha y(t) &= g(x(t), y(t)) = \beta x(t) - \\ & \quad (\mu + \theta) y(t). \end{cases} \quad (11)$$

To discuss the stability of system (11), we perturb the equilibrium point by adding $\varepsilon_i(t) > 0, \quad i = 1, 2$ such as

$$x(t) - \overline{x} = \varepsilon_1(t) > 0 \text{ and } y(t) - \overline{y} = \varepsilon_2(t) > 0. \quad (12)$$

Thus, we have

$$D_t^\alpha \varepsilon_1(t) \simeq f(\overline{x,y}) + \frac{\partial f(\overline{x,y})}{\partial x} \varepsilon_1(t) + \frac{\partial f(\overline{x,y})}{\partial y} \varepsilon_2(t),$$

and

$$D_t^\alpha \varepsilon_2(t) \simeq g(\overline{x,y}) + \frac{\partial g(\overline{x,y})}{\partial x} \varepsilon_1(t) + \frac{\partial g(\overline{x,y})}{\partial y} \varepsilon_2(t).$$

Using $f(\overline{x,y}) = g(\overline{x,y}) = 0$, we get a linearized system about $(\overline{x,y})$ as

$$D_t^\alpha Z = JZ \quad (13)$$

where $Z = (\varepsilon_1(t), \varepsilon_2(t))$ and J is the Jacobian matrix evaluated at $(\overline{x,y})$,

$$J = \begin{pmatrix} \frac{\partial f(\overline{x,y})}{\partial x} & \frac{\partial f(\overline{x,y})}{\partial y} \\ \frac{\partial g(\overline{x,y})}{\partial x} & \frac{\partial g(\overline{x,y})}{\partial y} \end{pmatrix}. \quad (14)$$

C is the diagonal matrix of J given by

$$C = \begin{pmatrix} \lambda_1 & 0 \\ 0 & \lambda_2 \end{pmatrix}, \quad (15)$$

where from $B^{-1}JB = C$, B represents the eigenvectors of J and $\lambda_i, \ i = 1, 2$ are the eigenvalues. Therefore, we get

$$\begin{cases} D_t^\alpha \eta(t) = \lambda_1 \eta_1 \\ D_t^\alpha \eta(t) = \lambda_2 \eta_2 \end{cases}, \quad (16)$$

where $\eta = \begin{pmatrix} \eta_1 \\ \eta_2 \end{pmatrix}$ and $\eta = B^{-1}Z$, whose solutions are given by the following Mittag-Leffler functions:

$$\eta_1(t) = \sum_{n=0}^\infty \frac{(\lambda_1)^n t^{n\alpha}}{\Gamma(n\alpha + 1)} \eta_1(0) = E_\alpha(\lambda_1 t^\alpha) \eta_1(0) \quad (17)$$

and

$$\eta_2(t) = \sum_{n=0}^\infty \frac{(\lambda_2)^n t^{n\alpha}}{\Gamma(n\alpha + 1)} \eta_2(0) = E_\alpha(\lambda_2 t^\alpha) \eta_2(0) \quad (18)$$

Using the result of [25], if $|arg\,(\lambda_i)| > \frac{\alpha\pi}{2}$, $i = 1, 2$, then $\eta_1(t)$ and $\eta_2(t)$ are decreasing; consequently, $\varepsilon_1(t)$ and $\varepsilon_2(t)$ are decreasing. For the existence of $(\varepsilon_1(t), \varepsilon_2(t))$ in (13), if the solution of (13) increases, then the equilibrium point $(\overline{x}, \overline{y})$ is unstable; otherwise, if $(\varepsilon_1(t), \varepsilon_2(t))$ decreases, then $(\overline{x}, \overline{y})$ is locally asymptotically stable.

The equilibrium points of system (12) are

Extinction of the habitat:

$$\Lambda_1 = (0, \ 0),$$

Non-sterilized stray dog population:

$$\Lambda_2 = \left(\frac{K\,(r - \mu - \theta)}{r}, \ 0\right)$$

for $r > \mu + \theta$ and $\beta = 0$,

Sterilized dog population system (Co-existing):

$$\Lambda_3 = \left(\frac{K\,(r - \mu - \beta - \theta)}{r}, \frac{K\beta\,(r - \mu - \beta - \theta)}{r\,(\mu + \theta)}\right)$$

for $r > \mu + \theta + \beta$ and $\beta > 0$.

2.2. Stability analysis of the equilibrium points

The Jacobian matrix of system (11) around an equilibrium point is as follows;

$$J\,(\overline{x}, \ \overline{y}) = \begin{pmatrix} r - \frac{2r\overline{x}}{K} - (\mu + \beta + \theta) & 0 \\ \beta & -(\mu + \theta) \end{pmatrix}.$$
(19)

For $\Lambda_1 = (0, \ 0)$, we have the characteristic equation

$$(r - (\mu + \beta + \theta) - \lambda_1)\,(-(\mu + \theta) - \lambda_2) = 0$$
$$\Longrightarrow \lambda_1 = r - (\mu + \beta + \theta) \text{ and } \lambda_2 = -(\mu + \theta).$$
(20)

Theorem 1. *Let* $\Lambda_1 = (0, \ 0)$ *be the extinction point of system (11). Then, the following statements are true:*

(i) *If* $r < \mu + \beta + \theta$, *then the equilibrium point* Λ_1 *is local asymptotic stable.*

(ii) *If* $r > \mu + \beta + \theta$, *then the equilibrium point* Λ_1 *is an unstable saddle point.*

Proof. Since $\lambda_2 = -(\mu + \theta) < 0$, we consider the conditions of the eigenvalue λ_1, which is negative if $r < \mu + \beta + \theta$, and positive if $r > \mu + \beta + \theta$. This completes the proof.

Remark 1. *Humans should never act with the intent of eradicating a species. Here we noticed that if the sterilization rate and the non-natural causes of death for the stray dogs are more significant than the growth rate, then population extinction happens. The unstable case of the equilibrium point* Λ_1 *is when the growth rate of the population is greater than the sterilization and death rates.*

The following scenario considers the case that sterilization is not applied, which means that only one compartment would exist, which is the $x(t)$ compartment.

The characteristic equation of Λ_2 is

$$(2\mu + 2\theta - r - \lambda_1)\,(-(\mu + \theta) - \lambda_2) = 0$$
$$\Longrightarrow \lambda_1 = 2\mu + 2\theta - r \text{ and } \lambda_2 = -(\mu + \theta).$$
(21)

Theorem 2. *Let* $\Lambda_2 = \left(\frac{K(r - \mu - \theta)}{r}, 0\right)$ *be the equilibrium point of the non-serialized dog population of system (11). Then the following statements are true.*

(i) *If* $r > 2\mu + 2\theta$, *then* Λ_2 *is local asymptotic stable.*

(ii) *If* $\mu + \theta < r < 2\mu + 2\theta$, *then* Λ_2 *is an unstable saddle point.*

Proof. From the definition of the equilibrium point, we obtained that Λ_2 exists for $r > \mu + \theta$ and $\beta = 0$. Moreover, $\lambda_2 < 0$. Considering the conditions for the eigenvalue λ_1, we obtain that Λ_2 is locally stable if $r > 2\mu + 2\theta$, and Λ_2 is a saddle point if $\mu + \theta < r < 2\mu + 2\theta$. This completes the proof.

Remark 2. *It is seen from Theorem 2 that the stray dog population would exist as single species if there is no sterilization and the growth rate of the species is greater than the death rate. The instability of the population exists if non-natural death causes increase.*

We analyze the characteristic equation around the equilibrium point to consider the co-existing case of both sterilized and non-sterilized dog populations. Λ_3, which is obtained as follows;

$$(2\,(\mu + \theta + \beta) - r - \lambda_1)\,(-(\mu + \theta) - \lambda_2) = 0$$
$$\Longrightarrow \lambda_1 = 2\,(\mu + \theta + \beta) - r \text{ and } \lambda_2 = -(\mu + \theta).$$
(22)

Theorem 3. *Let* Λ_3 *be the co-existing (positive) equilibrium point of system (11). Then the following statements hold.*

(i) *If* $r > 2\,(\mu + \theta + \beta)$, *then* Λ_3 *is local asymptotic stable.*

(ii) *If* $\mu + \theta + \beta < r < 2\,(\mu + \theta + \beta)$, *then* Λ_3 *is an unstable saddle point.*

Proof. The co-existing (positive) equilibrium point exists for $r > \mu + \theta + \beta$ and $\beta > 0$. Moreover, we obtained $\lambda_2 = -(\mu + \theta) < 0$. Therefore, we have to analyze the eigenvalue λ_1 to discuss the stability conditions. It can be seen that if $r > 2\,(\mu + \theta + \beta)$, then both compartments show local stability in the system, and if

$\mu + \theta + \beta < r < 2(\mu + \theta + \beta)$, then we have an unstable saddle point around the equilibrium point Λ_3. This completes the proof.

Remark 3. *A second compartment related to $x(t)$ exists if $\beta > 0$. This is the rate of sterilization from Theorem 3 we obtained that both compartments represent stable behavior if the growth rate of the non-sterilized dog population is greater than the sterilization rate and the death of non-natural causes. At the same time, it is unstable if the sterilization rate and the non-natural causes increase.*

3. Existence and uniqueness

Considering system (11) and the initial conditions $x(0) > 0$ and $y(0) > 0$, the initial value problem can be written such as

$$D_t^\alpha V(t) = AV(t) + x(t) BV(t), \ t \in [0, T], \ (23)$$

where, $V(t) = \begin{bmatrix} x(t) \\ y(t) \end{bmatrix}$ and $V(0) = \begin{bmatrix} x(0) \\ y(0) \end{bmatrix}$.

Let us assume that $x(t) > 0$ and $y(t) > 0$, when $t > \sigma \geq 0$. In this case, the IVP can be written as

$$D_t^\alpha V(t) = \begin{bmatrix} r - (\mu + \beta + \theta) & 0 \\ \beta & -(\mu + \theta) \end{bmatrix} \begin{bmatrix} x(t) \\ y(t) \end{bmatrix}$$
$$+ x(t) \begin{bmatrix} -\frac{r}{K} & 0 \\ 0 & 0 \end{bmatrix} \begin{bmatrix} x(t) \\ y(t) \end{bmatrix}. \quad (24)$$

Definition 4. *[21] Assume that $C^*[0, T]$ is the class of continuous column vector $V(t)$, whose components $x(t), y(t) \in C[0, T]$ is the class of continuous functions on $[0, T]$. The norm of $V(t) \in C^*[0, T]$ is given by $\|V\| = sup_t |e^{-Nt} x(t)| + sup_t |e^{-Nt} y(t)|$. When $t > \sigma \geq 0$, we write $C^*_\sigma[0, T]$ and $C_\sigma[0, T]$.*

Definition 5. *[21] $V(t) \in C^*[0, T]$ is a solution of the IVP in system (11) if the following (i) and (ii) hold.*

(i) $(t, V(t)) \in \mathcal{M}, \ t \in [0, T],$
    where $\mathcal{M} = [0, T] \times \mathcal{H},$
    $\mathcal{H} = \{(x(t), y(t) : |x(t)| \leq a, |y(t)| \leq b\}$
(ii) *$V(t)$ satisfies (23).*

Theorem 4. *Let $V(t) \in C^*[0, T]$ be a solution of the IVP given in (23). Then $V(t)$ is has unique solution for (23) if $0 \leq \frac{(A+aB)}{N^\alpha} < 1$.*

Proof. Let us write

$$I^{1-\alpha} \frac{d}{dt} V(t) = AV(t) + x(t) BV(t). \quad (25)$$

Operating with I^α, we obtain

$$V(t) = V(0) + I^\alpha \{AV(t) + x(t) BV(t)\}. \quad (26)$$

Now, let $F : C^*[0, T] \to C^*[0, T]$ be defined by

$$FV(t) = V(0) + I^\alpha \{AV(t) + x(t) BV(t)\}. \quad (27)$$

Then,

$$
\begin{aligned}
& e^{-Nt} \|FV - FU\| \\
=\ & e^{-Nt} \{I^\alpha \{A(V(t) - U(t)) \\
& + x(t) B(V(t) - U(t))\}\} \\
\leq\ & \frac{1}{\Gamma(\alpha)} \int_0^t (t-s)^{\alpha-1} e^{-N(t-s)} (V(s) - U(s)) \\
& e^{-Ns} (A + aB) ds \\
\leq\ & \frac{A+aB}{N^\alpha} \|V - U\| \int_0^t \frac{(t-s)^{\alpha-1}}{\Gamma(\alpha)} ds.
\end{aligned}
$$

This implies that $\|FV - FU\| \leq \frac{(A+aB)}{N^\alpha} \|V - U\|$. If we choose N^α such that $N^\alpha > A + aB$, then we obtain $\|FV - FU\| \leq \|V - U\|$, and the operator F given in (27) has a unique fixed point. Consequently, (26) has a unique solution $V(t) \in C^*[0, T]$. From (26), we have

$$V(t) = V(0) + \frac{t^\alpha}{\Gamma(\alpha+1)} (AV(0) + x(0) BV(0))$$
$$+ I^{\alpha+1} \{AV'(t) + x'(t) BV(t) + x(t) BV'(t)\},$$

and

$$\frac{dV(t)}{dt} = \frac{t^{\alpha-1}}{\Gamma(\alpha)} (AV(0) + x(0) BV(0))$$
$$+ I^\alpha \{AV'(t) + x'(t) BV(t) + x(t) BV'(t)\},$$
$$\implies e^{-Nt} \frac{dV(t)}{dt} = e^{-Nt} \left\{ \frac{t^{\alpha-1}}{\Gamma(\alpha)} (AV(0) + x(0) BV(0)) + I^\alpha \{AV'(t) + x'(t) BV(t) + x(t) BV'(t)\} \right\},$$

from which, we can deduce that $V'(t) \in C^*_\sigma[0, T]$. Thus, we have

$$\frac{dV(t)}{dt} = \frac{d}{dt} I^\alpha (AV(t) + x(t) BV(t))$$
$$\implies I^{1-\alpha} \frac{dV(t)}{dt} = I^{1-\alpha} \frac{d}{dt} I^\alpha (AV(t) + x(t) BV(t)),$$
$$\implies D_t^\alpha V(t) = AV(t) + x(t) BV(t),$$

and $V(0) = V_0$. Therefore, this IVP is equivalent to the initial value problem in (23).

4. Generalized Euler method

In this study, we used the Generalized Euler method to solve the initial value problem with the Caputo fractional derivative. Many mathematical models are composed of nonlinear systems, and solutions to these systems can be challenging. Analytical solutions cannot be found in most cases, and a numerical approach should be considered. One such approach is the Generalized Euler method [25]. Let $D_t^\alpha y(t) = f(t, y(t)), \ y(0) = y_0$, $0 < \alpha \leq 1, \ 0 < t < \alpha$ be the initial value problem. Let $[0, a]$ be the interval we want to find

the problem's solution. For convenience, subdivide the $[0, a]$ into n sub-intervals $[t_j, t_{j+1}]$, where $h = \frac{a}{n}$ and $j = 0, 1, \ldots, n - 1$. Suppose that $y(t)$, $D_t^\alpha y(t)$ and $D_t^{2\alpha} y(t)$ are continuous in the range $[0, a]$. Using the generalized Taylor's formula, the following equality is obtained [25, 26];

$$y(t_1) = y(t_0) + \frac{h^\alpha}{\Gamma(\alpha + 1)} f(t_0,\ y(t_0)). \quad (28)$$

This process will be repeated to create an array. Let $t_{j+1} = t_j + h$ for $j = 0, 1, \ldots, n - 1$. The generalized formula is given as follows;

$$y(t_{j+1}) = y(t_j) + \frac{h^\alpha}{\Gamma(\alpha + 1)} f(t_j,\ y(t_j)). \quad (29)$$

For every $k = 0, 1, \ldots, n - 1$ with step size h, we get

$$\begin{cases} x_{k+1} = x_k + \frac{h^\alpha}{\Gamma(\alpha+1)} \\ \qquad \left\{ rx_k \left(1 - \frac{x_k}{K}\right) - (\mu + \beta + \theta)x_k \right\}, \\ y_{k+1} = y_k + \frac{h^\alpha}{\Gamma(\alpha+1)} \left\{ \beta x_k - (\mu + \theta) y_k \right\}. \end{cases} \quad (30)$$

4.1. Local and global stability of the discretisized system

System (11) is discretized as (30) to analyze the dynamical effect of the habitat for sterilized and non-sterilized stray dogs in discrete time. The equilibrium points are the same as obtained in Section 2.

The Jacobian matrix of system (30) around the equilibrium point $(\overline{x},\ \overline{y})$ is obtained, such as

$$J((\overline{x}, \overline{y})) = \begin{pmatrix} 1 + \frac{h^\alpha \left(r - (\mu + \beta + \theta) - \frac{2r\overline{x}}{K}\right)}{\Gamma(\alpha+1)} & 0 \\ \frac{h^\alpha \beta}{\Gamma(\alpha+1)} & 1 - \frac{h^\alpha(\mu+\theta)}{\Gamma(\alpha+1)} \end{pmatrix}. \quad (31)$$

The eigenvalues of (4.4) are local asymptotic stable if $|\lambda_1| < 1$ and $|\lambda_2| < 1$. The saddle point exists for the condition if the absolute value of one of the eigenvalues is greater than 1. Thus, Theorem 4.1-Theorem 4.3. is given without proof.

Theorem 5. *Let Λ_1 be the equilibrium point of system (30). The following statements hold:*

  (i) *If $r < \mu + \beta + \theta$, then the equilibrium point Λ_1 is local asymptotic stable.*
  (ii) *If $r > \mu + \beta + \theta$, then the equilibrium point Λ_1 is an unstable saddle point.*

Theorem 6. *Let $\Lambda_2 = \left(\frac{K(r-\mu-\theta)}{r}, 0\right)$ be the equilibrium point of the non-serialized dog population of system (30). Then the following statements are true.*

  (i) *If $r > 2\mu + 2\theta$, then Λ_2 is local asymptotic stable.*
  (ii) *If $\mu + \theta < r < 2\mu + 2\theta$, then Λ_2 is an unstable saddle point.*

Theorem 7. *Let Λ_3 be the co-existing (positive) equilibrium point of system (30). Then the following statements hold.*

  (i) *If $r > 2(\mu + \theta + \beta)$, then Λ_3 is local asymptotic stable.*
  (ii) *If $\mu + \theta + \beta < r < 2(\mu + \theta + \beta)$, then Λ_3 is an unstable saddle point.*

Theorem 8. *Let Theorem 5.-(i) holds and assume that $\beta x_k < (\mu + \theta) y_k$, $k = 0, 1, 2, \ldots$. If*

$$h_1 < \left\{ \frac{2x_k \Gamma(\alpha + 1)}{rK^{-1}x_k^2 + x_k(\mu + \theta + \beta - r)} \right\}^{\frac{1}{\alpha}}$$

and

$$h_2 < \left\{ \frac{2y_k \Gamma(\alpha + 1)}{(\mu + \theta) y_k - \beta x_k} \right\}^{\frac{1}{\alpha}},$$

then the Λ_1 is global asymptotic stable.

Proof. We define the Lyapunov functions $W(x_k)$ and $\tilde{W}(y_k)$ such as

$$W(x_k) = (x_k - \overline{x})^2 \text{ and } \tilde{W}(y_k) = (y_k - \overline{y})^2, \quad (32)$$

$k = 0, 1, 2, \ldots$. The change along the solution of the first equation in system (4.3) around the equilibrium point Λ_1 is;

$$\begin{aligned} \Delta W(x_k) &= W(x_{k+1}) - W(x_k) \\ &= (x_{k+1})^2 - (x_k)^2 \\ &= (x_{k+1} - x_k)(x_{k+1} + x_k). \end{aligned}$$

From Theorem 5.(i), we obtain that

$$-x_k = \frac{h^\alpha}{\Gamma(\alpha+1)} \\ \left\{ -\frac{rx_k^2}{K} + (r - (\mu + \beta + \theta))x_k \right\} < 0. \quad (33)$$

Moreover,

$$\begin{aligned} x_{k+1} + x_k &= 2x_k + \frac{h^\alpha}{\Gamma(\alpha+1)} \\ &\quad \left\{ rx_k \left(1 - \frac{x_k}{K}\right) - (\mu + \beta + \theta) x_k \right\} > 0 \end{aligned}$$

if $h_1 < \left\{ \frac{2x_k \Gamma(\alpha+1)}{rK^{-1}x_k^2 + x_k(\mu+\theta+\beta-r)} \right\}^{\frac{1}{\alpha}}$. Thus, we obtain the condition for $\Delta W(x_k) < 0$.

Similarly,

$$\begin{aligned} \Delta \tilde{W}(y_k) &= \tilde{W}(y_{k+1}) - \tilde{W}(y_k) \\ &= (y_{k+1})^2 - (y_k)^2 \\ &= (y_{k+1} - y_k)(y_{k+1} + y_k). \end{aligned}$$

Computations showed that $\Delta \tilde{W}(y_k) < 0$, if

$$h_2 < \left\{ \frac{2y_k \Gamma(\alpha + 1)}{(\mu + \theta) y_k - \beta x_k} \right\}^{\frac{1}{\alpha}},$$

where $\beta x_k < (\mu + \theta) y_k$, for $k = 0, 1, 2, \ldots$. This completes the proof.

Theorem 9. and Theorem 10. have similar steps as Theorem 8 and therefore they will be omitted.

Theorem 9. *Let Theorem 6.-(i) holds and assume that* $x_k \in \left(\frac{K(r-\mu-\theta)}{r}, \frac{(\mu+\theta)y_k}{\beta} \right)$, $k = 0, 1, 2, \ldots$. *If*

$$h_1 < \left\{ \frac{2 \left(x_k - \frac{K(r-\mu-\theta)}{r} \right) \Gamma(\alpha+1)}{rK^{-1}x_k{}^2 + x_k(\mu+\theta+\beta-r)} \right\}^{\frac{1}{\alpha}}$$

and

$$h_2 < \left\{ \frac{2y_k \Gamma(\alpha+1)}{(\mu+\theta)y_k - \beta x_k} \right\}^{\frac{1}{\alpha}},$$

then the Λ_2 is global asymptotic stable.

Theorem 10. *Let Theorem 7.-(i) holds and assume that* $x_k \in \left(\frac{K(r-\mu-\beta-\theta)}{r}, \frac{(\mu+\theta)y_k}{\beta} \right)$ *and* $y_k > \frac{K\beta(r-\mu-\beta-\theta)}{r(\mu+\theta)}$, $k = 0, 1, 2, \ldots$. *If*

$$h_1 < \left\{ \frac{2 \left(x_k - \frac{K(r-\mu-\beta-\theta)}{r} \right) \Gamma(\alpha+1)}{rK^{-1}x_k{}^2 + x_k(\mu+\theta+\beta-r)} \right\}^{\frac{1}{\alpha}}$$

and

$$h_2 < \left\{ \frac{2 \left(y_k - \frac{K\beta(r-\mu-\beta-\theta)}{r(\mu+\theta)} \right) \Gamma(\alpha+1)}{(\mu+\theta)y_k - \beta x_k} \right\}^{\frac{1}{\alpha}},$$

then the Λ_3 is global asymptotic stable.

4.2. Semi-cycle analysis of positive solutions

In this section, we analyze the conditions of the semi-cycle of every oscillatory solution of system (30).

The definition is given for a different equation

$$x_{n+1} = f(x_n, x_{n-1})$$

and will be proven for a system constructed in (30).

From [27], a *positive semi-cycle* of a solution $\{x_n\}_{n=-1}^{\infty}$ of $x_{n+1} = f(x_n, x_{n-1})$ consists of a "string" of terms $\{x_k, x_{k+1}, \ldots, x_m\}$, all greater than or equal to the equilibrium point $\overline{x}$, with $k \geq -1$ and $m \leq \infty$, such that

either $k = -1$ or $k > -1$ and $x_{k-1} < \overline{x}$

and

either $m = \infty$ or $m < \infty$ and $x_{m+1} < \overline{x}$.

A *negative semi-cycle* of a solution $\{x_n\}_{n=-1}^{\infty}$ of $x_{n+1} = f(x_n, x_{n-1})$ consists of a "string" of terms $\{x_k, x_{k+1}, \ldots, x_m\}$, all less than the equilibrium point $\overline{x}$, with $k \geq -1$ and $m \leq \infty$, such that

either $k = -1$ or $k > -1$ and $x_{k-1} \geq \overline{x}$

and

either $m = \infty$ or $m < \infty$ and $x_{m+1} \geq \overline{x}$.

Theorem 11. *[31] Assume that* $f \in C\left[(0, \infty) \times (0, \infty), (0, \infty) \right]$ *and that* $f(x, y)$ *is decreasing in both arguments. Let* $\overline{x}$ *be a positive equilibrium point of* $x_{n+1} = f(x_n, x_{n-1})$. *Then every oscillatory solution of the difference equation* $x_{n+1} = f(x_n, x_{n-1})$ *has a semi cycle of the length at most two.*

Let system (30) be denoted as

$$\begin{cases} f(x,y) = x + \frac{h^{\alpha}}{\Gamma(\alpha+1)}\{rx(1-\frac{x}{K}) - (\mu+\beta+\theta)x\}, \\ g(x, y) = y + \frac{h^{\alpha}}{\Gamma(\alpha+1)}\{\beta x - (\mu+\theta)y\}. \end{cases}$$
(34)

Then, the following theorem can be obtained from Theorem 11.

Theorem 12. *Assume that* $\{(x_k, y_k)\}_{k=0}^{\infty}$ *is a positive solution to the system (30). If*

$$\begin{aligned} h &< \left(\frac{\mu+\theta}{\Gamma(\alpha+1)} \right)^{-\frac{1}{\alpha}} \\ &< \left(\frac{2r(\mu+\theta)+\beta K[r-(\mu+\beta+\theta)]}{\Gamma(\alpha+1)(K\beta+2r)} \right)^{-\frac{1}{\alpha}} \end{aligned}$$

and

$$\frac{\left(\Gamma(\alpha+1)h^{-\alpha}+r-(\mu+\beta+\theta) \right)K}{2r} < x < \frac{\mu+\theta-\Gamma(\alpha+1)h^{-\alpha}}{\beta},$$

where $r > \mu + \beta + \theta > \frac{\beta K(\mu+\beta+\theta)}{\mu+\beta+\beta K}$, *every oscillatory solution of system (30) has a semi-cycle of length at most two.*

Proof. The first derivative of (30) to the first equation concerning x is decreasing, if

$$1 + \frac{h^{\alpha}}{\Gamma(\alpha+1)} \left\{ r - (\mu+\beta+\theta) - \frac{2rx}{K} \right\} < 0,$$
(35)

which holds for $\frac{\left(\Gamma(\alpha+1)h^{-\alpha}+r-(\mu+\beta+\theta) \right)K}{2r} < x$, where $r > \mu + \beta + \theta$.

On the other side, the first derivative of (30) to the second equation concerning y, while x is fixed is decreasing, if

$$1 + \frac{h^{\alpha}}{\Gamma(\alpha+1)} \{\beta x - (\mu+\theta)\} < 0,$$
(36)

which holds for $x < \frac{\mu+\theta-\Gamma(\alpha+1)h^{-\alpha}}{\beta}$, where

$$h < \left(\frac{\mu+\theta}{\Gamma(\alpha+1)} \right)^{-\frac{1}{\alpha}}.$$

Considering both conditions of (35) and (36), we obtain

$$\frac{\left(\Gamma(\alpha+1)h^{-\alpha}+r-(\mu+\beta+\theta) \right)K}{2r} < x < \frac{\mu+\theta-\Gamma(\alpha+1)h^{-\alpha}}{\beta},$$
(37)

where

$$
\begin{aligned}
h \quad &< \quad \left(\frac{\mu+\theta}{\Gamma(\alpha+1)} \right)^{-\frac{1}{\alpha}} \\
&< \quad \left(\frac{2r(\mu+\theta)+\beta K[r-(\mu+\beta+\theta)]}{\Gamma(\alpha+1)(K\beta+2r)} \right)^{-\frac{1}{\alpha}},
\end{aligned} \tag{38}
$$

and $r > \mu + \beta + \theta > \frac{\beta K(\mu+\beta+\theta)}{\mu+\beta+\beta K}$. This completes the proof.

5. Numerical simulation of fractional dog population model

This section will show the numerical simulation and graphics of the fractional dog population model. Using the Generalized Euler method, we get the numerical simulation of the dynamical behavior of the constructed model [11]. Turkey has an average of 10 million dogs, of which 1,300,000 are sterilized [29]. The initial conditions and parameters a given, such as
$x(0) = 8.700.000, y(0) = 1.300.000, \beta = 0.15, \mu = 0.01, \theta = 0.05, r = 0.02, K = 10^7$ with a step size of $h = 0,1$. Hence the Euler method, we obtain the following;

Table 3. The values of $x(t)$, $y(t)$ and $N(t)$ at time t and $\alpha = 1$.

t	$x(t)$	$y(t)$	$N(t)$
0	8700000,00	1300000,00	10000000,00
1	8527300,00	1422700,00	9863572,00
2	8358226,70	1542073,30	9731314,11
3	8192703,93	1658194,26	9602943,31
4	8030657,15	1771135,65	9478200,81
5	7872013,35	1880968,69	9356849,72
6	7716701,07	1987763,08	9238672,96
7	7564650,35	2091587,02	9123471,50
8	7415792,69	2192507,25	9011062,55
9	7270061,04	2290589,10	8901278,24
10	7127389,76	2385896,48	8793964,14
11	6987714,58	2478491,95	8688978,14
12	6850972,57	2568436,71	8586189,35
13	6717102,15	2655790,68	8485477,12
14	6586043,00	2740612,47	8386730,12

Table 4. The values of $x(t)$, $y(t)$ and $N(t)$ at time t and $\alpha = 0.9$.

t	$x(t)$	$y(t)$	$N(t)$
0	8700000,00	1300000,00	10000000,00
1	8473941,27	1460610,33	9821420,15
2	8254096,53	1615520,71	9649946,47
3	8040294,94	1764897,91	9484953,02
4	7832370,41	1908904,04	9325883,28
5	7630161,37	2047696,68	9172241,56
6	7433510,71	2181428,98	9023585,59
7	7242265,66	2310249,85	8879520,20
8	7056277,61	2434303,97	8739691,67
9	6875402,06	2553732,01	8603782,95
10	6699498,47	2668670,68	8471509,53
11	6528430,18	2779252,86	8342615,67
12	6362064,27	2885607,71	8216831,25
13	6200271,47	2987860,76	8094068,93
14	6042926,09	3086134,01	7974021,67

Table 5. The values of $x(t)$, $y(t)$ and $N(t)$ at time t and $\alpha = 0.8$.

| t	$x(t)$	$y(t)$	$N(t)$
0	8700000,00	1300000,00	10000000,00
1	8406124,65	1508792,73	9767846,98
2	8122750,85	1707952,60	9547619,77
3	7849503,32	1897846,02	9337967,56
4	7586020,22	2078826,05	9137731,77
5	7331952,60	2251232,94	8945915,68
6	7086964,01	2415394,56	8761659,43
7	6850730,02	2571626,81	8584219,21
8	6622937,77	2720234,13	8412950,08
9	6403285,62	2861509,83	8247291,47
10	6191482,66	2995736,55	8086755,09
11	5987248,42	3123186,59	7930914,72
12	5790312,43	3244122,35	7779397,56
13	5600413,89	3358796,62	7631876,92
14	5417301,32	3467452,95	7488065,96
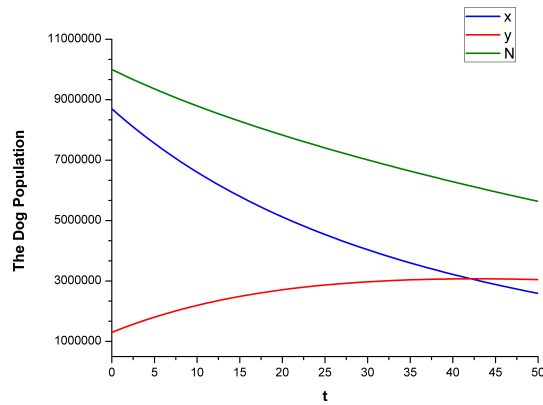
Figure 1. The graph of the change of the $x(t)$, $y(t)$ Compartment model and the N population with respect to time for $\alpha = 1$.
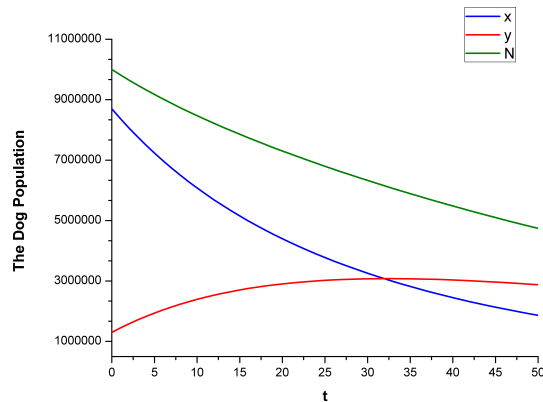
Figure 2. The graph of the change of the $x(t)$, $y(t)$ compartment model and the $N(t)$ population with respect to time for $\alpha = 0.9$.
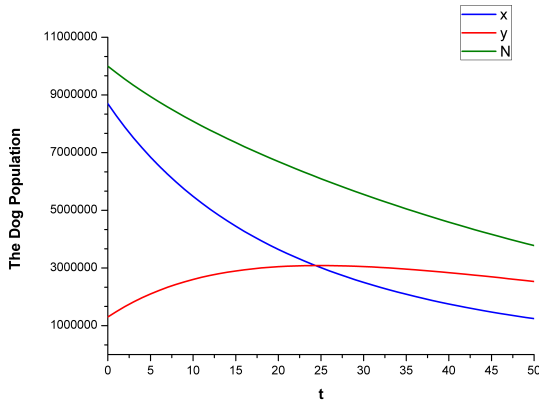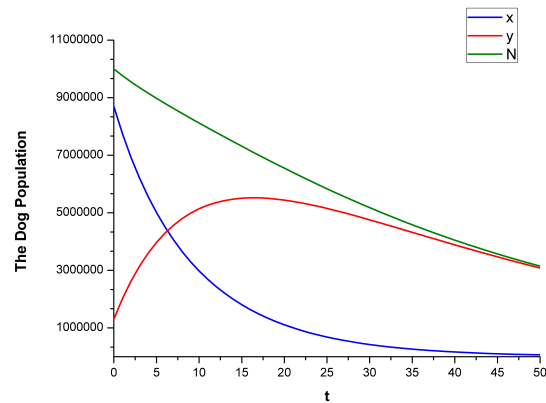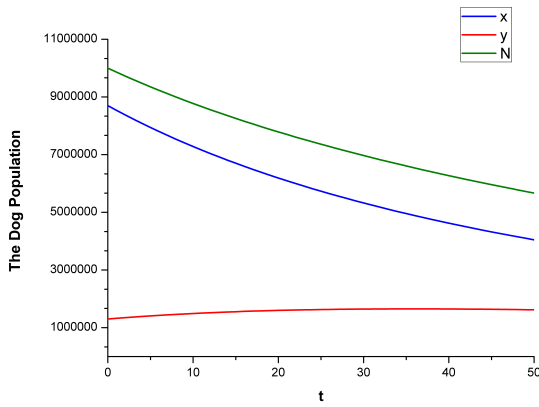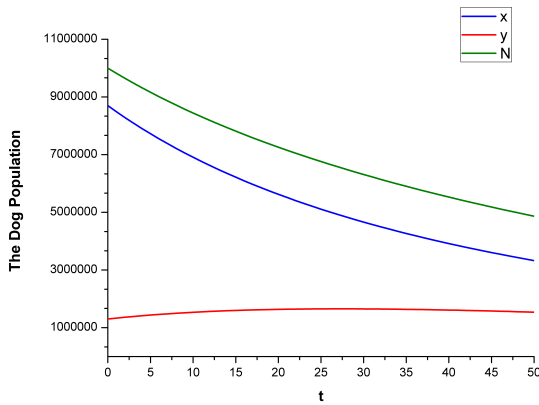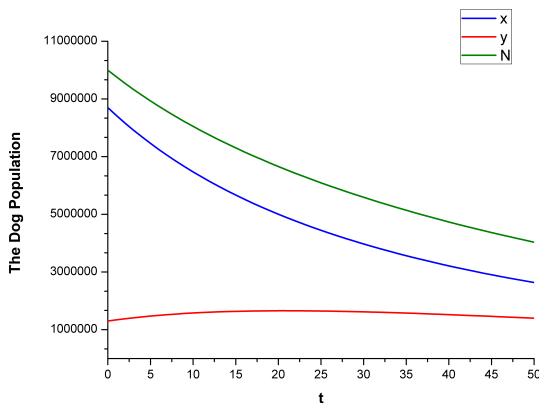
Figure 3. The graph of the change of the $x(t)$, $y(t)$ compartment model and the $N(t)$ population with respect to time for $\alpha = 0.8$.

In Table 3, Table 4, and Table 5, the changes in the $x(t)$, $y(t)$ compartments and the $N(t)$ population are observed for different states of α. According to the graphs above, we can make the following comments. It is observed that According to the graphs above, we can make the following comments.

- The number of dogs that have not been neutered will decrease over time (Fig-1).
- The number of neutered dogs will increase over time (Fig-2).
- The number of dogs in the population will decrease slowly over time (Fig-3).

5.1. Cases According to the Sterilization Rate

Case1. The number of spayings performed in the dog population must be kept at an acceptable level. If the annual sterilization rate $\beta = 0.5$ is taken, the following graphs are obtained.
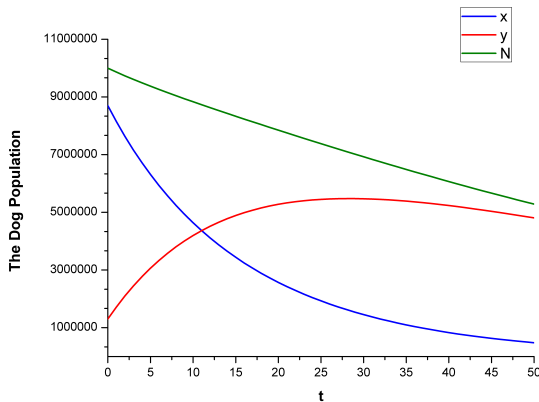
Figure 4. The graph of the change of the $x(t)$, $y(t)$ compartment model and the $N(t)$ population with respect to time for $\alpha = 1$.

Figure 5. The graph of the change of the $x(t)$, $y(t)$ compartment model and the $N(t)$ population with respect to time for $\alpha = 0.9$.

Figure 6. The graph of the change of the $x(t)$, $y(t)$ compartment model and the $N(t)$ population with respect to time for $\alpha = 0.8$.

In the above figures, we observe the following highlights:

- It is observed that the number of non-neutered dogs will decrease over time and become less than the number of neutered dogs (Fig-4).
- It is observed that the number of neutered dogs will increase over time and become more significant than the number of non-neutered dogs (Fig-5).
- It is observed that the number of dogs in the population will decrease slowly over time (Fig-6).

Case2. If the annual sterilization rate $\beta = 0.05$ is taken, the following graphs are obtained.

Figure 7. The graph of the change of the $x(t)$, $y(t)$ compartment model and the $N(t)$ population with respect to time for $\alpha = 1$.

Figure 8. The graph of the change of the $x(t)$, $y(t)$ compartment model and the $N(t)$ population with respect to time for $\alpha = 0.9$.

Figure 9. The graph of the change of the $x(t)$, $y(t)$ compartment model and the $N(t)$ population with respect to time for $\alpha = 0.8$.

In the above figures, we observe the following highlights:

- It is observed that the number of non-neutered dogs decreases slowly over time and progresses steadily (Fig-7).
- It is observed that the number of neutered dogs increases slowly over time and progresses steadily (Fig-8.
- It is observed that the number of dogs in the population progresses steadily, slowly decreasing over time (Fig-9).

6. Discussion

Over 10 million stray dogs are thought to exist in Turkey. Within ten years, it is predicted that there will be 60 million dogs without owners [29]. These numbers will inevitably lead to a rise in unattended dogs, dramatically raising the risk of unattended dog attacks that result in fatalities, serious injuries, and security issues. The attack on the unclaimed dogs resulted in numerous persons' death or severe injury. This study undertook the necessary analysis and demonstrated the significance of the sterilization method for managing the dog population. Our findings highlight the significance of managing the dog population and building up and implementing the mathematical model.

In order to promote the health and well-being of both dogs and people, dog population management tries to alter the indicators of population dynamics (cutting unintended births and abandonments, enhancing preventive treatment, and immigration control) [30]. Local sensitivity was examined by Baquero et al. (2016), who discovered that male and female sterilization have comparable effects [31]. Female animal sterilization is more effective than male animal sterilization, according to Amaku et al. (2010), and this activity depends on the size of the beginning population, the pace of growth, the rate of sterilization, and the timing of reproductive control [1].

The natural death rate, growth rate, sterilization rate, and carrying capacity of dogs were assessed while the dog population model was being developed. The logistical growth model was considered when creating the dog population model. Transportation capacity is one of the most valuable variables in simulations of dog population models. Neutering will no longer affect dogs as much as there will be more of them. Therefore, it is crucial to maintain population control.

Our findings highlight the significance of sterilization for managing the dog population. For extended periods, population dynamics-related factors will not have a single value. The model's parameters fall inside a reasonable range of values from a biological perspective and will become

more variable.

Concerning the interactions between populations of owned and stray dogs, the revised model allowed us to incorporate the effects of several factors on dog population dynamics. Thanks to our selected parameters, we could determine how the population number has changed. The impact of characteristics relating to natural mortality and transit capacity has also been considered in a more detailed model, and the impact of prospective interventions in the future sterilizing process has been quantified. The variance in the logistical growth model and the sterilization rate have demonstrated the possible effects of sterilization. The dynamics of the population will alter if the carrying capacity changes. This will impact the dynamics of leaving possessed dogs behind. Sterilization techniques and abandonment prevention will reduce population variance.

Our model enables us to get crucial knowledge regarding the dog population in the future through the neutering tactics of male and female dogs. Sustainable political, sanitary, moral, ethical, ecological, and human policies are needed to manage stray dog numbers on a social and environmental level. Such actions, like zoonoses like rabies and leishmaniasis control, should benefit animals and community members. Our findings show how crucial human variables are to the planning and execution of population control initiatives. The nation's governments benefit significantly from dog population models in their dog management initiatives.

7. Conclusions

In order to discuss the population of stray dogs, a new model of differential equations with fractal orders is constructed in this paper. The Routh-Hurwitz Criteria were used to analyze the equilibrium point's local stability. We applied the Generalized Euler Method to demonstrate the system's dynamical behavior in discrete time. This discretization technique proved the global and semi-cycle analyses. After the study, we use actual data to illustrate our findings and demonstrate how they align with our theoretical predictions. According to the graphs, the number of unsterilized dogs would gradually decline over time, the number of sterilized dogs would increase, and the overall number would gradually decline. The sterilization rate for the dog population was plotted and interpreted with $\beta = 0.05$ and $\beta = 0.5$. For the population of stray dogs, dog population models are particularly crucial. This was done using a mathematical model of controlling the dog population.

Figures 1-3 show that for $\beta = 0.15$, there is a regulated decline in the dog population due to neutering and natural causes. After around 43 years, if the sterilization rate stays constant, more neutered dogs will than unneutered dogs. After the fiftieth year, the population is anticipated to decline quickly. The drop in each compartment will be more pronounced with an increase in the parameter α. The number of dogs in each compartment reduced more quickly when the neutering rate was raised to $\beta = 0.5$ (see Fig. 4-6).

After 50 years, it is anticipated that the population will start to decline quickly in this circumstance. The drop in each compartment will be more pronounced with an increase in the parameter. The number of dogs in each compartment was observed to drop more quickly as the neutering rate rose (see Fig. 4-6). In this scenario, after roughly 31 years, there will be more neutered dogs than unneutered canines in the population, rapidly reducing the overall population. In this situation, the dog's extinction in the nation may one day be in jeopardy.

As a result, limiting the number of dogs in areas where people congregate is essential. Sterilization is the most ethical way to go about doing this. Despite this, sterilization must be carried out at a specific rate. In the absence of such measures, either the dog population will grow out of control or face extinction. The results of the model suggested in this article show that the value β should be maintained at or close to 0.1 to maintain the current dog population.

References

[1] Amaku, M., Dias, R.A. & Ferreira, F. (2010). Dynamics and control of stray dog populations. *Mathematical Population Studies*, 17 (2), 69-78.

[2] Fournier, A. & Geller, E. (2004). Behavior analysis of companion-animal overpopulation: a conceptualization of the problem and suggestions for intervention. *Behavior and Social Issues*, 68, 51-68.

[3] Thirthar, A. A., Majeed, S. J., Shah, K., & Abdeljawad, T. (2022). The dynamics of an aquatic ecological model with aggregation, fear and harvesting effect. *AIMS Mathematics*, 7(10), 18532-18552.

[4] Thirthar, A. A., Panja, P., Khan, A., Alqudah, M. A., & Abdeljawad, T. (2023). An ecosystem model with memory effect considering global warming phenomena and an exponential fear function. *Fractals*, 31(10), 1-19.

[5] Thirthar, A. A. (2023). A mathematical modelling of a plant-herbivore community with additional effects of food on the environment. *Iraqi Journal of Science*, 64(7),3551-3566.

[6] Yousef, A. & Bozkurt Yousef, F. (2019). Bifurcation and stability analysis of a system of fractional-order differential equations for a plant-herbivore model with Allee effect. *Mathematics*, 7 (454), 1-18.

[7] Morters, M. K., McKinley, T. J., Restif, O., Conlan, A. J. K., Cleaveland, S., Hampson, K., Whay, H. R., Damriyasa, I. M. & Wood, J.L.N. (2014).The demography free-roaming dog populations and applications to disease and population control. *Journal of Applied Ecology*, 51, 1096-1106.

[8] Sene, N. (2022). Theory and applications of new fractional-order chaotic system under Caputo operator. *An International Journal of Optimization and Control: Theories and Applications (IJOCTA)*, 12(1), 20-38.

[9] Kashyap, A.J., Bhattacharjee, D. & Sarmah, H.K. (2021). A fractional model in exploring the role of fear in mass mortality of pelicans in the Salton Sea. *An International Journal of Optimization and Control: Theories and Applications (IJOCTA)*, 11(3), 28-51.

[10] Podlubny, I. (1999). *Fractional Differential Equations.* Academy Press, San Diego CA.

[11] Nunes, C. M., de Lima, V. M. F., de Paula, H. B., Perri, S. H. V., de Andrade, A. M., Dias, F. E. F., & Burattini, M. N. (2008). Dog culling and replacement in an area endemic for visceral leishmaniasis in Brazil. *Veterinary Parasitology*, 153, 19-23.

[12] Linda, J.S.A. (2007). *An Introduction to Mathematical Biology.* Pearson Education Ltd., USA, 123-127.

[13] Bilgil, H., Yousef, A., Erciyes, A., Erdinç, Ü. & Öztürk, Z. (2022). A fractional-order mathematical model based on vaccinated and infected compartments of SARS-CoV-2 with a real case study during the last stages of the epidemiological event. *Journal of Computational and Applied Mathematics*, 115015.

[14] Hethcote, H., Zhien, M., & Shengbing, L. (2002). Effects of quarantine in six endemic models for infectious diseases. *Mathematical Biosciences*, 180, 141160.

[15] Öztürk, Z., Bilgil, H., & Sorgun, E. (2023). Application of fractional SIQRV model for SARS-CoV-2 and stability analysis. *Symmetry*, 15(5), 1-13.

[16] Slater, M. R. (2001). The role of veterinary epidemiology in the study of free-roaming dogs and cats. *Preventive Veterinary Medicine*, 48, 273-286.

[17] Allen L. J. S. (2007). *An Introduction to Mathematical Biology.* Department of Mathematics and Statistics, Texas Tech University, Pearson Education., 348.

[18] Santos Baquero, O., Amaku, M., & Ferreira, F. (2015). capm: An R package for Companion Animal Population Management.

[19] Öztürk, Z. , Bilgil, H., & Erdinç, Ü. (2022). An optimized continuous fractional grey model for forecasting of the time dependent real world cases. *Hacettepe Journal of Mathematics and Statistics*, 51 (1), 308-326.

[20] Kermack, W. O., & McKendrick, A. G. (1927). A contribution to the mathematical theory of epidemics, in: Proceedings of the Royal Society of London, Series A, Containing Papers of a Mathematical and Physical Character, 115 (772), 700-721.

[21] Yousef, A., Bozkurt, F., & Abdeljawad, A. (2020). Qualitative analysis of a fractional pandemic spread model of the novel coronavirus (COVID-19). *Comput Materials Continua*, 66, 843-869.

[22] Bozkurt Yousef, F., Yousef, A., Abdeljawad, T., & Kalinli, A. (2020). Mathematical modeling of breast cancer in a mixed immune-chemotherapy treatment considering the effect of ketogenic diet. *The European Physical Journal Plus*, 135(12), 1-23.

[23] Li, L., & Liu, J. G. (2016). A generalized definition of Caputo derivatives and its application to fractional ODEs. *SIAM Journal on Mathematical Analysis*, 50(3), 2867-2900.

[24] Kilbas, A. A., Srivastava, H. M., & Trujillo, J. J. (2006). *Theory and Applications of Fractional Differential Equations*, v.204, Elsevier.

[25] Yaro, D., Omari-Sasu, S. K., Harvim, P., Saviour, A. W. & Obeng, B. A. (2015). Generalized Euler method for modeling measles with fractional differential equations. *The International journal of Innovative Research and Development*, 4(4), 380-384.

[26] Nazir, G., Zeb, A., Shah, K., Saeed, T., Khan, R. A. & Khan, S. I. U. (2021). Study of COVID-19 mathematical model of fractional order via modified Euler method. *Alexandria Engineering Journal*, 60(6), 5287-5296.

[27] Gibbons, C., Kulenovic, M. R. S., Ladas, G. (2000). On the recursive sequence $x_{n+1}=(\alpha+\beta x_{n-1})/(\gamma+x_n)$. *Mathematical Sciences Research Hot-line*, 4(2), 1-11.

[28] Cunningham, K., Kulenović, M.R.S., Ladas, G. & Valicenti, S.V. (2001). On the recursive sequence $x_{n+1}=(\alpha+\beta x_{n-1})/(Bx_n+Cx_{n-1})$. *Nonlinear Analysis: Theory, Methods and Applications*, 47, 4603-4614.

[29] https://www.bbc.com, [Date Accessed 19 June 2023]

[30] Garcia, R.D.C.M., Calderón, N., & Ferreira, F. (2012). Consolidation of international guidelines for the management of canine populations in urban areas and proposal of indicators for their management. *Revista Panamericana de Salud Publica*, 32 , 140-144.

[31] Baquero, O. S., Akamine, L. A., Amaku, M., Ferreira, F. (2016). Dening priorities for dog population management through mathematical modeling. *Preventive Veterinary Medicine*, 123, 121-127.

Zafer Öztürk *currently a doctorate student of mathematics in department of Mathematics, Nevşehir Hacı Bektaş Veli University. His interests include fractional modeling and bifurcations.*

https://orcid.org/0000-0001-5662-4670

Ali Yousef *obtained his Ph.D. from the School of Mathematics, the University of Southampton, the UK. His main research area is sequential estimation and biological mathematics. He established the Department of Basic Sciences at Middle East University MEU in Jordan and was the statistical consultation center manager. In February 2016, he established and co-ordinated the mathematics program at Kuwait College of Science and Technology until September 2020. He published papers in sequential estimation and biomathematics related to HIV, breast cancer, Monoclonal Tumors, and Covid-19 in high-impact journals. Recently, he has been the chair of the Department of Natural Sciences and Mathematics at the International University of Science and Technology in Kuwait. In addition, a member of several committees in the university. He teaches mathematics, probability, and statistics to science and engineering students.*

https://orcid.org/0000-0002-8824-5947

Halis Bilgil *received Ph.D. in Mathematics from Erciyes University, Turkiye in 2010. He is a Professor with the Department of engineering basic sciences, Kayseri University, Turkiye. His current research interests include fractional differential systems, nonlinear evaluation equations, grey modeling, fluid mechanics and numerical analysis.*

https://orcid.org/0000-0002-8329-5806

Sezer Sorgun *is an associate professor at Department of Mathematics, Science and Letter Faculty, Nevşehir Hacı Bektaş Veli University. He received his PhD degree from the Erciyes University, Kayseri, Turkey. His research interests include ODEs, graf theory and matrix theory.*

https://orcid.org/0000-0001-8708-1226

An International Journal of Optimization and Control: Theories & Applications (http://www.ijocta.org)

RESEARCH ARTICLE

Dislocation hyperbolic augmented Lagrangian algorithm in convex programming

Lennin Mallma Ramirez[a*], Nelson Maculan[b], Adilson Elias Xavier[a], Vinicius Layter Xavier[c]

[a] *Federal University of Rio de Janeiro, Systems Engineering and Computer Science Program (COPPE), Rio de Janeiro, Brazil*
[b] *Federal University of Rio de Janeiro, Systems Engineering and Computer Science Program-Applied Mathematics (IM/COPPE), Rio de Janeiro, Brazil*
[c] *Rio de Janeiro State University, Institute of Mathematics and Statistics, Graduate Program in Computational Sciences, Rio de Janeiro, Brazil*
lenninmr@cos.ufrj.br, maculan@cos.ufrj.br, adilson.xavier@gmail.com, viniciuslx@ime.uerj.br

ARTICLE INFO	ABSTRACT
	The dislocation hyperbolic augmented Lagrangian algorithm (DHALA) is a new approach to the hyperbolic augmented Lagrangian algorithm (HALA). DHALA is designed to solve convex nonlinear programming problems. We guarantee that the sequence generated by DHALA converges towards a Karush-Kuhn-Tucker point. We are going to observe that DHALA has a slight computational advantage in solving the problems over HALA. Finally, we will computationally illustrate our theoretical results.

1. Introduction

We are interested in the convex nonlinear programming problem subject to inequality constraints, as follows

$$min\left\{f(x) \mid x \in S\right\}, \qquad (1)$$

where $S = \left\{x \in I\!R^n \mid g_i(x) \geq 0, \ i = 1, ..., m\right\}$, f and $g_i, \ i = 1, ..., m$ are real-valued functions defined on $I\!R^n$, and where the functions f and $g_i, \ i = 1, ..., m$ are continuously differentiable. The problem (1) is solved in particular by the augmented Lagrangian methods. The methodology of this method consists of solving a subproblem, that is, minimizing an augmented Lagrangian function (this is an unconstrained optimization problem), in this way, a primal solution is obtained. Subsequently the Lagrange multipliers are estimated. Some augmented Lagrangian algorithms known in the literature are: exponential Lagrangian [1], Log-sigmoid Lagrangian [2], nonlinear rescaling principle [3] and [4].

These augmented Lagrangian algorithms are called nonquadratic augmented Lagrangian algorithms, these algorithms are often C^2 if the objective and constraints are also twice continuously differentiable.

The quadratic augmented Lagrangian is differentiable only once [5]. The hyperbolic augmented Lagrangian algorithm (HALA) also solves the problem (1), see [6], HALA is a nonquadratic augmented Lagrangian. Adilson Elias Xavier introduces the hyperbolic penalty function (HPF) in [7] and the dislocation hyperbolic penalty function (DHPF) in [8]. With this last function, we are going to propose our algorithm called dislocation hyperbolic augmented Lagrangian algorithm (DHALA).

*Corresponding Author

This algorithm has two interesting characteristics: the function DPF is continuously differentiable unlike the classic quadratic penalty function, see for example [5], and the rule for updating its multipliers naturally generates a kind of safeguards for them.

This does not occur with other augmented Lagrangian type algorithms, i.e., to bound the multipliers, these algorithms have to generate a projection on a box, thus limiting the multipliers (see [9]). The main contributions of our work are:

- We introduce the dislocation hyperbolic augmented Lagrangian algorithm (DHALA), to solve the convex optimization problem with constraints. We guarantee that the sequence generated by DHALA converges to a Karush-Kuhn-Tucker (KKT) point. With this new approach, we notice that our algorithm DHALA converges to the solution in less time when compared to HALA (see the computational illustration of this work).
- This algorithm is based on the dislocation hyperbolic augmented Lagrangian function (DHALF). This function belongs to class C^∞ if the involved functions $f(x)$ and $g_i(x)$, $i = 1, ..., m$, do too.

The paper is organized as follows: Section 2 presents some basic definitions; Section 3 introduces the algorithm DHALA and assurance its convergence; Section 4 presents computational illustrations of our theoretical results; Section 5 presents some conclusions of our work, and discusses idea for future work.

2. Basic results

Throughout this paper, we are interested in studying the following optimization problem:

$$(P) \qquad x^* \in X^* = argmin\{f(x) \mid x \in S\},$$

where

$$S = \{x \in \mathbb{R}^n \mid g_i(x) \geq 0, \ i = 1, ..., m\},$$

is the convex feasible set of the problem (P) and where the function $f : \mathbb{R}^n \to \mathbb{R}$ is convex, $g_i : \mathbb{R}^n \to \mathbb{R}$, $i = 1, ..., m$, are concave functions, assuming that f, g_i are continuously differentiable in that way, (P) is a convex optimization problem. Let us consider the following assumptions:

C1. The optimal set X^* is nonempty, closed, bounded and, consequently, compact.

C2. Slater constraint qualification holds, i.e.,

there exists $\hat{x} \in S$ which satisfies $g_i(\hat{x}) > 0$, $i = 1, ..., m$.

The Lagrangian function of the problem (P), $L : \mathbb{R}^n \times \mathbb{R}^m_+ \to \mathbb{R}$, is defined as

$$L(x, \lambda) = f(x) - \sum_{i=1}^{m} \lambda_i g_i(x),$$

where, $\lambda_i \geq 0$, $i = 1, ..., m$, are the Lagrange multipliers. We know that due to assumption **C2**, the following results will occur: there exists $\lambda^* = (\lambda_1^*, ..., \lambda_m^*)$ such that the KKT conditions hold true, i.e.,

$$\nabla_x L(x^*, \lambda^*) = \nabla f(x^*) - \sum_{i=1}^{m} \lambda_i^* \nabla g_i(x^*) = 0,$$

$$\lambda_i^* g_i(x^*) = 0, \quad i = 1, ..., m,$$
$$g_i(x^*) \geq 0, \quad i = 1, ..., m,$$
$$\lambda_i^* \geq 0, \quad i = 1, ..., m.$$

Moreover, the set of optimal Lagrange multipliers λ^* is denoted by

$$\Lambda^* = \left\{ \lambda \in \mathbb{R}^m_+ \mid \nabla f(x^*) - \sum_{i=1}^{m} \lambda_i \nabla g_i(x^*) = 0, \right.$$
$$\left. x^* \in X^* \right\},$$

which is a bounded set (and hence compact set) due to **C2**. The dual function $\Phi : \mathbb{R}^m_+ \to \mathbb{R}$, is defined as follows

$$\Phi(\lambda) = \inf_{x \in \mathbb{R}^n} L(x, \lambda), \qquad (2)$$

and the dual problem consists of finding

$$(D) \qquad \lambda \in \Lambda^* = argmax\{\Phi(\lambda) \mid \lambda \in \mathbb{R}^m_+\}.$$

2.1. Hyperbolic and dislocation hyperbolic penalty function

The hyperbolic penalty algorithm (HPA) is meant to solve the problem (P). HPA adopts the HPF as

$$P(y, \lambda, \tau) = -\lambda y + \sqrt{(\lambda y)^2 + \tau^2}, \qquad (3)$$

where $P : \mathbb{R} \times \mathbb{R}_+ \times \mathbb{R}_{++} \to \mathbb{R}$. HPF is originally proposed in [7] and studied in [10]. This function is a smoothing of the exact penalty function studied by Zangwill [11]. HPF is used in HALA. On the other hand, in [8], DHPF is proposed and defined as follows:

$$p(g_i(x), \lambda_i, \tau) = -\lambda_i g_i(x) + \sqrt{(\lambda_i g_i(x))^2 + \tau^2} - \tau, \qquad (4)$$

for $i = 1, ..., m$, where $p : \mathbb{R} \times \mathbb{R}_+ \times \mathbb{R}_{++} \to \mathbb{R}$. Using (4), we will introduce DHALA in the next section.

3. Dislocation hyperbolic augmented Lagrangian algorithm

In this section, the are going to consider function (4) to define DHALF of problem (P) by $l_H : I\!\!R^n \times I\!\!R^m_{++} \times I\!\!R_{++} \to I\!\!R$,

$$l_H(x, \lambda, \tau) = f(x) + \sum_{i=1}^{m} p(g_i(x), \lambda_i, \tau)$$

$$= f(x) + \sum_{i=1}^{m} \left(-\lambda_i g_i(x) + \sqrt{(\lambda_i g_i(x))^2 + \tau^2} - \tau \right),$$

$$(5)$$

where $\tau > 0$ is the penalty parameter. Note that this function belongs to class C^∞ if the involved functions $f(x)$ and $g_i(x)$, $i = 1, ..., m$, do too. We can rewrite (5) as follows:

$$l_H(x, \lambda, \tau)$$

$$= f(x) - \sum_{i=1}^{m} \tau \left(\frac{\lambda_i g_i(x)}{\tau} - \sqrt{\left(\frac{\lambda_i g_i(x)}{\tau} \right)^2 + 1} + 1 \right)$$

$$(6)$$

$$= f(x) - \sum_{i=1}^{m} \tau \, h \left(\frac{\lambda_i g_i(x)}{\tau} \right),$$

where the function $h : I\!\!R \to I\!\!R$, is defined as

$$h(t) = t - \sqrt{t^2 + 1} + 1,$$

with $h \in C^\infty$. Henceforth, we will call the h function the dislocation hyperbolic function. Some properties of h are:

(H1) $h(0) = 0$ and $h'(0) = 1$.

(H2) h is increasing, i.e.,

$$h'(t) = 1 - \frac{t}{\sqrt{t^2 + 1}} > 0, \quad \forall t \in I\!\!R,$$

where $0 < h'(t) < 2$.

(H3) The h function is strictly concave, i.e.,

$$h''(t) = \frac{-1}{(t^2 + 1)^{\frac{3}{2}}} < 0, \quad \forall t \in I\!\!R.$$

By (H2), we get that $0 < h'(t) < 2$, which is also a characteristic similar to log-sigmoid Lagrangian (LST), see [2]. Now we present DHALA to solve the convex nonlinear programming problem (P).

Algorithm DHALA:

Step 1. Let $k := 0$. Take initial values $\lambda^0 = (\lambda_1^0, ..., \lambda_m^0) \in I\!\!R^m_{++}$ and $\tau \in I\!\!R_{++}$.

Step 2. Solve the unconstrained minimization problem:

$$x^{k+1} \in argmin_{x \in I\!\!R^n} \, l_H(x, \lambda^k, \tau)$$

$$= argmin_{x \in I\!\!R^n} \left\{ f(x) - \sum_{i=1}^{m} \tau h \left(\frac{\lambda_i g_i(x)}{\tau} \right) \right\}.$$

Step 3. Update the Lagrange multipliers:

$$\lambda_i^{k+1} = \lambda_i^k h' \left(\frac{\lambda_i^k g_i(x^{k+1})}{\tau} \right), \quad i = 1, ..., m. \quad (7)$$

Step 4. If the pair (x^{k+1}, λ^{k+1}) satisfies the stopping criteria, then stop.

Step 5. $k := k + 1$. Go to Step 2.

The methodology of our algorithm is as follows: in **Step 2**, we solve a subproblem that is unconstrained; in **Step 3**, the new Lagrange multipliers are estimated and in **Step 4**, a stop condition is considered. The only difference between (3) and (4) is the term $-\tau$. The word "dislocation" in our algorithm comes specifically from this term. Let us consider the following assumption:

C3. For every $\tau > 0$ and $\lambda \in I\!\!R^m_{++}$, the level set

$$M = \{ x \in I\!\!R^n \mid l_H(x, \lambda, \tau) \le \alpha \},$$

is bounded for every $\alpha < \infty$.

The Assumption **C3** can be verified when the function f is strongly convex. The strong convexity assumption for f is also studied in [5] and [12].

Remark 1. *From (7) and (H2) we note the following:*

$$\lambda_i^{k+1} = \lambda_i^k h' \left(\frac{\lambda_i^k g_i(x^{k+1})}{\tau} \right)$$

$$= \lambda_i^k \left(1 - \frac{\lambda_i^k g_i(x^{k+1})}{\sqrt{(\lambda_i^k g_i(x^{k+1}))^2 + \tau^2}} \right), \quad i = 1, ..., m.$$

On the other hand, by **C3**, there exists $x^{k+1} \in I\!\!R^n$ such that

$$l_H(x^{k+1}, \lambda^k, \tau) = min_{x \in I\!\!R^n} l_H(x, \lambda^k, \tau),$$

$$\nabla_x l_H(x^{k+1}, \lambda^k, \tau) = 0 \text{ holds, i.e.,}$$

$$\nabla f(x^{k+1}) - \sum_{i=1}^{m} \lambda_i^k h' \left(\frac{\lambda_i^k g_i(x^{k+1})}{\tau} \right) \nabla g_i(x^{k+1}) = 0.$$

$$(8)$$

Substituting (7) in (8), we have

$$\nabla_x l_H(x^{k+1}, \lambda^k, \tau) = \nabla f(x^{k+1}) - \sum_{i=1}^{m} \lambda_i^{k+1} \nabla g_i(x^{k+1}),$$

$$= \nabla_x L(x^{k+1}, \lambda^{k+1}) = 0, \quad (9)$$

for any $\tau > 0$. We observe that x^{k+1} and λ^{k+1} satisfy $\nabla_x L(x^{k+1}, \lambda^{k+1}) = 0$, showing that x^{k+1} is the minimizer of $L(x, \lambda^{k+1})$, i.e.,

$$\Phi(\lambda^{k+1}) = L(x^{k+1}, \lambda^{k+1}) = \min_{x \in I\!\!R^n} L(x, \lambda^{k+1})$$

with

$$\lambda^{k+1} \in I\!\!R^m_{++},$$

which follows that

$$\Phi(\lambda^{k+1}) = f(x^{k+1}) - \sum_{i=1}^{m} \lambda_i^{k+1} g_i(x^{k+1}). \quad (10)$$

From (10), we obtain $-g(x^{k+1})$

$$= \left(-g_1(x^{k+1}), \cdots, -g_m(x^{k+1})\right)^T \in \partial\Phi(\lambda^{k+1}),$$

where $\partial\Phi(v) = \{-v : v \in \partial(-\Phi)(\lambda)\}$ is the sub-differential of $\Phi(v)$ at $v = \lambda^{k+1}$. In the following remark, we analyze what happens with Lagrange multipliers depending on the type of restriction. Let us define the following sets of indices

$$I_0 = \{i \in \{1, ..., m\} \mid g_i(x) = 0\},$$
$$I_- = \{i \in \{1, ..., m\} \mid g_i(x) < 0\},$$
$$I_+ = \{i \in \{1, ..., m\} \mid g_i(x) > 0\}.$$

Remark 2. *Let $\{\lambda^k\}$ be a sequence generated by DHALA such that $\lambda_i^k > 0$, $i = 1, ..., m$ and let $\tau > 0$ fixed. Let us consider the following cases:*

(c1) *If $i \in I_0$, then at the k-th iteration we have $g_i(x^{k+1}) = 0$. Then, from (7) and (H1), we get $\lambda_i^{k+1} = \lambda_i^k$. Thus, $\left(\lambda_i^k - \lambda_i^{k+1}\right) g_i(x^{k+1}) = 0, \forall i \in I_0$.*

(c2) *If $i \in I_+$, then at the k-th iteration we have $g_i(x^{k+1}) > 0$. Then, from (H3), we have*

$$\frac{\lambda_i^k g_i(x^{k+1})}{\tau} > 0, \ i = 1, ..., m,$$

$$\lambda_i^k h'(0) < \lambda_i^k h'\left(\frac{\lambda_i^k g_i(x^{k+1})}{\tau}\right), \ i = 1, ..., m.$$

It follows from (7) and (H1) that $\lambda_i^k > \lambda_i^{k+1}$. Thus, $\left(\lambda_i^k - \lambda_i^{k+1}\right) g_i(x^{k+1}) > 0, \forall i \in I_+$.

(c3) *If $i \in I_-$, then at the k-th iteration we have $g_i(x^{k+1}) < 0$. Then, from (7) and following a similar approach to case (c2), we can obtain $\lambda_i^k < \lambda_i^{k+1}$. Thus, $\left(\lambda_i^k - \lambda_i^{k+1}\right) g_i(x^{k+1}) > 0, \forall i \in I_-$.*

From the three previous cases, we can note that we have the following

$$\left(\lambda_i^k - \lambda_i^{k+1}\right) g_i(x^{k+1}) \geq 0, \quad i = 1, ..., m. \quad (11)$$

3.1. Convergence esult

We are going to guarantee the convergence of DHALA. This section is mainly based on [3] and [6]. In the following result, we will demonstrate the positivity of the updated Lagrange multipliers.

Proposition 1. *Let*

$$\left\{\lambda^k = (\lambda_1^k, ..., \lambda_m^k) \mid k = 1, 2, ...\right\} \subset I\!\!R^m.$$

If $\lambda^k \in I\!\!R_{++}^m$,   then $\lambda^{k+1} \in I\!\!R_{++}^m$.

Proof. We can easily obtain the following, by making $\lambda_i^k > 0$, $i = 1, ..., m$. Thus, from (H2), we have

$$0 < \lambda_i^k h'\left(\frac{\lambda_i^k g_i(x^{k+1})}{\tau^k}\right) < 2\lambda_i^k, \ i = 1, ..., m,$$

from the inequality above and (7), we obtain $\lambda_i^{k+1} > 0$, $i = 1, ..., m$. ∎

Remark 3. *From **C3** and Proposition 1, we conclude that DHALA is well defined.*

From Proposition 1, we get

$$0 < \lambda_i^{k+1} < 2\lambda_i^k, \ i = 1, ..., m, \quad (12)$$

see Proposition 3.2.1 of [6]. Since we have (12), (H1), (H2) and (H3), we can see that DHF has similar properties to the Log-Sigmoid transformation (LST), see Section 3 of [2] and Section 3 of [13].

Theorem 1. *Let $\{\lambda^k\}$ be a sequence generated by DHALA. The sequence $\{\Phi(\lambda^k)\}$ is monotone nondecreasing for all $k \in I\!\!N$.*

Proof. From the concavity of $\Phi(\cdot)$ and since $-g(x^{k+1}) \in \partial\Phi(\lambda^{k+1})$, we have

$$\Phi(\lambda^{k+1}) - \Phi(\lambda^k) \geq \sum_{i=1}^{m} \left(g_i(x^{k+1})\right)\left(\lambda_i^k - \lambda_i^{k+1}\right). \quad (13)$$

From Remark 1, it follows

$$\lambda_i^k - \lambda_i^{k+1} = \frac{\left(\lambda_i^k\right)^2 g_i(x^{k+1})}{\sqrt{\left(\lambda_i^k g_i(x^{k+1})\right)^2 + \tau^2}}, \ i = 1, ..., m. \quad (14)$$

Then, expression (14) is replaced on the right side of inequality (13), and we get

$$\Phi(\lambda^{k+1}) - \Phi(\lambda^k) \geq \sum_{i=1}^{m}\left(\frac{\left(\lambda_i^k g_i(x^{k+1})\right)^2}{\sqrt{\left(\lambda_i^k g_i(x^{k+1})\right)^2 + \tau^2}}\right) \geq 0. \quad (15)$$

Thus, $\Phi(\lambda^{k+1}) \geq \Phi(\lambda^k)$. ∎

Proposition 2. *The sequence of dual objective function values $\{\Phi(\lambda^k)\}$ is bounded and monotone nondecreasing, hence it converges.*

Proof. By Theorem 1, we obtain $\Phi(\lambda^{k+1}) \geq \Phi(\lambda^k)$, then $\{\Phi(\lambda^k)\}$ is a nondecreasing sequence for all $k \in I\!\!N$ and considering the weak duality theorem, we obtain $\Phi(\lambda^k) \leq \Phi(\lambda^{k+1}) \leq f^*$, $\forall k$,

i.e., $\{\Phi(\lambda^k)\}$ is bounded from above by the optimal value. Then $\{\Phi(\lambda^k)\}$ is convergent. ∎

Proposition 3. *The sequence $\{\lambda^k\}$ generated by the DHALA is bounded.*

Proof. From **C2**, we know that Λ^* is nonempty and compact. So, one level set of $\Phi(\cdot)$ is compact. Then all level sets are compact, see Corollary 8.7.1 of [14]. From Proposition 2, we obtain in particular that $\lambda^k \in \Gamma = \{\lambda \in I\!\!R_+^m \mid \Phi(\lambda^0) \leq \Phi(\lambda)\}$ for all $k \in I\!\!N$. Hence, $\{\lambda^k\}$ is a bounded sequence. ∎

The following result is important to ensure the complementarity condition.

Lemma 1. *Let $d > 0$ and a sequence $\{a^k\} \subset I\!\!R_+$. If*

$$\lim_{k\to\infty} \left(a^k/\sqrt{a^k + d} \right) = 0, \quad then \quad \lim_{k\to\infty} a^k = 0.$$

Proof. See, pag. 19, Lemma 3.2.1 of [6]. ∎

The following result is similar to Proposition 4.3 of [3] and letter (c) of the Lemma 3.2 of [1], also see [6].

Theorem 2. *Let the sequences $\{x^k\}$ and $\{\lambda^k\}$ be generated by DHALA. Then,*

$$\lim_{k\to\infty} \left(\lambda_i^k g_i(x^k) \right) = 0, \quad i = 1, ..., m. \qquad (16)$$

Proof. Let be $\tau > 0$ be fixed. Since $\Phi(\cdot)$, is concave and $-g_i(x^{k+1}) \in \partial\Phi(\lambda^{k+1})$ we have

$$\Phi(\lambda^k) \leq \Phi(\lambda^{k+1}) + \sum_{i=1}^{m} \left(-g_i(x^{k+1}) \right) \left(\lambda_i^k - \lambda_i^{k+1} \right).$$

Considering the inequality above and the Remark 2, we obtain

$$0 \leq \sum_{i=1}^{m} \left(\lambda_i^k - \lambda_i^{k+1} \right) g_i(x^{k+1}) \leq \Phi(\lambda^{k+1}) - \Phi(\lambda^k). \qquad (17)$$

On the other hand, by (7), we have

$$\lambda_i^{k+1} = \lambda_i^k h' \left(\frac{\lambda_i^k g_i(x^{k+1})}{\tau} \right), i = 1, ..., m.$$

In the expression above, we subtract λ_i^k, $i = 1, ..., m$, and perform some operations, as follows for all $i = 1, ..., m$:

$$\lambda_i^{k+1} - \lambda_i^k = \lambda_i^k h' \left(\frac{\lambda_i^k g_i(x^{k+1})}{\tau} \right) - \lambda_i^k,$$

$$\lambda_i^{k+1} - \lambda_i^k = \lambda_i^k \left(h' \left(\frac{\lambda_i^k g_i(x^{k+1})}{\tau} \right) - 1 \right),$$

$$\lambda_i^k - \lambda_i^{k+1} = \lambda_i^k \left(1 - h' \left(\frac{\lambda_i^k g_i(x^{k+1})}{\tau} \right) \right). \qquad (18)$$

Replacing (18) in (17), we have

$$0 \leq \sum_{i=1}^{m} \left(\lambda_i^k \left(1 - h' \left(\frac{\lambda_i^k g_i(x^{k+1})}{\tau} \right) \right) \right) g_i(x^{k+1})$$
$$\leq \Phi(\lambda^{k+1}) - \Phi(\lambda^k).$$

Rewriting the above:

$$0 \leq \sum_{i=1}^{m} \left(1 - h' \left(\frac{\lambda_i^k g_i(x^{k+1})}{\tau} \right) \right) \left(\lambda_i^k g_i(x^{k+1}) \right)$$
$$\leq \Phi(\lambda^{k+1}) - \Phi(\lambda^k). \qquad (19)$$

Let us verify that the series in (19) is convergent:

$$0 \leq \sum_{k=1}^{\infty} \sum_{i=1}^{m} \left(1 - h' \left(\frac{\lambda_i^k g_i(x^{k+1})}{\tau} \right) \right) \left(\lambda_i^k g_i(x^{k+1}) \right)$$
$$\leq \sum_{k=1}^{\infty} \left(\Phi(\lambda^{k+1}) - \Phi(\lambda^k) \right).$$

We notice that $\sum_{k=1}^{\infty} \left(\Phi(\lambda^{k+1}) - \Phi(\lambda^k) \right)$ is a convergent series (i.e., the partial sum is bounded above), so it follows:

$$0 \leq \sum_{k=1}^{\infty} \sum_{i=1}^{m} \left(1 - h' \left(\frac{\lambda_i^k g_i(x^{k+1})}{\tau} \right) \right) \left(\lambda_i^k g_i(x^{k+1}) \right)$$
$$\leq \lim_{k\to\infty} \left(\Phi(\lambda^k) - \Phi(\lambda^1) \right)$$
$$\leq f^* - \Phi(\lambda^1) < \infty.$$

Therefore, for the test of comparison, we obtain

$$\lim_{k\to\infty} \sum_{i=1}^{m} \left(1 - h' \left(\frac{\lambda_i^k g_i(x^{k+1})}{\tau} \right) \right) \left(\lambda_i^k g_i(x^{k+1}) \right)$$
$$= 0. \qquad (20)$$

We note that each term in the summation (20) is nonnegative, thus

$$\lim_{k\to\infty} \left(1 - h' \left(\frac{\lambda_i^k g_i(x^{k+1})}{\tau} \right) \right) \left(\lambda_i^k g_i(x^{k+1}) \right) = 0, \qquad (21)$$

$\forall i = 1, ..., m$.

Now, let us prove (16) similar the proof by contradiction. What follows is similar argument to Proposition 4.3 of [3]. Suppose that there exists a subsequence (for any fixed i) $U \subset \{1, 2, ...\}$ and an $\epsilon > 0$ such that

$$\mid \lambda_i^k g_i(x^{k+1}) \mid \geq \epsilon > 0, \quad \forall k \in U. \qquad (22)$$

Then from (21), we obtain

$$\left\{ 1 - h' \left(\frac{\lambda_i^k g_i(x^{k+1})}{\tau} \right) \right\}_U \to 0,$$

so,

$$\left\{ h' \left(\frac{\lambda_i^k g_i(x^{k+1})}{\tau} \right) \right\}_U \to 1.$$

Since we have (H1), we obtain

$$\left\{ \frac{\lambda_i^k g_i(x^{k+1})}{\tau} \right\}_U \to 0,$$

thus,

$$\left\{ \lambda_i^k g_i(x^{k+1}) \right\}_U \to 0. \qquad (23)$$

We see that (23) contradicts the expression (22). So, we get

$$\lim_{k\to\infty} \left(\lambda_i^k g_i(x^{k+1}) \right) = 0, \ i = 1, ..., m. \qquad (24)$$

Because $\Phi(\cdot)$ is a concave function and from Remark 2, we get

$$\Phi(\lambda^{k+1}) - \Phi(\lambda^k)$$

$$\geq \sum_{i=1}^{m} \left(g_i(x^{k+1}) \right) \left(\lambda_i^k - \lambda_i^{k+1} \right) \geq 0. \qquad (25)$$

From Proposition 2 we know that $\{\Phi(\lambda^k)\}$ is convergent, so it follows:
$\lim_{k\to\infty} \left\{ \Phi(\lambda^{k+1}) - \Phi(\lambda^k) \right\} = 0$, and from (25) we obtain

$$\lim_{k\to\infty} \sum_{i=1}^{m} \left(g_i(x^{k+1}) \right) \left(\lambda_i^k - \lambda_i^{k+1} \right) = 0. \qquad (26)$$

Since $\left(g_i(x^{k+1}) \right) \left(\lambda_i^k - \lambda_i^{k+1} \right) \geq 0$ from (26) and (24), it follows that

$$\lim_{k\to\infty} \left(\lambda_i^{k+1} g_i(x^{k+1}) \right) = 0, \ i = 1, ..., m. \qquad (27)$$

∎

Let us consider the last assumption:

C4. The whole sequence to be $\{x^k\}$ is convergent to $\tilde{x}$, where $\tilde{x}$ is assumed a feasible point, i.e., $g_i(\tilde{x}) \geq 0, \ i = 1, ..., m.$

A similar assumption to **C4** can also be seen in [15]. Finally, we ensure that the subsequence generated by the algorithm DHALA converges to a KKT point.

Theorem 3. *The convex problem (P) satisfies* **C1**, **C2**, **C3** *and* **C4**. *Let sequences* $\{x^k\}$ *and* $\{\lambda^k\}$ *be generated by DHALA. Then, any limit point of a subsequence* $\{x^k\}$ *and* $\{\lambda^k\}$ *is an optimal solution Lagrange multiplier pair for the problem (P).*

Proof. Let $\tau > 0$ be fixed. By hypothesis, we have that $\lim_{k\to\infty} x^k = \bar{x}$ and $\lim_{k\to\infty} \lambda^k = \bar{\lambda}$. Henceforth, we can consider the following convergent subsequences $\lim_{k\to\infty} x^k = \bar{x}$ and $\lim_{k\to\infty} \lambda^k = \bar{\lambda}$ with $k \in K_2 \subset \mathbb{N}$.

In a previous result, we ensure feasibility, i.e., $g_i(\bar{x}) \geq 0, \ i = 1, ..., m.$ From Proposition

1, we obtain, $\lim_{k\to\infty} \lambda_i^k = \bar{\lambda}_i \geq 0, \quad i = 1, ..., m.$ Passsing the limit in (27), we have $\lim_{k\to\infty} \left(\lambda_i^k g_i(x^k) \right) = \bar{\lambda}_i g_i(\bar{x}) = 0, \ \forall i = 1, ..., m.$ Moreover, passing the limit in (9), we obtain

$$\nabla_x L(\bar{x}, \bar{\lambda}) = \nabla f(\bar{x}) - \sum_{i=1}^{m} \bar{\lambda}_i \nabla g_i(\bar{x}) = 0.$$

Thus, $(\bar{x}, \bar{\lambda})$ satisfies the KKT conditions for all $i = 1, ..., m$, and $(\bar{x}, \bar{\lambda})$ is a KKT point. Thus $\bar{x}$ is optimal for the problem (P) and $\bar{\lambda}$ is a Lagrange multiplier. ∎

4. Computational illustration

In this section, we are going to use the algorithms HALA and DHALA to solve the same problems. After obtaining the results, we will observe and comment the differences between these two algorithms.

The computational results presented below were obtained with a preliminary Fortran implementation for HALA and DHALA. The program was compiled with the GNU Fortran compiler version 4:7.4.0-1ubuntu2.3. The numerical Experiments were conducted on a Notebook with operating system Ubuntu 18.04.5, CPU i7-3632QM and 8GB RAM. The unconstrained minimization tasks were carried out by means of a Quasi-Newton algorithm employing the BFGS updating formula, with the function VA13 from HSL library [16]. The algorithm stops when the solution is viable (feasible) and the absolute value of the difference between two consecutives solutions is less than 10^{-7}.

For a better understanding of our work, we are going to present the algorithm HALA (for more details see [6]) below:

Algorithm HALA

Step 1. Let $k := 0$. Take initial values $\lambda^0 = (\lambda_1^0, ..., \lambda_m^0) \in \mathbb{R}_{++}^m$ and $\tau \in \mathbb{R}_{++}.$

Step 2. Solve the unconstrained minimization problem:

$$x^{k+1} \in argmin_{x\in\mathbb{R}^n} L_H(x, \lambda^k, \tau)$$

$$= argmin_{x\in\mathbb{R}^n} \left\{ f(x) + \sum_{i=1}^{m} P(g_i(x), \lambda_i, \tau) \right\}.$$

Step 3. Update the Lagrange multipliers:

$$\lambda_i^{k+1} = \lambda_i^k \left(1 - \frac{\lambda_i^k g_i(x^{k+1})}{\sqrt{(\lambda_i^k g_i(x^{k+1}))^2 + \tau^2}} \right), \quad (28)$$

$$\forall \ i = 1, ..., m.$$

Step 4. If the pair (x^{k+1}, λ^{k+1}) satisfies the stopping criteria, then stop.

Step 5. $k := k + 1$. Go to Step 2.

4.1. Test problems

The problems can be found in the book [17].

Problem 1. *Problem 11 (HS11) of [17].*

$$\min_{x \in I\!\!R^2} f(x) = (x_1 - 5)^2 + x_2^2 - 25$$

$$s.t. \qquad g_1(x) = -x_1^2 + x_2 \geq 0.$$

Starting with $x^0 = (4.9, \ 0.1)$ (not feasible) and $f(x^0) = -24.98$. The minimum value is $f(x^*) = -8.498464223$.

Problem 2. *Problem 66 (HS66) of [17].*

$$\min_{x \in I\!\!R^3} f(x) = 0.2x_3 - 0.8x_1$$

$$s.t. \ g_1(x) = x_2 - e^{x_1} \geq 0,$$
$$g_2(x) = x_3 - e^{x_2} \geq 0,$$
$$g_3(x) = x_1 \geq 0,$$
$$g_4(x) = x_2 \geq 0,$$
$$g_5(x) = x_3 \geq 0,$$
$$g_6(x) = 100 - x_1 \geq 0,$$
$$g_7(x) = 100 - x_2 \geq 0,$$
$$g_8(x) = 10 - x_3 \geq 0.$$

Starting with $x^0 = (0, 1.05, 2.9)$ (feasible) and $f(x^0) = 0.58$. The minimum value is $f(x^*) = 0.5181632741$ and the optimal solution is $x^* = (0.1841264879, 1.202167873, 3.327322322)$.

4.2. Results

Table 1 presents the time used by the algorithm to converge. Both algorithms use 5 iterations to solve problem HS11 and 12 iterations to solve problem HS66.

Table 1. Comparison of HALA and DHALA (time in seconds)

Problem	τ	*HALA*	*DHALA*
HS11	0.10E-01	0.000336	0.000226
HS66	0.10E-02	0.001239	0.000759

- Example 1
  - HALA:
    $x^* = (0.123477247E + 01, 0.152466328E + 01)$,

    $\lambda^* = 0.304888381E + 01$,

    $f(x^*) = -0.849846350E + 01$.

- DHALA:
    $x^* = (0.123477247E+01, 0.152466328E+01)$,

    $\lambda^* = 0.304888381E + 01$,

    $f(x^*) = -0.849846350E + 01$.

- Example 2
  - HALA:
    $x^* = (0.184127435E+00, 0.120216896E+01, 0.332732602E + 01)$,

    $\lambda^* = (0.665503228E+00, 0.199999462E+00, 0.147229064E-05, 0.345744295E-07, 0.451311477E-08, 0.501818042E-11, 0.512143031E-11, 0.112318220E-08)$,

    $f(x^*) = 0.518163256E + 00$.

  - DHALA:
    $x^* = (0.184127436E+00, 0.120216896E+01, 0.332732603E + 01)$,

    $\lambda^* = (0.665502922E+00, 0.199999546E+00, 0.147229063E-05, 0.345744284E-07, 0.451311477E-08, 0.501818042E-11, 0.512254052E-11, 0.112318220E-08)$,

    $f(x^*) = 0.518163257E + 00$.

5. Conclusions

In this work, we observed that the convergence of DHALA is similar to the convergence of HALA. The computational illustrations show that DHALA solves the problems in less time when compared to HALA. Additionally both DHALA and HALA solve the same problems in the same number of iterations (see, Table 1). Our algorithms DHALA and HALA converge to the exact solution within the precision of the computer. A limitation of our algorithm is that parameter τ is fixed, despite this limitation, our algorithm converges. For future work, we plan the convergence theory of our algorithm to address multiobjective optimization problems, subsequently applying this expanded framework to the problem investigated in [18]. We are also interested in doing a complexity analysis for our algorithm, similar to work [19]. We also have the interest of solving the subproblem generated by DHALA, with the Quasi Newton algorithm studied in [20].

Acknowledgments

References

[1] Tseng, P., & Bertsekas, D.P. (1993). On the convergence of the exponential multiplier method for convex programming. *Mathematical Programming*, 60, 1-19. https://doi.org/10.1007/BF01580598

[2] Polyak, R.A. (2001). Log-sigmoid multipliers method in constrained optimization. *Annals of Operations Research*, 101, 427-460. https://doi.org/10.1023/A:1010938423538

[3] Polyak, R., & Teboulle, M. (1997). Nonlinear rescaling and proximal-like methods in convex optimization. *Mathematical Programming*, 76, 265-284. https://doi.org/10.1007/BF02614440

[4] Kort, B.W., & Bertsekas, D.P. (1976). Combined primal-dual and penalty methods for convex programming. *SIAM Journal on Control and Optimization*, 14, 268-294. https://doi.org/10.1137/0314020

[5] Rockafellar, R.T. (1976). Augmented Lagrangians and applications of the proximal point algorithm in convex programming. *Mathematics of Operations Research*, 1, 97-116. https://doi.org/10.1287/moor.1.2.97

[6] Mallma-Ramirez, L. (2022). *The Hyperbolic Augmented Lagrangian Algorithm.* Ph.D. Thesis. Federal University of Rio de Janeiro/COPPE, Rio de Janeiro, Brazil. https://www.cos.ufrj.br/uploadfile/publicacao/3038.pdf

[7] Xavier, A.E. (1982a). *Penalização Hiperbólica-Um Novo Método para Resolução de Problemas de Otimização* . MSc Thesis. Federal University of Rio de Janeiro/COPPE, Rio de Janeiro, Brazil.

[8] Xavier, A.E. (1992). *Penalização Hiperbólica.* Ph.D. Thesis. Federal University of Rio de Janeiro/COPPE, Rio de Janeiro, Brazil.

[9] Kanzow, C., & Steck, D. (2017). An example comparing the standard and safeguarded augmented Lagrangian methods. *Operations Research Letters*, 45, 598-603. https://doi.org/10.1016/j.orl.2017.09.005

[10] Xavier, A. E. (2001). Hyperbolic penalty: a new method for nonlinear programming with inequalities. *International Transactions in Operational Research*, 8, 659-671. https://doi.org/10.1111/1475-3995.t01-1-00330

[11] Zangwill, W.I. (1967). Non-linear programming via penalty function. *Management Science*, 13, 344-358. https://doi.org/10.1287/mnsc.13.5.344

[12] Auslender, A., Teboulle, M., & Ben-Tiba, S. (1999). Interior proximal and multiplier methods based on second order homogeneous kernels. *Mathematics of Operations Research*, 24, 645-668. https://doi.org/10.1287/moor.24.3.645

[13] Polyak, R.A. (2002). Nonlinear rescaling vs. smoothing technique in convex optimization. *Mathematical Programming*, 92, 197-235. https://doi.org/10.1007/s101070100293

[14] Rockafellar, R.T. (1970). *Convex Analysis.* Princeton University Press, Princeton, NJ.

[15] Hartman, J.K. (1975). Iterative determination of parameters for an exact penalty function. *Journal of Optimization Theory and Applications*, 16, 49-66. https://doi.org/10.1007/BF00935623

[16] Harwell Subroutine Library (2002). A collection of Fortran codes for large scale scientific computation, https://www.hsl.rl.ac.uk/

[17] Hock, W., & Schittkowski, K. (1981). *Test Examples for Nonlinear Programming Codes.* Lecture Notes in Economics and Mathematical Systems 187, Springer-Verlag, Berlin, Germany. https://doi.org/10.1007/978-3-642-48320-2

[18] Tirkolaee, E.B., Goli, A., Gütmen, S., Weber, G.W., & Szwedzka, K. (2023). A novel model for sustainable waste collection arc routing problem: Pareto-based algorithms. *Annals of Operations Research*, 324, 189-214. https://doi.org/10.1007/s10479-021-04486-2

[19] Grapiglia, G.N. (2021). Worst-case evaluation complexity of a quadratic penalty method for nonconvex optimization. *Optimization Methods and Software*, 38, 781-803. https://doi.org/10.1080/10556788.2023.2189711

[20] Belloufi, M., Benzine, R., & Laskri, Y. (2013). Modification of the Armijo line search to satisfy the convergence properties of HS method. *An International Journal of Optimization and Control: Theories & Applications (IJOCTA)*, 3, 145-152. https://doi.org/10.11121/ijocta.01.2013.00141

Lennin Mallma Ramirez *received his Ph.D degrees in PESC/COPPE/UFRJ, Brazil (2022). He was a visiting research at the ICTEAM/UCLouvain, Belgium.nHe is currently doing a Postdoc in PESC/COPPE/UFRJ, Rio de Janeiro, Brazil. He is interested in researching continuous optimization algorithms.*
https://orcid.org/0000-0003-3579-1167

Nelson Maculan *Professor Emeritus Federal University of Rio de Janeiro, DHR Management Sciences, University of Paris-Dauphine, PhD Production Engineering, Federal University of Rio de Janeiro. Editor in Chief of RAIRO Operations Research journal.*
https://orcid.org/0000-0002-3897-3356

Adilson Elias Xavier *received his Ph.D degrees in PESC/COPPE/UFRJ, Brazil (1992). He is a professor at PESC/COPPE/UFRJ, Brazil. Working mainly*

on the following topics: Hyperbolic Penalty, Optimization, Nonlinear Programming, Multiplier Methods.

ⓘ https://orcid.org/0000-0003-4337-8049

Vinicius Layter Xavier *received his Ph.D degrees in PESC/COPPE/UFRJ, Brazil (2016). He is a professor at the IME/UERJ, Rio de Janeiro, Brazil. Working mainly on the following topics: Multivariate Statistics, Cluster Analysis, Nondifferentiable Programming, Min-Sum-Min Problems, Statistical Learning and Pattern Recognition.*

ⓘ https://orcid.org/0000-0002-7290-0652

An International Journal of Optimization and Control: Theories & Applications (http://www.ijocta.org)

RESEARCH ARTICLE

Fractional model for blood flow under MHD influence in porous and non-porous media

Fatma Ayaz[a], Kübra Heredağ[b*]

[a] *Department of Mathematics, Gazi University, Turkey*
[b] *Graduate School of Natural and Applied Sciences, Department of Mathematics, Gazi University, Turkey*
 fayaz@gazi.edu.tr, kubra.heredag@gazi.edu.tr

ARTICLE INFO	ABSTRACT
	In this research, the Magnetohydrodynamic flow model within a porous vessel containing blood was examined. What makes this study intriguing is the inclusion of a fractional-order derivative term in the Magnetohydrodynamic flow system equations. Fractional derivatives were chosen for their ability to encompass both integer and fractional-order derivatives, leading to more realistic modeling results. The numerical solution for the partial differential equation system was obtained using the finite differences method. Solutions were derived using both central difference and backward difference approaches to enhance the reliability of the results. The Grünwald-Letnikov derivative approach was employed for the fractional derivative term, while the Crank-Nicolson method was applied for other terms. Solutions were obtained for velocity, temperature, and concentration profiles. Subsequently, a thorough analysis was conducted to investigate variations in these solutions for changing values of significant flow parameters such as Hartmann number, Grashof number, solute Grashof number, a small positive constant, radiation parameter, Prandtl number, and Schmidt number. Additionally, the study analyzed changes in the fractional derivative order. Finally, the impact of flow parameters on flow in a non-porous medium was investigated, and the results were presented graphically. The study highlighted the significant effects of various parameters on blood flow.

1. Introduction

The blood vessels should allow a sufficient amount of blood flow. However, when the vessels are not permeable enough and the blood flow rate changes, circulation disorders occur. As a result, the tissues surrounding the arteries cannot be nourished adequately, and when sufficient blood flow is not provided, organs are damaged. For these reasons, mathematical models known for blood flow are crucial for biomedical researchers, physiologists, and medical doctors [1].

When examining fluids from a fluid mechanics perspective, blood is generally defined as a non-Newtonian fluid. Studies have shown that blood flow can be described as Newtonian when blood

cells are small relative to vessel diameter and the vessels are long [2]. Non-Newtonian fluids have variable viscosity. If the shear rate reaches a certain level, viscosity decreases and stabilizes, behaving like a Newtonian fluid. Newtonian fluids have a linear relationship between the applied shear stress and the resulting deformation rate (shear rate). Fluids like water, air, and oils are examples of Newtonian fluids, and their viscosity only changes with temperature [3].

Biomagnetic fluids are physiological fluids influenced by the presence of magnetic fields. The most characteristic biomagnetic fluid that can be considered a magnetic fluid is blood, as it contains hemoglobin molecules found in high concentrations, particularly in mature red blood cells,

---

*Corresponding Author

which are iron oxides. Nowadays, biocompatible magnetic materials are used in magnetic hyperthermia, where some very special magnetic particles are pushed into the blood. One method currently in use for treating tumors is to place a magnet near the tumor to capture magnetic particles in the tumor region. In the presence of an applied magnetic field, these particles act as heat sources. With this process, tumor treatment becomes more sensitive to radiotherapy and chemotherapy. Another application of magnets is occlusion, which prevents agents from reaching the tumor region, thus reducing blood flow [4]. This important field has attracted the interest of researchers, especially in the field of biomedical engineering and medical technology, due to its physiological applications during surgery, reducing blood flow, separating red blood cells from blood, and drug targeting.

Mathematical modeling is crucial for solving problems encountered in daily life in physics and engineering applications. Models often involve linear and nonlinear differential equations of integer order. However, in recent years, it has been suggested that these models may be insufficient to describe certain phenomena, and models involving fractional-order derivatives may be more realistic. Fractional calculus is considered effective in analyzing complex cases, including disease models, and plays a significant role in incorporating material memory effects [5]. In industry, fractional mathematics is preferred because it is more successful in modeling real systems compared to classical mathematics [6].

Fluid mechanics studies complex nonlinear systems that arise in various branches of science and often require simplification of models. On the other hand, research suggests that fractional-order models may offer more accurate representations of real-life problems compared to integer-order models [7]. Therefore, fractional differential equations have attracted the attention of many researchers in the 21st century.

The expression of fractional-order derivatives was first introduced in 1695 when L'Hôpital asked Leibniz about the meaning of D^n f for n being a fraction. Subsequently, famous mathematicians such as Euler, Laplace, Fourier, Abel, Liouville, Riemann, and Laurent were drawn to fractional calculus [8]. Euler developed the gamma function to use the factorial concept for rational numbers [9]. Thus, the gamma function became an important concept in fractional analysis. Fractional analysis has evolved to the present day. The theory of fractional differential equations be-comes one of the most interesting and attractive topics and has shown an increasing development. Differential equations involving fractional order derivatives are used to model a variety of systems has important applied sciences and engineering aspects [10]. Modeling utilizing fractional-order derivatives can yield more accurate results compared to integer-order derivatives. Consequently, there has been a substantial expansion in the realm of fractional research [11]. When electromagnetic fields are applied to fluid materials like blood, the flow behavior is affected. Changes in blood flow and viscosity are essential for understanding and treating certain diseases. Various studies have investigated the effects of magnetic fields on flow behavior and temperature changes. For example, J.C. Misra and his colleagues demonstrated that as the magnetic field strength increases, the fluid velocity decreases, but the temperature increases [12]. M. S. Abel and N. Mahesha showed that the combined effect of variable thermal conductivity, radiation, and uneven heat sources significantly influences the heat transfer rate at the boundary layer [13]. J.C. Misra and S.D. Adhikary found that blood viscoelasticity significantly reduces flow velocity, and wall shear stress is greatly affected by the Reynolds number [14]. V. Nagendramma and others explained various parameters related to fluid velocity, temperature, and density. They showed that as the Prandtl number increases, the temperature decreases [15]. S. Maiti and his colleagues demonstrated that fractional-degree flow models are faster than integer-order flow models, and as the Sc number increases, the density of blood decreases [16]. B. Tripathi and B. K. Sharma expressed that blood velocity is influenced by parameters, and medical doctors can take advantage of these effects in surgical procedures thanks to the magnetic field effects [17]. M. Alam and his colleagues studied heat transfer over a two-dimensional stretching plate with a viscoelastic fluid property in MHD flow [18]. A. A. Raptis examined the effects of magnetic fields on flow and the effects of porous medium permeability. It was concluded that increasing permeability increases the axial velocity [19]. S. Dinarvand and his colleagues found that as the magnetic field strength increases, blood flow velocity decreases [20]. E. Nader and his colleagues focused on blood viscosity and investigated how changes in conditions affect blood viscosity [21].

This study includes numerical solutions of the system of equations resulting from the selection of fractional-order time derivatives in an unstable

MHD blood flow model through a porous vessel. Calculations previously performed for classical derivatives (Misra et al. [22]) are obtained here with fractional-order time derivatives, and the results are compared with results containing integer-order derivatives for varying parameter values. In addition, the impact of taking the fractional time derivative in a non-porous medium on flow and how changes in the derivative order affect the flow are also explored.

2. Displayed mathematical equations

Blood flow can be considered as a flow model of fluid through a channel in fluid mechanics. Blood has a certain viscosity and is an incompressible, electrically conductive liquid. Blood flow occurs in a porous medium with time-dependent permeability, and this study examines the unstable hydromagnetic flow of a conductive fluid. Additionally, radiation is taken into account in the heat transfer within the fluid.

In the system shown in Figure 1, there is a uniform magnetic field applied in a different direction than the normal flow direction of the fluid. The magnetic Reynolds number is assumed to be very small, so the effect of the applied magnetic field can be neglected due to the induced magnetic field. The properties of the fluid are assumed to be constant except for density, which changes only with temperature. The basic flow in the system is a result of the buoyancy force due to the temperature difference between the inner medium and the wall.
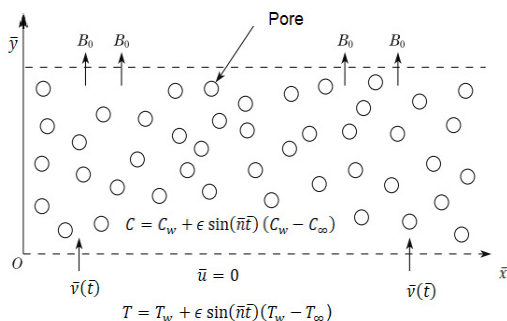
Figure 1. Physical sketch of problem

When $\bar{t} \leq 0$, it is assumed that the plate and the fluid are at the same temperature. However, when $\bar{t} > 0$, the plate's temperature is instantly raised or lowered to the surface temperature (Tw), and at the same time, the concentration of species is instantly raised or lowered to the concentration of the fluid in the plate (Cw).

$$\frac{\partial \bar{u}}{\partial \bar{x}} = 0, \tag{1}$$

$$\frac{\partial \bar{u}}{\partial \bar{t}} + \bar{v}\frac{\partial \bar{u}}{\partial \bar{y}} = \nu \frac{\partial^2 \bar{u}}{\partial \bar{y}^2} - \frac{\nu \bar{u}}{K} + g\beta(T - T_\infty)$$
$$+ g\beta^*(C - C_\infty) - \frac{\sigma B_0^2}{\rho}\bar{u}, \tag{2}$$

$$\frac{\partial T}{\partial \bar{t}} + \bar{v}\frac{\partial T}{\partial \bar{y}} = \frac{k_1}{\rho c_p}\frac{\partial^2 T}{\partial \bar{y}^2} - \frac{1}{\rho c_p}\frac{\partial q_r}{\partial \bar{y}}, \tag{3}$$

$$\frac{\partial C}{\partial \bar{t}} + \bar{v}\frac{\partial C}{\partial \bar{y}} = D\frac{\partial^2 C}{\partial \bar{y}^2} \tag{4}$$

Here, ν is the kinematic viscosity, β is the thermal expansion coefficient, β^* is the concentration-dependent thermal expansion coefficient, T is the temperature, T_∞ is the temperature of the ambient fluid, C is the concentration, C_∞ is the concentration of the ambient fluid, B_0 is the strength of the applied magnetic field, c_p is the specific heat at constant pressure, q_r is the radiative heat flux, D is the thermal molecular diffusion, and k_1 is the thermal conductivity. The term $\frac{\nu \bar{u}}{K}$' in (2) is related to the permeability of the wall. The boundary conditions are as follows:

$$\bar{u} = 0, T = T_w + \epsilon \sin(\bar{n}\bar{t})(T_w - T_\infty), \tag{5}$$

$$C = C_w + \epsilon \sin(\bar{n}\bar{t})(C_w - C_\infty); \bar{y} = 0 \tag{6}$$

and

$$\bar{u} \to 0, T \to T_\infty, C \to C_\infty, \bar{y} \to \infty \tag{7}$$

The relative heat flux, using the Rosseland approximation [23], is obtained as follows:

$$q_r = -\frac{4\sigma^*}{3k^*}\frac{\partial T^4}{\partial \bar{y}} \tag{8}$$

It is assumed that the temperature difference within the flow is quite small. Therefore, T^4 can be approximated as a linear function using a Taylor series around the temperature T_∞. In this approximation, higher-order terms are neglected.

$$T^4 = 4T_\infty^3 T - 3T_\infty^4 \tag{9}$$

With equations (8) and (9), the following equality is obtained:

$$\frac{\partial q_r}{\partial \bar{y}} = -\frac{16\sigma^* T_\infty^3}{3k^*}\frac{\partial^2 T^2}{\partial \bar{y}^2} \tag{10}$$

Now, let's discuss dimensionless equations.

$$u = \frac{\bar{u}}{v_0}, \tag{11}$$

$$\theta = \frac{T - T_\infty}{T_w - T_\infty}, \tag{12}$$

$$\phi = \frac{C - C_\infty}{C_w - C_\infty}, \tag{13}$$

The dimensionless coordinates are as follows:

$$y = \frac{\overline{y}v_0}{\nu}, \tag{14}$$

$$t = \frac{\overline{t}v_0^2}{4\nu}, \tag{15}$$

The dimensionless parameters are as follows:

$$K = \frac{K_0 v_0^2}{v^2}, \tag{16}$$

$$n = \frac{4\overline{n}\nu}{v_0^2} \tag{17}$$

If we substitute equations (11) - (17) into equations (2) - (4), we obtain the following system of equations. When K is taken as the permeability of the porous medium, the equations governing the fluid motion are as follows:

$$\frac{1}{4}\frac{\partial^\alpha u}{\partial t^\alpha} + (1 + \epsilon \sin(nt))\frac{\partial u}{\partial y} = \frac{\partial^2 u}{\partial y^2} \tag{18}$$

$$-\frac{u}{K(1 + \epsilon \sin(nt))} + Gr\theta + Gm\phi - M^2 u,$$

$$\frac{1}{4}\frac{\partial^\alpha \theta}{\partial t^\alpha} + (1 + \epsilon \sin(nt))\frac{\partial \theta}{\partial y} = \frac{(1 + Nr)}{\text{Pr}}\frac{\partial^2 \theta}{\partial y^2}, \tag{19}$$

$$\frac{1}{4}\frac{\partial^\alpha \phi}{\partial t^\alpha} + (1 + \epsilon \sin(nt))\frac{\partial \phi}{\partial y} = \frac{1}{Sc}\frac{\partial^2 \phi}{\partial y^2} \tag{20}$$

The boundary conditions are defined as follows

$$u = 0, \theta = 1 + \epsilon \sin(nt), \quad \phi = 1 + \epsilon \sin(nt),$$

$$nt = \frac{\pi}{2}, \quad y = 0, \tag{21}$$

$$u \to 0, \quad \theta \to 0, \quad \phi \to 0, \quad y \to \infty, \tag{22}$$

$$u_i^0 = 0.012ih(5 - ih)^4, \quad \theta_i^0 = 0.02, \quad \phi_i^0 = 0.02 \tag{23}$$

Here, u represents the velocity of the fluid, θ denotes temperature, and ϕ represents concentration. In general, simple blood flow models consider steady flow. However, in reality, the periodic nature of the cardiac cycle leads to non-continuous pulsatile flow, and pulsatile flow has significant effects on flow velocities and stress distributions. A time step of $h = 0.025$ seconds is set, and the highest velocity for pulsatile flow is 3.072 m/s, while the lowest velocity is 0 m/s [1].

3. Numerical calculations

The finite difference approximations for the derivative terms taken with respect to y in equations,(18) - (20) given above are as follows.

$$\frac{\partial F}{\partial y} = \frac{F_{i+1}^j - F_{i-1}^j}{2h}, \tag{24}$$

$$\frac{\partial^2 F}{\partial y^2} = \frac{F_{i+1}^{j+1} - 2F_i^{j+1} + F_{i-1}^{j+1} + F_{i+1}^j - 2F_i^j + F_{i-1}^j}{h^2}, \tag{25}$$

In which F stands for u, θ, ϕ.

When dealing with fractional derivative terms with respect to time, the Grünwald-Letnikov [24], [25] approach is employed, while for second-order derivative terms, the Crank-Nicolson method is used. Additionally, both central differencing and backward differencing methods are utilized for first-order derivative terms. A comparison between these two methods has been conducted, with separate graphs plotted for each method.

$$\frac{\partial^\alpha F}{\partial t^\alpha} = \frac{1}{h^\alpha}\sum_{r=0}^{m+1}\omega_r^\alpha F_i^{(j-r+1)}, 0 < \alpha < 1, \tag{26}$$

$$\omega_i^\alpha = \sum_{i=0}^{m+1}\left(1 - \left(\frac{\alpha + 1}{i}\right)\right)\omega_{(i-1)}^\alpha (i - 1),$$

$$\omega_0^\alpha = 1 \tag{27}$$

After the adjustments were made, the finite difference scheme obtained is given below.

$$A_1 u_{i-1}^{j+1} + B_1 u_i^{j+1} + C_1 u_{i+1}^{j+1}$$

$$+\frac{1}{2h^{\alpha-2}}\left(\sum_{r=2}^m u_i^{(j-r+1)}\omega_r^\alpha\right) = D1_i^j, \tag{28}$$

$$A_2 \theta_{i-1}^{j+1} + B_2 \theta_i^{j+1} + C_2 \theta_{i+1}^{j+1}$$

$$+\frac{1}{2h^{\alpha-2}}\left(\sum_{r=2}^m \theta_i^{(j-r+1)}\omega_r^\alpha\right) = D2_i^j, \tag{29}$$

$$A_3 \phi_{i-1}^{j+1} + B_3 \phi_i^{j+1} + C_3 \phi_{i+1}^{j+1}$$

$$+\frac{1}{2h^{\alpha-2}}\left(\sum_{r=2}^m \phi_i^{(j-r+1)}\omega_r^\alpha\right) = D3_i^j \tag{30}$$

Here, with $f = 1 + \epsilon \sin(nt)$ and h as the time step distance, it is expressed as

$$A1 = -fh - 2, \quad B1 = 4 + \frac{1}{2h^{(\alpha-2)}}\omega_0^\alpha,$$

$$C1 = fh - 2, \tag{31}$$

$$A2 = -2\left(\frac{1 + Nr}{\text{Pr}}\right) - fh,$$

$$B2 = 4\left(\frac{1 + Nr}{\text{Pr}}\right) + \frac{1}{2h^{(\alpha-2)}}\omega_0^\alpha,$$

$$C2 = -2\left(\frac{1 + Nr}{\text{Pr}}\right) + fh, \tag{32}$$

$$A3 = -\frac{2}{Sc} - fh, \quad B3 = \frac{4}{Sc} + \frac{1}{2h^{\alpha-2}}\omega_0^\alpha,$$

$$C3 = fh - \frac{2}{Sc} \tag{33}$$

Additionally, it is expressed as

$$D1_i^j = -fh(u_{(i+1)}^j - u_{(i-1)}^j) - 4\frac{u_i^j h^2}{Kf} + 2(u_{(i+1)}^j$$
$$- 2u_i^j + u_{(i-1)}^j) + 4h^2(Gr\theta_i^j + Gm\phi_i^j - M^2 u_i^j)$$
$$- \frac{1}{2h^{(\alpha-2)}}(\omega_{(m+1)}^\alpha u_i^0 + \omega_i^\alpha u_i^j), \qquad (34)$$

$$D2_i^j = -fh(\theta_{(i+1)}^j - \theta_{(i-1)}^j) + 2(\frac{1+Nr}{Pr})(\theta_{(i+1)}^j$$
$$- 2\theta_i^j + \theta_{(i-1)}^j) - \frac{1}{2h^{(\alpha-2)}}(\omega_{(m+1)}^\alpha \theta_i^0 + \omega_i^\alpha \theta_i^j)$$
$$\qquad (35)$$

$$D3_i^j = -fh(\phi_{(i+1)}^j - \phi_{(i-1)}^j) - \frac{2}{Sc}(\phi_{(i+1)}^j - 2\phi_i^j$$
$$+ \phi_{(i-1)}^j) - \frac{1}{2h^{(\alpha-2)}}(\omega_{(m+1)}^\alpha \phi_i^0 + \omega_i^\alpha \phi_i^j)$$
$$\qquad (36)$$

(28), (30) since it is a tridiagonal linear equation system, it can be solved using the Thomas Algorithm. The matrix is a square band matrix consisting of 2500 rows and columns. Numerical solutions for a single time step were obtained using the Maple 2021 program, and changes in parameters were shown using graphs. Each of matrix calculation time about forty minutes.

4. Guidelines for tables

In this section, graphs obtained when the flow parameters in the equation system were changed are presented. The differences observed are compared.

4.1. Presentation of figures

4.1.1. Blood flow problem under the influence of MHD in porous media

Differences in the time derivative of the flow velocity, temperature, and density of blood in unstable MHD flow, which arise from taking integer derivatives of time in the previous study (see [22]) and fractional derivatives of time in this study, have been investigated. Taking α as 1 coincides with the previous study. Thus, the differences between the use of integer derivatives and fractional derivatives can be examined with the help of graphs. Furthermore, changes in the absence of porosity have been investigated. Under the given boundary conditions,$h = 0.002$, $\alpha = 0.8$, and ϵ are taken between 0.005 and 0.03, and numerical computations were performed.$j = 0$and i are processed between 0 and 2500, and results are obtained in 2500 steps. To make the comparison more accurate, calculations were made using the parameter values specified below (see [22]).

$$M^2 = 0.5, 0.8, 1.0, 1.5, 2.0,$$
$$Gr = -20, -13.8, -10, 5, 10, 20,$$
$$Gm = 5, 10, 15, 20,$$
$$Pr = 0.025, 0.2, 0.7, 0.71, 1.5, 7.0, 10.0,$$
$$Nr = 1.0, 1.5, 2.0, 3.0, 3.5, 4.5,$$
$$Sc = 0.01, 0.05, 0.1, 0.2, 0.22, 0.5,$$
$$K = 10.0$$

In Figure 2, it is observed that as M increases, the axial velocity decreases. This is an expected result because as the M value increases, the Lorentz force increases. The Lorentz force opposes the flow.

Figure 3 is plotted using the data from the Figure 2. The only difference is that a backward difference has been used for the derivative term with respect to y. When comparing the two graphs, no significant difference is observed. This situation indicates that the obtained results are more reliable.

In Figure 4, both positive and negative values of Gr were examined. It was observed that as the Gr number decreases, meaning the amount of heat generated decreases, the velocity also decreases.

In Figure 5, when the positive values of Gm are examined, it is seen that the velocity also decreases as Gm decreases.

In Figure 6, it was observed that the velocity also decreases when the amplitude parameter ϵ decreases.

Figure 7 is plotted using the data from Figure 6. The only difference is that a backward difference has been used for the derivative term with respect to y. When comparing the two graphs, no significant difference is observed. This situation indicates that the obtained results are more reliable.

Figure 8 examines how temperature is influenced by Nr. As Nr decreases, the temperature also decreases.

Figure 9 is plotted using the data from Figure 8. The only difference is that a backward difference has been used for the derivative term with respect to y. When comparing the two graphs, no significant difference is observed. This situation indicates that the obtained results are more reliable.

In Figure 10, temperature is examined again. When Pr number increases, the temperature decreases.

In Figure 11, the change in Sc number is examined with concentration. When the channel walls

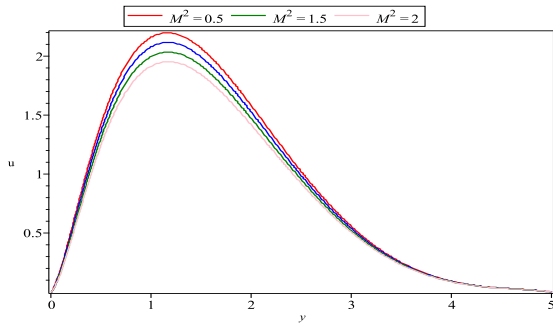cool, an increase in Sc leads to a decrease in concentration.

Figure 2. Velocity distribution for different values of M^2
(The graph plotted using central differencing method)
$Sc = 0.22$, $Pr = 0.71$, $Nr = 1$, $Gm = 10$, $Gr = 10$, $\epsilon = 0.005$, $K = 10$, $nt = \pi/2$.
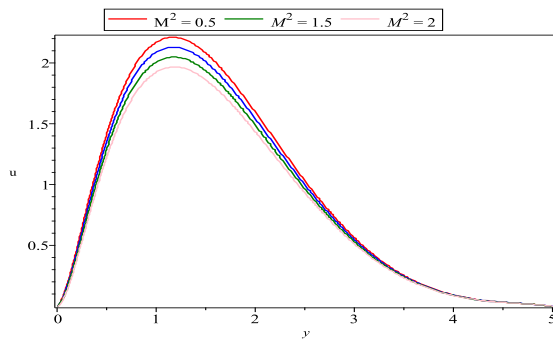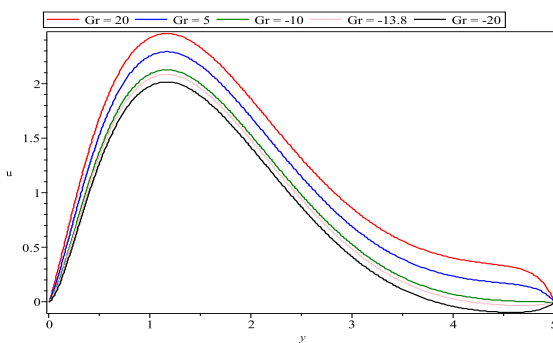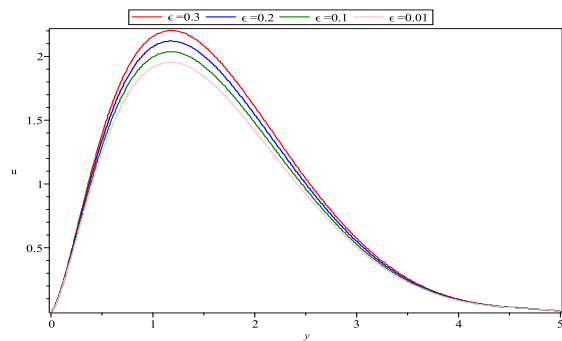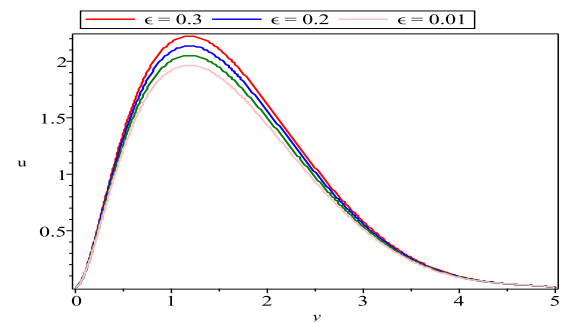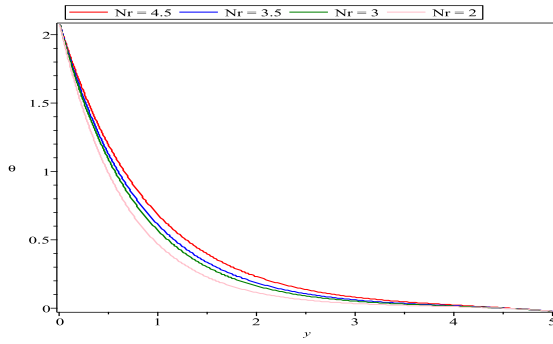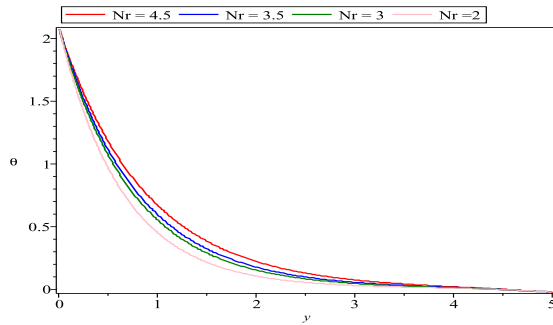

Figure 3. Velocity distribution for different values of M^2
(The graph plotted using backward differencing method)
$Sc = 0.22$, $Pr = 0.71$, $Nr = 1$, $Gm = 10$, $Gr = 10$, $\epsilon = 0.005$, $K = 10$, $nt = \pi/2$.

Figure 4. Velocity distribution for different values of Gr
$Sc = 0.22$, $Pr = 0.71$, $Nr = 1$, $Gm = 10$, $\epsilon = 0.005$, $K = 10$, $M^2 = 0.8$, $nt = \pi/2$.
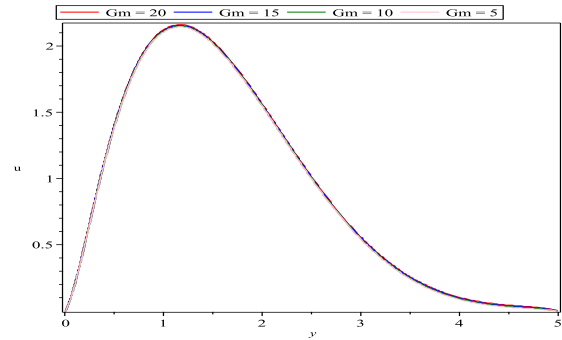
Figure 5. Velocity distribution for different values of Gm
$Sc = 0.22$, $Pr = 0.71$, $Nr = 1$, $Gm = 10$, $\epsilon = 0.005$, $K = 10$, $M^2 = 0.8$, $nt = \pi/2$.

Figure 6. Velocity distribution for different values of ϵ
(The graph plotted using central differencing method)
$Sc = 0.22$, $Pr = 0.71$, $Gr = 10$, $Gm = 10$, $Nr = 1$, $K = 10$, $M^2 = 0.8$, $nt = \pi/2$.

Figure 7. Velocity distribution for different values of ϵ
(The graph plotted using backward differencing method)
$Sc = 0.22$, $Pr = 0.71$, $Gm = 10$, $K = 10$, $Gr = 10$, $Nr = 1$, $M^2 = 0.8$, $nt = \pi/2$.

Figure 8. Temperature distribution for different values of Nr (The graph plotted using central differencing method) $Sc = 0.22$, $Pr = 0.2$, $Gm = 10$, $Gr = 10$, $\epsilon = 0.05$, $K = 10$, $M^2 = 0.8$, $nt = \pi/2$.

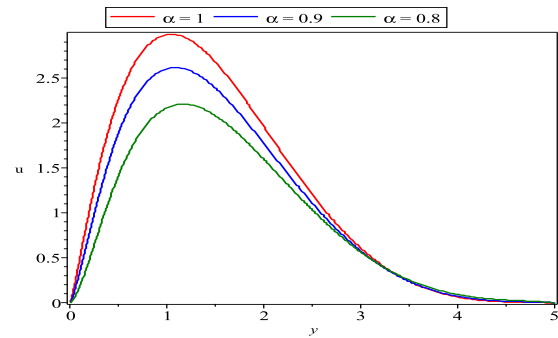**Figure 9.** Temperature distribution for different values of Nr (The graph plotted using backward differencing method) $Sc = 0.22$, $Pr = 0.2$, $Gm = 10$, $Gr = 10$, $\epsilon = 0.05$, $K = 10$, $M^2 = 0.8$, $nt = \pi/2$.


Figure 10. Temperature distribution for different values of Pr $Sc = 0.22$, $Nr = 1$, $Gm = 10$, $Gr = 10$, $\epsilon = 0.05$, $K = 10$, $M^2 = 0.8$, $nt = \pi/2$.

Figure 11. Concentration distribution for different values of Sc $Pr = 0.2$, $Nr = 1$, $Gm = 10$, $Gr = 10$, $\epsilon = 0.005$, $K = 10$, $M^2 = 0.8$, $nt = \pi/2$.

In Figures 12-19, different values of the derivative order α, with $\alpha = 1, 0.9$, and 0.8, were taken, and the changes in the results for various flow parameters were observed.

As the order of the fractional derivative approaches 1, the result obtained tends to resemble that of the classical derivative.

In Figure 12, with $Sc = 0.22$, $Pr = 0.71$, $Nr = 1$, $Gm = 10$, $Gr = 10$, $\epsilon = 0.005$, $K = 10$, $M^2 = 0.5$; and $nt = \pi/2$, the variation of the derivative order α for $\alpha = 1, 0.9$ and 0.8 was investigated. When α is taken as 0.9 and 0.8 a velocity profile similar to $\alpha = 1$ is obtained, but the flow velocity decreases.

In Figure 13, with $Sc = 0.22$, $Pr = 0.71$, $Nr = 1$, $Gr = 10$, $Gm = 20$, $\epsilon = 0.005$, $K = 10$, $M^2 = 0.8$ and $nt = \pi/2$, similar velocity profiles to those in Figure 12 were observed for varying values of the derivative order α.

Figure 14 is plotted using the data from the Figure 13. The only difference is that a backward difference has been used for the derivative term with respect to y. When comparing the two graphs, no significant difference is observed. This situation indicates that the obtained results are more reliable.

In Figure 15, with $Sc = 0.22$, $Pr = 0.71$, $Nr = 1$, $Gr = 10$, $Gm = 10$, $\epsilon = 0.3$, $K = 10$; $M^2 = 0.8$; and $nt = \pi/2$ similar velocity profiles to those in Figure 12 were observed for varying values of the derivative order α.

In Figure 16, with $Sc = 0.22$, $Pr = 0.2$, $Nr = 4.5$, $Gr = 10$, $Gm = 10$, $\epsilon = 0.05$; $K = 10$; $M^2 = 0.8$; and $nt = \pi/2$, similar velocity profiles to those in Figure 12 were observed for varying values of the derivative order α.

In Figure 17, with $Sc = 0.22$, $Pr = 0.2$, $Nr = 4.5$, $Gr = 10$, $Gm = 10$, $\epsilon = 0.05$, $K = 10$, $M^2 = 0.8$; and $nt = \pi/2$, it was observed that as α decreases, the temperature increases.

In Figure 18, with $Sc = 0.22$, $Pr = 0.025$, $Nr = 1$, $Gr = 10$, $Gm = 10$, $\epsilon = 0.05$, $K = 10$, $M^2 = 0.8$; and $nt = \pi/2$, it was observed that as α decreases, the temperature increases.

In Figure 19, with $Sc = 0.01$, $Pr = 0.2$, $Nr = 1$, $Gr = 10$, $Gm = 10$, $\epsilon = 0.05$, $K = 10$, $M^2 = 0.8$; and $nt = \pi/2$, it was observed that as α decreases, the concentration increases.

It is evident that the distributions of velocity, temperature, and concentration are significantly impacted by the fractional order parameter.

Figure 14. Velocity distribution for different values of α and $Gr=20$ (The graph plotted using backward differencing method) $Sc = 0.22$, $Pr = 0.71$, $Gm = 10$, $\epsilon = 0.005$, $Nr = 1$, $K = 10$, $M^2 = 0.8$, $nt = \pi/2$

.
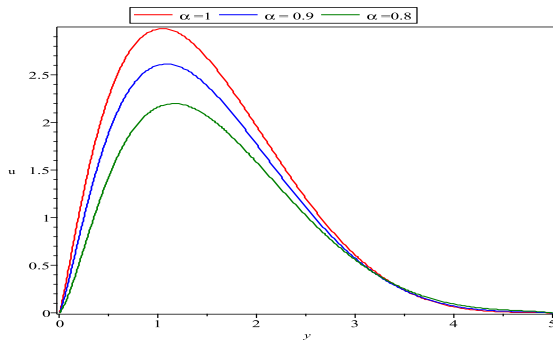
Figure 12. Velocity distribution for different values of α and $M^2=0.5$ $Sc = 0.22$, $Pr = 0.71$, $Gm = 10$, $Gr = 10$, $\epsilon = 0.05$, $Nr = 1$, $K = 10$, $nt = \pi/2$

.
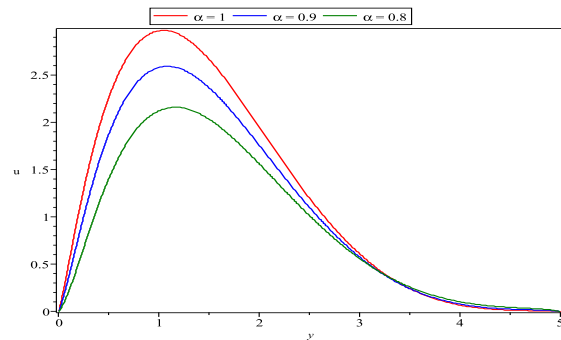
Figure 15. Velocity distribution for different values of α and $Gm=20$ $Sc = 0.22$, $Pr = 0.71$, $Gr = 10$, $\epsilon = 0.05$, $Nr = 1$, $K = 10$, $M^2 = 0.8$, $nt = \pi/2$

.
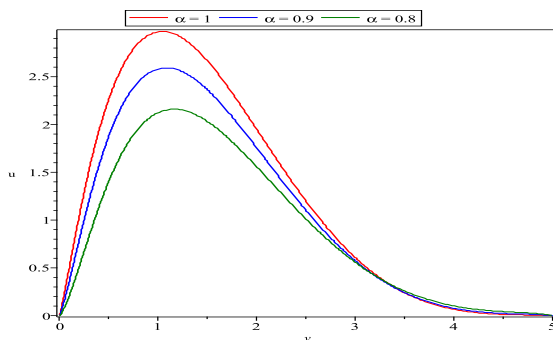
Figure 13. Velocity distribution for different values of α and $Gr=20$ (The graph plotted using central differencing method) $Sc = 0.22$, $Pr = 0.71$, $Gm = 10$, $\epsilon = 0.005$, $Nr = 1$, $K = 10$, $M^2 = 0.8$, $nt = \pi/2$

.
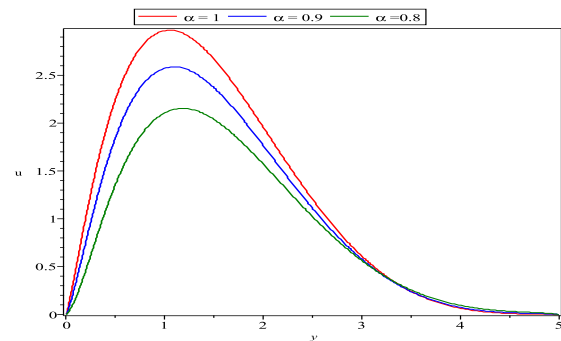
Figure 16. Velocity distribution for different values of α and $\epsilon=0.3$. $Sc = 0.22$, $Pr = 0.71$, $Nr = 1$, $Gm = 10$, $Gr = 10$, $K = 10$, $M^2 = 0.8$, $nt = \pi/2$.
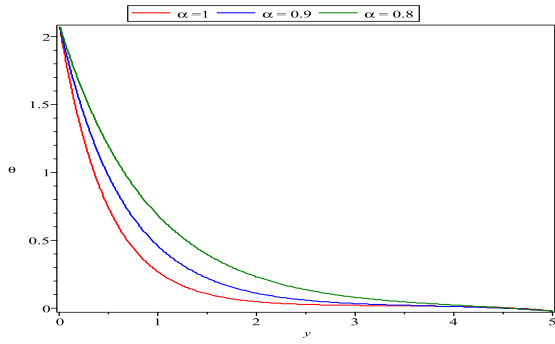
Figure 17. Temperature distribution for different values of α and Nr=4.5.
$Sc = 0.22$, $Pr = 0.2$, $Gm = 10$,
$Gr = 10$, $\epsilon = 0.05$, $K = 10$,
$M^2 = 0.8$, $nt = \pi/2$.
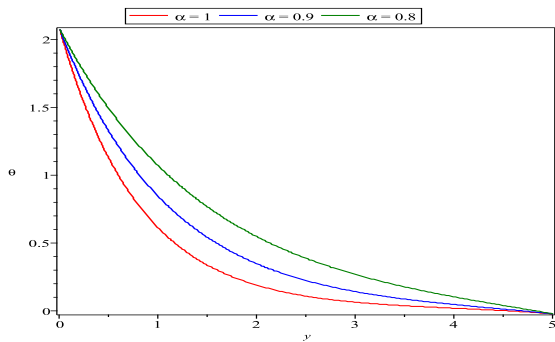
Figure 18. Temperature distribution for different values of α and Pr=0.025.
$Sc = 0.22$, $Nr = 1$, $Gm = 10$,
$Gr = 10$, $\epsilon = 0.05$, $K = 10$,
$M^2 = 0.8$, $nt = \pi/2$

.
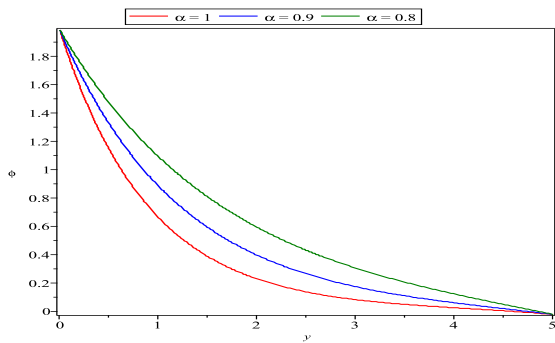
Figure 19. Concentration distribution for different values of α and $Sc = 0.01$,
$Pr = 0.2$, $Nr = 1$, $Gm = 10$,
$Gr = 10$, $\epsilon = 0.005$, $K = 10$,
$M^2 = 0.8$, $nt = \pi/2$

.

4.1.2. Blood flow problem under the influence of MHD in non-porous media

In this section, an unstable MHD blood flow problem along a non-porous vessel has been examined.

Figures 20, 21, 22, 23 and 24 show the variations in blood flow velocity. Similar to the porous medium, the velocity first increases and then decreases. The effect of parameters is very similar to that in the porous medium.

In Figure 20, it is observed that the axial velocity decreases as M^2 increases. In Figure 21, when the Gr number decreases, the velocity also decreases. Figure 22 shows that when Gm decreases, the velocity decreases similar to what is observed in Figure 21. Figure 23 is plotted using the data from the Figure 22. The only difference is that a backward difference has been used for the derivative term with respect to y When comparing the two graphs, no significant difference is observed. This situation indicates that the obtained results are more reliable. In Figure 24, it is observed that the velocity also decreases when ϵ decreases.
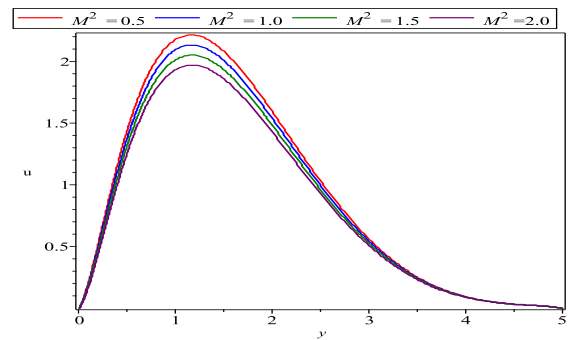
Figure 20. Velocity distribution for different values of M^2 in non-porous media
$Sc = 0.22$, $Pr = 0.71$, $Nr = 1$,
$Gm = 10$, $Gr = 10$, $\epsilon = 0.005$,
$nt = \pi/2$.

.
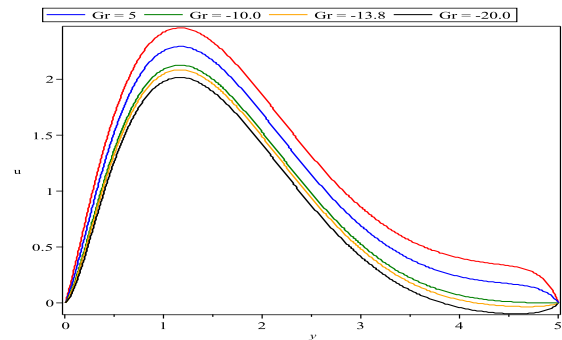
Figure 21. Velocity distribution for different values of Gr in non-porous media
$Sc = 0.22$, $Pr = 0.71$, $Nr = 1$,
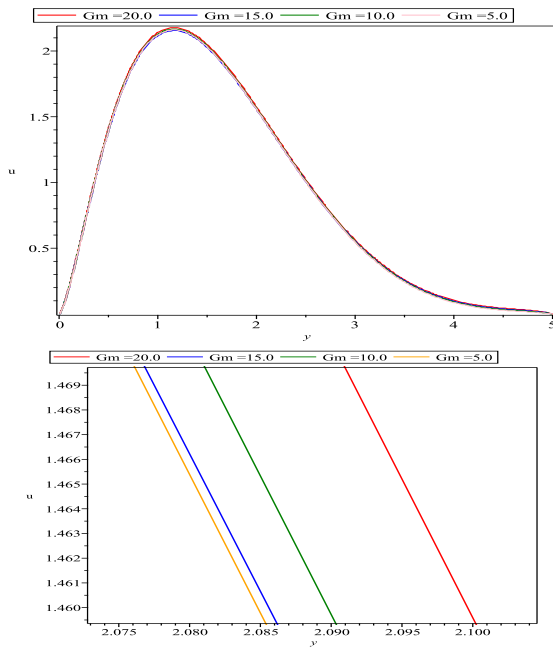$Gm = 10$, $\epsilon = 0.005$, $nt = \pi/2$.

.

Figure 22. Velocity distribution for different values of Gm in non-porous media
(The graph plotted using central differencing method)
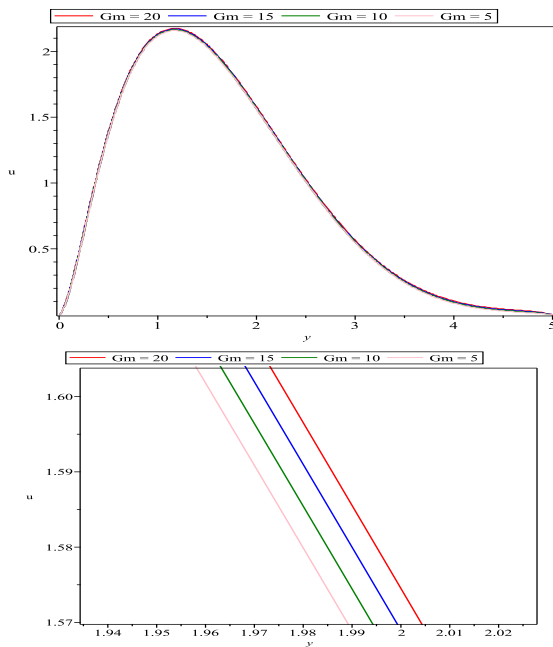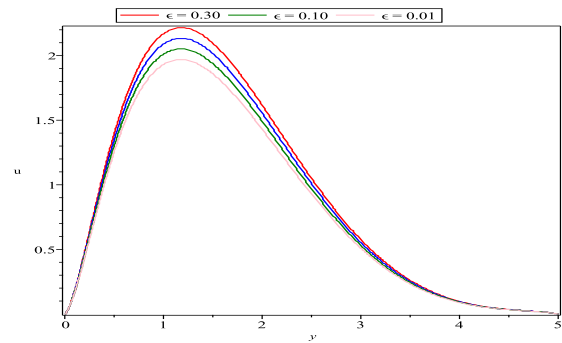$Sc = 0.22$, $Pr = 0.71$, $M^2 = 0.8$, $Gr = 10$, $\epsilon = 0.005$, $Nr = 1$, $nt = \pi/2$

Figure 23. Velocity distribution for different values of Gm in non-porous media
(The graph plotted using backward differencing method)
$Sc = 0.22$, $Pr = 0.71$, $M^2 = 0.8$, $Gr = 10$, $\epsilon = 0.005$, $Nr = 1$, $nt = \pi/2$

Figure 24. Velocity distribution for different values of ϵ in non-porous media
$Sc = 0.22$, $Pr = 0.71$, $M^2 = 0.8$, $Gr = 10$, $Gm = 10$, $Nr = 1$, $nt = \pi/2$.

5. Conclusions

In this article, a flow model considering the MHD effect and the time-fractional derivative in a porous medium, with the fluid assumed to be blood, was initially studied. Finite differences and Grünwald-Letnikov approaches were employed in numerical computations. The research aimed to investigate whether there were differences between integer-order derivatives and fractional-order derivatives for varying parameter values. For example, the increase in the M number has led to a decrease in speed, indicating a decrease in velocity due to the effect of the magnetic field. Erdem Murat, and their colleagues have also obtained similar results. They explained this change as being caused by the retarding effect of the Lorentz force [26]. When Figure 8 is examined, it can be seen that as Nr decreases, the temperature also decreases. Similar results were obtained by C. D. K. Bansi and colleagues [27].

Also when $Sc = 0.22, Pr = 0.71, Nr = 1, Gm = 10, Gr = 10, \epsilon = 0.005, K = 10, M^2 = 0.5$ and $nt = \pi/2$, the change in the order of the derivative was examined for $\alpha = 1.0, 0.9$, and 0.8. When α decreased to 0.9, it exhibited a similar but lower velocity profile to $\alpha = 1$, and when $\alpha = 0.8$, a lower velocity profile compared to the previous case was observed. As we moved away from the integer order derivative, the flow velocity decreased.

Additionally, in this study, the non-porous medium scenario was considered and the investigation showed that there was not a significant difference in the flow model with varying parameters and fractional derivatives when the medium is non-porous.

6. Symbols

Gr,   Grashof number,

Gm, solute Grashof number

K,   permeability parameter,

M,   Hartmann number,

Nr, radiation parameter,

Pr, Prandtl number,

Sc, Schmidt number,

u,   dimensionless velocity,

ϵ,   small positive constant ($\ll 1$),

g,   acceleration due to gravity,

β,   coefficient of thermal expansion,

β^*, coefficient of thermal expansion with concentration,

B_0, applied magnetic field,

v_0, scale of suction velocity (non-zero constant),

ν,   kinematic coefficient of viscosity,

σ,   electrical conductivity,

ρ,   density of fluid,

T,   temperature,

T_w, surface temperature,

T_∞, temperature of the ambient fluid,

C,   concentration,

C_w, concentration of fluid at the sheet,

C_∞, concentration of the ambient fluid,

D,   thermal molecular diffusivity,

k_1,   thermal conductivity,

K_0, constant permeability of the medium,

n',   frequency of oscillation,

q_r,   radiative heat flux,

c_p,   specific heat at constant pressure,

σ^*, Stefan-Boltzmann constant,

k^*,   mean absorption coefficient.

References

[1] Kucur, M. (2021). Stenoz oluşmuş y-seklinde bir damarın akışkan-katı etkileşiminin openfoam ile analizi. *Avrupa Bilim ve Teknoloji Dergisi*, (32), 872-877.

[2] Ku, D .N. (1997). Blood flow in arteries. *Annual Review of Fluid Mechanics*, 29(1), 399-434.

[3] Panton, R. L. (2024). *Incompressible Flow*, John Wiley & Sons, New York.

[4] Misra, J. C., Shit, G. C.(2019). Biomagnetic viscoelastic fluid flow over a stretching sheet. *Applied Mathematics And Computation*, 210(2), 350-361

[5] Bonyah, E., Sagoe, A. K., Kumar, D., & Deniz, S. (2021). Fractional optimal control dynamics of coronavirus model with Mittag–Leffler law. *Ecological Complexity*, 45, 100880.

[6] Yüce, A. (2022). Kesir dereceli temel transfer fonksiyon yapıları için yaklaşık analitik zaman cevabı modeli. *Adıyaman Üniversitesi Mühendislik Bilimleri Dergisi*, 9(16), 49-60.

[7] Modanlı, M., & Aksoy, A. (2022). Kesirli telegraf kısmi diferansiyel denklemin varyasyonel iterasyon metoduyla çözümü. *Balıkesir Üniversitesi Fen Bilimleri Enstitüsü Dergisi*, 24(1), 182-196.

[8] Miller K. S., & Ross B., (1993). *An Introduction To The Fractional Calculus And Fractional Differential Equations*, Wiley, New York.

[9] Çağ, C., (2010). *Gamma fonksiyonu ile ilgili bazı eşitsizlikler*, M.Sc. Thesis. Yüzüncü Yıl Üniversitesi.

[10] Modanlı, M. (2019). On the numerical solution for third order fractional partial differential equation by difference scheme method. *An International Journal of Optimization and Control: Theories & Applications (IJOCTA)*, 9(3), 1-5.

[11] Kalimuthu, K., & Muthuvel, K. (2023). A study on the approximate controllability results of fractional stochastic integro-differential inclusion systems via sectorial operators. *An International Journal of Optimization and Control: Theories & Applications (IJOCTA)*, 13(2), 193-204.

[12] Misra, J. C., Shit, G. C., & Rath, H. J. (2008). Flow and heat transfer of a MHD viscoelastic fluid in a channel with stretching walls: some applications to Haemodynamics. *Computers & Fluids*, 37(1), 1-11.

[13] Abel, M. S. & Mahesha N., (2008). Heat transfer in MHD viscoelastic fluid flow over a stretching sheet with variable thermal conductivity, non-uniform heat source and radiation. *Applied Mathematical Modelling*, 32(10), 1965-1983.

[14] Misra J. C. & Adhikary S. D. (2016). MHD oscillatory channel flow, heat and mass transfer in A physiological fluid in presence of chemical reaction. *Alexandria Engineering Journal*, 55(1), 287-297.

[15] Nagendramma V., Kumar K., Prasad D., Leelaratnam A. & Varma K. (2016). Multiple slips and thermophoresis effects of maxwell nanofluid over a permeable stretching surface in the presence of radiation and dissipation. *Journal Of Nanofluids*, 5, 1-9.

[16] Maiti, S., Shaw, S. & Shit, G. C. (2020). Caputo–Fabrizio fractional order model on MHD blood flow with heat and mass transfer through a porous vessel in the presence of thermal radiation. *Physica A: Statistical Mechanics and İts Applications*, 540, 123149.

[17] Tripathi, B. & Sharma, B. K. (2018). Effect of variable viscosity on MHD inclined arterial blood flow with chemical reaction. *International Journal of Applied Mechanics and Engineering*, 23(3), 767-785.

[18] Alam, M. J., Murtaza, M. G., Tzirtzilakis, E. E. & Ferdows, M. (2021). Effect of thermal radiation on biomagnetic fluid flow and heat transfer

over an unsteady stretching sheet. *Computer Assisted Methods in Engineering and Science*, 28(2), 81-104.

[19] Raptis, A. A. (1983). Effects of a magnetic field on the free convective flow through a porous medium bounded by an infinite vertical porous plate with constant heat flux. *Journal of the Franklin Institute*, 316(6), 445-449.

[20] Dinarvand, S., Nademi, Rostami, M., Dinarvand, R. & Pop, I. (2019). Improvement of drug delivery micro-circulatory system with a novel pattern of Cuo-Cu/blood hybrid nanofluid flow towards a porous stretching sheet. *International Journal of Numerical Methods for Heat & Fluid Flow*, 29(11), 4408-4429.

[21] Nader, E., Skinner, S., Romana, M., Fort, R., Lemonne, N., Guillot, N., Gauthier, A., Antoine-Jonville, S., Renoux, C., Hardy-Dessources, M-D., Stauffer, E., Joly, P., Bertrand, Y. & Connes, P. (2019). Blood rheology: key parameters, impact on blood flow, role in sickle cell disease and effects of exercise. *Frontiers In Physiology*, 29(11), 10, 1329.

[22] Sinha, A. & Misra, J. C. (2012). Numerical study of flow and heat transfer during oscillatory blood flow in diseased arteries in presence of magnetic fields. *Applied Mathematics And Mechanics*, 33, 649-662.

[23] Brewster, M. Q. (1992). *Thermal Radiative Transfer Properties*. John Wiley & Sons, New York.

[24] Polat, R. (2018). Finite difference solution to the space-time fractional partial differential-difference toda lattice equations. *Journal of Mathematical Sciences and Modelling*, 1(3), 202-205.

[25] Cui, M. (2009). Compact finite difference method for the fractional diffusion equation. *Journal of Computational Physics*, 228(20), 7792-7804.

[26] Erdem, M., Fırat, M., & Varol, Y. (2021). Al2O3-Su nanoakışkanının manyetik alan altında akış karakteristiklerinin sayısal analizi. *Fırat Üniversitesi Mühendislik Bilimleri Dergisi*, 33(2), 401-412.

[27] Bansi, C. D. K., Tabi, C. B., Motsumi, T. G., & Mohamadou, A. (2018). Fractional blood flow in oscillatory arteries with thermal radiation and magnetic field effects. *Journal of Magnetism and Magnetic Materials*, 456, 38-45.

Fatma Ayaz *is a professor in the Department of Mathematics at Gazi University, specializing in applied mathematics. She completed her Ph.D. at the University of Leeds (United Kingdom). Her research interests include numerical and approximate solutions of differential equations, natural sciences, engineering, and technology.*
🆔 https://orcid.org/0000-0003-4346-9821

Kübra Heredağ *is a doctoral student in the field of applied mathematics at the Mathematics Department of the Institute of Science at Gazi University. She works as a mathematics teacher at the Ministry of National Education in Ankara. She completed her undergraduate studies at Karadeniz Technical University and her graduate studies at Karabük University.*
🆔 https://orcid.org/0000-0002-1830-1093

INSTRUCTIONS FOR AUTHORS

Aims and Scope

An International Journal of Optimization and Control: Theories & Applications (IJOCTA) is a scientific, peer-reviewed, open-access journal that publishes original research papers and review articles of high scientific value in all areas of applied mathematics, optimization and control. It aims to focus on multi/inter-disciplinary research into the development and analysis of new methods for the numerical solution of real-world applications in engineering and applied sciences. The basic fields of this journal cover mathematical modeling, computational methodologies and (meta)heuristic algorithms in optimization, control theory and their applications. Note that new methodologies for solving recent optimization problems in operations research must conduct a comprehensive computational study and/or case study to show their applicability and practical relevance.

Journal Topics

The topics covered in the journal are (not limited to):

Applied Mathematics, Financial Mathematics, Control Theory, Optimal Control, Fractional Calculus and Applications, Modeling of Bio-systems for Optimization and Control, Linear Programming, Nonlinear Programming, Stochastic Programming, Parametric Programming, Conic Programming, Discrete Programming, Dynamic Programming, Nonlinear Dynamics, Stochastic Differential Equations, Optimization with Artificial Intelligence, Operational Research in Life and Human Sciences, Heuristic and Metaheuristic Algorithms in Optimization, Applications Related to Optimization in Engineering.

Submission of Manuscripts

New Submissions

Solicited and contributed manuscripts should be submitted to IJOCTA via the journal's online submission system. You need to make registration prior to submitting a new manuscript (please click here to register and do not forget to define yourself as an "Author" in doing so). You may then click on the "New Submission" link on your User Home.

IMPORTANT: If you already have an account, please click here to login. It is likely that you will have created an account if you have reviewed or authored for the journal in the past.

On the submission page, enter data and answer questions as prompted. Click on the "Next" button on each screen to save your work and advance to the next screen. The names and contact details of at least four internationally recognized experts who can review your manuscript should be entered in the "Comments for the Editor" box.

You will be prompted to upload your files: Click on the "Browse" button and locate the file on your computer. Select the description of the file in the drop down next to the Browse button. When you have selected all files you wish to upload, click the "Upload" button. Review your submission before sending to the Editors. Click the "Submit" button when you are done reviewing. Authors are responsible for verifying all files have uploaded correctly.

You may stop a submission at any phase and save it to submit later. Acknowledgment of receipt of the manuscript by IJOCTA Online Submission System will be sent to the corresponding author, including an assigned manuscript number that should be included in all subsequent correspondence. You can also log-on to submission web page of IJOCTA any time to check the status of your manuscript. You will receive an e-mail once a decision has been made on your manuscript.

Each manuscript must be accompanied by a statement that it has not been published elsewhere and that it has not been submitted simultaneously for publication elsewhere.

Manuscripts can be prepared using LaTeX (.tex) or MSWord (.docx). However, manuscripts with heavy mathematical content will only be accepted as LaTeX files.

Preferred first submission format (for reviewing purpose only) is Portable Document File (.pdf). Please find below the templates for first submission.

Click here to download Word template for first submission (.docx)

Click here to download LaTeX template for first submission (.tex)

Revised Manuscripts

Revised manuscripts should be submitted via IJOCTA online system to ensure that they are linked to the original submission. It is also necessary to attach a separate file in which a point-by-point explanation is given to the specific points/questions raised by the referees and the corresponding changes made in the revised version.

To upload your revised manuscript, please go to your author page and click on the related manuscript title. Navigate to the "Review" link on the top left and scroll down the page. Click on the "Choose File" button under the "Editor Decision" title, choose the revised article (in pdf format) that you want to submit, and click on the "Upload" button to upload the author version. Repeat the same steps to upload the "Responses to Reviewers/Editor" file and make sure that you click the "Upload" button again.

To avoid any delay in making the article available freely online, the authors also need to upload the source files (Word or LaTex) when submitting revised manuscripts. Files can be compressed if necessary. The two-column final submission templates are as follows:

Click here to download Word template for final submission (.docx)

Click here to download LaTeX template for final submission (.tex)

Authors are responsible for obtaining permission to reproduce copyrighted material from other sources and are required to sign an agreement for the transfer of copyright to IJOCTA.

Article Processing Charges

There are **no charges** for submission and/or publication.

English Editing

Papers must be in English. Both British and American spelling is acceptable, provided usage is consistent within the manuscript. Manuscripts that are written in English that is ambiguous or incomprehensible, in the opinion of the Editor, will be returned to the authors with a request to resubmit once the language issues have been improved. This policy does not imply that all papers must be written in "perfect" English, whatever that may mean. Rather, the criteria require that the intended meaning of the authors must be clearly understandable, i.e., not obscured by language problems, by referees who have agreed to review the paper.

Presentation of Papers

Manuscript style

Use a standard font of the **11-point type: Times New Roman** is preferred. It is necessary to single line space your manuscript. Normally manuscripts are expected not to exceed 25 single-spaced pages including text, tables, figures and bibliography. All illustrations, figures, and tables are placed within the text at the appropriate points, rather than at the end.

During the submission process you must enter: (1) the full title, (2) names and affiliations of all authors and (3) the full address, including email, telephone and fax of the author who is to check the proofs. Supply a brief **biography** of each author at the end of the manuscript after references.

- Include the name(s) of any **sponsor(s)** of the research contained in the paper, along with **grant number(s).**
- Enter an **abstract** of no more than 250 words for all articles.

Keywords

Authors should prepare no more than 5 keywords for their manuscript.

Maximum five **AMS Classification number** (http://www.ams.org/mathscinet/msc/msc2010.html) of the study should be specified after keywords.

Writing Abstract

An abstract is a concise summary of the whole paper, not just the conclusions. The abstract should be no more than 250 words and convey the following:

1. An introduction to the work. This should be accessible by scientists in any field and express the necessity of the experiments executed.
2. Some scientific detail regarding the background to the problem.
3. A summary of the main result.
4. The implications of the result.
5. A broader perspective of the results, once again understandable across scientific disciplines.

It is crucial that the abstract conveys the importance of the work and be understandable without reference to the rest of the manuscript to a multidisciplinary audience. Abstracts should not contain any citation to other published works.

Reference Style

Reference citations in the text should be identified by numbers in square brackets "[ ]". All references must be complete and accurate. Please ensure that every reference cited in the text is also present in the reference list (and vice versa). Online citations should include date of access. References should be listed in the following style:

Journal article

Author, A.A., & Author, B. (Year). Title of article. Title of Journal, Vol(Issue), pages.

Castles, F.G., Curtin, J.C., & Vowles, J. (2006). Public policy in Australia and New Zealand: The new global context. Australian Journal of Political Science, 41(2), 131–143.

Book

Author, A. (Year). Title of book. Publisher, Place of Publication.

Mercer, P.A., & Smith, G. (1993). Private Viewdata in the UK. 2nd ed. Longman, London.

Chapter

Author, A. (Year). Title of chapter. In: A. Editor and B. Editor, eds. Title of book. Publisher, Place of publication, pages.

Bantz, C.R. (1995). Social dimensions of software development. In: J.A. Anderson, ed. Annual review of software management and development. CA: Sage, Newbury Park, 502–510.

Internet document

Author, A. (Year). Title of document [online]. Source. Available from: URL [Accessed (date)].

Holland, M. (2004). Guide to citing Internet sources [online]. Poole, Bournemouth University. Available from: http://www.bournemouth.ac.uk/library/using/guide_to_citing_internet_sourc.html [Accessed 4 November 2004].

Newspaper article

Author, A. (or Title of Newspaper) (Year). Title of article. Title of Newspaper, day Month, page, column.

Independent (1992). Picking up the bills. Independent, 4 June, p. 28a.

Thesis

Author, A. (Year). Title of thesis. Type of thesis (degree). Name of University.

Agutter, A.J. (1995). The linguistic significance of current British slang. PhD Thesis. Edinburgh University.

<u>Illustrations</u>

Illustrations submitted (line drawings, halftones, photos, photomicrographs, etc.) should be clean originals or digital files. Digital files are recommended for highest quality reproduction and should follow these guidelines:

- 300 dpi or higher
- Sized to fit on journal page
- TIFF or JPEG format only
- Embedded in text files and submitted as separate files (if required)

<u>Tables and Figures</u>

Tables and figures (illustrations) should be embedded in the text at the appropriate points, rather than at the end. A short descriptive title should appear above each table with a clear legend and any footnotes suitably identified below.

<u>Proofs</u>

Page proofs are sent to the designated author using IJOCTA EProof system. They must be carefully checked and returned within 48 hours of receipt.

<u>Offprints/Reprints</u>

Each corresponding author of an article will receive a PDF file of the article via email. This file is for personal use only and may not be copied and disseminated in any form without prior written permission from IJOCTA.

Submission Preparation Checklist

As part of the submission process, authors are required to check off their submission's compliance with all of the following items, and submissions may be returned to authors that do not adhere to these guidelines.

1. The submission has not been previously published, nor is it before another journal for consideration (or an explanation has been provided in Comments for the Editor).
2. The paper is in PDF format and prepared using the IJOCTA's two-column template.
3. All references cited in the manuscript have been listed in the References list (and vice-versa) following the referencing style of the journal.
4. There is no copyright material used in the manuscript (or all necessary permissions have been granted).
5. Details of all authors have been provided correctly.
6. ORCID profile numbers of "all" authors are mandatory, and they are provided at the end of the manuscript as in the template (visit https://orcid.org for more details on ORCID).
7. The text adheres to the stylistic and bibliographic requirements outlined in the Author Guidelines.
8. Maximum five AMS Classification number (http://www.ams.org/mathscinet/msc/msc2010.html) of the study have been provided after keywords.
9. The names and email addresses of at least FOUR (4) possible reviewers have been indicated in "Comments for the Editor" box in "Paper Submission Step 1-Start". Please note that at least two of the recommendations should be from different countries. Avoid suggesting reviewers you have a conflict of interest.

Peer Review Process

All contributions, prepared according to the author guidelines and submitted via IJOCTA online submission system are evaluated according to the criteria of originality and quality of their scientific content. The corresponding author will receive a confirmation e-mail with a reference number assigned to the paper, which he/she is asked to quote in all subsequent correspondence.

All manuscripts are first checked by the Technical Editor using plagiarism detection software (iThenticate) to verify originality and ensure the quality of the written work. If the result is not satisfactory (i.e. exceeding the limit of 30% of overlapping), the submission is rejected and the author is notified.

After the plagiarism check, the manuscripts are evaluated by the Editor-in-Chief and can be rejected without reviewing if considered not of sufficient interest or novelty, too preliminary or out of the scope of the journal. If the manuscript is considered suitable for further evaluation, it is first sent to the Area Editor. Based on his/her opinion the paper is then sent to at least two independent reviewers. Each reviewer is allowed up to four weeks to return his/her feedback but this duration may be extended based on his/her availability. IJOCTA has instituted a blind peer review process where the reviewers' identities are not known to authors. When the reviews are received, the Area Editor gives a decision and lets the author know it together with the reviewer comments and any supplementary files.

Should the reviews be positive, the authors are expected to submit the revised version usually within two months the editor decision is sent (this period can be extended when the authors contact to the editor and let him/her know that they need extra time for resubmission). If a revised paper is not resubmitted within the deadline, it is considered as a new submission after all the changes requested by reviewers have been made. Authors are required to submit a new cover letter, a response to reviewers letter and the revised manuscript (which ideally shows the revisions made in a different color or highlighted). If a change in authorship (addition or removal of author) has occurred during the revision, authors are requested to clarify the reason for change, and all authors (including the removed/added ones) need to submit a written consent for the change. The revised version is evaluated by the Area editor and/or reviewers and the Editor-in-Chief brings a decision about final acceptance based on their suggestions. If necessary, further revision can be asked for to fulfil all the requirements of the reviewers.

When a manuscript is accepted for publication, an acceptance letter is sent to the corresponding author and the authors are asked to submit the source file of the manuscript conforming to the IJOCTA two-column final submission template. After that stage, changes of authors of the manuscript are not possible. The manuscript is sent to the Copyeditor and a linguistic, metrological and technical revision is made, at which stage the authors are asked to make the final corrections in no more than a week. The layout editor prepares the galleys and the authors receive the galley proof for final check before printing. The authors are expected to correct only typographical errors on the proofs and return the proofs within 48 hours. After the final check by the layout editor and the proofreader, the manuscript is assigned a DOI number, made publicly available and listed in the forthcoming journal issue. After printing the issue, the corresponding metadata and files published in this issue are sent to the databases for indexing.
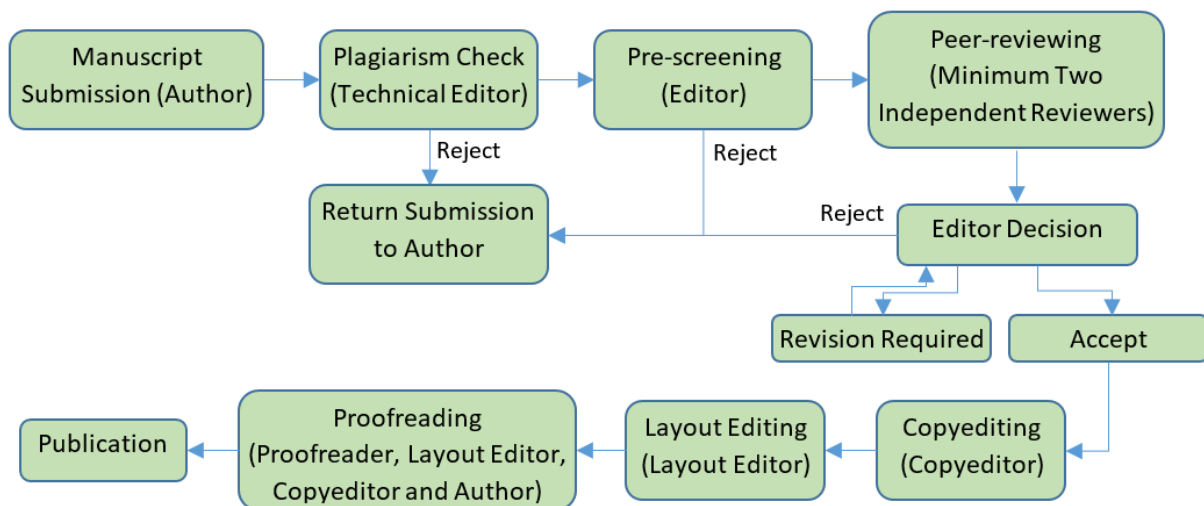
Publication Ethics and Malpractice Statement

IJOCTA is committed to ensuring ethics in publication and quality of articles. Conforming to standards of expected ethical behavior is therefore necessary for all parties (the author, the editor(s), the peer reviewer) involved in the act of publishing.

International Standards for Editors

The editors of the IJOCTA are responsible for deciding which of the articles submitted to the journal should be published considering their intellectual content without regard to race, gender, sexual orientation, religious belief, ethnic origin, citizenship, or political philosophy of the authors. The editors may be guided by the policies of the journal's editorial board and constrained by such legal requirements

as shall then be in force regarding libel, copyright infringement and plagiarism. The editors may confer with other editors or reviewers in making this decision. As guardians and stewards of the research record, editors should encourage authors to strive for, and adhere themselves to, the highest standards of publication ethics. Furthermore, editors are in a unique position to indirectly foster responsible conduct of research through their policies and processes.

To achieve the maximum effect within the research community, ideally all editors should adhere to universal standards and good practices.

- Editors are accountable and should take responsibility for everything they publish.
- Editors should make fair and unbiased decisions independent from commercial consideration and ensure a fair and appropriate peer review process.
- Editors should adopt editorial policies that encourage maximum transparency and complete, honest reporting.
- Editors should guard the integrity of the published record by issuing corrections and retractions when needed and pursuing suspected or alleged research and publication misconduct.
- Editors should pursue reviewer and editorial misconduct.
- Editors should critically assess the ethical conduct of studies in humans and animals.
- Peer reviewers and authors should be told what is expected of them.
- Editors should have appropriate policies in place for handling editorial conflicts of interest.

Reference:

Kleinert S & Wager E (2011). Responsible research publication: international standards for editors. A position statement developed at the 2nd World Conference on Research Integrity, Singapore, July 22-24, 2010. Chapter 51 in: Mayer T & Steneck N (eds) Promoting Research Integrity in a Global Environment. Imperial College Press / World Scientific Publishing, Singapore (pp 317-28). (ISBN 978-981-4340-97-7) [Link].

International Standards for Authors

Publication is the final stage of research and therefore a responsibility for all researchers. Scholarly publications are expected to provide a detailed and permanent record of research. Because publications form the basis for both new research and the application of findings, they can affect not only the research community but also, indirectly, society at large. Researchers therefore have a responsibility to ensure that their publications are honest, clear, accurate, complete and balanced, and should avoid misleading, selective or ambiguous reporting. Journal editors also have responsibilities for ensuring the integrity of the research literature and these are set out in companion guidelines.

- The research being reported should have been conducted in an ethical and responsible manner and should comply with all relevant legislation.
- Researchers should present their results clearly, honestly, and without fabrication, falsification or inappropriate data manipulation.
- Researchers should strive to describe their methods clearly and unambiguously so that their findings can be confirmed by others.
- Researchers should adhere to publication requirements that submitted work is original, is not plagiarised, and has not been published elsewhere.
- Authors should take collective responsibility for submitted and published work.
- The authorship of research publications should accurately reflect individuals' contributions to the work and its reporting.
- Funding sources and relevant conflicts of interest should be disclosed.
- When an author discovers a significant error or inaccuracy in his/her own published work, it is the author's obligation to promptly notify the journal's Editor-in-Chief and cooperate with them to either retract the paper or to publish an appropriate erratum.

Reference:

Wager E & Kleinert S (2011) Responsible research publication: international standards for authors. A position statement developed at the 2nd World Conference on Research Integrity, Singapore, July 22-24, 2010. Chapter 50 in: Mayer T & Steneck N (eds) Promoting Research Integrity in a Global Environment.

Basic principles to which peer reviewers should adhere

Peer review in all its forms plays an important role in ensuring the integrity of the scholarly record. The process depends to a large extent on trust and requires that everyone involved behaves responsibly and ethically. Peer reviewers play a central and critical part in the peer-review process as the peer review assists the Editors in making editorial decisions and, through the editorial communication with the author, may also assist the author in improving the manuscript.

Peer reviewers should:

- respect the confidentiality of peer review and not reveal any details of a manuscript or its review, during or after the peer-review process, beyond those that are released by the journal;
- not use information obtained during the peer-review process for their own or any other person's or organization's advantage, or to disadvantage or discredit others;
- only agree to review manuscripts for which they have the subject expertise required to carry out a proper assessment and which they can assess within a reasonable time-frame;
- declare all potential conflicting interests, seeking advice from the journal if they are unsure whether something constitutes a relevant conflict;
- not allow their reviews to be influenced by the origins of a manuscript, by the nationality, religion, political beliefs, gender or other characteristics of the authors, or by commercial considerations;
- be objective and constructive in their reviews, refraining from being hostile or inflammatory and from making libellous or derogatory personal comments;
- acknowledge that peer review is largely a reciprocal endeavour and undertake to carry out their fair share of reviewing, in a timely manner;
- provide personal and professional information that is accurate and a true representation of their expertise when creating or updating journal accounts.

Reference:

Homes I (2013). COPE Ethical Guidelines for Peer Reviewers, March 2013, v1 [Link].

CONTENTS